Two-dimensional Materials for Energy Storage and Harvesting

A report submitted to the University of Dublin, Trinity College

for the degree of Doctor of Philosophy in Chemistry

By

Meiying Liang

Under the supervision of Prof. Valeria Nicolosi

Feb 2020

Trinity College Dublin

I declare that this thesis has not been submitted as an exercise for a degree at this or any other university and it is entirely my own work.

I agree to deposit this thesis in the University's open access institutional repository or allow the Library to do so on my behalf, subject to Irish Copyright Legislation and Trinity College Library conditions of use and acknowledgement.

I consent to the examiner retaining a copy of the thesis beyond the examining period, should they so wish (EU GDPR May 2018).

Meiying Jenny Liang

……

Meiying Liang

Summary

Energy storage and harvesting have become a global concern due to the ever-increasing demand for energy and upcoming depletion of natural resources. As a family of Van der Waals layered crystals, metal chalcogenides (MCs) and transition metal chalcogenides (TMDs) possess unique electronic and photonic properties, enabling high-performance electronic devices for broad applications. However, the potential application of MCs and TMDs in energy devices remains relatively unexplored, partially due to their challenges in exfoliation as well as poor electrical conductivity. This PhD thesis mainly discussed the preparation and energy application of two-dimensional (2D) metal chalcogenides (MCs) and transition metal chalcogenides (TMDs). Layered MCs and TMDs crystals consist of strong in-plane covalently bonded metal (M) and chalcogenide (X) layers (e.g. X-M-X or X-M-M-X) that interact weakly in the out-of-plane direction *via* Wan der Waals forces. As such, layered MCs and TMDs allow the efficient exfoliation into few-layered flakes. To obtain 2D MCs and TMDs nanosheets, the layered crystals were sonicated in a certain solvent. Such a process is so-called liquid phase exfoliation (LPE), which typically employs the sonic energy or shear force to overcome the weak van der Waals coupling of the layers and delaminate them into few-layered 2D nanosheets. In this work, the LPE method was demonstrated as a viable method to give large-scale 2D MCs and TMDs nanosheets at low cost, enabling efficient solution processing of thin films, composites and devices. The resultant 2D MCs and TMDs nanosheets were utilized to fabricate high-performance lithium-ion batteries (LiBs) and solar cells (SCs).

First, four different 2D MCs (i.e. GaS, gallium (II) selenide [GaSe], gallium (II) telluride [GaTe] and indium (II) selenide [InSe]) were demonstrated as anodes of lithium ion batteries (LiBs). They are considered as promising candidates for the next-generation battery anode materials due to their relatively high theoretical capacity (> 550 mAh g^{-1}), excellent charge carrier mobility (up to 10^3 cm^2 V^{-1} s^{-1}), and multi-valences, enabling a variety of conversion/alloy reactions with lithium. However, poor electrical conductivity limits their potential LiB application. Here, we prepare few-layered 2D MCs flakes *via* the LPE method, and percolate the 2D MCs with single wall carbon nanotube (SWCNT) networks for flexible anode to store lithium (Li). According to their electrochemical tests (capacity, rate performance, and cycling stability, etc.), we could prove these 2D MC-

SWCNT composite anodes have a great potential to be used as anodes of batteries. Among these four different 2D MCs, we found that the InSe-SWCNT composite anode showed the best battery performance, especially exotic cycling performance. Improving of the capacity during charging and discharging process was observed for InSe-SWCNT anodes.

Based on the general comparison of four different 2D MCs, we decided to further explore the 2D InSe anode and its electrochemical mechanism because of their exotic electrochemical performance. 2D InSe nanoflakes were obtained *via* LPE of the wet-chemistry-synthesized layered InSe crystals. Then, 2D InSe was further percolated in the SWCNT networks through a colloidal solution processing approach to obtain the conductive InSe-SWCNT composite anode. Due to shortened Li^+ diffusion paths and enhanced electron transport kinetics, the binder-free flexible composite exhibits a superior electrochemical performance (including high capacity and excellent rate capability) to that of bulk InSe. Importantly, the capacity per InSe of 2D InSe-SWCNT composite anode increases over prolonged cycling up to 1224 mAh g^{-1} from 520 mAh g^{-1} (after 254 cycles, at 500 mA g^{-1}), which is believed to largely relate with the reversible alloy reaction, as confirmed by the operando X-ray diffraction results. Combining with the density-function theory (DFT) calculations and post-cycling scanning electron microscope (SEM) images, we reveal that the in-situ formed In particles gradually reduce their domain size, forming nanoclusters upon cycling which are capable to accommodate four Li^+ instead of one per atomic In, and leading to extra capacity as increasing the cycling numbers. Such a new "nanocluster-alloying" Li storage mechanism could shed light on the exploration of other metal chalcogenides to build new architectures with excellent performance in LiBs.

Last, 2D TMDs (e.g. molybdenum disulphide [MoS_2], molybdenum diselenide [$MoSe_2$], etc.) obtained by LPE method were used to fabricate solar cell devices for energy applications. Exfoliation process switches the bandgap of TMDs, coupled with excellent charge carrier mobility, quantum Hall effect and other anomalous optical responses at room temperature. They were tested as 1) an absorber, 2) a hole transport layer (HTL), and 3) a buffer layer of solar cells. Through this study, we could know that 2D TMDs obtained *via* LPE method is not suitable to be an active layer of solar cells because of the limitation of reducing of thickness of TMDs. However, they have potential to be used as a HTL or a buffer layer of perovskite solar cells (PSCs) to reduce the cost and improve the stability of the device. But there is still a large space to improve the PV

performance of solar cells with 2D TMDs nanosheets, and this practical built the foundation for further research.

Table of Contents

Acknowledgements

Upon the completion of this thesis, I am grateful to those who have offered me encouragement and support during my study.

First, special acknowledgment is given to my respectable supervisor Prof. Valeria Nicolosi whose patient instruction and constructive suggestions are beneficial to me a lot. She gave the great encouragement to overcome the most difficult time during my PhD years, without which I could have already given up. She treats us just as her children, always encouraging us to share the difficulties with her and coming up with efficient solutions to help. She gives us both mental and scientific tutorial all way around. I really appreciated her guiding and supports.

Also, I would like to express my sincere gratitude to Dr. Fadwa El-Mellouhi who have helped and taught me to try the new research area that greatly broadened my horizon and enriched my knowledge in my study. Her inspirational and conscientious teaching have provided me with a firm basis for the composing of this thesis and will always be of great value to my future academic research.

In addition, I would like to present my thanks to Prof. Nouar Tabet, Dr. Abdelhak, Dr. Adnan Ali. I have benefited a lot from their helpful guidance, training, and valuable suggestions to my CRANQSolar project during my visit to Qatar Environment and Energy Research Institution (QEERI). Without their kind assistants, I probably could not get to here.

My thanks also go to the Dr. Sang-Hoon Park, Dr. Joao Coelho, Dr. Sonia Metal. I studied a lot from them during these years, from experiments to writing. They give me much help and advice for my PhD project, from experiments to writing, which has made my accomplishments possible. I would like to say thank you to every member of Nicolosi Group who give me many helps and generous support during these years. In addition, I really appreciate the computational work done by Dr. Mohamed Istiaque Hossain from QEERI and Yonggang Wang from Fudan University in China.

Finally, I would like to extend my deep gratefulness to my family and friends for their loving considerations and great confidence in me all through these years. Thanks

for their supporting without a word of complaint. Their company is a great consolation to me.

Achievements

Publications:

- Chuanfang Zhang, Sang-Hoon Park, Sean E.O'Brien, Andrés Seral-Ascaso, Meiying Liang, Damien Hanlon, Dileep Krishnan, Alison Crossley, Niall McEvoy, Jonathan N. Coleman, and Valeria Nicolosi, Liquid Exfoliation of Interlayer Spacing-Tunable 2D Vanadium Oxide Nanosheets: High Capacity and Rate Handling Li-ion Battery Cathodes, Nano energy, 2017, 39,151-161.
- Zhang, Chuanfang, Liang, Meiying, Park, Sang-Hoon, Lin, Zifeng, Seral-Ascaso, Andrés, Wang, Longlu, Pakdel, Amir, Coileáin, Cormac Ó, Boland, John, Ronan, Oskar, McEvoy, Niall, Lu, Bingan, Wang, Yonggang, Xia, Yongyao, Coleman, Jonathan N., Nicolosi, Valeria, Extra lithium-ion storage capacity enabled by liquid-phase exfoliated indium selenide nanosheets conductive network, Energy & Environmental Science, 2020,13, 2124-2133.
- Meiying Liang, Adnan Ali, Abdelhak Belaidi, M. Ishtique Hossain, Oskar Ronan, Clive Downing, Nouar Tabet, Stefano Sanvito, Fadwa EI-Mellouhi, and Valeria Nicolosi Improving stability of organometallic-halide perovskite solar cells using exfoliated two-dimensional molybdenum chalcogenides, Accepted by 2D Materials and Applications, 2020.

Presentations:

- 2D Metal Chalcogenides for Li-ion Battery Applications, European Materials Research Society (EMRS) 2018 Fall Meeting (Oral Presentation).
- Two-dimensional Hexagonal Indium Selenide Nanosheets for Li-ion Battery Applications, Materials Research Society (MRS) 2018 Meeting (Poster Presentation).
- Improving stability of perovskite solar cells using two-dimensional transition metal dichalcogenides, Flatland 2019 (Poster Presentation).

- Improving Stability of Organometallic-halide Perovskite Solar Cells Using Exfoliation 2D Transition Metal Dichalcogenides, International Conference on Sustainable Energy-Water-Environment NEXUS in Desert Climate (IC-SEWEN) 2019 (Oral and Poster Presentation).
- Two-dimensional hexagonal InSe nanosheets: High capacity and long life-time Li-ion battery anodes, Dorgan Prize Finalists, 2018.

1 Introduction

1.1 2D metal and transition metal chalcogenides

The family of two-dimensional (2D) materials has grown appreciably since the first exfoliation of graphene *via* Scotch tape in 2004.[1] Understanding the different unusual physical properties and applications of graphene provided researchers with the path to explore the vibrant area of 2D layered materials that possess similar layered structure features but versatile properties, such as hexagonal boron nitride (h-BN), metal chalcogenides (MCs), transition metal dichalcogenides (TMDs), layered metal oxides, and layered double hydroxides (LDHs).[2-11] This unique class of nanomaterials has shown many unprecedented properties and thus is being developed for numerous promising applications.[12] Among various 2D materials, MCs and TMDs have attracted our attention. This kind of materials present many promising opportunities for future technologies due to their remarkable characteristics.[13-20] First, since a broad range of metals and chalcogenides is included in this class, an equally broad range of properties is observed, giving the opportunity of tuning the desired properties by controlling the composition of the materials.[21] Second, the high carrier mobility and 2D nanostructures of MCs and TMDs endow them with great electronic performances, including enhanced integration levels and suppressed short-channel effects.[18, 22-25] Third, the indirect-direct bandgap transition between the bulk and monolayer in some MCs and TMDs affords various optoelectronic applications.[5, 26-28]

MCs and TMDs comprise a large family, including over 72 members with the formula MX or MX_2, where M is a metal or transition metal element from group IVB – VIIIB or IIIA, and X is a chalcogen atom (Figure 1.1).[29] The structural characteristics of MCs and TMDs are represented in Figure 1.2. 2D platelets are weakly packed to form three-dimensionally (3D) structured layered materials. Within each layer, atoms are covalently bonded (e.g. X-M-X) whereas the individual layers are bound by van der Waals interactions through the *c*-axis.[22] Therefore, these materials apparently possess strong chemical bonds in-plane, but show weak interaction out-of-plane. As van der Waals packed layered materials, ultrathin 2D MCs and TMDs can be prepared by exfoliation from bulk single crystals. Moreover, many 2D MCs or TMDs have several crystal phases. Multiple thermodynamically stable phases can coexist in some 2D MCs

or TMDs and can be controlled by altering the fabrication processes.[30] The crystal phases can also be transformed under different external conditions, such as temperature, strain, pressure, and electronic doping.[31-34]

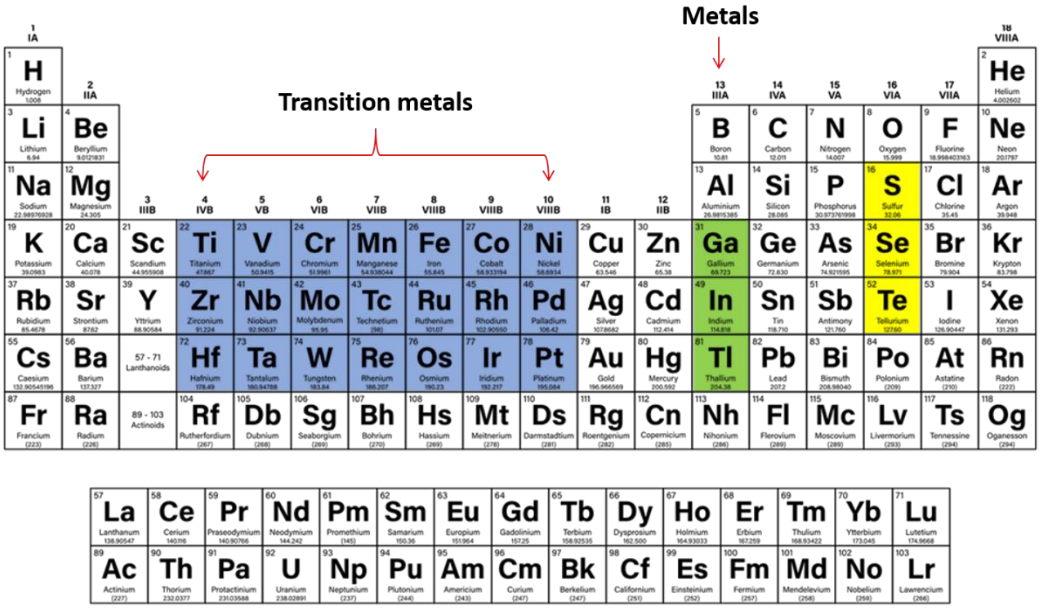

Figure 1.1 Metal (green) or transition metal (blue) and chalcogen (yellow) elements that form MCs and TMDs are highlighted in the periodic table.

2D nanosheets possess dramatically different fundamental properties compared to their bulk counterparts, making them potentially interesting for various fields including energy storage and conversion, such as photovoltaics, batteries, and supercapacitors.[35-47] 2D MCs and TMDs exhibit intensely thickness-dependent characteristics. For example, 2D TMDs materials have exotic electronic structures, unlike other semiconductors' typical characteristics. When the thickness of semiconducting TMDs is reduced to a singer layer, the band structure of TMD transforms from an indirect band gap to a direct band gap. As shown in Figure 1.3a, bulk MoS_2 has an indirect band gap of 1.2 eV, whereas single layer MoS_2 has a direct band gap of 1.8 – 1.9 eV.[17] A similar transition from an indirect band gap to a direct band gap has been verified for other single layer TMDs such as $MoSe_2$, WS_2 and WSe_2.[17, 48] All these 2D TMD materials exhibit an indirect band gap property at the Γ–point for bulk TMDs, but they gradually shift to direct band gaps for monolayer TMDs, covering the bandgap energy range of 1.1–1.9 eV.[17, 48]

Besides, MC materials also present the tuneable band gap characteristic. Table 1.1 introduce the crystal structure and characteristics of several typical 2D MCs and TMDs.

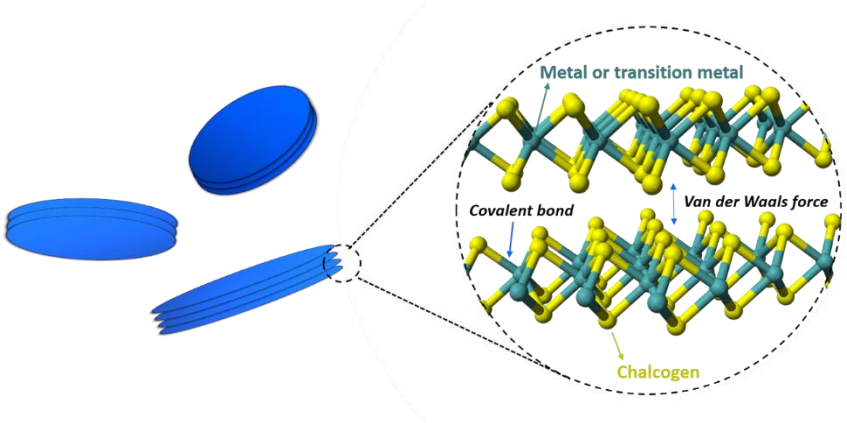

Figure 1.2 Layered structures of MCs and TMDs: single nanocrystal is composed of multiple layers stacked along the *c*-axis by weak van der Waals force.

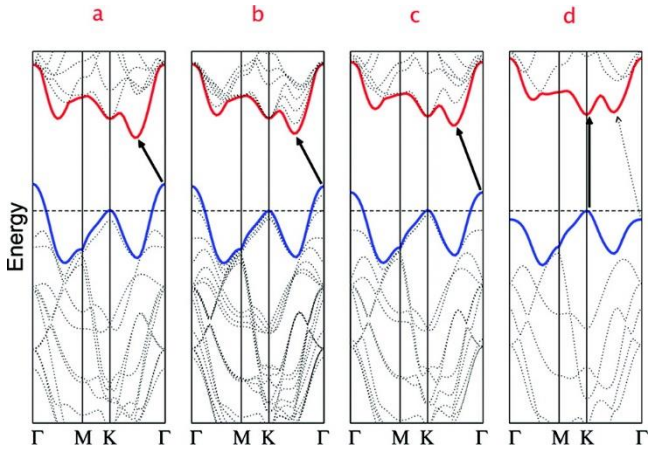

Figure 1.3 Electronic band structure of (a) bulk MoS_2, (b) quadrilayer (4L) MoS_2, (c) bilayer (2L) MoS_2, and (d) monolayer (1L) MoS_2 from left to right. The solid arrows indicate the lowest energy transition. (Images taken from ref. 17, copyright 2010 American Chemical Society).

Table 1.1 Characteristics of 2D MCs and TMDs

MCs or TMDs	Crystal structures	Electric conductivity	Band gap (eV)	Ref.

GaS	Hexagonal	Semiconductor	Indirect 2.52	49, 50
GaSe	β-Hexagonal ε-Hexagonal	Semiconductor p-type	Indirect 2.0	51-53
GaTe	γ-Monoclinic	Semiconductor p-type	Direct 1.7	54-56
InSe	β-Hexagonal γ-Rhombohedral	Semiconductor n-type	(Bulk) Direct 1.26 (Monolayer) Direct 2.6	57-59
MoS_2	2H hexagonal 1T	(2H) Semiconductor (1T) Metal	(Bulk) Indirect 1.2 (Monolayer) Direct 1.9	17, 30
WS_2	2H hexagonal 1T	(2H) Semiconductor n-type (1T) Metal	(Bulk) Indirect 1.3 (Monolayer) Direct 2.1	60-62
$MoSe_2$	2H hexagonal 1T	(2H) Semiconductor ambipolar (1T) Metal	(Bulk) Indirect 1.4 (Monolayer) Direct 1.58	60, 63, 64
WSe_2	2H hexagonal 1T	(2H) Semiconductor ambipolar (1T) Metal	(Bulk) Indirect 1.2 (Monolayer) Direct 1.65	63, 64

1.2 Preparation of 2D metal and transition metal chalcogenides

1.2.1 Mechanical exfoliation

Mechanical exfoliation (or 'Scotch Tape' exfoliation) previously used for graphene is one of the main techniques used to obtain 2D MCs and TMDs.[1, 65] The process relies on the probability of cleaving the bulk MC and TMDs crystal so that all layers except one remain adhered to the tape and only a monolayer is transferred onto the desired substrate (Figure 1.4).[1, 65] The size of monolayers obtained by standard tape-

exfoliation is relatively small (~ 5 μm), their yield is poor, and the process is not selective towards the number of layers.

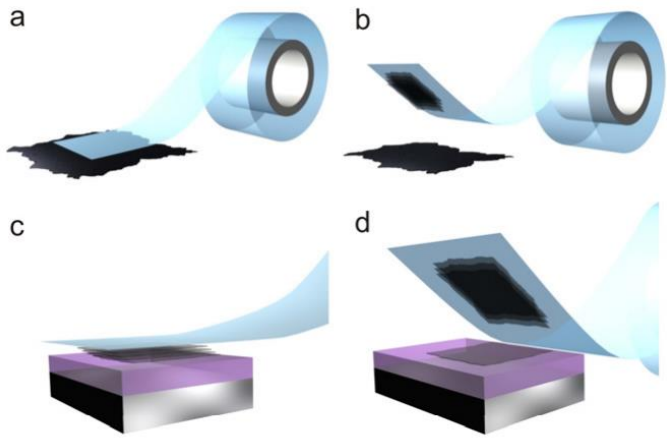

Figure 1.4 Mechanical exfoliation method: Micromechanical exfoliation of 2D crystals. (a) Adhesive tape is pressed against a 2D crystal so that the top few layers are attached to the tape (b). (c) The tape with crystals of layered material is pressed against a surface of choice. (d) Upon peeling off, the bottom layer is left on the substrate. (Images taken from ref. 65, copyright © 2012 The Royal Swedish Academy of Sciences).

1.2.2 Chemical vapour deposition

To apply 2D MCs and TMDs to real devices, their large-scale growth is essential. The chemical vapour deposition (CVD) method is an effective way to achieve large-area growth. This method can be divided into two types, the sulfurization (or selenization) of metal thin films and vapour phase reaction of metal oxides with chalcogen precursor. For instance, synthesis MoS_2 layers by the simple sulfurization of Mo metal thin films (Figure 1.5).[66] The size and thickness of the pre-deposited Mo film determine the size and thickness of the MoS_2 thin film, respectively. The direct sulfurization of the Mo metal thin film provides a quick and easy way to access atomically thin MoS_2 layers on insulating substrates (such as a SiO_2/Si substrate). However, it is challenging to deposit a uniform Mo film. Besides, attempts have also been made to prepare lager-area semiconducting MoS_2 thin layers *via* the direct sulfurization of a MoO_3 thin layer (Figure 1.5b-e).[67] However, the synthesis of TMDs by the direct sulfurization (selenization) of a metal oxide thin film has several limitations, such as the difficulty to control the thickness

of the pre-deposited metal oxide or metal thin film, which affects the uniformity. Generally speaking, while CVD provides a relatively simple route for synthesizing 2D materials, these methods do not always provide precise control over the grown materials and can often result in inhomogeneous films.[67]

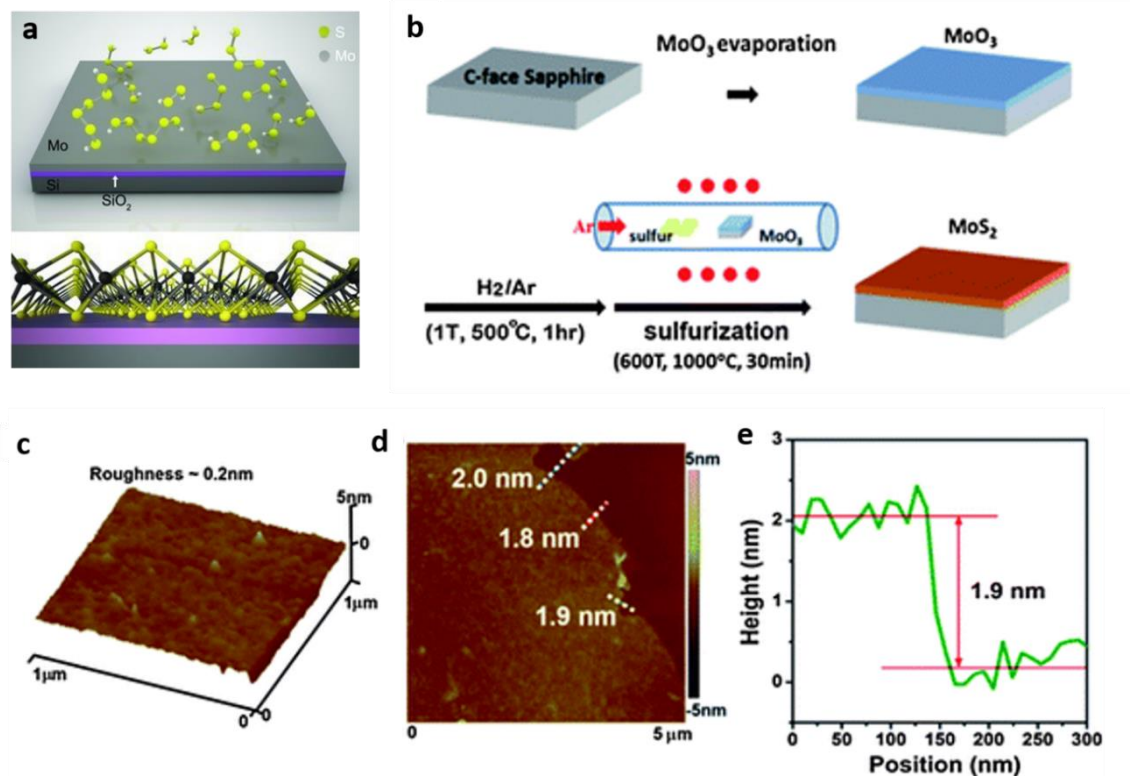

Figure 1.5 (a) Introducing S on the Mo thin film that was pre-deposited on the SiO_2 substrate and MoS_2 films that are directly gown on the SiO_2 substrate; (b) Schematic illustration for the synthesis of MoS_2 layers by MoO_3 sulfurization. A layer of MoO_3 (~3.6 nm) was thermally evaporated on the sapphire substrate. The MoO_3 was then converted to a MoS_2 by a two-step thermal process; (c, d) Surface topographic images of MoS_2 obtained by AFM. (e) A selected cross-sectional height profile showing the thickness of the MoS_2 layer. (Images taken from ref. 66, copyright © 2012 The Royal Society of Chemistry, and ref. 67, © 2012 Wiley-VCH Verlag GmbH & Co. KGaA, Weinheim, respectively).

1.2.3 Liquid phase exfoliation

To exploit the great potential of these layered materials, large quantities of MCs and TMDs nanosheets are required. To obtain large amounts of single- or few- layer 2D

MCs and TMDs nanosheets, a solution processing strategy would be more appropriate. The first report on the liquid phase exfoliation of sheets of clay materials in the early 1960s has inspired many studies into methods of exfoliating bulk layered materials.[68] Professors Coleman and Nicolosi at Trinity College Dublin developed an effective and reliable LPE technique to produce 2D nanosheets in common organic solvents.[14] LPE is a simple process, involving placing bulk layered materials into certain solvents and applying the ultrasonication to overcome relatively weak van der Waals forces to produce 2D nanosheets. In a typical exfoliation procedure, the bulk material is immersed in a suitable solvent, or aqueous surfactant or polymer solution and undergone ultrasonication *via* a bath or tip sonicator, or shear force mixers, respectively.[69] After the actual exfoliation, the dispersion is then subjected to centrifugation to remove unexfoliated material and perform size selection.[69] This method is non-destructive, insensitive to environment (e.g. air and water), and gives defect-free graphene at a high yield. For example, as shown in Figure 1.6a-d, high quality MoS_2 and WS_2nanosheets can also be obtained *via* LPE method.[14] There are various solvents that can be applied; however, an optimal solvent for LPE must fulfil the following general criteria: 1) It must be able to vigorously exfoliate the material at the highest concentration possible; and 2) It needs to stabilise the exfoliated 2D materials for the longest duration possible.[70] After the dispersion and ultrasonication of each inorganic starting materials in about 30 common solvents with varying surface tensions and adsorption properties, it was demonstrated that the best solvents have a surface tension close to 40 mJ/m^2 as demonstrated by using optical absorption spectroscopy (Figure 1.6e and f). Based on theoretical investigation, they proposed that successful solvents are those that minimize the energy of exfoliation. Typical solvents that are known to give stable dispersions include N-methyl-pyrrolidone (NMP), N-cyclo-2-pyrrolidone, dimethylformamide (DMF), dimethylsulfoxide (DMSO) and isopropanol (IPA).[14, 69]

Moreover, as mentioned, this approach could also realise the size and thickness selection of nanosheets by controlling centrifugation of the exfoliated dispersions.[71] For example, as shown in Figure 1.7, any unexfoliated crystallites had been removed by low speed centrifugation (here1,500 rpm). This “stock” dispersion contains nanosheets with a broad distribution of sizes and thickness and a small but nonnegligible population of monolayers with varying lateral sizes. The stock is then centrifuged at a higher speed (here 2,000 rpm) and the sediment collected. This sediment contains nanosheets from the

larger end of the size distribution. The supernatant produced during the 2000 rpm centrifugation contains all but the largest nanosheets. It can be centrifuged at a higher rate to give a sediment with slightly smaller nanosheets. The associated supernatant can be centrifuged again (gradually increasing the centrifuging rate), and these steps continued for as many as are required with each step using a continually increasing centrifugation rate. Critically, because the heavier, few-layer nanosheets are removed in each step, the resultant supernatants become more and more monolayer enriched. After each step, the sediment contains smaller and smaller nanosheets, resulting in effective size selection. Size selection is important, as the size of nanosheets strongly influences the electronic and optoelectronic properties of 2D MCs and TMDs.[72]

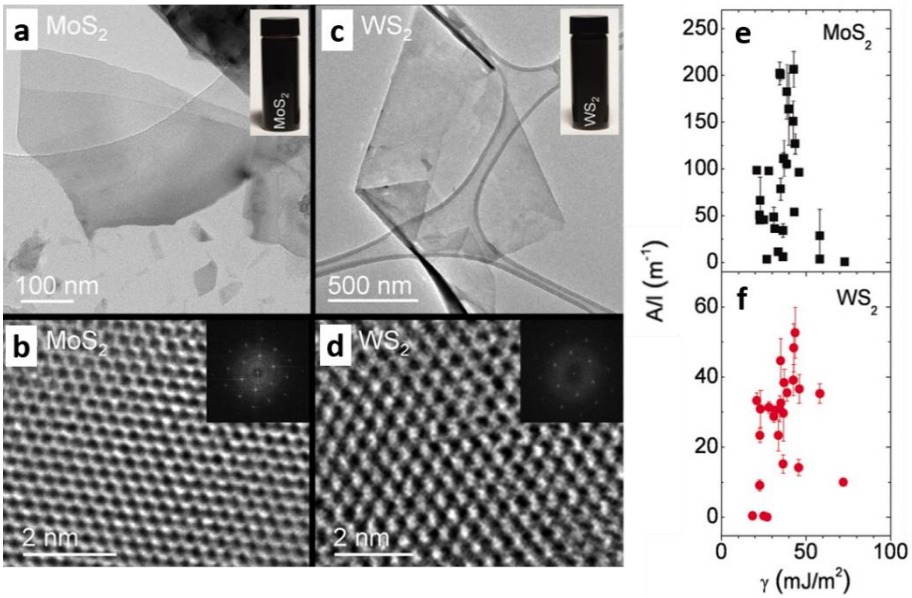

Figure 1.6 Transmission electron microscopy (TEM) of nanosheets (a, c) low-resolution TEM images of MoS_2 and WS_2, (Inset) photographs of dispersions of MoS_2 (in NMP), WS_2 (in NMP); (b, d) High-resolution TEM images of MoS_2 and WS_2 monolayers (Insets: Fast Fourier transforms of the images); (e, f) Concentration remaining after centrifugation (plotted as A/l) for MoS_2 and WS_2 dispersed in a range of solvents, plotted versus solvent surface tension, γ. (Images taken from ref. 14, Copyright © 2011, American Association for the Advancement of Science).

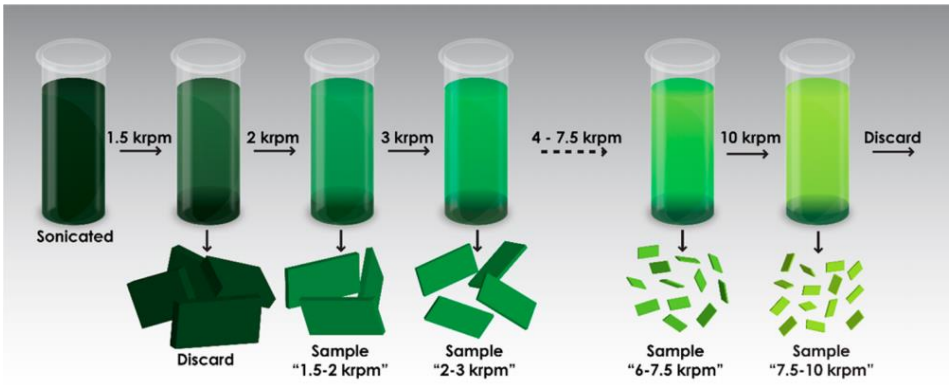

Figure 1.7 Size selection mechanism *via* controlling centrifugation conditions. (Reproduced with permission from ref. 71, copyright 2016, American Chemical Society).

1.3 Applications of 2D metal and transition metal chalcogenides

2D MCs and TMD materials are considered attractive for a variety of applications including electronics, photonics, sensing, and energy devices. These applications are inspired by the unique properties of layered materials such as thin atomic profile that represents the ideal conditions for maximum electrostatic efficiency, mechanical strength, tunable electronic structure, optical transparency, and sensor sensitivity.[73-77] Specifically, 2D MCs and TMDs possess unique electrical and optical properties which are derived from the quantum confinement and surface effects that occur during the transition from an indirect bandgap to a direct bandgap when bulk materials are scaled down to monolayers.[78] This tunable bandgap in MCs and TMDs is accompanied by strong photoluminescence (PL) and large exciton binding energy, making them promising candidates for various optoelectronic devices, such as solar cells, photo-detectors, light-emitting diodes, and photo-transistors. [79-83] For example, unique properties of MoS_2 include direct bandgap (~1.8 eV), good mobility (~700 $cm^2\ V^{-1}\ s^{-1}$), high current on/off ratio of $\sim 10^7$–10^8, large optical absorption (~$10^7\ m^{-1}$ in the visible range) and a giant PL arising from the direct bandgap (1.8 eV) in monolayer; thus, it has been studied widely for electronics and optoelectronics applications.[84] On the other hand, van der Waals (vdW) gaps between each neighboring layer and large specific surface area due to sheet-like structures are distinct features that make 2D MCs and TMDs highly attractive for capacitive energy storage (e.g. supercapacitors and batteries) and sensing applications.[85, 86] The large surface-to-volume ratio enables sensors based on 2D MCs and TMDs to have

higher sensitivity, selectivity and low power consumption. Unlike digital sensors, MCs or TMDs based sensors have no physical gates to selectively react with the targeted gas molecules or biomolecules.[87, 88] Here, we introduce several applications of 2D MCs and TMDs materials focusing on energy storage and photovoltaic devices.

1.3.1 Energy storage

2D MCs and TMDs have received extensive attention as energy storage electrode materials, such as supercapacitors and Li-ion batteries, owing to their atomically layered structure, high surface area and excellent electrochemical properties. Such layered structures provide more sites for ions in energy storage while maintaining structure stability during charge and discharge cycles. The high surface area of 2D materials (e.g. the surface area of graphene shows 2630 m^2/g, which is the highest among carbon materials) combined with surface functionality and electrical conductivity, making them an ideal electrode for energy storages.[89]

In order to evaluate the electrochemical performance of the electrode materials, cyclic voltammetry (CV) and galvanostatic charge-discharge (GCD) tests are usually performed.

CV is a powerful tool in the field of electrochemistry. It has been used extensively to characterize the performance of various electrical energy storing devices such as batteries. In CV techniques, electric potential is imposed at the electrodes which varies periodically and linearly with time. The resulting electric current is recorded. The total charge accumulated at the surface of electrode can be calculated by integrating the electric current with respect to time. Finally, the capacitance can be estimated as the total charge divided by the potential window. Specific capacitance derived from CV tests can be calculated from the equation (1):

$$SC = \frac{1}{mv(V_b - V_a)} \int_{V_a}^{V_b} I \mathrm{d}V \qquad (1)$$

Where *SC* (F/g) is the specific capacitance, *m* (mg) is the mass of active materials of the electrode, *v* (V/s) is the scan rate, *I* (A) is the discharge current; V_b and V_a (V) are the high and low potential limit of the CV tests.

The GCD is a reliable method to evaluate the electrochemical capacitance of materials under controlled current conditions. The technique is very different from CV because the current is controlled, and the voltage is measured. In this method, a current pulse is applied to the working electrode and the resulting potential is measured against a reference electrode as a function of time. At the moment current is applied, the measured potential abruptly changes due to the internal resistance loss and after that it gradually changes because concentration over-potential is developed across the electrodes, as the concentration of the reactant is exhausted at the electrode surface. The voltage variation is given by the equation (2):

$$V(t) = \text{IR} + \frac{t}{C}I \tag{2}$$

Where *V(t)* (V) is the voltage as a function of time, R (Ω) is the resistance, *C* (F/g) is the capacitance and *I* (A) is the current. As can be seen from equation (2), the capacitance of the battery can be calculated from the slope of the GCD curve. Thus, the capacitance can be calculated by integrating the current over the discharge time or charge time:

$$C = \frac{I\Delta t}{\Delta V} \tag{3}$$

Where I is the set current, $\triangle t$ is the discharge time (or charge time), and $\triangle V$ is the potential window. Therefore, specific capacitance derived from GCD tests can be calculated from the equation (4):

$$SC = \frac{I\Delta t}{m\Delta V} \tag{4}$$

Where *SC* (F/g) is the specific capacitance; *I* (A) is the discharge current; $\triangle t$ (s) is the discharge time; $\triangle V$ (V) is the potential window; and *m* (g) is the mass of active materials of the electrode.

1.3.1.1 Supercapacitor

A supercapacitor is a high-capacity electrochemical capacitor with capacitance values one order higher than Li-ion batteries consisting of two symmetric electrodes separated by a membrane, and an electrolyte ionically connecting both electrodes. When the electrodes are polarized by an applied voltage, ions in the electrolyte form electric

double layers of opposite polarity to the electrode's polarity. In certain electrode materials, some ions may permeate the double layer and become specifically adsorbed ions and contribute with pseudocapacitance to the total capacitance of the supercapacitor. MoS_2 exhibits large electrical double layer capacitance (EDLC) due to its stacked-sheet-like structure and large pseudo-capacitance owing to different Mo oxidation states (+2 to +6) and has become a promising supercapacitor electrode material in the 2D materials fraternity.[90] Tour et al.[91] fabricated edge oriented/vertically aligned MoS_2 nanosheets that opened more van der Waals gaps and offered reactive dangling bonds sites to the electrolyte ions and thereby present large capacitive properties. The sponge-like vertically aligned MoS_2 flexible supercapacitor electrodes demonstrated a high areal capacitance up to 12.5 mF cm^{-2}. The limited electrical conductivity of the most common 2H-MoS_2 phase makes it less attractive material for supercapacitor electrode as reported at instances.[92] This compels Rutgers university researchers to develop a metallic MoS_2 phase (1T) which has 107 times higher conductance than semiconducting phase.[44] The chemically exfoliated MoS_2 nanosheets-derived supercapacitor electrodes demonstrated excellent capacitive performance, with capacitance values ranging from 400 to 700 F cm^{-3} in a variety of aqueous electrolytes.[44] Choudhary et al.[93] reported the direct fabrication of a large-scale and unique 3D-porous MoS_2 supercapacitor electrode on flexible substrates (copper, polyimide) using magnetron sputtering techniques. The unique 3D porous surface facilitated the large intercalation of electrolyte ions and exhibited a high areal capacitance of 33 mF cm^{-2} (~330 F cm^{-3}) at a discharge current density of 25.47 mA/cm^2. Moreover, the electrode showed about 97% capacitance retention over 5000 cycles, which indicates its excellent cyclic stability.

1.3.1.2 Li-ion battery

A Li-ion battery is another widely used energy storage device at present. It is an advanced battery technology that uses lithium ions as a key component of its electrochemistry. As shown in Figure 1.8, working mechanism is quite simple. Li-ion batteries are composed of three parts: anode, cathode, and electrolyte. Batteries also have separators that separate the anode and the cathode to prevent explosions and short circuits. In the discharge process of the Li-ion battery, the anode is electrochemically oxidized,

this causes the Li ions to be released into the electrolyte. During this process, electrons move through the external circuit and travel towards the cathode. Meanwhile, the Li ions travel across the electrolyte and reimburse for the negative charge that is flowing into the cathode from the external circuit. This causes the Li ions to be absorbed by the cathode. When plugging in the battery, the opposite happens. Lithium ions are released by the cathode and received by the anode. The Li-ion battery technology evolution, which enabled the commercialization of the rechargeable, high energy density batteries that are conquering the market, emerged due to the introduction of graphite as the anode material. For graphite, which is the first commercialized anode material, Li ions intercalate into and de-intercalate out of the graphite layers during the charging and discharging cycles (Figure 1.8).[94] During the charging process of LiBs with graphitic materials as negative electrodes, lithium ions intercalate into graphene layers to form lithium–graphite intercalation compounds.[95]

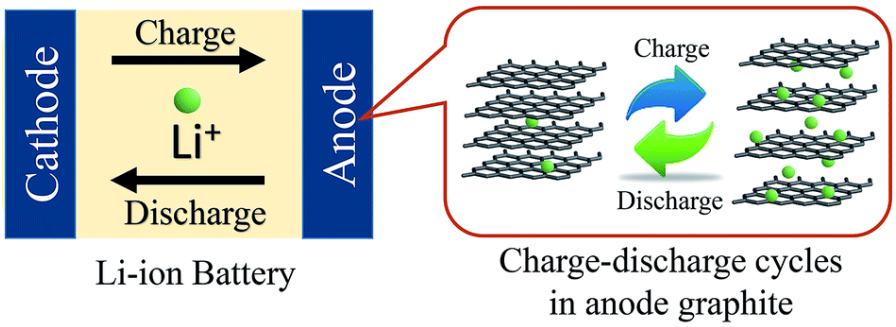

Figure 1.8 Li-ion battery's energy storage mechanism and charge-discharge cycles in anode graphite. (Reproduced with permission from ref. 94, copyright © The Royal Society of Chemistry 2017).

However, graphite's theoretical capacity is only 370 mAh/g, and this limit its further development in the battery market. The Theoretical capacity of a cell can be calculated by Faraday's law: $Q_{theoretical}$ = (nF) / (3600 × Mw) mAh/g, where n is the number of charge carrier, F is the Faraday constant and Mw is the molecular weight of the active material used in the electrode. While the theoretical capacity of the graphite anode can be almost fully utilized resulting in a practical capacity of 360 mAh/g,[96] the practical capacity of layered cathodes is limited, due to their structural instability at low Li contents, that is, high state-of-charge. One strategy to improve the capacity is

reducing its dimensionality to 2D limit.[94] As shown in Figure 1.9, layered graphite can be exfoliated to 2D graphene nanosheets. Graphene nanosheets have high specific surface areas which offer more electrochemically active sites for Li ion storage, and also open 2D channels for fast ion transport.[94] To date, anodes with graphene nanosheets have reached specific capacity of ~ 1200 mAh/g at 100 mA/g current rate in half cell (Figure 1.10), while the graphite anode shows ~ 300 mAh/g of capacity at 100 mA/g current density.[97, 98] Although graphene and its derivatives are promising with great properties, there remain some problems like rapid energy loss and high cost. It is proposed that the energy loss takes place in the first cycle may be caused by the formation of solid electrolyte interface (SEI) and the variation of morphology, as shown in Figure 1.11.[99] The SEI is a layer that forms at the anode surface for all alkali metal ion batteries which utilize liquid electrolytes. The SEI allows Li^+ transport and blocks electrons in order to prevent further electrolyte decomposition and ensure continued electrochemical reactions.[100]

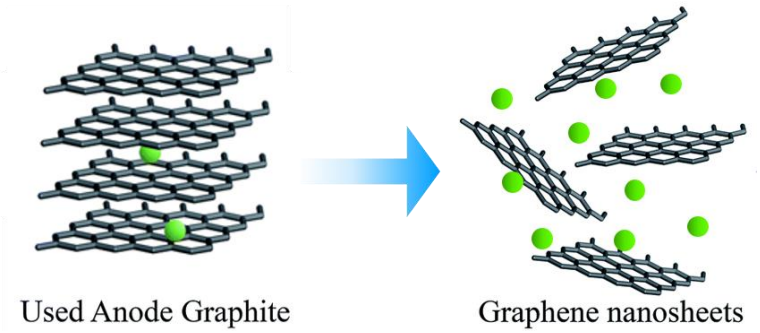

Figure 1.9 Exfoliating the layered graphite to obtain 2D graphene nanosheets. (Reproduced with permission from ref. 94, copyright © The Royal Society of Chemistry 2017).

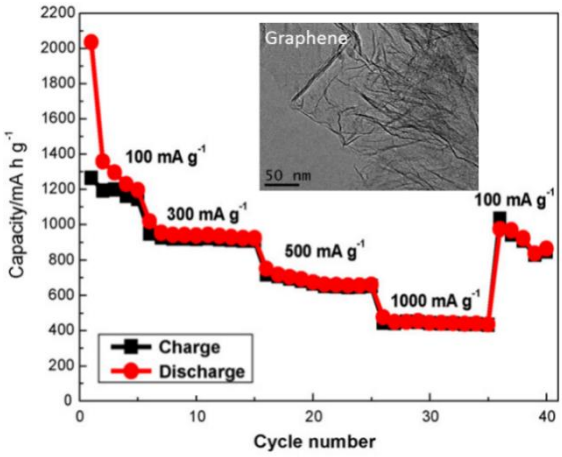

Figure 1.10 Cycle performance of graphene nanosheets at current densities from 100 mA/g to 1000 mA/g. Insert is HRTEM image of graphene nanosheets. (Reproduced with permission from ref. 97, copyright© 2010 Elsevier Ltd.).

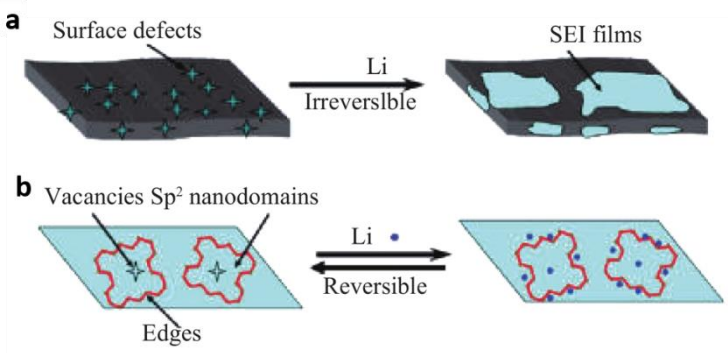

Figure 1.11 Diagrammatic representation of surface interaction between graphene nanosheets and electrolyte: (a) irreversible Li ion storage at the interface between the graphene nanosheets and electrolyte, (b) reversible Li ion storage at edge sites and internal defects (vacancies etc.) of nanodomains embedded in graphene nanosheets. (Reproduced with permission from ref. [99], copyright © 2009American Chemical Society).

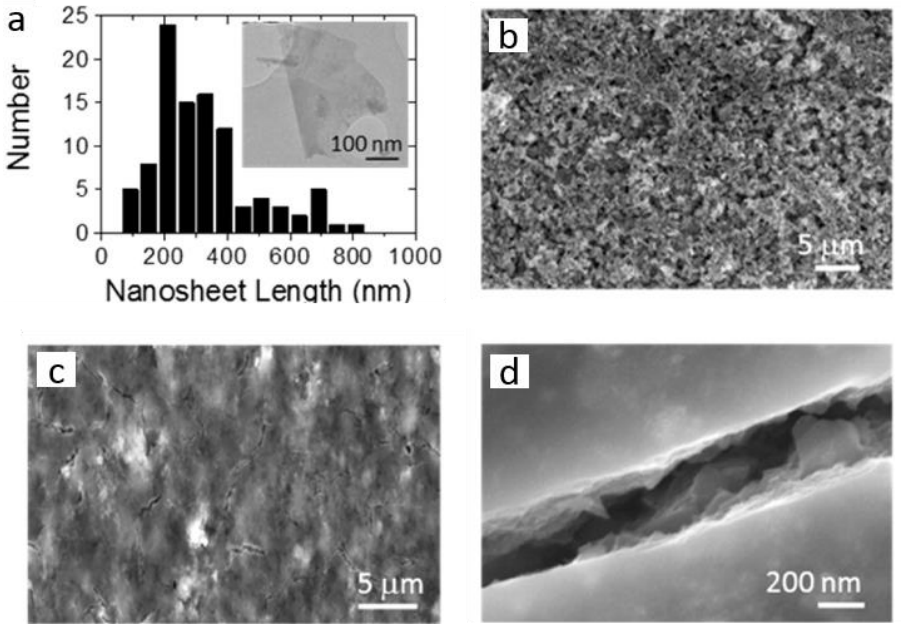

Figure 1.12 (a) TEM image of a liquid exfoliated MoS_2 nanosheet (inset). Main panel: Histogram of nanosheet length with $\langle L \rangle$ = 332 nm; (b) SEM image of a lithium ion battery electrode fabricated from MoS_2 nanosheets before cycling;(c) SEM image of a lithium ion battery electrode fabricated from MoS_2 nanosheets after cycling; (e) High-magnification image of a crack. (Reproduced with permission from ref. 101, Copyright © 2016 American Chemical Society).

Based on the study of 2D graphene nanosheets, recently, 2D MC and TMDs materials, which have similar structure as graphene but have higher theoretical capacity,[20, 78, 102] have been actively investigated as electrode materials in LiBs, either in their pristine 2D forms, forming heterostructures with other 2D materials or composited with carbon materials, such as carbon nanotubes. As a representative member of TMDs, MoS_2 was widely studied first as it offers a high theoretical capacity of ~670 mAh/g and large van der Waal gaps between MoS_2 layers that allow the intercalation of Li^+ ions into the structure without significant volume change and preclude the disintegration of active materials during charging and discharging.[102, 103] The electrochemical reaction of Li with MoS_2 involves 4 moles of Li per mole of MoS_2 based on the reaction: $MoS_2 + 4Li^+ + 4e^- \leftrightarrow 2Li_2S + Mo$, offering ~2 times higher storage capacity than that of graphite electrode. In spite of large specific capacity observed in different MoS_2 morphologies, concerns about its poor cyclic stability and low electronic conductivity have been serious.[104] To optimize the electrochemical property of MoS_2, conductive

materials (such as graphene, carbon nanotubes, and polyaniline, *etc.*) are added to form the MoS_2/conductive material composite electrodes. For instance, Prof. Coleman's group have carried out a systematic study on composite anodes of MoS_2, produced by LPE (Figure 1.12a), mixed with single-walled nanotubes (SWCNTs) (Figure 1.14a).[101] Adding conductive SWCNTs increased the conductivity of the electrodes resulting in up to a 100 times capacity enhancement to ~1200 mAh/g at 100 mA/g and high rate capability (~600 mAh/g at 20 A/g) (Figure 1.13a).[101] This is because MoS_2 has low conductivity, so electrodes of MoS_2 alone can only store lithium in regions where electrons can be supplied effectively. However, adding SWCNTs provide an extensive conducting network which connects the current collector to distant parts of the electrode, allowing electrons to be supplied throughout the electrode *via* the network with only a small portion of the journey through the MoS_2.

The improved toughness significantly boosts cycle stability as well (Figure 1.13b and c). Figure 1.12b-d show the SEM images of a lithium-ion battery electrode fabricated from MoS_2 nanosheets before and after cycling.[101] From them, it appears clear that the expansion/contraction associated with charge/discharge cycling will result in mechanical degradation (cracking appears to be much more extensive than before cycling) of LiB electrodes prepared from brittle materials such as nanosheet networks. Such cracks limit the insertion and extraction of Li^+ ions during charge and discharge cycles. However, addition of SWCNTs not only dramatically improves the toughness of the electrode, reducing the likelihood of mechanical failure, but also in the event of cracks it keeps the two fragments in contact (Figure 1.14b-d).[101] This should have a significant impact on electrode stability, and it is clear from the data in Figure 1.13b and c that the electrodes become more stable when SWCNTs are added.

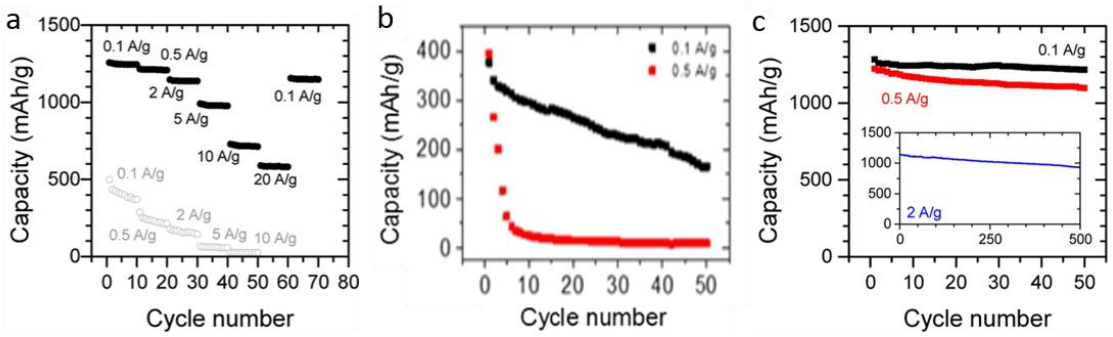

Figure 1.13 (a) Rate capability data for MoS_2 electrodes (gray) and MoS_2/SWCNTs composite electrodes (black); (b, c) capacity *versus* cycle number for MoS_2 electrodes

(red) and MoS_2/SWCNTs composite electrodes (black), respectively. (Reproduced with permission from ref. 101, Copyright © 2016 American Chemical Society).

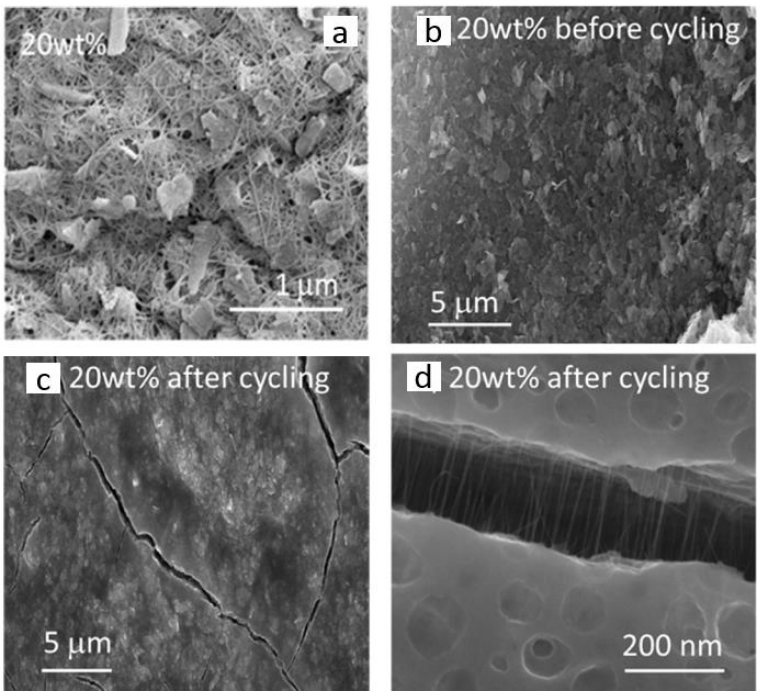

Figure 1.14 (a) SEM image of a film consisting of MoS_2 nanosheets mixed with 20 wt % SWCNT;(b, c) SEM image of the surface of a MoS_2/SWCNT (20 wt %) before and after cycling, respectively; (d) Magnified image of a crack showing bridging by nanotubes. (Reproduced with permission from ref.101, Copyright © 2016 American Chemical Society).

Similar study has been carried out using 2D gallium (II) sulphide (GaS) nanosheets.[20] Because group III A metal monochalcogenide also shows a great potential to be used as an anode material of LiBs due to their 2D layered structure and high theoretical capacity. However, compared to TMDs, they are relatively unexplored. As shown in Figure 1.15a, layered GaS was exfoliated to nanosheets (Figure 1.15b) using LPE method. Then, SWCNTs were added for maximizing the electrochemical performance of the electrode (Figure 1.15c). Figure 1.15d and e show a cross-section SEM image of the electrode. From it, we could observe that GaS nanosheets were uniformly spread within the SWCNTs network. Also, the elemental mapping of Ga, S, and C performed by EDX, confirmed the homogeneous distribution of both nanotubes and nanosheets within the composite (Figure 1.15f).Consequently, as shown in Figure

1.15g-i, high specific capacity (838 mAh/g at 0.1 A/g) (Figure 1.15g), good rate capability (~530 mAh/g at 20 A/g) (Figure 1.15g) and cycling stability were achieved (Figure 1.15h and i). This work opens up opportunities for other families of MC nanosheets to be utilized as an anode of LiBs.[20]

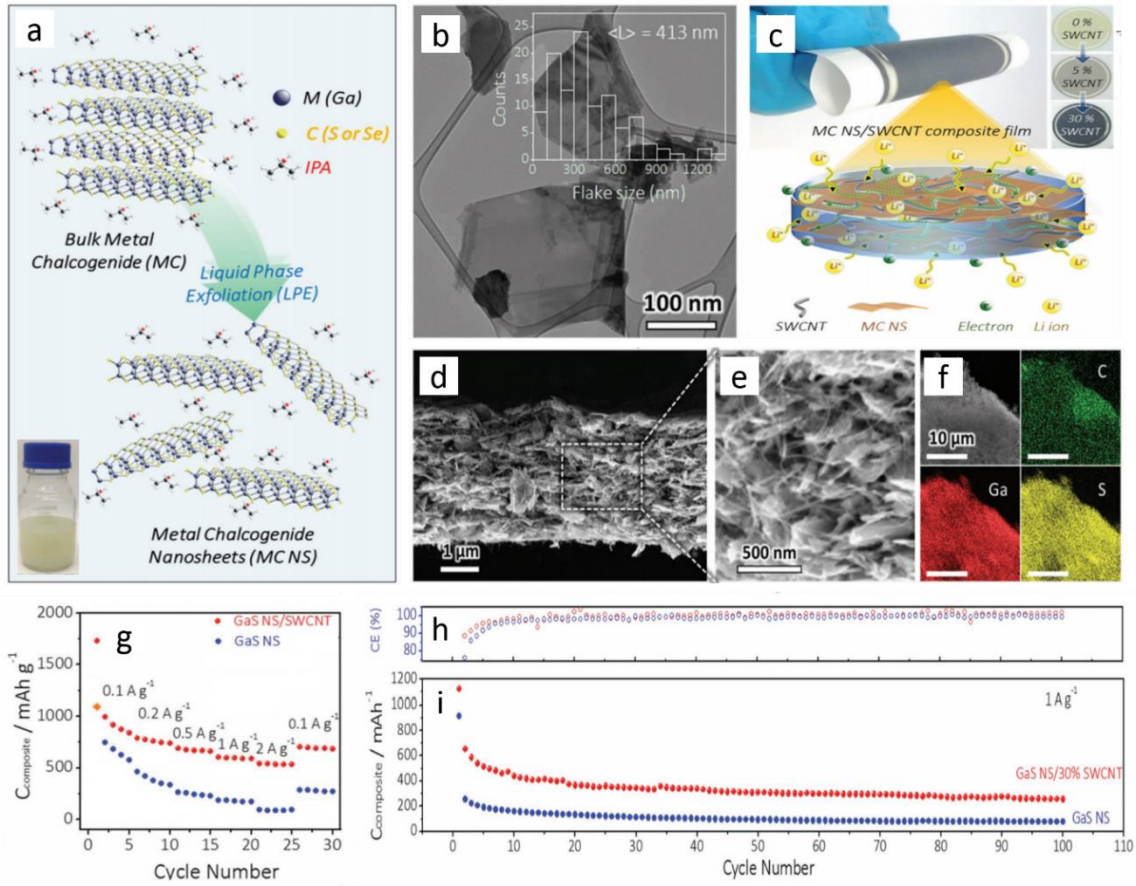

Figure 1.15 (a) Schematic of MC nanosheets production through a liquid-phase exfoliation approach; (b) TEM of exfoliated GaS nanosheets; (c) Schematic describing the critical role of SWCNTs in constructing a multiscaled hierarchical nanostructure. Insets are the GaS nanosheets-based thin films with 0%, 5%, and 30% CNT; (d, e) Cross-sectional SEM images of GaS nanosheets/SWCNTs composite (30% SWCNT, 5 µm) at low and high magnification; (f) EDX mapping of Ga, S, and C in GaS nanosheets/SWCNTs composite;(g) Rate performance of GaS nanosheets and GaS nanosheets/SWCNTs composites at different current densities ranging from 100 mA/g to 2 A/g; (h) Coulombic efficiency and (i) cycling performance of GaS NS and GaS NS/CNT composite at 1 A/g. (Reproduced with permission from ref. 20, Copyright © 2017 Wiley-VCH Verlag GmbH & Co. KGaA, Weinheim).

1.3.2 Energy conversion

The photovoltaic effect is an important physical phenomenon in which the illumination can induce the formation of a spontaneous voltage in devices. Applications based on the photovoltaic effect are an important direction for clean energy technology. The photovoltaic effect was primarily used to convert solar energy into electric energy based on silicon p-n junctions in 1954.[105] The first generation cells (also called conventional, or traditional cells) are made of crystalline silicon, the commercially predominant PV technology, that includes materials such as polysilicon and monocrystalline silicon. These silicon-based devices are still the mainstream solar cells. However, they are expensive to produce, so research led the next generation of solar cells away from silicon.[106] Second generation solar cells are called thin film solar cells. These solar cells are made of thin film semiconductor materials such as copper indium gallium selenide ($CuIn_xGa_{1-x}Se_2$, CIGS) and cadmium telluride (CdTe). They are lower in cost compared to the silicon cells, but they have environmental issues and the efficiencies are lower. Therefore, there is an urgent need to develop new, cheap, efficient solar cells.[107, 108] High-performance, economically viable, abundant and scalable device components are key to developing the third generation solar cells.[107, 108] Most technologies in this generation are not yet commercial, but there is a lot of research going on in this area. The chemical, physical, electrical and mechanical properties of 2D materials match with the requirements that the various building blocks of the third generation photovoltaics should have in order for these devices to deliver exceptional performance and become attractive alternatives to silicon-based or thin film solar cells.[109] Recent advances in 2D MCs and TMDs (e.g. MoS_2, WS_2, $MoSe_2$ and WSe_2) have introduced numerous promising applications in solar cells.[86-116] This section highlights the contributions of 2D MCs and TMDs toward the construction of high power conversion efficiency (PCE) and of long lifetime, solution-processed solar cells. PCE and the stability are two important parameters for evaluating the quality of solar cells. PCE is defined as the ratio of energy output from the solar cell to input energy from the sun. In addition to reflecting the performance of the solar cell itself, the efficiency depends on the spectrum and intensity of the incident sunlight and the temperature of the solar cell. Therefore, conditions under which efficiency is measured must be carefully controlled in order to compare the performance of one device to another. Typically, solar cells are measured under AM1.5

conditions and at a temperature of 25°C. The PCE of a solar cell is determined as the fraction of incident power which is converted to electricity and is defined as:

$$P_{max} = V_{oc} \cdot I_{sc} \cdot FF$$

$$PCE = P_{max} / P_{in}$$

Where V_{oc} is the open-circuit voltage, I_{sc} is the short-circuit current, FF is the fill factor and η is the PCE. The I_{sc} and the V_{oc} are the maximum current and voltage respectively from a solar cell. FF is a parameter which, in conjunction with V_{oc} and I_{sc}, determines the maximum power from a solar cell.

1.3.2.1 2D transition metal dichalcongenides as an absorber of solar cells

Light absorption in the active layers of a solar cell is one of the key performance metrics that dictates device efficiency. For semiconductors, the absorption is governed by the electronic band structure and energy bandgap. There is an essential balance between bandgap (and voltage) with absorption (and photocurrent). Figure 1.16 summarizes the bandgap energies and absorption coefficients for all major photovoltaic materials investigated to date at the commercial and research scales.[110] Most materials considered for photovoltaic applications have energy bandgaps close to the optimum value of 1.34 eV because the maximum solar conversion efficiency occurs at this band gap.[110] The TMDs (both bulk and monolayers) of Mo and W have some of the highest absorption coefficients among known materials (Figure 1.16).[110] Therefore, 2D TMDs materials including MoS_2, $MoSe_2$, WS_2, WSe_2, have great potential to be used as an absorber of solar cell devices. To further assess the viability of 2D semiconductor photovoltaics, it is worth evaluating their estimated efficiency limits. The estimated efficiency limits of TMD-based photovoltaic devices are shown in Figure 1.17, being even competitive to silicon based solar cells.[110]

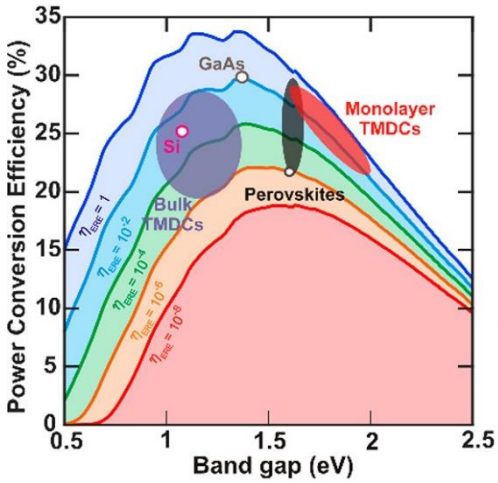

Figure 1.16 Comparison of energy bandgaps (eV) and absorption coefficients (cm^{-1}) for a variety of semiconductor materials used for commercial as well as research-scale photovoltaics. (Reproduced with permission from ref. 110, Copyright © 2017 American Chemical Society).

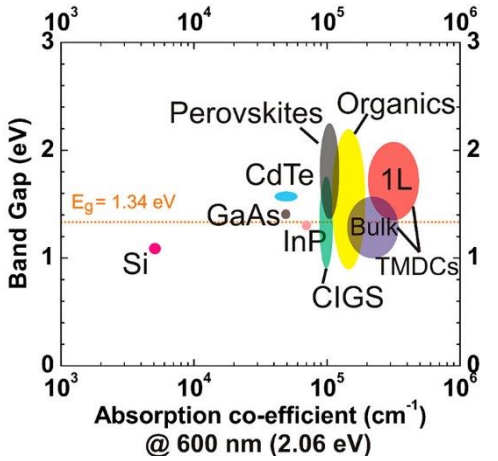

Figure 1.17 Comparing TMDs with established photovoltaic technologies: Photovoltaic efficiency of a single junction cell using a modified Shockley-Queisser detailed balance model that assumes a nonunity external radiative efficiency (ERE) of the semiconductor absorber layer. Some of the2D material absorbers have been included, based on known or estimated values of ERE from PLQY reported or achieved in literature. (Reproduced with permission from ref. 110, Copyright © 2017 American Chemical Society).

Fabrication of solar cells using 2D TMDs materials as an active layer has been actively studied in both theoretical and experimental ways.[5, 111-118] The PCE of a solar

cell, is the percentage of the solar energy shining on a PV device that is converted into usable electricity. Improving this PCE is a key goal of research and helps make PV technologies cost-competitive with conventional sources of energy. Table 1.2 summarizes the PCE of solar cells using 2D TMDs as a photoactive layer. However, although several initial concepts for photovoltaic devices based on atomically thin TMDs have been demonstrated, there are few approaches to immediately integrate it into functional devices, and even fewer methods are potentially cost-effective and scalable.[110]

Table 1.2 Type and basic features of solar cells with a TMDs active layer

Type	Material	Layer number	PCE	Ref.
Pn	WSe_2	1 L	0.01 % 0.02 (640 nm)	5
Pn	WSe_2	1 L	0.5 % (halogen lamp, 14000 W m^{-2})	114
Pn	$MoSe_2$	10 L	14 % (Solar simulator)	115
Pn	MoS_2	~ 120 nm	2.8 % (Solar simulator)	116
Schottky	MoS_2	50 nm	2.5 % (532 nm)	117
Schottky	MoS_2	2 L, 3 L	0.7 % (Solar simulator)	118

1.3.2.2 2D transition metal dichalcongenides as a hole transport layer of solar cells

Perovskite solar cells (PSCs) are one of the most promising candidates as the next generation solar cell technology.[119-121] Emerging perovskite materials have opened the way to producing efficient, low-cost solar cells. Perovskites have intense light absorption coefficient (1.5×10^4 cm^{-1} at 550 nm), long electron and hole diffusion length (from 100 nm to 1 mm), high carrier mobility (1 – 10 cm^2 V^{-1} s^{-1}), and the possibility of solution-processing.[122-125] Normally, a standard PSC consists of a perovskite layer (i.e. photoactive layer) to generate charges (holes and electrons), a hole transport layer (HTL) and an electron transport layer (ETL) to separate the generated charges, and front and back electrodes to collect charges (Figure 1.18).[126] The main function of the hole transporting

materials (HTMs) in devices is to collect and transport after holes injection from light harvester, realizing effective separation of electrons and holes, which is an essential part of the PSCs.[127] Therefore, proper choice of HTM is important for efficient charge extraction and stability in PSCs. In order to achieve high performance PSCs, HTMs should have: (1) suitable highest occupied molecular orbital (HOMO) energy levels for matching with the valence band energy (VBE) of perovskite materials, and ensure holes injection and transporting at each interfaces; (2) high hole mobility and photochemical stability; (3) good film-forming ability for processing and device fabrication; (4) suitable light absorption in visible and near-IR region of the solar spectrum for high photocurrent.[128, 129] Among a variety of HTMs, discovery of the 2,2′,7,7′-tetrakis-(N,N-di-4-methoxyphenylamino)-9,9′-spirobifluorene (spiro-MeOTAD) is a milestone in the history of PSCs.[130] It is proven to be the most suitable HTM for testing PSCs due to its facile implementation and high performance. However, spiro-MeOTAD is under debate regarding the topics of cost-performance, long-term stability, degradation issues (induced by temperature, additives, film quality, and environmental conditions), and so on. Therefore, low cost candidates to replace spiro-OMeTAD for PSCs need to be explored and studied for high performance photovoltaic devices with low cost, promising for affordable large-scale energy production to expand the PSCs market. One good motivation to develop PSCs is utilization of already scaled HTMs. Therefore, TMDs and MCs are good potential candidates due to their high carrier mobility, high transparency, tunable band gap, low cost, and solution-processable properties. Combining perovskite and 2D TMDs and MCs gives us an opportunity to obtain solar cell devices with improved PV performance such as higher efficiency and longer-term stability, which could be commercialized and compete with solar cells based on crystalline silicon. It is reported that the ultrafast and efficient charge transfer were detected in the perovskite-TMDs heterostructures.[131] It suggests great promise in application of 2D TMDs and MCs as a HTL or ETL of the components of PSCs.

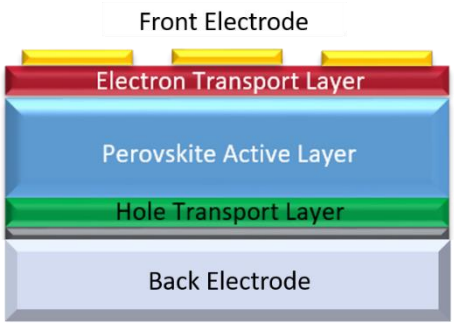

Figure 1.18 Scheme of the standard structure of a perovskite solar cell.

Abdollahi et al. simulated the MoS_2 thin film as a HTL of the heterojunction PSC shown in Figure 1.19.[132] It showed that a single sheet of MoS_2 could effectively enhance the PCE of the device by up to 20.43%, which is comparable with sprio-OMeTAD.[132]

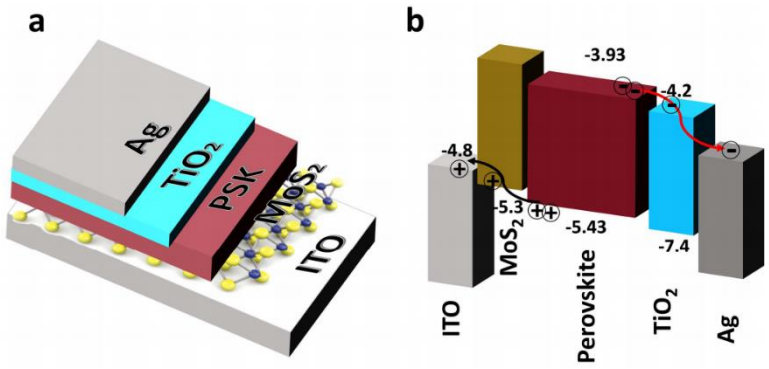

Figure 1.19 (a) Schematic of device architecture, and (b) energy level diagrams for transparent conductive oxide (TCO) / MoS_2 / Methylammonium lead halide ($CH_3NH_3PbI_3$) / titanium dioxide (TiO_2) / Silver (Ag). (Reproduced with permission from ref. 132, copyright ©2018 Nanotechnology).

Li et al.[133] demonstrated the application of water soluble 2D TMDs as a HTL of p-i-n PSCs. The structure of the PSC is presented in Figure 1.20a. The highest PCEs obtained by this system are 14.35% with MoS_2 and 15% with WS_2, respectively (Figure 1.20b). In addition, the stability of the PSCs also gets improved with the TMDs HTL (Figure 1.20c).

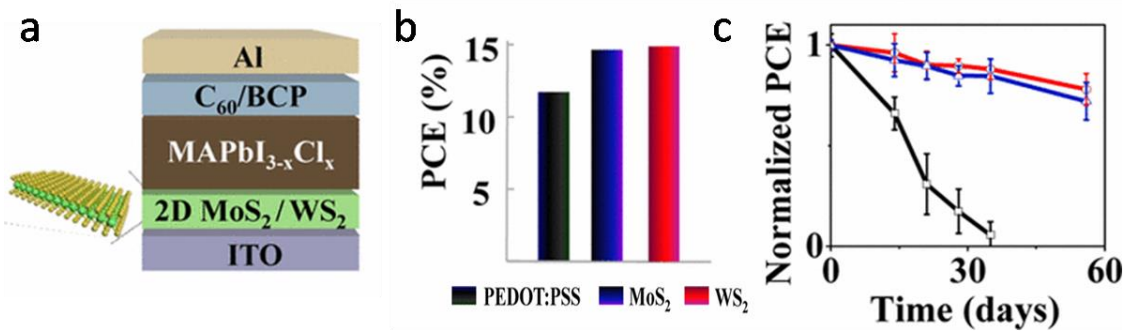

Figure 1.20 (a) Structure of the PSCs with 2D TMDs as a HTL and comparison of (b) PCE and (c) stability of PSCs with PEDOT:PSS, MoS_2 and WS_2 HTLs. (Reproduced with permission from ref. 133, copyright ©2017 American Chemical Society).

Yun et al.[134] reported the application of MoS_2 as an HTL in organic solar cells. They modified the work function of the MoS_2 nanosheets through p-type doping by using gold chloride trihydrate ($HAuCl_4 \cdot 3H_2O$) as a p-doping agent, and n-type doping by using reductants including alkali metals as n-doping agents. As a result, PCE of 3.38 and 2.73% were achieved with p-type MoS_2 as HTL and n-type MoS_2 as ETL, respectively.[134]

1.3.2.3 2D transition metal dichalcongenides as a buffer layer of solar cells

As mentioned in previous section, perovskite solar cells (PSCs) are new trend for the next generation solar cell technology. However, for further commercialization, poor stability is the bottleneck of PSCs. One strategy to improve the stability of the PSCs could be replace the spiro-OMeTAD with other HTM such as copper (I) thiocyanate (CuSCN), nickel (II) oxide (NiO), and poly(3,4-ethylenedioxythiophene)polystyrene sulfonate (PEDOT:PSS).[26, 135-137] However, they are not easy to replace the position of the spiro-OMeTAD. Another strategy is adding a buffer layer between the perovskite and the spiro-OMeTAD layer to prevent intermigration of iodine and metals between the perovskite layer and the spiro-OMeTAD layer. What's more, a buffer layer can also prevent a direct contact between the perovskite and the metal electrode which can occur in solution-processed PSCs due to the incomplete coverage of the perovskite by the HTL and resulting in a decrease of V_{oc} and FF because of high recombination losses.[138-142]

It is believed that the presence of lone pairs of electrons at the surfaces of 2D TMDs and MCs, the presence of non-covalent interactions and the absence of dangling bonds could enhance their resistances to reactions with other chemical species.[134] Therefore, 2D TMDs and MCs could be utilized as a buffer layer to stabilize the PSCs. Bonaccorso et al.[143]showed that zero-dimensional MoS_2 quantum dots (QDs), derived by liquid phase exfoliated MoS_2 flakes, provide both hole-extraction and electron-blocking properties. They reported that graphene interface engineering strategy based on van der Waals MoS_2 QD/graphene hybrids enables $MAPbI_3$-based PSCs to achieve a PCE up to 20.12 % (average PCE of 18.8%).[143]

1.4 Objective of the thesis

As mentioned before, 2D materials for energy applications is still a hot topic for scientific research. Among various 2D families, we focus on 2D MCs and TMDs materials which present many promising opportunities for energy applications due to their remarkable mechanical, electronic, and optoelectronic properties.[5, 18, 22-28] However, their application in electronic devices still fairly undeveloped due to various challenges such as exfoliation and poor conductivity.

First, in order to further commercialization and application, high-quality 2D MCs and TMDs nanosheets should be prepared by a simple and low-cost method. In this project, we used the sonication assisted LPE method to prepare 2D MCs and TMDs nanosheets. The LPE method is known as a cost-effective, efficient, and extraordinarily versatile method that has the potential for large-scale production of defect-free 2D materials.

Then, these resultant 2D MCs and TMDs nanosheets were further tried to fabricate high performance energy storage and conversion devices, such as batteries or solar cells (Figure 1.21). The first application is regarding energy storage. The main objective is exploring novel electrodes based on 2D MCs nanosheets. Because compared to 2D TMDs, MCs are less studied in LiBs. However, as we know, 2D MCs nanosheets are optimistic to be used as an anode material of a LiB. First, MCs materials possess higher theoretical specific capacities for rechargeable lithium-ion batteries compared to traditional intercalation electrode materials.[20] In addition, MCs tend to be more

electrochemically reversible as compared to metal oxide counterparts due to their faster charge transfer kinetics.[144] However, the poor conductivity is the main bottleneck for their utilization as an electrode material. Therefore, improving the conductivity of 2D MCs is the key to optimize their electrochemical performance. In this project, we try to add conducting carbon nanotubes (CNTs) to improve the conductivity of 2D MCs and TMDs nanosheets. In 2D MCs-CNTs composite, 2D MCs nanosheets are percolated in conductive CNTs networks to accelerate the electron transfer during the charge and discharge process. Therefore, based on this novel electrode structure, we could further explore more 2D MCs materials for LiBs. The second application is about energy conversion. Here, we investigate the possibility to use 2D TMDs as an absorber, a hole or electron transport layer, or a buffer layer of solar cells. Based on the large number of studies, there is no doubt that ultrathin 2D MCs and TMDs semiconductors represent some of the most promising materials due to their unique electronic and photonic properties.[86-116] These types of materials can realise large-scale commercial production of high-performance devices with low-cost and a simple process. Therefore, they meet the requirement for new generation solar cells. Because high-performance, economically viable, large-scale producing and rich resources are the key to developing novel solar cells.[107, 108]

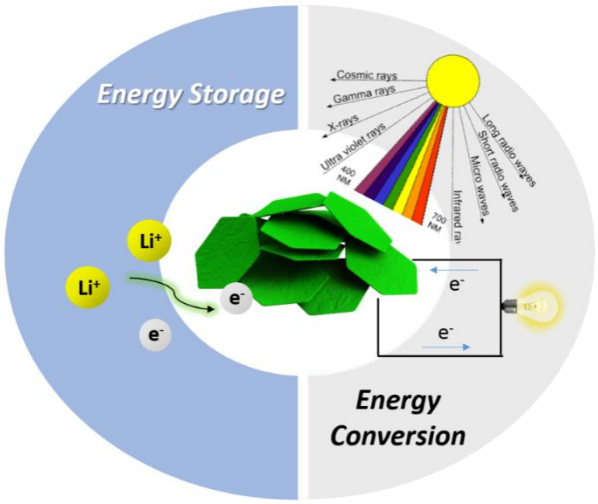

Figure 1.21 2D MCs and TMDs can serve as a versatile platform for energy storage and conversion.

2 2D metal chalcogenides for lithium-ion battery applications

2.1 Introduction

Today, LiBs have been one of the most important energy storage devices owing to their high energy and power density. They are being used in a variety of products ranging from cell phones up to electric vehicles. Since LiBs have become the indispensable source of electrochemical energy storage, a great volume of research in LiBs has been conducted in order to improve their performance. Batteries' performance can be judged by their capacity and cycling stability. One of the most common approach to improve their performance is to study the electrode materials. As for anode materials of LiBs, graphite was first commercialized material and up to now it is still being used in most LiBs.[145, 146] However, there is a limitation of improving the capacity and cycling stability because of the limitation in its theoretical capacity (only 372 mAh/g). Later, silicon has attracted great interests due to their high specific capacity (4200mAh/g).[147] But silicon suffers from up to 400 % volume expansion/contraction in LiBs, which causes rapid capacity fading and poor cyclic stability.[148, 149] Recently, 2D nanomaterials have emerged as efficient candidates for LiBs' electrodes owing to their high specific capacities (> 550 mAh/g), allowing a rapid Li^+ insertion/extraction process without inducing significant volume changes.[20, 150-154] However, stability is still a big concern with most LiBs. Some capacity deterioration is noticeable after one year, whether the battery is in use or not. Although Tesla's LiBs could cycle over 5000 cycles, normally, the battery frequently fails after 300 to 500 charge cycles. Thus, finding suitable electrode materials with good cycling stability is also an essential requirement of research for advancing the LiBs.

Among various 2D nanomaterials, the 2D MC family (where M is Ga/In, C is S/Se/Te, etc.) shows remarkable potential for use as an anode in LiBs due to the multielectron conversion reaction and the lamellar structure.[155] However, this kind of materials are relative unexploreddue to their low electronic conductivity and challenges in exfoliation.In this project, we prepared four different few-layered 2D MC nanosheets (i.e. GaS, GaSe, GaTe, and InSe) through LPE of bulk layered MC crystals. However, these 2D MCs nanosheets have high surface energy and van der Waals attraction unavoidably result in severe stacking/restacking and agglomeration, generating many

inaccessible active sites. In addition, their relatively low conductivity also limits the rapid charge/discharge capability.[156-158] In order to address this problem, 2D MCs were percolated in single wall carbon nanotubes (SWCNTs) networks to simultaneously accelerate the transfer of electrons and maintain well-dispersed 2D nanomaterials during the repeated charge/discharge process.2D MCs-SWCNTs composites electrodes were demonstrated as anodes of LiBs and showed the optimistic electrochemical performance. According to this work, we believe that the LPE-based facile approach to fabricate 2D MC-conductive porous scaffold could be generalized to other 2D materials, which may inspire new electrode architectures, thus enabling a wide range of applications.

2.2 Results and discussion

2.2.1 Preparation of 2D metal chalcogenide nanosheets

Layered MCs (i.e. GaS, GaSe, GaTe and InSe) were exfoliated *via* sonication assisted LPE approach. MCs were exfoliated in N-Methyl-2-pyrrolidone (NMP) in the very first, since NMP has suitable surface energy and Hansen's solubility parameters (HSPs).[159] However, NMP is a toxic solvent (Health code ≥ 2, NFPA 704) with a high boiling point (202 °C).[160] Therefore, exfoliated 2D MC nanosheets were centrifuged and then re-dispersed in isopropanol (IPA) solvent, which is a nontoxic solvent (Health code 1; NFPA 704) with a low environmental impact and a low boiling point (82.6 °C).[160] Finally, exfoliated 2D MC nanosheets dispersion in IPA was obtained as shown in Figure 2.1a-d (inset pictures). Replacement of dispersion solvent from NMP to IPA allows the dispersion to be easily handled, environmentally-friendly, and available to fabricate high-performance devices.

Figure 2.1a-d show the exfoliated GaS, GaSe, GaTe and InSe dispersions (inset) and their transmission electron microscopy (TEM) images. TEM images of these dispersions indicated that they are well exfoliated with high quality showing electron transparency and distinctive edges. However, these dispersions were comprised of different shapes and sizes of exfoliated MCs nanosheets. GaS, GaSe and GaTe nanosheets have similar shapes, while InSe exhibited distinct hexagonal shaped nanosheets. This is because bulk GaS, GaSe and GaTe we used the commercial products,

but the bulk InSe was obtained in the lab *via* phase-controlled synthesisinstead of commercial one.

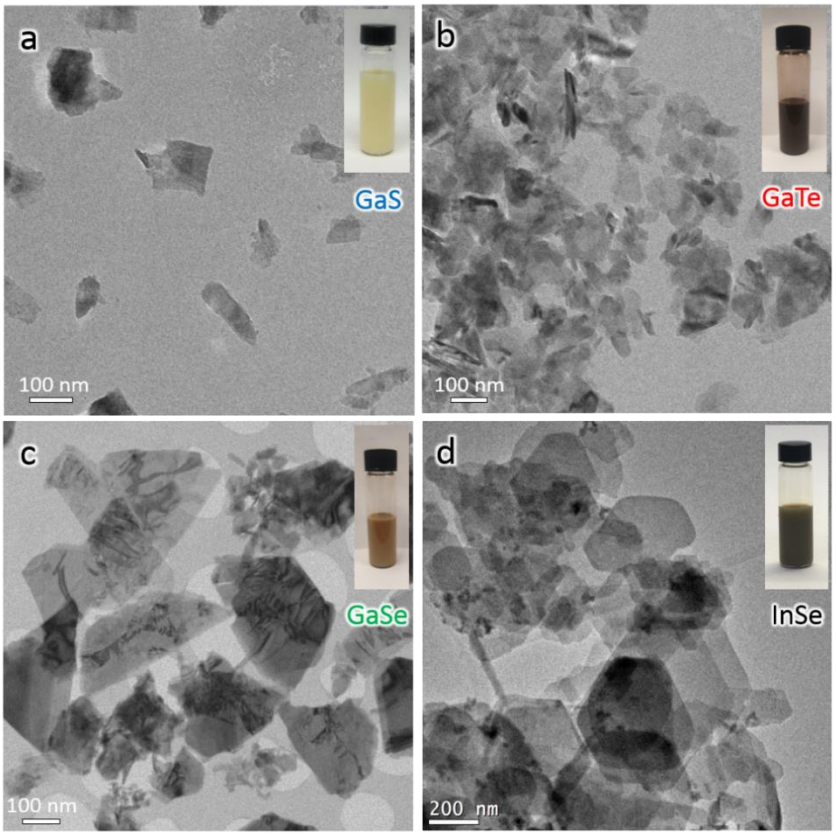

Figure 2.1 TEM images of exfoliated (a) GaS, (b) GaSe, (c) GaTe and (d) InSe nanosheets (insides are photos of exfoliated GaS, GaSe, GaTe and InSe nanosheets dispersions, respectively).

Figure 2.2a-d illustrate size distribution histogramof exfoliated GaS, GaSe, GaTe and InSe nanosheets' sizes, respectively. This statistical analysis was based on around 100 of nanosheets for each sample. As Figure 2.1a-d shown, although the same LPE process was applied, the average length of GaS, GaSe, GaTe and InSe nanosheets were varied from 138 nm (InSe) to 319 nm (GaSe). Actually, a number of process parameters are crucial for the outcome of the exfoliation for LPE.[69] For instance, solvent, initial concentration of the bulk materials, process time and volume, power output and amplitude of sonicators, centrifuging speed, etc. Stabilization using additive-free solvents can be described using solution thermodynamics, which predicts that efficient stabilization or dissolution occurs when the net energetic cost of mixing is minimized.[69] Since nanomaterials are rather large and rigid compared to molecules, the entropic

contribution can be neglected which means that stabilization is achieved when the solubility parameters (such as the surface tension or Hansen parameters) of solvent and solute match.[69] Here, we used same solvent, initial concentration of the bulk materials, process time and volume, power output and amplitude of sonicators, centrifuging speed. According to previous report, we have known that dispersion appeared to occur for solvents with surface tensions in the range 30 – 40 mJ/m^2. Therefore, we used NMP (41 mJ/m^2) as an initial exfoliation solvent to exfoliate these layered MCs to get relatively high-quality 2D nanosheets. Then, these exfoliated MCs nanosheets were dispersed in IPA (22 mJ/m^2) in the end. As we know, the surface energy of four different MCs is different. Thus, in order to stabilize exfoliated, or de-bundled, 2D MCs nanosheets in solvents, the surface energy of the solvent should be different. However, four different layered MCs were dispersed in the same solvent (i.e. IPA). Therefore, different size of 2D MCs dispersions were obtain though the same LPE protocol.

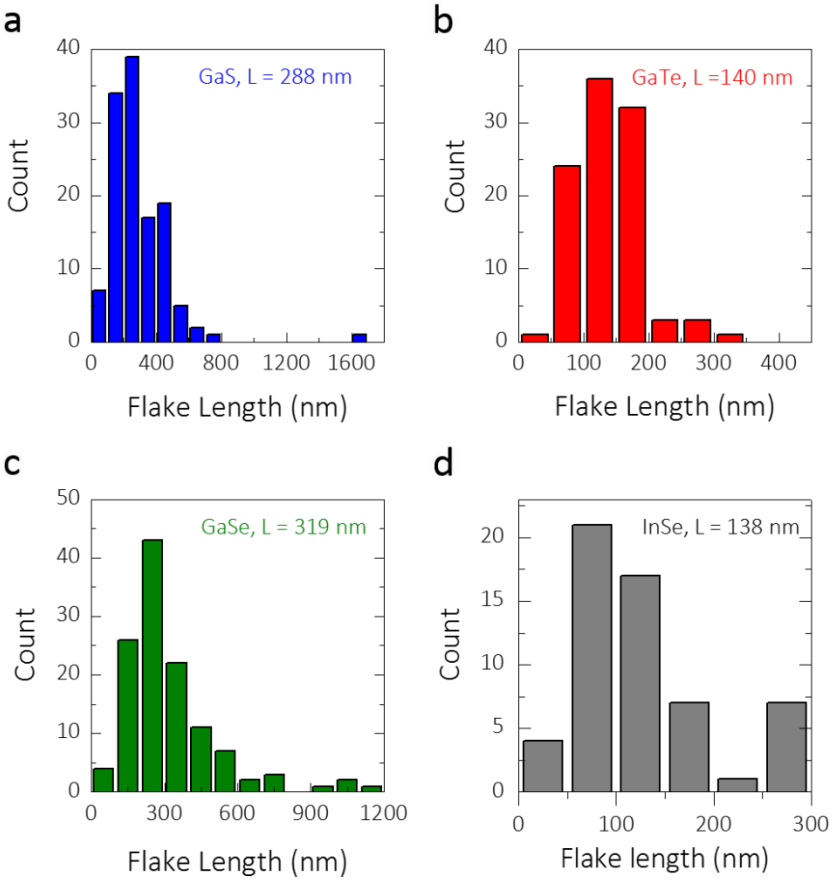

Figure 2.2 Size distribution histograms of exfoliated 2D (a) GaS, (b) GaSe, (c) GaTe and (d) InSe nanosheets.

2.2.2 Preparation and electrochemical performances of 2D metal chalcogenide nanosheets and SWCNTs composite anodes for lithium-ion battery

2D MC nanosheets have a promising prospect as anode materials owing to their high theoretical capacity and 2D graphene-like structure. However, they suffer from problems with relatively low electronic conductivity and volume changes, which have limited their applications in LiBs' anodes. Taking these problems into consideration, SWCNTs are being used as additives to enhance the conductivity of these composites and reduce the structural degradation. Therefore, adding 1D SWCNTs to obtain a 1D and 2D hybrid heterostructure MC nanosheets and SWCNTs composite could allow us to improve the conductivity and flexibility of 2D MC materials. Here, the SWCNT loading percentage was fixed at 20 wt% for all composites. Specifically, 0.1 g/mL of SWCNTs dispersion (using IPA as a solvent) was added to 2D MCs dispersion (in IPA solvent), and bath sonicated for 30 mins to obtain their mixture. Then, a binder-free flexible 2D MCs-SWCNTs composite electrode was obtained *via* a facile vacuum filtration approach (as shown in Figure 2.3). In this system, the SWCNTs could work as both conductive additive and binder, without any additional carbon black or polymer binder. More experiment details are described in the experiment part.

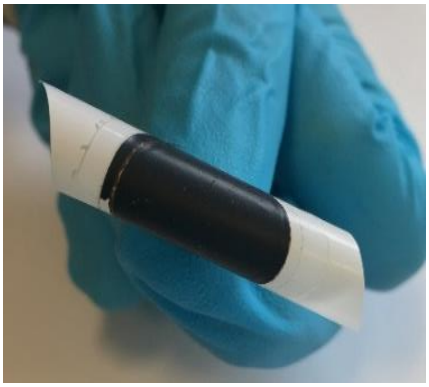

Figure 2.3 A flexible binder-free InSe-SWCNTs composite film for the LiB's anode.

Figure 2.4a-d and Figure 2.5a-d show the top and cross-section scanning electron microscope (SEM) images of these four different MC-SWCNTs composite electrodes. According to them, we could see that SWCNTs were well interlaced with the MC nanosheets to produce stable MC-SWCNTs networks, revealing that simply blending and sonicating of the exfoliated 2D MC nanosheets and the SWCNTs dispersions could

obtain the uniform MC-SWCNTs composite. The homogeneous distribution of both nanotubes and nanosheets within the composite was confirmed by elemental mapping of Metal (e.g. Ga and In), Chalcogenide (e.g. S, Se, and Te), and carbon (C) performed by energy-dispersive X-ray spectroscopy (EDS) of MC-SWCNTs composite electrodes (Figure 2.6a-d). Owing to its one-dimensional structure and superior electrical property, SWCNTs improved the both conductivity and flexibility of the electrodes. As we know, 2D MCs themselves show very low conductivity (less than 1 S/m), however, when we added the SWCNTs, the conductivity of MC-SWCNTs composites obviously got enhanced. Conductivity of each MC-SWCNTs electrode was measured and they were119.7 S/m, 232.5 S/m, 264.7 S/m, and 231.4 S/m for GaS-SWCNTs, GaSe-SWCNTs, GaTe-SWCNTs, and InSe-SWCNTs composite electrodes, respectively. In addition, taking a InSe-SWCNTs composite film as an example, the structure of the composite film can be well maintained even the film is bent at a certain angle (Figure 2.7a and b). Furthermore, even if the film is cracked, there are also SWCNTs linked each part (Figure 2.7c and d). Therefore, SWCNTs can be proved to enhance the mechanical strength of these films.

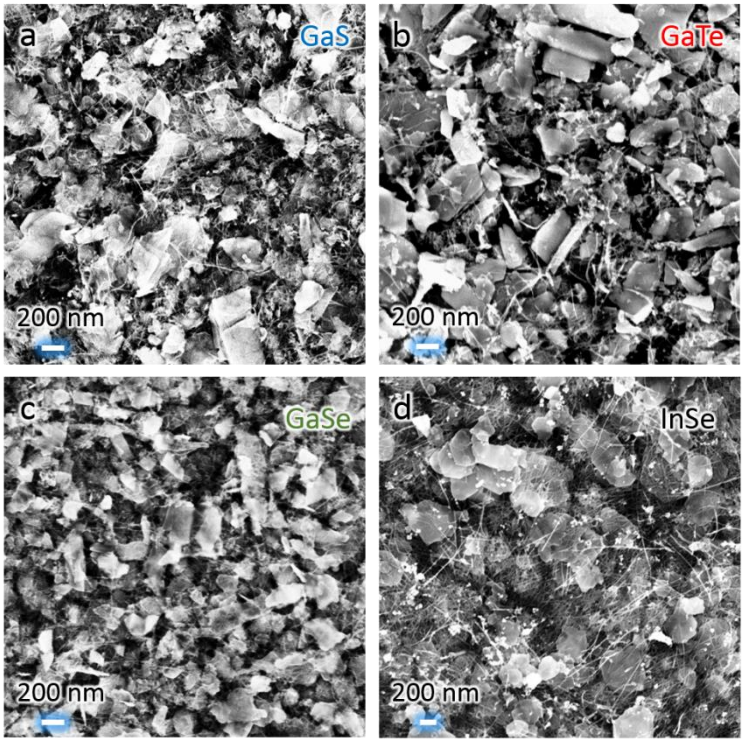

Figure 2.4 Top SEM images of exfoliated (a) GaS-SWCNTs, (b) GaSe-SWCNTs, (c) GaTe-SWCNTs and (d) InSe-SWCNTs composite electrodes.

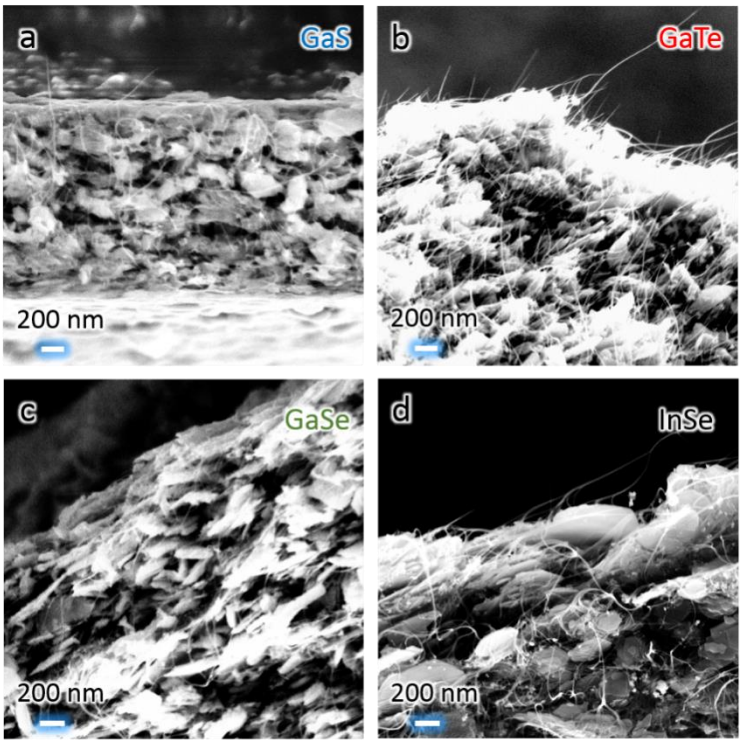

Figure 2.5 Cross-section SEM images of exfoliated (a) GaS-SWCNTs, (b) GaSe-SWCNTs, (c) GaTe-SWCNTs and (d) InSe-SWCNTs composite electrodes.

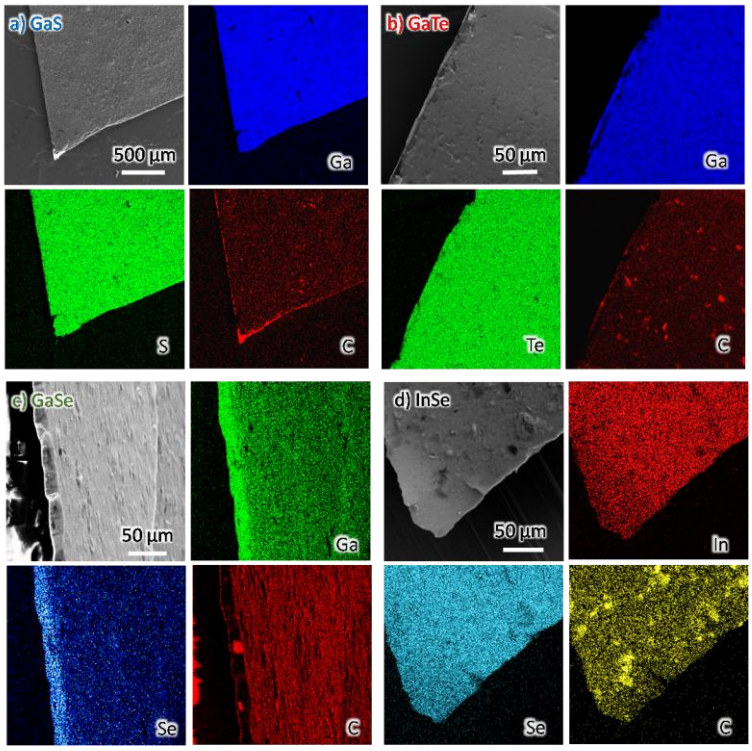

Figure 2.6 EDS mappings of (a) GaS-SWCNTs, (b) GaSe-SWCNTs, (c) GaTe-SWCNTs and (d) InSe-SWCNTs composite electrodes.

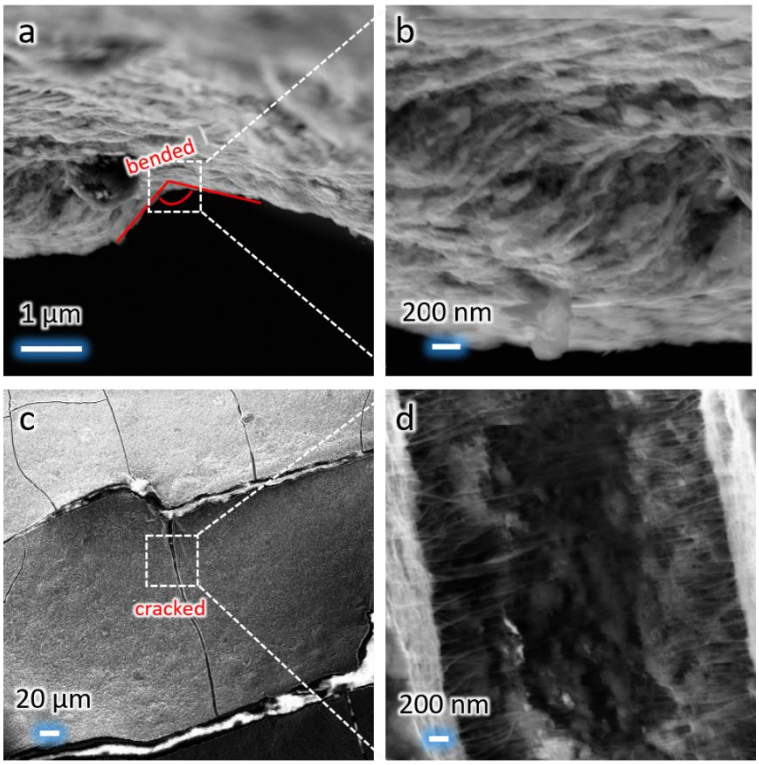

Figure 2.7 (a) low magnification SEM image and (b) high magnification SEM image of a bended InSe-SWCNTs composite film, (c) low magnification SEM image and (d) high magnification SEM image of a cracked InSe-SWCNTs composite film.

The electrochemical performance of the MC-SWCNTs composite anodes were studied *via* CV and GCD measurements. Experiment details could be found in the experiment section below. Figure 2.8a shows the rate performances of four different MC-SWCNTs composite anodes. Compared to GaS-SWCNTs, GaSe-SWCNTs and GaTe-SWCNTs, the InSe-SWCNTs composite electrode displayed much better rate capability. Specifically, as shown in Figure 2.8b, at low current density (of 50 mA/g), the specific capacities of GaS-SWCNTs, GaSe-SWCNTs, GaTe-SWCNTs and InSe-SWCNTs composite electrodes were 761.8 mAh/g, 517.6 mAh/g, 515.8 mAh/g, and 762.1mAh/g, respectively. Here, the specific capacity was calculated using the total mass of MC and SWCNTs as the mass of active materials. If the specific capacity is calculated by the mass of MC only, their values would be 952.3 mAh/g, 647.0 mAh/g, 644.8 mAh/g, and 952.6 mAh/g, respectively, which are relatively high among MC- or TMD-containing electrode systems.[150, 161-175] The specific capacity of MC-SWCNTs composite electrodes decreased with the increasing of the rate, however, the InSe-SWCNTs composite anode showed the

minimum reduction of the capacity and maintained the highest value among these four MC-SWCNTs composite anodes. As shown in Figure 2.8b, at high current density (of 2 A/g), the specific capacity of the InSe-SWCNTs composite electrode was 744 mAh/g, almost double that of the GaS-SWCNTs composite electrode (379 mAh/g) and more than 10 times higher than the capacity of GaSe-SWCNTs and GaTe-SWCNT composite electrodes (9 mAh/g and 29 mAh/g, respectively). Compared to other MCs or TMDs electrodes, the specific capacities of InSe-SWCNTs sample (744 mAh/g) belongs to the top level. It should be specially noted that, in order to eliminate the effect of the materials' morphology on the capacities, only materials with a 2D layered structure, such as nanosheets, nanoflakes, or nanoplates were chosen from the large MC family. However, it is rather challenging to make a direct comparison among various systems due to many variables, such as mass loading/film thickness, potential range, binder/conductive additive fractions, and nanosheet size. Taking this into account as much as possible, firstly the literature-specified capacities were normalized based on the mass of active MC or TMD and total electrode, and then categorized the values according to the mass loading as well as the potential range. As shown in Figure 2.8a, when the current density was switched back to 50 mA/g after increasing to 2 A/g (highest current density in this work), the capacity of the InSe-SWCNTs sample returned to 1157mAh/g, which is relatively high among LiBs.[150, 161-177] What's more interesting is that the capacity of the InSe-SWCNTs composite electrode increased slightly after each five cycles under the same current density, while for the other three MC-SWCNTs composite electrodes their capacity dropped with the increase in cycle number. Improvement of the capacity could be observed more obviously in the cycling test (Figure 2.9a).

Figure 2.8c represents the CV curves of these four MC-SWCNTs composite electrodes at a scan rate of 0.2 mV/s. CV curves were scanned three time for each sample, and Figure 2.8c shows the third CV curve. The GaS-SWCNTs and GaSe-SWCNTs electrodes had similar shape of CV curves, while the GaTe-SWCNTs and InSe-SWCNTs electrodes were different. It means that GaS-SWCNTs and GaSe-SWCNTs electrodes probably have similar Li-ion storage mechanism, but GaTe-SWCNTs and InSe-SWCNTs electrodes have other kinds of mechanisms. For GaS-SWCNTs and GaSe-SWCNTs anodes, taking GaS-SWCNTs as an example, conversion reactions could be expressed by following equations (1) and (2), which has been already studied by Nicolosi. et al:[20, 151]

$$GaS + 2Li^{+} + 2e^{-} \rightarrow Ga + Li_2S \quad (1)$$

Moreover, the cathodic peaks centred at 0.6 and 0.1 V could be attributed to the formation of LiGa and Li_2Ga alloy phases, respectively, according to the following overall reaction:[178, 179]

$$Ga + 2Li^{+} + 2e^{-} \leftrightarrow Li_2Ga \quad (2)$$

For anodic scanning, peaks centred at 0.5 V and 0.8 V were found, corresponding to the de-alloying of the Li_2Ga and LiGa phases, respectively, to Ga.[178, 179] In addition, the peak corresponding to reaction (1) in the anodic scanning indicated that the conversion mechanism of GaS is reversible. Besides, the small oxidation peak ~1.8 V might be ascribed to the reaction of Li with hydrogen functional groups on the CNT surfaces.[180]

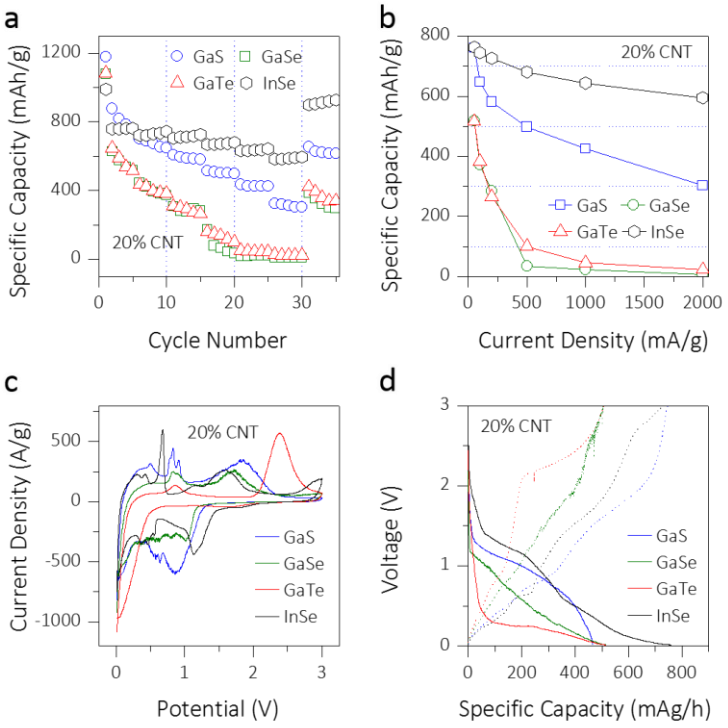

Figure 2.8 (a) Rate performance (current density: 50 mA/g, 100 mA/g, 200 mA/g, 500 mA/g, 1000 mA/g, 2000 mA/g, 50 mA/g) of four different 2D MC-SWCNTs composites plotted as a function of cycle number, (b) Rate performance of four different 2D MC-SWCNTs composites plotted as a function of current density, (c) CV curves of these four

MC-SWCNTs composite electrodes at a scan rate of 0.2 mV/s at the potential range of 0.01~3 V, (d) GCD profile of four different 2D MC-SWCNTs composites at current density of 50 mA/g, solid lines are discharge and dotted lines are charge processes.

This agrees with the GCD profiles (Figure 2.8d); that is, the charge and discharge plateaus of the samples all had corresponding CV peaks (Figure 2.8d). For the GaS sample, CV peaks were more obvious and stronger than for GaSe. Thus, the integrated area of the GaS is much higher than that of GaSe, which means the specific capacity of GaS was higher than that of GaSe, and this agrees with the GCD measurement results (Figure 2.8c and d). For GaTe sample, there was no sharp peak during CV scanning. It is similar to a graphene anode. There was only intercalation and de-intercalation during the charging and discharging process. For InSe sample, it also presented sharp cathodic and anodic peaks, however, those were different from GaS and GaSe. Because In has the different redox potentials from Ga. In addition, InSe has many different phases (e.g. InSe, In_4Se_3 or In_2Se_3). Both morphology and stoichiometry play an important role in the lithium insertion process Therefore, for the InSe-SWCNTs electrode, the process may be more complicated than GaS-SWCNTs or GaSe-SWCNTs electrode. For InSe sample, it is discussed more in detail in Chapter 3.

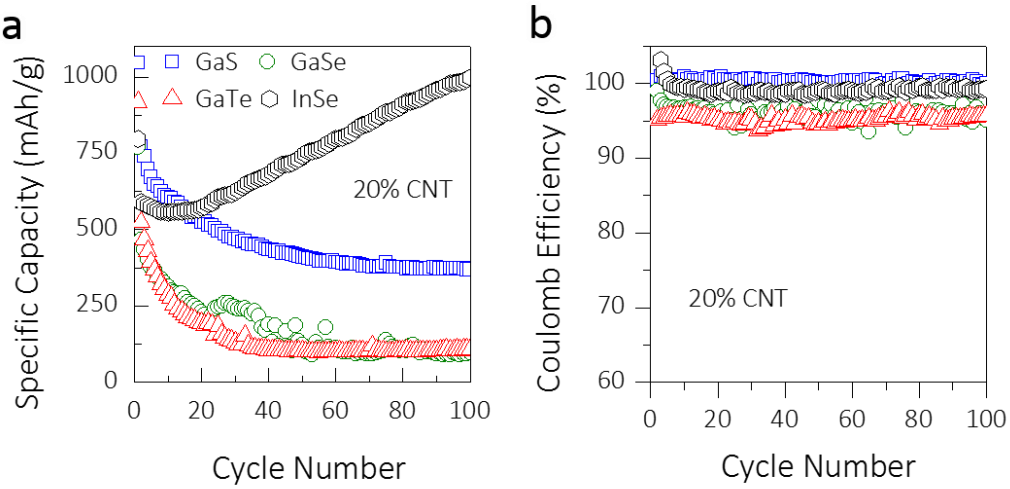

Figure 2.9 (a) Specific capacity and (b) coulombic efficiency of four different MC-SWCNTs composite electrodes over 100 cycles at 500 mA/g.

Figure 2.9a (specific capacity) and b (coulombic efficiency) illustrates the cycling test results of the MC-SWCNTs composite anodes. Among four different composites anodes, the specific capacity of GaTe sample decreased fastest among these four MC-SWCNTs samples. What's more interesting is the specific capacity of InSe-SWCNTs sample increased during cycling, while the other three decreased. Specifically, the specific capacity of InSe-SWCNTs sample increased from 737.3 mAh/g (at the first cycle) to 1245.2 mAh/g after 100 cycles. Similar phenomenon also observed in Figure 2.8a that the specific capacity of InSe-SWCNTs increased slightly after five cycles under each current density. Thus, not only did the InSe-SWCNTs composite have an excellent cycling stability, but its specific capacity also improved over cycling. This kind of phenomenon has never been found in other electrode materials. Therefore, the InSe-SWCNTs sample was chosen to study more in detail, and it is presented in Chapter 3. After cycling, the MC-SWCNTs composite still preserves their 2D layered morphology, demonstrating the percolated network maintains the structural integrity upon repeated charging and discharging.[20]

Figure 2.10 and Table 2.1 compare the electrochemical performances of MC-containing electrodes in detail. It should be specially noted that, in order to eliminate the effect of the materials' morphology on the capacities, only materials with a 2D layered structure, such as nanosheets, nanoflakes, or nanoplatelets, were chosen from the large MC family. We emphasize that it is rather challenging to make a direct comparison among various systems due to many variables, such as mass loading/film thickness, potential range, binder/conductive additive fractions, and nanosheet size. Taking this into account as much as possible, firstly the literature-specified capacities were normalized based on the mass of active MC and total electrode, and then categorized the values according to the mass loading as well as the potential range. It is worth mentioning that an anode with lower potential is more desirable for achieving a higher energy/power density in LiBs. Unlike the half-cell configuration that emphasizes the discharge capacity regardless of the electrode being anode or cathode, a full-cell battery system relies on the charge capacity of the anode. Therefore, for those systems tested in the 0.01–3 V window, the charge capacities that were achieved in the range 0.01–3 V were extracted to facilitate our comparison. The compiled plot shows that our binder-free MC-SWCNT composites perform much better than any other 2D MC-based electrode systems in terms of capacity per active MC and per electrode in the 0.01–3 V window.

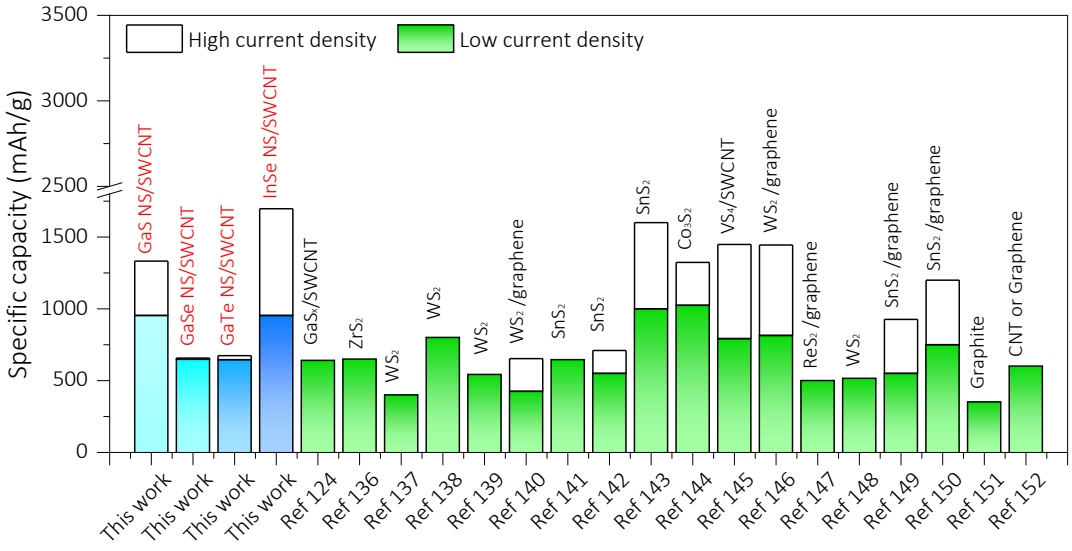

Figure 2.10 Comparison of the specific capacities at low (~50 mA/g) and high current densities (~2 A/g) of this work to various 2D MC or TMD containing electrode systems. Table 2.1 provides details and references. For the purpose of comparison, we also include graphite and SWCNT/graphene anodes.

Table 2.1 Comparison of the specific capacities at low and high current densities of this work to various 2D MC or TMD containing electrode systems.

Type of MC	Synthetic method	Electrode composition	Electrode mass loading	V window	Specific capacities	Ref.
GaS/SWCNT	LPE	GaS : SWCNT = 80 :20	0.2 mg cm^{-1}	0.01 ~ 3 V	$C_{composite}$: 762mAh g^{-1} @ 50 mA g^{-1} 648mAh g^{-1} @ 100 mA g^{-1} 303mAh g^{-1} @ 2 A g^{-1} C_{GaS}: 953mAh g^{-1} @ 50 mA g^{-1} 810mAh g^{-1} @ 100 mA g^{-1} 379mAh g^{-1} @ 2 A g^{-1}	This work
GaSe/SWCNT	LPE	GaSe : SWCNT = 80 :20	0.2 mg cm^{-1}	0.01 ~ 3 V	$C_{composite}$: 518mAh g^{-1} @ 50 mA g^{-1}	This work

					373mAh g $^{-1}$ @ 100 mA g $^{-1}$ **7mAh g $^{-1}$ @ 2 A g $^{-1}$** **C_{GaSe}:** **648mAh g $^{-1}$ @ 50 mA g $^{-1}$** **466mAh g $^{-1}$ @ 100 mA g $^{-1}$** **9mAh g $^{-1}$ @ 2 A g $^{-1}$**	
GaTe/SWCNT	**LPE**	**GaTe : SWCNT = 80 :20**	**0.2 mg cm^{-1}**	**0.01 ~ 3 V**	**$C_{composite}$:** **516mAh g $^{-1}$ @ 50 mA g $^{-1}$** **383mAh g $^{-1}$ @ 100 mA g $^{-1}$** **23mAh g $^{-1}$ @ 2 A g $^{-1}$** **C_{GaTe}:** **645mAh g $^{-1}$ @ 50 mA g $^{-1}$** **479mAh g $^{-1}$ @ 100 mA g $^{-1}$** **29mAh g $^{-1}$ @ 2 A g $^{-1}$**	**This work**
InSe/SWCNT	**LPE**	**InSe : SWCNT = 80 :20**	**0.2 mg cm^{-1}**	**0.01 ~ 3 V**	**$C_{composite}$:** **762mAh g $^{-1}$ @ 50 mA g $^{-1}$** **743mAh g $^{-1}$ @ 100 mA g $^{-1}$** **595mAh g $^{-1}$ @ 2 A g $^{-1}$** **C_{InSe}:** **953mAh g $^{-1}$ @ 50 mA g $^{-1}$** **929mAh g $^{-1}$ @ 100 mA g $^{-1}$** **744mAh g $^{-1}$ @ 2 A g $^{-1}$**	**This work**
GaS_xnano film coated onto SWCNT	ALD	GaS_x-30%CNT:CB:PVDF = 80:10:10	Unknown	0.01 ~ 2 V	$C_{composite}$: ~ 800 mAh g $^{-1}$ @ 120 mA g $^{-1}$ ~600 mAh g $^{-1}$ @ 600 mA g $^{-1}C_{electrode}$:	150

					~640 mAh g^{-1} @ 120 mA g^{-1} ~480 mAh g^{-1} @ 600 mA g^{-1}	
ZrS_2nano disc	Colloidal synthesis	ZrS_2:CB:PVDF = 60:20:20	Unknown	0.01 ~ 2 V	$C_{electrode}$: ~390 mAh g^{-1}@ 69 mA g^{-1} ~312 mAh g^{-1} @ 552 mA g^{-1} C_{ZrS2}: ~650mAh g^{-1}@ 69 mA g^{-1} ~520mAh g^{-1} @ 552 mA g^{-1}	161
WS_2nano sheets	High T hexadecylamin based solution synthesis	WS_2:CB:PVDF =80:10:10	Unknown	0.005 ~ 2 V	$C_{electrode}$: ~320 mAh g^{-1}@ 100 mA g^{-1} C_{WS2}: ~400mAh g^{-1} @ 100 mA g^{-1}	162
WS_2nano sheets	Rheological phase reaction	WS_2:CB:PTFE =70:20:10	Unknown	0.01 ~ 3 V	$C_{electrode}$: ~560mAh g^{-1} @ 47.5 mA g^{-1} C_{ZrS2}: ~800mAh g^{-1} @ 47.5 mA g^{-1}	163
WS_2nano sheets	Solid-state synthesis	WS_2:CB:PTFE =80:10:10	Unknown	0.01 ~ 3 V	$C_{electrode}$: ~434mAh g^{-1} @ 43.5 mA g^{-1} ~240mAh g^{-1} @ 870 mA g^{-1} C_{ZrS2}: ~542mAh g^{-1} @ 43.5 mA g^{-1} ~300mAh g^{-1} @ 870 mA g^{-1}	164
WS_2nano sheets/graphene	Hydrothermal method	WS_2-20% graphen:CB:PVDF =85:5:10	Unknown	0.01 ~ 3 V	$C_{composite}$: ~ 500 mAh g^{-1}@ 100 mA g^{-1} ~339mAh g^{-1} @ 2 A g^{-1} ~179mAh g^{-1} @ 4 A g^{-1} $C_{electrode}$: ~ 425mAh g^{-1}@ 100 mA g^{-1}	165

					~228mAh g^{-1} @ 2 A g^{-1} ~152mAh g^{-1} @ 4 A g^{-1}	
SnS_2nano sheets	Thermal decomposition in organic solvent	SnS_2:CB:PVDF 80:10:10	Unknown	0.001 ~ 1.1 V	$C_{electrode}$: ~516mAh g^{-1}@ 323 mA g^{-1} C_{SnS2}: ~645mAh g^{-1} @ 323 mA g^{-1}	166
SnS_2nano sheets	Hydrothermal method	SnS_2:CB:PVDF 60:20:20	Unknown	0.005 ~ 1.15 V	$C_{electrode}$: ~330mAh g^{-1}@ 323 mA g^{-1} ~96mAh g^{-1}@ 3.23 A g^{-1} C_{SnS2}: ~550mAh g^{-1} @ 323 mA g^{-1} ~160mAh g^{-1}@ 3.23 A g^{-1}	167
SnS_2nano plates	Solution synthesis	SnS_2:SWCNT:PVDF 80:10:10	Unknown	0.005 ~ 3 V	$C_{electrode}$: ~800mAh g^{-1}@ 100 mA g^{-1} ~480mAh g^{-1}@ 2 A g^{-1} ~320mAh g^{-1}@ 5 A g^{-1} C_{SnS2}: ~1000mAh g^{-1} @ 100 mA g^{-1} ~600mAh g^{-1}@ 2 A g^{-1} ~400mAh g^{-1}@ 5 A g^{-1}	168
Co_3S_2nan osheets	Hydrothermal method	Co_3S_4:CB:Teflon-AB = 72:14:14	~1 mg cm^{-2}	0.01 ~ 3 V	$C_{electrode}$: 737mAh g^{-1}@ 50 mA g^{-1} 215mAh g^{-1}@ 2 A g^{-1} 90mAh g^{-1}@ 4 A g^{-1} C_{Co3S4}: 1024mAh g^{-1} @ 50 mA g^{-1} 299mAh g^{-1}@ 2 A g^{-1}	169

					126mAh g^{-1}@ 4 A g^{-1}	
VS_4nanofilm coated onto SWCNT	Hydrothermal method	VS_4-3% graphene:CB:PVDF =80:10:10	~1 mg cm^{-2}	0.01 ~ 3 V	$C_{composite}$: 924mAh g^{-1}@ 90 mA g^{-1} ~820mAh g^{-1} @ 1.8 A g^{-1} 766mAh g^{-1} @ 4.5 A g^{-1} $^1C_{electrode}$: 793mAh g^{-1}@ 90 mA g^{-1} ~656mAh g^{-1} @ 1.8 A g^{-1} 613mAh g^{-1} @ 4.5 A g^{-1}	170
WS_2nanosheets/n-doped graphene	Hydrothermal method	WS_2-24% graphen:PVDF =90:10	~1 mg cm^{-2}	0.01 ~ 3 V	$C_{composite}$: 905mAh g^{-1}@ 100 mA g^{-1} ~700mAh g^{-1} @ 2 A g^{-1} ~650mAh g^{-1} @ 5 A g^{-1} $^1C_{electrode}$: 815mAh g^{-1}@ 100 mA g^{-1} ~630mAh g^{-1} @ 2 A g^{-1} ~585mAh g^{-1} @ 5 A g^{-1}	171
ReS_2nanowall grown on 3D graphene foam	CVD	ReS_2:3D graphene = unknown	1.77 mg cm^{-2}	0.01 ~ 3 V	C_{ReS2}: ~500mAh g^{-1} @ 100 mA g^{-1} ~300mAh g^{-1}@ 2 A g^{-1} ~100mAh g^{-1}@ 5 A g^{-1}	172
WS_2nanosheets	Superacid exfoliation	WS_2:CB:PVDF =80:10:10	2.5 mg cm^{-2}	0.01 ~ 3 V	$C_{electrode}$: 413mAh g^{-1}@ 10 mA g^{-1} 376mAh g^{-1}@ 25 mA g^{-1} 330mAh g^{-1}@ 50 mA g^{-1} C_{WS2}: 516mAh g^{-1}@ 10 mA g^{-1} 470mAh g^{-1}@ 25 mA g^{-1} 413mAh g^{-1}@ 50 mA g^{-1}	173
SnS_2nanoplate/graphene	CVD	SnS_2-5% graphene:CB:PVDF = 80:10:10	2~3 mg cm^{-2}	0 ~ 1.3 V	$C_{composite}$: 687mAh g^{-1}@ 50 mA g^{-1}	174

					480mAh g^{-1} @ 1.6 A g^{-1} 230mAh g^{-1} @ 6.4 A g^{-1} $C_{electrode}$: 550mAh g^{-1}@ 50 mA g^{-1} 376mAh g^{-1} @ 1.6 A g^{-1} 330mAh g^{-1} @ 6.4 A g^{-1}	
SnS_2nano plate/graphene	Hydrothermal method	SnS_2-30% graphene:CB:PVDF = 75:10:15	~2 mg cm^{-2}	0.005 ~ 3 V	$C_{composite}$: 1000mAh g^{-1}@ 100 mA g^{-1} 600mAh g^{-1} @ 6.4 A g^{-1} $C_{electrode}$: 750mAh g^{-1}@ 100 mA g^{-1} 450mAh g^{-1} @ 6.4 A g^{-1} (Asymmetric charging discharging)	175
Other anode materials						
Graphite	Various method	-	-	0.01 ~ 0.9 V	$C_{electrode}$: 300 ~ 350mAh g^{-1}	176
CNT or Graphene	Various method	-	-	0.01 ~ 1.5 V	$C_{electrode}$: 200 ~ 600mAh g^{-1}	177

2.3 Conclusion

This work focussed on the preparation and energy application of 2D MC nanosheets (e.g. GaS, GaSe, GaTe and InSe) in LiBs. First, 2D MC nanosheets were successfully obtained *via* sonication-assisted LPE method. After that, exfoliated 2D MC nanosheets were studied as anode materials of LiBs. To maximize the electrochemical property of these 2D MC nanosheets, SWCNTs were added to increase the conductivity and flexibility of the electrodes. Using a colloidal solution processing approach, these MC nanosheets' matrices embedded well in the SWCNTs percolated networks. Then, according to their electrochemical tests, we could safely make the conclusion that 2D MC-SWCNTs composite electrodes are promising to be used as anode materials of LiBs. What's more, among these 2D MCs, 2D InSe-SWCNTs composite electrodes displayed

the best rate capability and high specific capacitance. In addition, according to cycling test, we could see the improvement of the capacity during charging and discharging cycling. It is a quite interesting phenomenon for battery application, as it means that the quality of a battery will be improved when the battery is used, which is extremely exotic. However, it should be studied more in detail to confirm our results and to further understand the mechanism inside.

This work opens vast opportunities for2D MC family to be scalably processed into flexible conductive composite films with applications in energy storage system. In the meanwhile, according to comparison of four different 2D MC nanosheets, we found the novel and exotic electrode material, that is 2D InSe, for LiBs. Therefore, based on this study, we further explore InSe for LiBs' electrode material.

2.4 Experimental methods

2.4.1 Materials

Indium acetate (InAcO), selenium (Se, 99.5 %), gallium (II) sulfide (GaS), gallium (II) selenide (GaSe), and gallium (II) telluride(GaTe) powders and N-Methyl-2-pyrrolidone (NMP), isopropyl alcohol (IPA),hexadecylamine, dodecylamine used throughout these experiments were purchased from Sigma Aldrich. Single wall carbon nanotube (SWCNT, P3-CNT) was purchased by Carbon Solutions, Inc. And polypropylene membrane (K2045 coated PP) was from Celgard LLC, Charlotte, NC.

2.4.2 Preparation of 2D metal chalcogenide nanosheets

2D MC (GaS, GaSe, GaTe and InSe) nanosheets were obtained *via* sonication assisted LPE approach. Firstly, bulk MC materials were exfoliated in NMP solvent *via* a bath sonication. More specifically, bulk MC powder was added into 20 mL of NMP at an initial concentration of 30 mg/mL, then the suspension was sonicated for 6 h at a frequency of 37 kHz and an amplitude of 100 %. During sonication, the temperature of the bath was cooled to around 20 ℃by continuous flow of cooling water. Once sonicated,

the dispersion was subjected to centrifugation for 2 h at 1000 rpm to remove any unexfoliated materials. Then, the top 60 % supernatant was collected (Figure 2.11).

Secondly, the exfoliated MC nanosheets were transferred from NMP to IPA. Specifically, exfoliated MC nanosheets in NMP solvent were centrifuged at high spin rate (10,000 rpm) to obtain the MC nanosheets. Then, these MC nanosheets were re-dispersed in IPA through bath sonication and exfoliated 2D MC nanosheets dispersion in IPA were obtained (Figure 2.11).

The TEM analysis of the MC nanosheets and SWCNT was performed on a FEI Titan at 150 kV (FEI, USA). The nanosheet dispersion was drop cast onto holey carbon grids (Agar Scientific, UK).

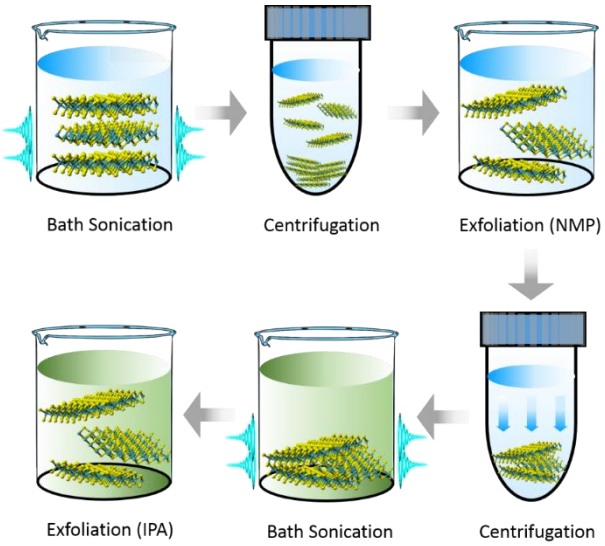

Figure 2.11 Preparation of 2D MC nanosheets *via* sonication assisted LPE method.

2.4.3 Assembly and electrochemical tests of the lithium-ion battery using 2D metal chalcogenide nanosheets and SWCNTs composites as anodes

1) Preparation of MC nanosheets-SWCNT composites electrodes

Firstly, SWCNTs were exfoliated in IPA solvent *via* both tip and bath sonication. 4 g of SWCNTs powder was added to 40 mL of IPA, and a probe sonic tip was utilised to sonicate the dispersion for 40 min (power: 40% amplitude). Then, the dispersion was

continuously sonicated using sonication bath for 1 h. Finally, SWCNT dispersion in IPA was obtained.

Secondly, 1D SWCNTs and 2D MCs nanosheets composites (Figure 2.12a) were formed *via* simple mixing and sonicating processes. 1D SWCNTs dispersion and 2D MCs nanosheets dispersion were mixed together and the SWCNT loading fraction was fixed at 20 % for all samples. Then, the mixture was sonicated using sonic bath for 30 min.

Thirdly, the 1D SWCNTs and 2D MCs nanosheets hybrid electrodes (Figure 2.12c) were prepared *via* a facile vacuum filtration method. A polyethylene (Celgard K2045, 0.06 μm pore size), which can also act as separator of LiBs, was used as a filter membrane. Blended 1D SWCNTs and 2D MCs nanosheets composites dispersion was filtered and the 1D SWCNTs and 2D MCs nanosheets composites films were obtained (Figure 2.12b). When the mass loading of the active material increased, the 2D MC-SWCNTs composite film could be peeled off. Therefore, it is a free-standing composite film. To avoid degradation over time, the films were immediately transferred to a glove box. The natural dried films were then cut into individual electrodes with diameter of 12 mm (geometric area ≈ 113 mm^2). It is worth nothing that the attached membrane was utilized as a second separator in the coin cells.

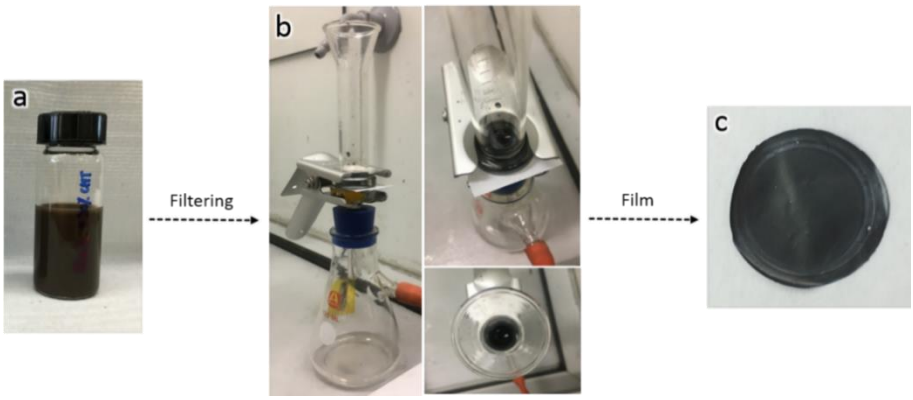

Figure 2.12 Preparation of MC-SWCNTs composite electrodes: (a) the mixture of an exfoliated MC nanosheets dispersion and a SWCNTs dispersion, (b) a MC and SWCNTs mixture was filtered, and (c) a free-standing MC-SWCNTs composite film was obtained.

2) Assembly of the Li-ion coin cells

GaS-SWCNT, GaSe-SWCNT, GaTe-SWCNT and InSe-SWCNT composites were used to assemble CR-2032 coin cells. CR-2032 coin cells were assembled using

those 2D MC-SWCNT composite as anodes and Li foil as cathodes. The electrolyte was 1.2 m lithium hexafluorophosphate ($LiPF_6$) dissolved in ethylene carbonate (EC), ethyl methyl carbonate (EMC) and fluoroethylene carbonate (FEC)in a mass ratio 9:1 of (EC+EMC):FEC. Two layers of surfactant-coated polypropylene membrance (K2045 coated PP) were used as a separator. The MC-SWCNT composite film (attached on the K2045 coated PP) was cut as a 16 mm disk for the LiB's working electrode while a lithium metal disc with a diameter of 16 mm was used as both the counter and reference electrodes. The K2045 coated PP membrance was cut as a 16 mm disk and weighed. The main function of a separator is to keep the two electrodes apart to prevent electrical short circuits while also allowing the transport of ionic charge carriers that are needed to close the circuit during the passage of current in a bettery. The active mass of each electrode was measured by subtracting the mass of a 16 mm the K2045 coated PP membrance disk from the total mass of the MC-SWCNT working electrode. The electrode thickness was determined with a digital micrometer (Mitutoyo).The MC-SWCNT working electrodes were placed in a coin cell base, followed by a PP separator with a diameter of 18 mm wetted with electrolyte, lithium foil as the counter electrode, a spacer, a spring for improved contact and the coin cell lid (see Figure 2.13). The spacer and wave spring within the cell serve to increase the thickness of the internal components such that a complete circuit is formed.

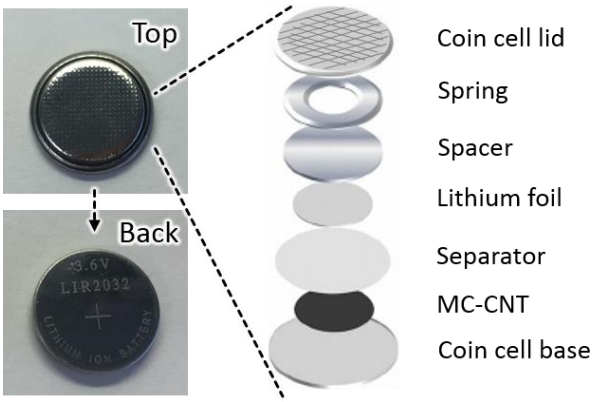

Figure 2.13 Coin cell assembly of the electrode half-cells.

Top and cross-section SEM images were obtained on a Zeiss Ultra Plus (Carl Zeiss, Germany) working at 5 keV of acceleration voltage. Energy-dispersive X-ray spectroscopy (EDS) was performed using the same microscope at 20 keV of acceleration voltage and analysed with the INCA program.

The DC electrical conductivity of the composites was measured using the two-point probe technique. Two parallel electrode contacts were created on the film surface using conductive silver paint (Agar Scientific). The resistance of each sample was measured using a Keithley 2400 source meter. The electrode thickness was determined with a digital micrometer (Mitutoyo). Figure 2.14 shows a piece of resistive material with electrical contacts on both ends. And the conductivities (σ) of electrodes were calculated according to the equation (3):

$$\sigma = \frac{t}{R \cdot w \cdot l} \tag{3}$$

Here, R (Ω) is the resistance, t (m) is the thickness, w (m) is the width, and l(m) is the length.

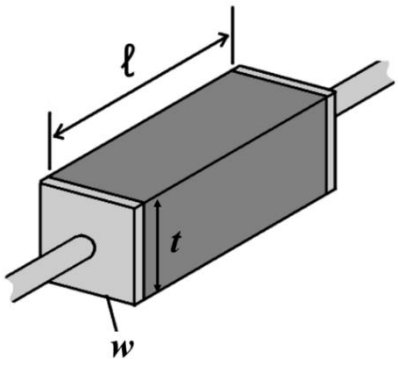

Figure 2.14 A piece of resistive material with electrical contacts on both ends; *t* is the thickness, *w* is the width, and *l*is the length.

3) Electrochemical tests of the LiBs based on MC nanosheets-SWCNT composites anodes

The electrochemical performances of the GaS, CaSe, GaTe and InSe and SWCNT composites were investigated using CR-2032 coin cells. Electrochemical tests were performed *via* cyclic voltammetry (CV) and galvanostatic charge/discharge (GCD) with a voltage range of 0.01–3 V on a potentiostat (VMP3, Biologic). For CV tests, electrodes were cycled three times at 0.2 mV/s. For GCD measurements, tests were conducted with current densities ranging from 50 to 2000 mA/g. The capacities reported here were those obtained from the fifth discharge profile at each current density and normalised to either the mass of active materials (i.e. GaS, GaSe, GaTe, or InSe) or the total mass of

composites (i.e. GaS-SWCNTs. GaSe-SWCNTs, GaTe-SWCNTs, or InSe-SWCNTs). The cycling performance of the electrodes was evaluated at 500 mA/g for 100 cycles.

3 2D indium selenide for lithium-ion batteries' anodes

3.1 Introduction

According to previous study (Chapter 2), 2D MCs could be considered as promising candidates for the next-generation battery anode materials due to their exotic properties and multi-valences enabling a variety of conversion/alloy reactions with lithium. Among them, we confirmed high capacity in the 2D InSe-SWCNT composite electrode that raising from 737 mAh/g to 1245 mAh/g over prolonged cycling, coupling with excellent rate handling and cycling performance. Therefore, 2D InSe was chosen to study more in detail for the LiB's anode material.

As mentioned before, MCs materials have shown a great potential as LiBs' anodes, especially when their size is reduced to the nanoscale. However, these kinds of materials are very expensive because of their high-cost and complex synthesis process. Thus, if we develop a simple and low-cost routine to synthesize nanostructured MCs, it will further allow industrial scale fabrication and application. Regarding this, starting from studying synthesis of InSe is necessary and meaningful.

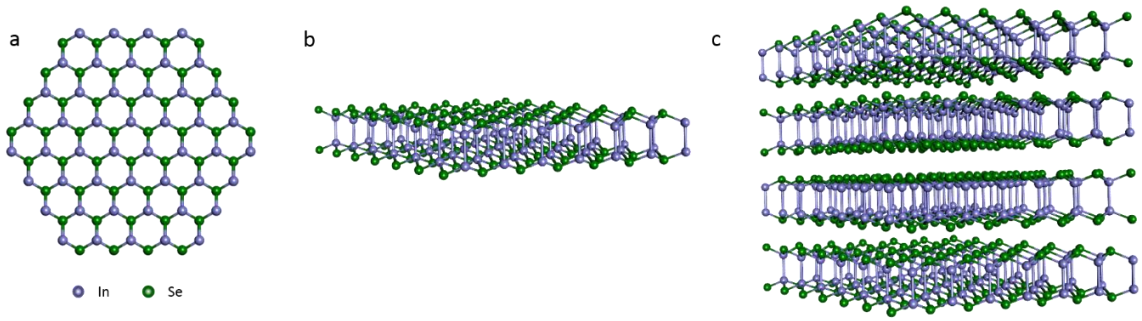

Figure 3.1 (a) Top and (b) side views of a single layer of InSe and (c) bulk InSe crystal.

The shape of nanoparticles can have a big impact on their properties.[181-183] It is reported that the chemical and physical properties of indium selenides are mainly determined by their intrinsic structural characteristics, including compositions, phases, crystal structures, and structural imperfection. From the structural point, indium selenides belong to a complex system with different stoichiometric ratios, including In_4Se_3, In_2Se_3, InSe, In_6Se_7, and In_3Se_4.[184-191] Among them, InSe studied in this work is made of stacked layers of Se-In-In-Se atoms (Figure 3.1a,b) with van der Waals bonding (Figure 3.1c).

Therefore, it is possible to attain nanosheets with a highly crystalline quality by exfoliating the bulk layered InSe crystal (Figure 3.1c).

In this work, we report on the 2D InSe-SWCNT flexible thin film as a high-performance LiB anode. 2D InSe nanosheets were liquid-phase exfoliated from the wet-chemical synthesized InSe crystals and percolated with high-aspect-ratio SWCNTs to form a conductive percolated network. We confirm high capacity, excellent rate and cycling performance that raising from 520 mAh/g to 1224 mAh/g over prolonged cycling. Such excellent electrochemical performance is ascribed to the excellent mechanical strength of SWCNT network, as well as new "nanocluster-alloying" Li storage mechanism, as revealed by the *in-situ* X-ray diffraction (XRD) and density functional theory (DFT) calculation results. This new Li storage mechanism may shed light on the exploration of novel 2D materials with excellent performance in LiBs, wearable electronics and smart energy storage devices.

3.2 Results and discussion

3.2.1 Synthesis of hexagonal shape layered InSe

Developing a simple and cheap method to synthesize InSe is an urgent and important task to deal with. On the basis of In-Se binary phase diagram (Figure 3.2), extensive methods, such as solid state reaction melting, and annealing, with or without the assistance of high pressure sintering techniques, have been used to fabricate bulk indium selenides to build their relationship between compositions and structures.[184] These methods mainly employ In and Se elemental powder as raw materials. Through melting of raw materials or annealing of mixed powder, diffusion of In and Se are promoted and chemical bonding between indium (In) and selenium (Se) are realized. Specifically, melting of mixed elemental powders in precise stoichiometric proportions followed by annealing were applied to fabricate α-In_2Se_3,[185, 192-194] γ-InSe,[185] γ-In_2Se_3,[192] In_4Se_3,[195-200] and In_6Se_7.[201] However, it should be noted that indium selenide bulk materials synthesized by these methods have low or no proportion of nanoscale inclusions. It remains as an open question that how nanoscale inclusions with tunable diameter and concentration can be effectively introduced into these bulk materials.

In recent years, the vapor-phase method has been constantly employed to grow indium selenide nanostructures. Using the vapour transport method, β-InSe nanowires were fabricated by using Argon (Ar) as carrier gas at 500 – 600 ˚C (Figure 3.3a).[202] Compared to the vapour-phase growth, the solution-phase synthesis of indium selenide nanomaterials is more difficult and relatively less studied than other metal selenides, possibly because various indium selenides can thermodynamically coexist in the same reaction system.[203] In terms of pressure in reaction systems, the synthesis can be divided into two categories: solution phase synthesis at ambient pressure and solvothermal synthesis under generated pressure in sealed systems. InSe quantum dots (Figure 3.3b) and nanoplates (Figure 3.3c) were synthesized by the thermolysis of $[In(Se_2CNEt_2)_3]$ in tri-n-octylphosphine oxide (TOPO) or 4-ethylpyridine [204] or through the benzenethiol-catalyzed reaction between $t\text{-}Bt_3In$ and H_2Se,[205] respectively. Yang and Kelly synthesized InSe nanoparticles by injecting trimethylindium trioctylphosphine (TOP) solutions into hot TOP-Se solutions.[206] Park et al. used $InCl_3$ and Se as the precursors and oleyamine as the solvent to synthesize γ-InSe nanoplates and cubic structured InSe nanowires, as shown in Figure 3.3d and e.[207] Zhou et al. reported the synthesis of γ-InSe nanodandelions (Figure 3.3f) by the reaction between $In(acac)_3$ and TOP-Se in the solvent of 1-octadecene and oleic acid at 170˚C, and also realized the size control from 1.5 μm down to 300 nm by varying the molar ratio between oleic acid and $In(acac)_3$.[208] In the case of solvothermal syntheses, there are limited reports on the synthesis of indium selenide nanostructure. Hsiang et al. synthesized InSe nanoparticles by a citric acid - modified solvothermal method through the reaction of indium nitrate with Se in dimethyl foramide (DMF).[209] There are more examples, and Table 3.1 presents a comprehensive summary of nanostructure InSe synthesis *via* vapour-phase and solution-phase methods.[184]

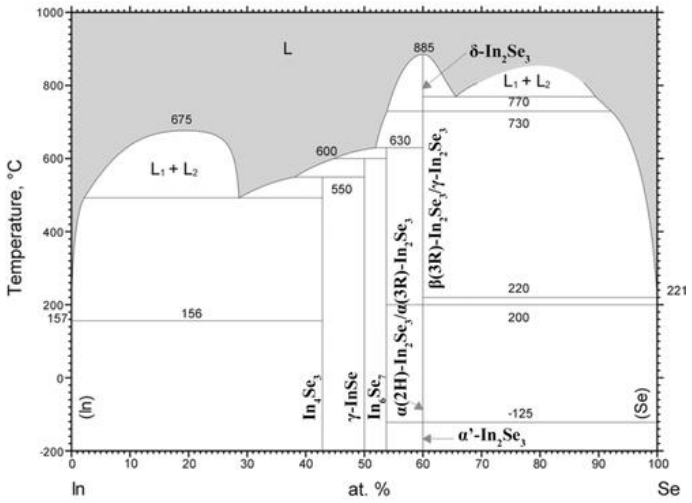

Figure 3.2 In-Se binary phase diagram (Reproduced and revised with permission. Ref. 184 Copyright 2006, ASM International).

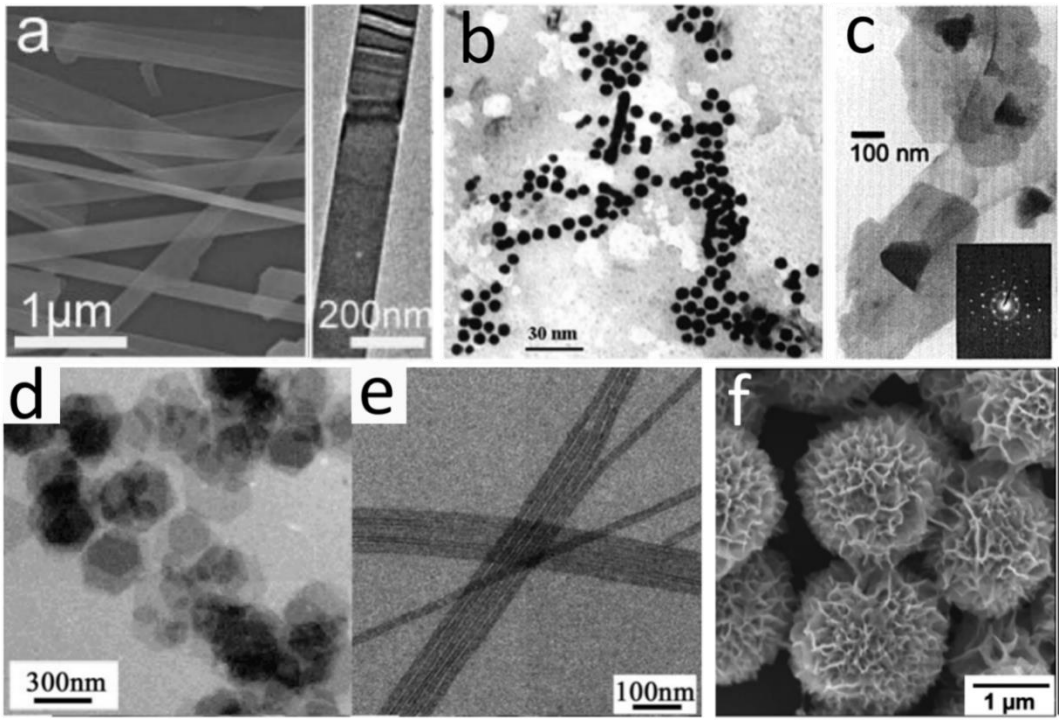

Figure 3.3 (a) β-InSe nanowires. Reproduced with permission Ref. 202 Copyright 2009, American Chemical Society, (b) TEM micrograph of 4-Ethylpyridine capped InSe nanoparticles. Reproduced with permission Ref. 204 Copyright 1999, The Royal Society of Chemistry, (c) InSe platelets approximating hexagonal shapes; inset, electron-diffraction pattern collected along the [0001] zone axis of a platelet. Reproduced with

permission Ref. 205 Copyright 2000, American Chemical Society, (d) β-InSe nanoplates. Reproduced with permission Ref. 207 Copyright 2006, American Chemical Society, (e) cubic structured InSe nanowires. Reproduced with permission Ref. 207 Copyright 2006, American Chemical Society, (f) SEM image of InSe dandelion-shaped nanostructures. Reproduced with permission Ref. 208 Copyright 2011, IOP Publishing Ltd.

Table 3.1 A comprehensive summary on the synthesis of indium (II) selenide nanostructures

Product	**Morphology**	**Synthetic method**	**Precursors**	**Reaction atmosphere or solvent**	**Growth temperature ℃**	**Ref.**
β-InSe	Nanowires	Vapor transport	Bulk In_2Se_3	Ar	500 - 600	202
β-InSe	Nanowires	Thermal evaporation	InSe powder	Ar	-	210
InSe	Nanoparticles	Thermolysis	$In(Se_2CNEt_2)_3$	TOPO	240	204
InSe	Nanoparticles	Thermolysis	$In(Se_2CNEt_2)_3$	4-ethylpryidine	167	204
InSe	Nanoplates	Solution-phase method	$t\text{-}Bu_3In$ and H_2Se	$1,3\text{-}i\text{-}Pr_2C_6H_4$	203	205
InSe	Nanoparticles	Solution-phase method	Trimethylindium-TOP and TOP-Se	TOP and TOPO	233-248	206
InSe	Nanoplates and nanowires	Solution-phase method	$InCl_3$ and Se	Oleyamine	215	207
γ-InSe	Dandelion-shaped nanostructures	Solution-phase method	$In(acac)_3$ and TOP-Se	1-octadecene and oleic acid	170	208
InSe	Nanoparticles	Solution-phase method	$InCl_3$ and selenourea	Oleyamine	260	211

InSe	Nanoparticles	Solution-phase method	$In(NO_3)_3$ and Se	DMF and citric acid	180	209

InSe crystals can exist in three polytypes denoted as β, γ and ε phases. γ-InSe is the mostly studied polytype with ABCABC stacking arrangement. Monolayer and few-layer γ-InSe have been proved to possess high electron mobility, excellent metal contact and moderate band gap range.[212, 213] However, the intrinsic instability of γ-InSe hinders its practical application either in electronics or optoelectronics.[214] The ε–InSe has ACAC layer arrangement and exhibits indirect band structure with a band gap value of 1.4 eV with high photoresponsivity of 34.7 mA/W in few-layer structure.[215] The β-InSe is of great significant since it has been exfoliated into individual layer with hexagonal structure, with different electronic and optical properties compared to the bulk β-InSe and it is the most stable phase of InSe due to the ABAB crystal stacking mode.[216]

In this work, we used wet-chemical synthesis method to obtain the layered hexagonal shape β-InSe nanomaterials using the indium acetate ($In(CH_3COO)_3$) as In source and selenium powder as Se source. The key strategy of this synthesis is the use of poor solubility of Se powder in long-chain amines (here we used a solution mixture of hexadecylamine and dodecylamine), which can further control the Se/In flux ratio to form hexagonal shaped InSe crystal.[217, 218] We could obtain nanocrystals with uniform shape and size through the wet-chemical synthesis. Very often, the compound used as metal source cannot be decomposed at room temperature, even in the presence of strong reducing agents. However, thermolytic reduction at higher temperatures can be achieved. Both hexadecylamine (323 ˚C) and dodecylamine (259 ˚C) used in this work have high boiling point so that they can be used as medium for chemical synthesis of nanoscale materials. They allow to carry out reactions at temperatures high enough to induce decomposition of metal and chalcogen precursors and their further reaction at atmospheric pressure.[219] In addition, easy removal (by centrifugation) and low cost give the opportunity for large-scale synthesis of high quality nanomaterials. Furthermore, the role of long-chain amines as a surfactant and template prevents agglomeration and enables crystal growth in a certain direction.[217, 218]

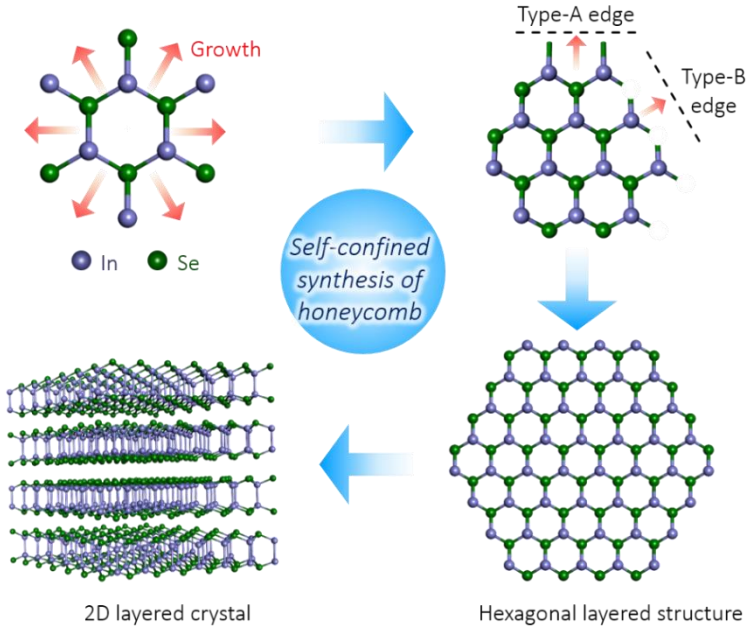

Figure 3.4 Diagram of self-confined synthesis of hexagonal shape layered InSe crystal.

The Se/In ratio affects the shape of the monolayer InSe domain.[217] This phenomenon is considered to relate with the crystal structure of InSe. As shown in Figure 3.4, the hexagonal InSe crystal plane has two different kinds of domain edges, indicated as “type-A edge” and “type-B edge”. It is expected that incorporation rates of In source and Se source at the type-A edge are different from those at the type-B edge. An incoming Se atom joins with one In atom while an incoming In atom makes bonds with two Se atoms at the type-A edge. One the contrary, at the type-B edge an incoming Se atom joins with two In atoms, while an incoming In atom makes a bond with one Se atom. Thus, incorporation rate of Se atoms at the type-B edge is faster than that at the type-A edge, while the incorporation rate of In atoms at the type-A edge is faster than that the type-B edge. When a large amount of Se atoms is supplied (i.e. the Se/In ratio is high), triangular InSe domains surrounded by the type-B edges grow. When the amount of Se is decreased, the growth speed of the type-A edge and type-B edge become similar. Therefore, grown InSe domains come to possess both type-A and type-B edges, and become hexagonal. If the amount of Se is further decreased (the Se/In ratio becomes extremely low) the growth of the type-A edge is slower than that of the type-B edge, which results in the growth of triangular InSe domains surrounded by the type-A edges. Here, as shown in Figure 3.4, we synthesized hexagonal shape layered InSe at high temperature using long-chain primary alkylamines to control the amount of Se atoms’ supplement. The growth speed

of the type-A edge and type-B edge could remain similarby controlling the supplement amount of Se. Therefore, hexagonal shape InSe which possess both type-A and type-B edges could be obtained in the end. Then, the high surface area of the 2D nanoplates, as compared with 0D or 1D nanomaterials, allows 2D hexagonal InSe nanoplates self-assemble to form the layerd InSe crystal.[220]

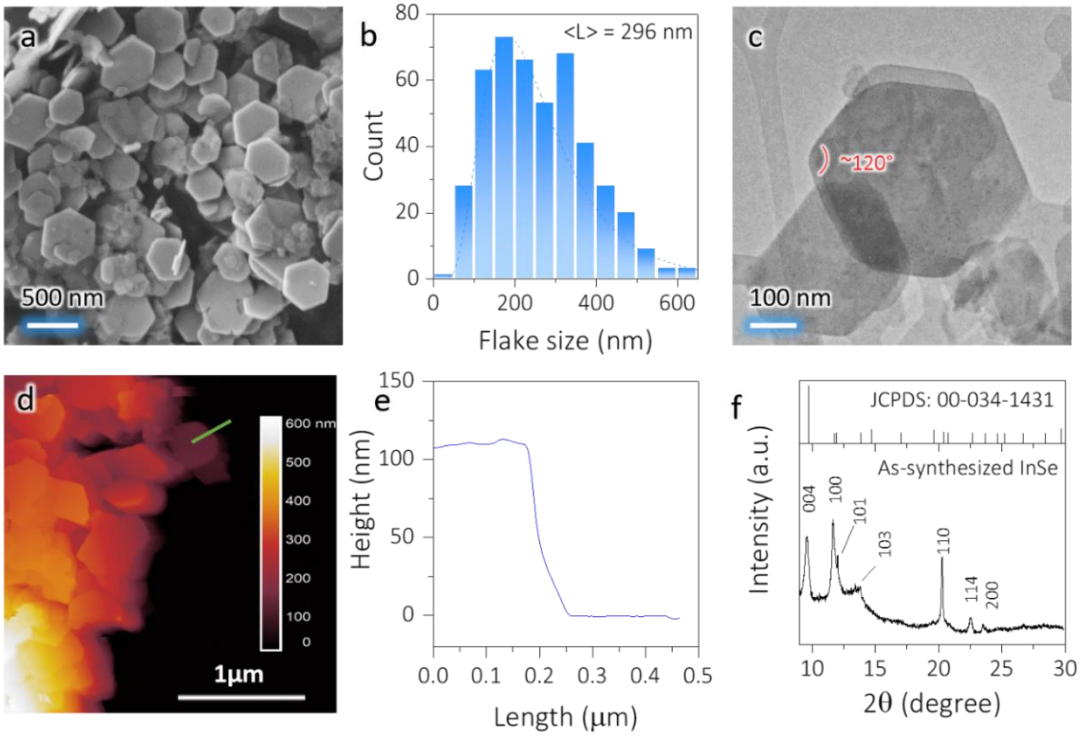

Figure 3.5 (a) SEM image of as-synthesized layered InSe crystal; (b) size distribution histogram of as-synthesized layered InSe crystal; (c) TEM image of as-synthesized layered InSe crystal; (d) AFM image of the as-synthesized layered InSe. We note that the platelets tend to aggregate during the AFM sample preparation, rendering it quite challenging to obtain the intrinsic thickness of the flake. Despite that, we still managed to find one flake that dispersed separately and obtained its height profile along the line in (d), as shown in (e);(f) XRD spectrum of as-synthesized layered InSe crystal.

Such a self-confined synthesis assisted by long-chain amines represent an easy route to high-quality layered InSe semiconductors. This is evidenced by the scanning electron microscopy (SEM) images in Figure 3.5a, where hexagonal layered crystals with uniform size are observed. Through statistical analysis based on the SEM images, those crystals have an average size of <L> = 296±4 nm, according to the size distribution

histogram in Figure 3.5b. Transmission electron microscope (TEM) and atomic force microscope (AFM) images (Figure 3.5c and Figure 3.5d,e) further suggest the shape of hexagonal InSe crystals, which are ~110 nm in thickness according to the height profile (Figure 3.5e). Figure 3.5f shows representative powder X-ray diffraction (XRD) of as-synthesized hexagonal InSe. The powder XRD patterns showed four sharp peaks at 9.7, 11.7, 11.9 and 20.4˚ originating from (004), (100), (101) and (110), which are very close to those reported for hexagonal P63/mmc InSe crystal (JCPDS card 00-034-1431).[185]

3.2.2 Preparation of 2D InSe nanosheets

Sonication-assisted LPE method was carried out to exfoliate as-synthesized hexagonal-shape bulk layered InSe crystals. As shown in Figure 3.6, as-synthesized layered InSe crystal is hexagonally packed planes, which exhibits strong in-plane covalent bonds and vertical weak van der Waals interactions between the adjacent layers. Therefore, we could use ultrasonic energy to easily break the weak van der Waals forces between each layer to produce exfoliated 2D InSe nanosheets and these 2D nanosheets were stabilized in a certain solvent. There is various choice of solvents. However, according to the basic theoretical analysis of LPE, different materials have different appropriate solutions for exfoliating. More specifically, if the Hansen solubility parameters and surface energy of the solvent is comparable to that of the layered material, the energy difference between the exfoliated and re-aggregated states will be very small, which means that the driving force for re-aggregation will be removed. This can improve the probability of successful sample preparation. Among numerous solvent, NMP is the most promising one for the exfoliation of bulk layered InSe, as the surface energy of it matched with them.[14] Therefore, as schematically demonstrated in Figure 3.6,we used NMP as the LPE solvent to exfoliate as-synthesized layered InSe. After LPE, the resultant nanosheets were transferred to IPA, forming an environmentally friendly and easily handled colloidal solution (Figure 3.7a) with concentration up to 5 mg/mL. Compared with the other mechanical exfoliation and chemical vapor deposition(CVD) methods, LPE is convenient and cost-effective method, and it is also available to a large-scale production.[4, 221]

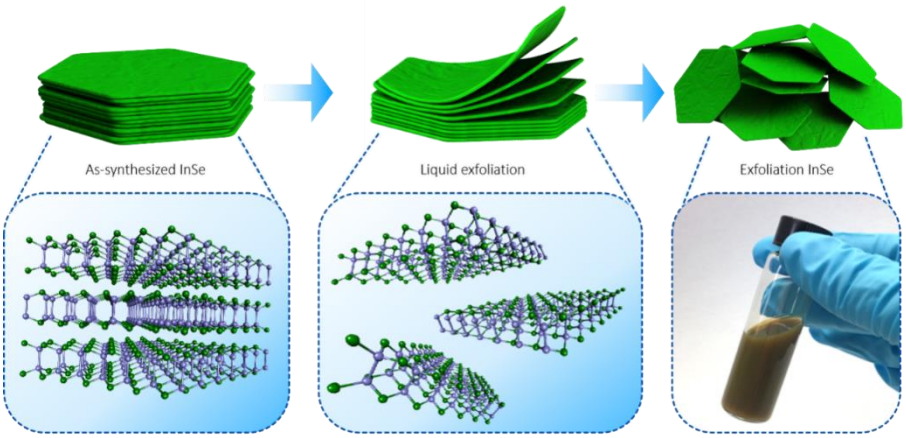

Figure 3.6 Scheme of LPE process of as-synthesized bulk layered InSe crystal to 2D InSe nanosheets.

The effective re-dispersion of hexagonal InSe nanosheets in IPA solvent is evaluated by means of morphological, chemical, and structural analyses. To investigate whether defects were introduced to the InSe nanosheets during ultrasonication, XRD measurement of the sonicated InSe sample was conducted. As shown in Figure 3.7b, the XRD spectra of exfoliated InSe suggested that the InSe phase has not changed during the LPE process. XRD peaks of exfoliated 2D InSe nanosheets were similar as in the bulk layered InSe crystal. SEM image (Figure 3.7c) confirm the efficient exfoliation into 2D InSe nanosheets, however, at the cost of uniformity. This is expected and normally occurred due to the "scissor effect" during LPE.[20, 69] TEM images (Figure 3.7d) indicate plenty of exfoliated flakes with well-defined edges and no apparent damages in the basal planes, suggesting the exfoliated material is of high quality. This is further verified by the selected area electron diffraction (SAED, inset of Figure 3.7d), high-resolution TEM (HRTEM, Figure 3.7e top image) and fast Fourier transform (FFT, Figure 3.7e down image) patterns, respectively, where hexagonal lattice symmetry is observed in the exfoliated InSe flakes with a highly-crystalline structure. These exfoliated InSe nanosheets possess a mean lateral size of <L> = 138 ± 2 nm (Figure 3.7f) and a much smaller thickness (~10 nm) compared to that of bulk InSe, according to the size histogram (Figure 3.7f) and AFM/height profile (Figure 3.7g), respectively. Nevertheless, the crystal structure of hexagonal InSe was well-maintained; no apparent defects were introduced to the exfoliated InSe flakes during sonication, best evidenced by the almost identical X-ray photoelectron spectroscopy (XPS) spectra in Figure 3.7h.[222, 223] However,

the exfoliation process in IPA caused as well a slight oxidation of Se, as indicated by the features located at 59.436 eV due to Se-O/OH formation during the sonic treatment.[223]

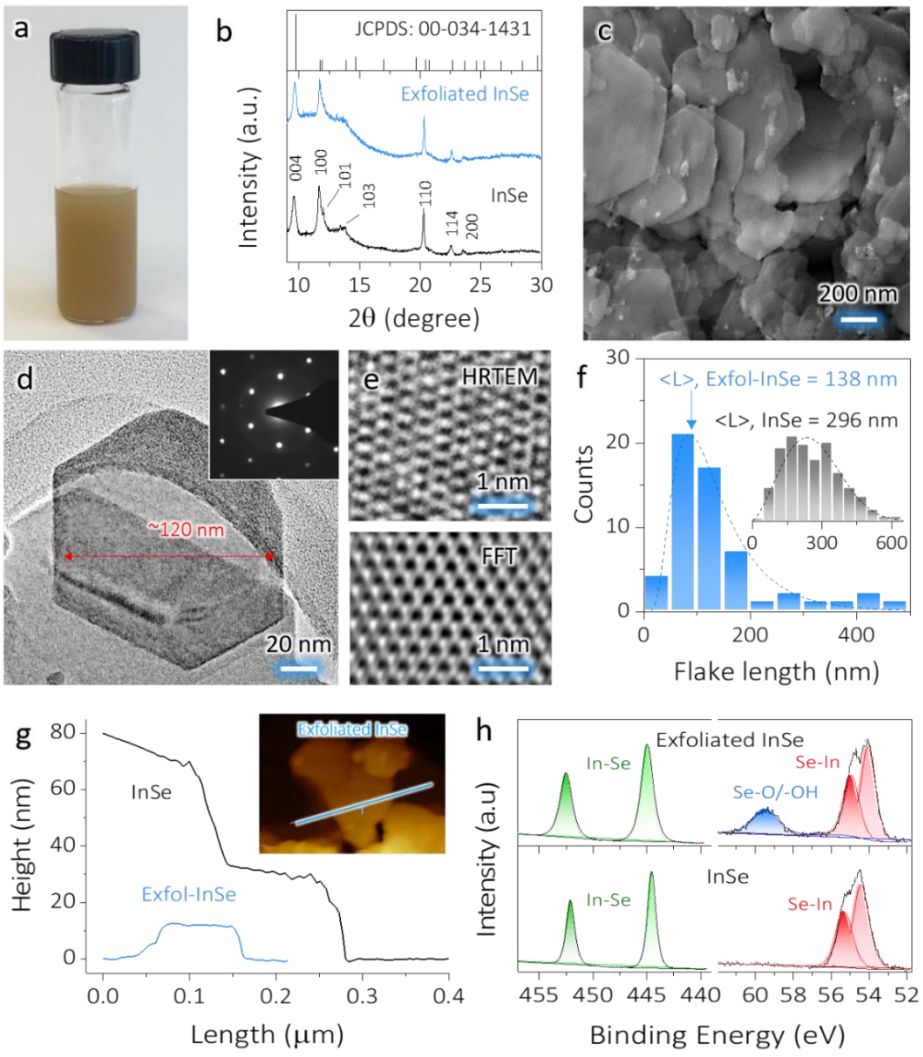

Figure 3.7 (a) Photo of exfoliated 2D InSe dispersion in IPA solvent; (b) XRD spectrum of as-synthesized bulk InSe and exfoliated InSe nanosheets; (c) SEM image of exfoliated 2D InSe; (d) TEM image of exfoliated 2D InSe; (e) HR-TEM of exfoliated 2D InSe; (f) size distribution histograms of as-synthesized bulk InSe and exfoliated InSe nanosheets;(g) AFM results of as-synthesized layered InSe and exfoliated InSe nanosheets; (h) XPS spectra of as-synthesized layered InSe and exfoliated InSe nanosheets.

3.2.3 Preparation and electrochemical performances of 2D InSe nanosheets and SWCNTs composite anodes for lithium-ion battery

As mentioned in the previous chapter, in order to improve the conductivity and flexibility of electrodes, 1D SWCNTs were added to fabricate a 1D and 2D hybrid heterostructure InSe-SWCNTs composite. As shown in Figure 3.8a, a binder-free flexible electrode could be obtained *via* a vacuum filtration of the mixture of exfoliated InSe nanosheets and SWCNTs dispersions. As references, controlled samples including as-synthesized layered InSe, commercial layered InSe, and liquid phase exfoliated commercial InSe nanosheets were also percolated with SWCNTs with similar thickness (~3 μm). Top-view and cross-sectional SEM images of a typical sample (2D InSe with 20 wt.% SWCNTs) indicate that the 2D InSe nanosheets are uniformly embedded in the SWCNTs percolated network (Figure 3.8b, c and Figure 3.8d). Such a homogeneous distribution of both SWCNTs and 2D InSe nanosheets is also confirmed by elemental mapping of In, Se and C, according to energy-dispersive X-ray spectroscopy (EDX) mapping in the SEM (Figure 3.8e). However, in the layered InSe-SWCNTs composite film, SWCNTs could not be well embedded into the layered structure (Figure 3.8g and h). Compared with the layered structure, the exfoliated 2D nanosheets increase the chance of contacts with SWCNTs by exposing the thinner sheets to the SWCNTs network. In addition, the exfoliated 2D nanosheets have smaller lateral size and larger specific surface area than the layered material. Thus, SWCNTs could more easily and uniformly mix with nanosheets than the layered material. Raman spectrum of 2D InSe-20% SWCNTs in Figure 3.8f indicates characteristic lattice vibrations at ~ 116 cm^{-1}, ~ 176 cm^{-1} and ~ 227 cm^{-1}, corresponding to the InSe A_1', E", and A_1' modes, respectively. The color-coded map, showing contributions from both SWCNTs and 2D InSe flakes based on the Raman spectrum, also implies the flexible thin film is uniform (inset of Figure 3.8f).[224] We believe the homogeneous distribution of 2D InSe nanosheets among the SWCNTs percolated conductive network not only forms sufficient voids for rapid Li^+ diffusion as well as volume expansion, but also promotes electron transport pathways for better rate handling properties, as discussed below.

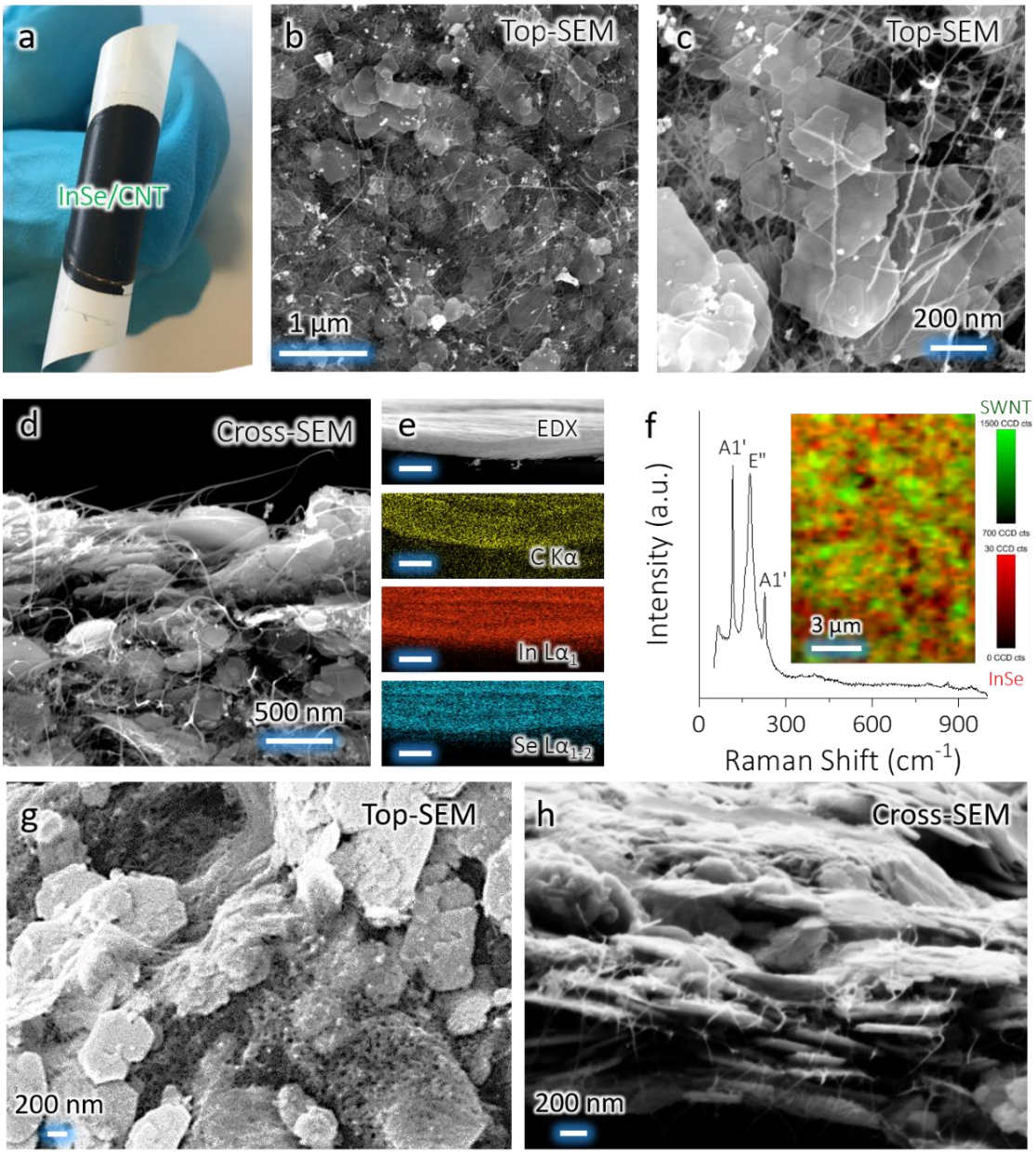

Figure 3.8 (a) Photograph of the exfoliated InSe-20%SWCNTs composite electrode; (b) and (c) are top SEM images of the exfoliated InSe-20%SWCNTs composite electrode with low and high magnetic; (d) Cross-section SEM image of the exfoliated InSe-20%SWCNTs composite electrode; (e) EDX mapping of the exfoliated InSe-20%SWCNTs composite electrode, scale bar corresponding to 50 µm; (f) Raman spectra of the exfoliated InSe-20%SWCNTs composite electrode; (g) Top SEM image of the layered InSe-20%SWCNTs composite electrode; (h) Cross-section SEM image of the layered InSe-20%SWCNTs composite electrode.

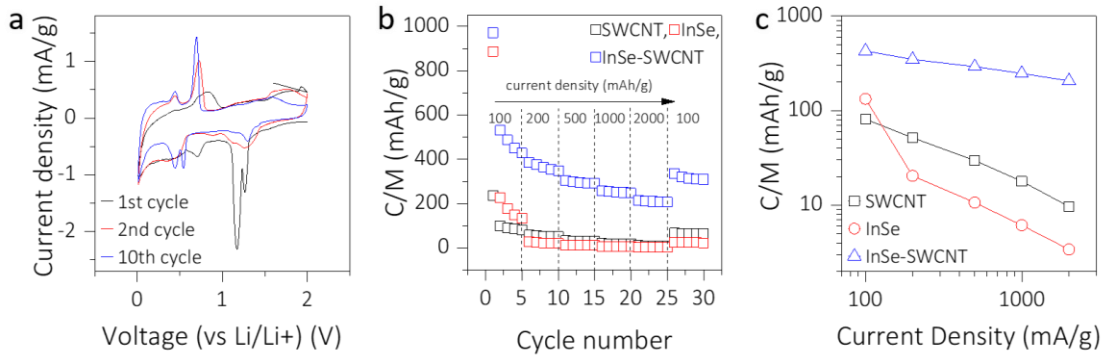

Figure 3.9 (a) CV curves of layered InSe-20%SWCNT at 2mV/s; (b-c) Rate performance of SWCNT, layered InSe, and layered InSe-20%SWCNT electrodes at different current densities.

Electrochemical performance, including CV and GCD tests of various samples were conducted. A strong cathodic peak centering at 1.17 V (vs Li/Li^+) is observed in the first cycle CV curve of layered InSe-20%SWCNT electrode, which disappears in the subsequent cycles (Figure 3.9a), suggesting the composite possibly undergoes structural change as well as the formation of SEI.[225] Locations of other cathodic and anodic peaks are well defined and agreed with previous reports on InSe thin films.[226] More specifically, three InSe characteristic cathodic current peaks at 1.31, 0.55 and 0.44 V are observed in CV (Figure 3.9a). In addition, there are four anodic peaks at 0.19, 0.45, 0.69 and 1.61 V after the first cycle and these peaks remain at the same position in subsequent cycles, indicating well cycle stability. The peaks at 0.19, 0.45 and 0.69 V should be due to the decomposition of In–Li alloy and the peak at 1.61 V may be attributed to the selenidation of In during the charge process.[226] Apparently, the electrochemical reaction of InSe with lithium involves multi-steps for its decomposition and formation. As shown in Figure 3.9b and c, the as-synthesized hexagonal layered InSe-20%SWCNT electrode exhibits an initial capacity up to 970 mAh/g at 100 mA/g, and decreases to 428 mAh/g after 5 cycles, similar to those of InSe thin films with different structures.[226, 227] Quite interestingly, unlike the layered InSe-20%SWCNTs, the capacity of exfoliated hexagonal shaped 2D InSe-20%SWCNT gradually increases after 10 cycles, and reaches 740 mAh/g per InSe after 50 cycles (Figure 3.10a and b). This could be possibly explained by the differences on the electrode structure. While bulk InSe crystals are percolated with SWCNTs, both the Li^+ diffusion and electron transport kinetics within the layered thick flakes are sluggish. On the other hand, 2D InSe nanosheets increase the chance of fully

contacts with SWCNTs by exposing thinner sheets to the conductive network, leading to much enhanced InSe utilization and improved capacity and cycling, as schematically illustrated in Figure 3.10c.

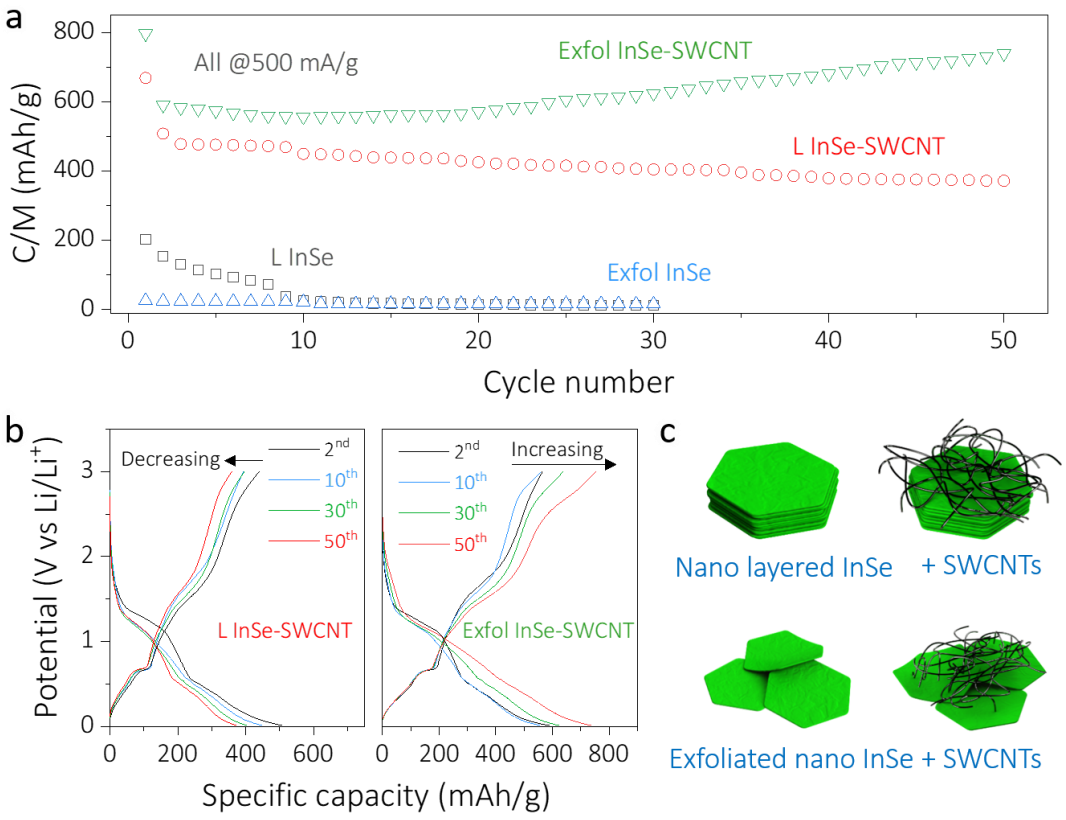

Figure 3.10 (a) Cycling performances of InSe, InSe-SWCNTs, and exfoliated InSe and InSe-SWCNTs electrodes; (b) Comparison of charge and discharge curves of bulk InSe-SWCNTs and exfoliated InSe-SWCNTs electrodes; (c) Scheme of incorporation of bulk InSe and exfoliated InSe with SWCNTs.

To better understand the conductivity effect, we fabricated a series of 2D InSe-SWCNT films with different SWCNT mass fraction while similar in thickness, and evaluated their electrical and electrochemical properties. As shown in Figure 3.11a, the electrical conductivity of InSe nanosheets film is quite low, however, adding 30 wt.% SWCNTs dramatically improved the conductivity up to 560 S/m from 0.3 S/m for 5 wt.% SWCNTs composites. The scaling of electrical conductivity of the composites can be well fitted and interpreted using the percolation theory:[228]

$$\sigma \propto (M_f - M_{f,c})^n \quad (5)$$

where σ is electrical conductivity, M_f is CNT mass fraction, $M_{f,c}$ is CNT fraction threshold to form the first conductive paths and n is the exponent.[228] Despite SWCNT volume fraction is frequently used when plotting the results, it's still reasonable to make appropriate analysis using the mass fraction, since the latter is directly proportional to SWCNT volume. The good fitting gives a n = 2.7 and a percolation threshold of ~ 1 wt.% in the 2D InSe-SWCNTs composites (Figure 3.11a), very similar to numbers achieved for MoS_2-SWCNT composites by Liu et al.[101] The substantially improved conductive network greatly benefits the composites' capacity and rate performance, as evidenced in Figure 3.11a (down panel). For instance, adding 20 wt.% SWCNTs dramatically boosts the capacity from 462 mAh/g (5 wt.% SWCNT) to 762 mAh/g at 50 mA/g, which still maintains 595 mAh/g as the charge-discharge rate increased by 40-fold (Figure 3.11a, down panel), confirming that the conductive percolated SWCNTs network dramatically influences the capacity as well as rate handling properties. Such an effect is even more clear when normalizing the capacity to InSe mass. CVs of various thin films are presented in Figure 3.11b, showcasing increased integrated area as adding SWCNT up to 20%, beyond which it starts to decrease, indicative of an optimum SWCNT fraction in boosting both capacity and rate performance. As displayed in Figure 3.11c and d, the capacity per InSe in the 2D InSe-SWCNT composite increases from 486 mAh/g (5 wt.% SWCNT, 50 mA/g) to 953 mAh/g for 20 wt.% SWCNTs. At 2000 mA/g, the 20 wt.% SWCNT sample still preserves 743 mAh/g per InSe, and bounces back to 1157 mAh/g when the current density switches to 50 mA/g (Figure 3.11c), demonstrating excellent reversibility and rate capability. Apparently, repeated charging-discharging leads to increased capacity per InSe at 35th cycle compared to that of 5th cycle (Figure 3.11e).

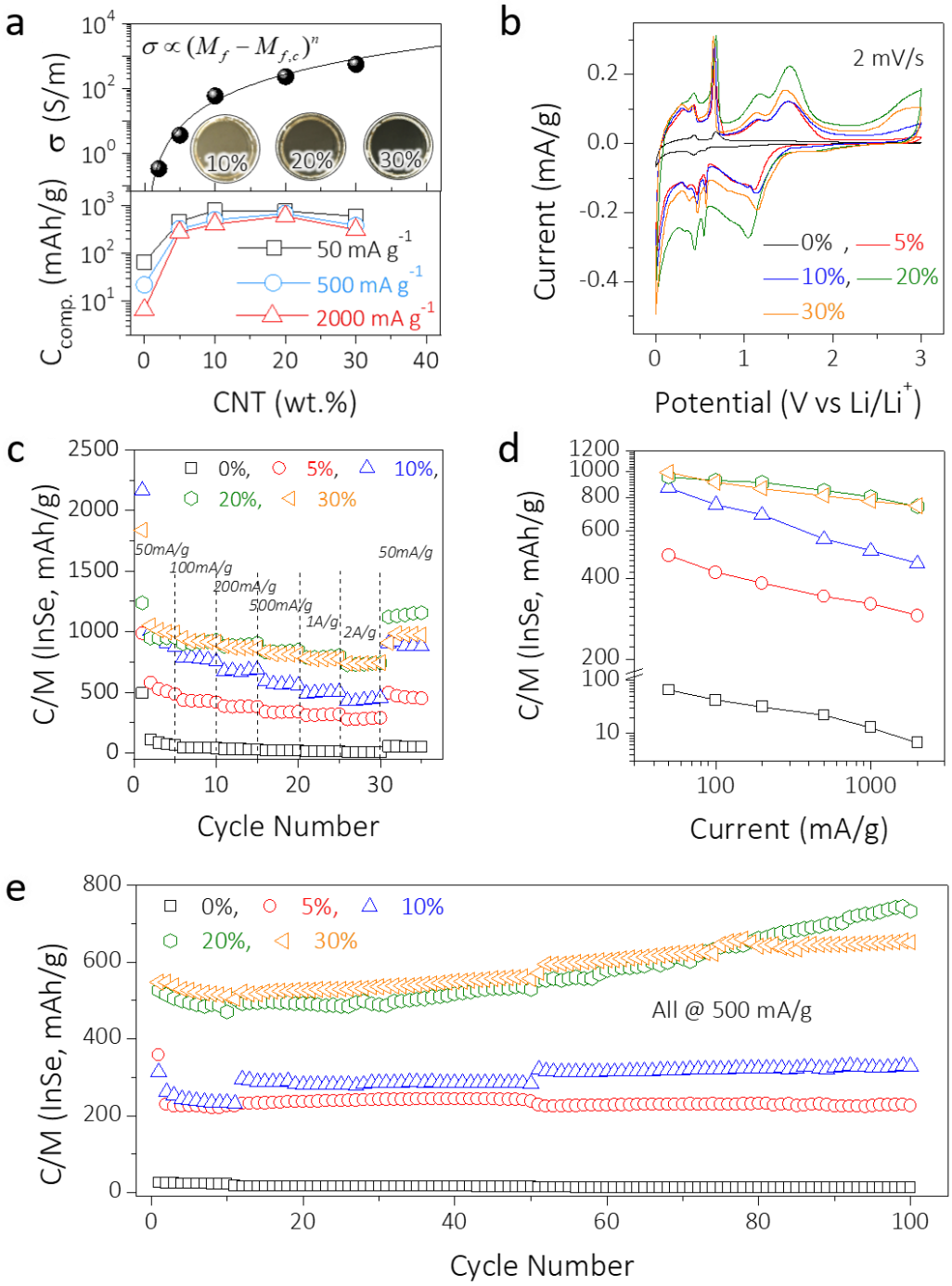

Figure 3.11 (a) Electrical conductivity (up panel) and capacity of composite (down panel) plotted as a function of SWCNT mass fraction. Insets in the up panel are optical images of 2D InSe-SWCNT films with different SWCNT contents; (b) CV curves at 2 mV/s; (c,d) Rate performance of different composites plotted as a function of cycle number (c) and current density (d); (e) Cycling at 500 mA/g of composites with different CNT contents.

In order to further study this unique performance, CV curves and GCD profiles of 2D InSe-SWCNTs samples with different SWCNTs mass loading percentages (5 %, 10 %, 20 %, and 30 %) were compared (Figure 3.12a-d and Figure 3.13a-d). First, comparing CV curves of these samples after different cycles (1st, 10th, 50th and 100th), the redox peaks of these 2D InSe-SWCNTs electrodes gradually strengthen in the following cycles (10th, 50th and 100th) after the first cycle. The degree of enhancement was becoming more and more obvious with the increase of SWCNTs percentage until it reached to 20 %. After that, it decreased when the percentage of SWCNTs became 30 %. It means 20 % is enough for SWCNTs for InSe nanosheets to demonstrate its outstanding electrochemical performance. The addition of 20 wt % SWNTs is beyond the electrical and electrochemical percolation thresholds. Too much or too few SWCNTs both limit the overall battery performance of InSe-SWCNTs composite anodes. GCD curves of these samples were also compared (Figure 3.13a-d). The charge and discharge plateaus of the samples all had corresponding CV peaks. They agree with the result obtained from CV curves. After the first cycle, the capacity of 2D InSe-SWCNTs composite electrodes gradually increased and it depends on the SWCNTs mass fraction. Further, in order to study the detail of enhancement of the capacity, reduction peaks of CV curves after different cycles were divided into three different voltage ranges: 0.1 ~ 0.6 V, 0.6 ~ 1.5 V, and 1.5 ~3.0 V.

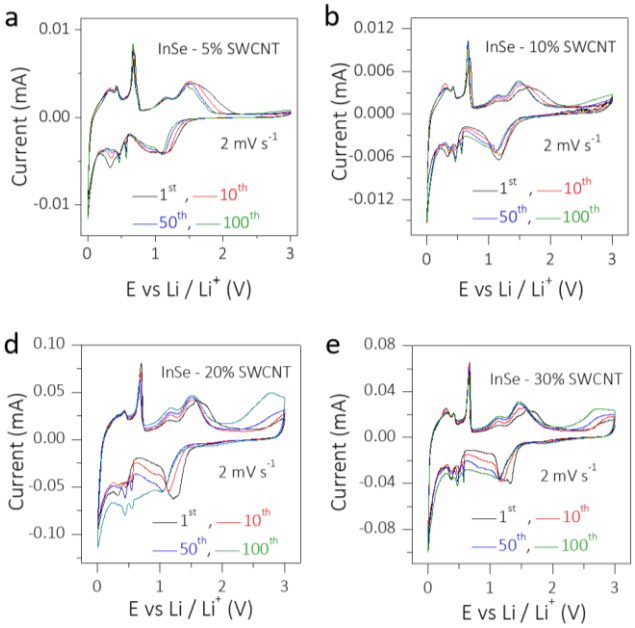

Figure 3.12 CV curves of (a) InSe-5% SWCNTs, (b) InSe-10% SWCNTs, (c) InSe-20% SWCNTs, and (d) InSe-30% SWCNTs composite electrodes after 1st, 10th, 50th, and 100th cycling.

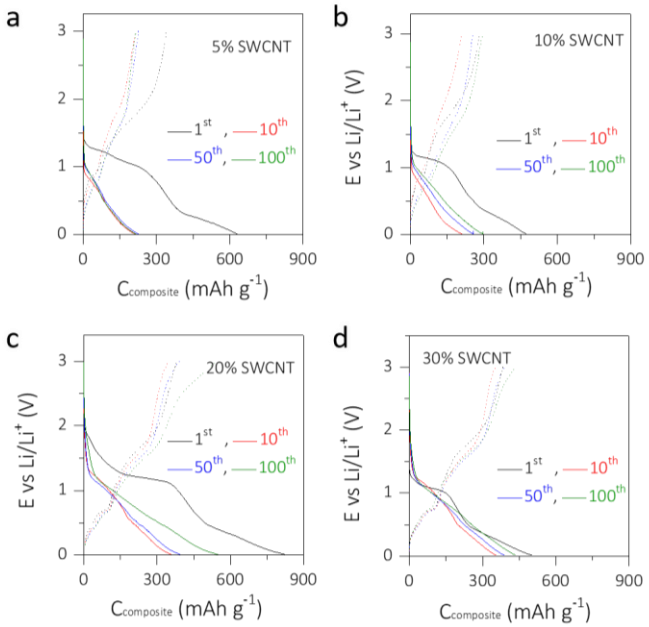

Figure 3.13 GCD profiles of (a) InSe-5% SWCNTs, (b) InSe-10% SWCNTs, (c) InSe-20% SWCNTs, and (d) InSe-30% SWCNTs composite electrodes at a current density of 500 mA/g.

Taking 20 % SWCNTs sample (the best performance sample) as an example, Figure 3.14a is CV reduction curves were divided into three voltage ranges of reduction peaks as mentioned before, and Figure 3.14c-d presented these three different ranges of CV reduction curves of this exfoliated InSe nanosheets with 20 % SWCNTs sample. According to them, it is apparent that capacity is significantly enhanced with the increasing of the cycling number (after the first cycle). For the first cycle lithiation (discharge) process is distinctively different from that in all subsequent cycles. It's essentially the first cathodic peak that is shifted cathodically. This will be discussed in the next chapter regarding the mechanism of capacity evolution in the 2D InSe-20% SWCNTs composite electrodes. What's more, curves' changes at the lower voltage range (0.1 ~ 0.6 V and 0.6 ~ 1.5 V) were more distinct than at in relatively higher voltage range (1.5 ~3.0 V). Indeed, according to the capacity calculation from integrated area of CV curves (Figure 3.15c), capacity growth rates at the range of 0.1 ~ 0.6 V and 0.6 ~ 1.5 V were higher than the range of 1.5 ~3.0 V, which means that they contribute more, and the improvement of capacity is mainly from the reduction at the lower voltage ranges. In addition, the capacity's proportion of .1 ~ 0.6 V and 0.6 ~ 1.5 V voltage ranges in the total capacity were much larger than 1.5 ~3.0 V one.

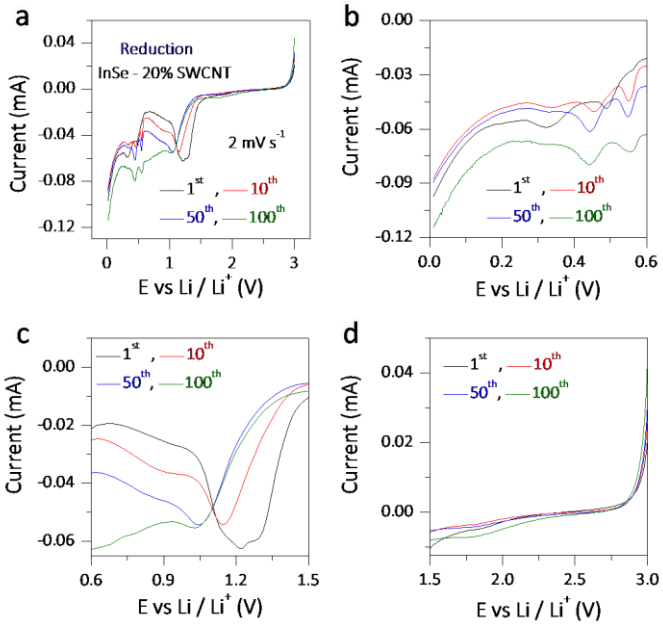

Figure 3.14 Separation of reduction peaks of CV after different cycling (1st, 10th, 50th and 100th): (a) CV reduction peaks of exfoliated 2D InSe-SWCNTs sample; (b) CV reduction peaks from 0 to 0.6 V; (c) CV reduction peaks from 0.6 to 1.5 V; (d) CV reduction peaks from 1.5 to 3 V.

The capacity (i.e. Q value) calculated from the integral area of each range CV reduction peaks for different mass loading percentage of SWCNTs in InSe-SWCNTs composite samples were presented in Figure 3.15 and Table 3.2. Exact Q values corresponding to the bar charts were showed in Table 3.2. Furthermore, using the data presented in Table 3.2, we draw the graphs (Figure 3.16) to show the trends of Q changing and exact value of the changing speed. Because we only have three points to do the linear fitting, so some samples are not very good fits to the line. However, most of samples are suitable to do the linear fitting, so it is worth to be used to analyse the data. According to the bar charts (Figure 3.15a-d), we found that the 20% SWCNTs sample has the fastest Q increasing rate (which corresponding to the slope of Figure 3.16a-d) among those four different SWCNTs percentage 2D InSe-SWCNTs composites. As shown in Figure 3.15a and 16a, for a 2D InSe-5%SWCNTs sample, capacity increased slightly during cycling between 0.1 ~ 0.6 V (Slope = 0.008) and 1.5 ~ 3.0 V (Slope = 0.010), but it is reduced at 0.6 ~ 1.5 V voltage range (Slope = - 0.175). For a InSe-10% SWCNTs composite sample (Figure 3.16b), the capacity decreased slightly at the 1.5 ~ 3.0 V range (Slope = - 0.030). However, this part contributes very small to the capacity, so the total trend of capacity is

still increasing during cycling. For the other two samples, all the capacity increased over cycling at all the ranges of voltage (Slope values are all positive). However, the speed of increasing is different. Capacity of InSe-20 % SWCNTs composite sample increased much faster than InSe-30% SWCNTs one (Figure 3.16c and d). Therefore, once again we showed that 2D InSe-20% SWCNTs is the best sample. It not only has the highest capacity, but also shows the largest capacity enhancement over cycling.

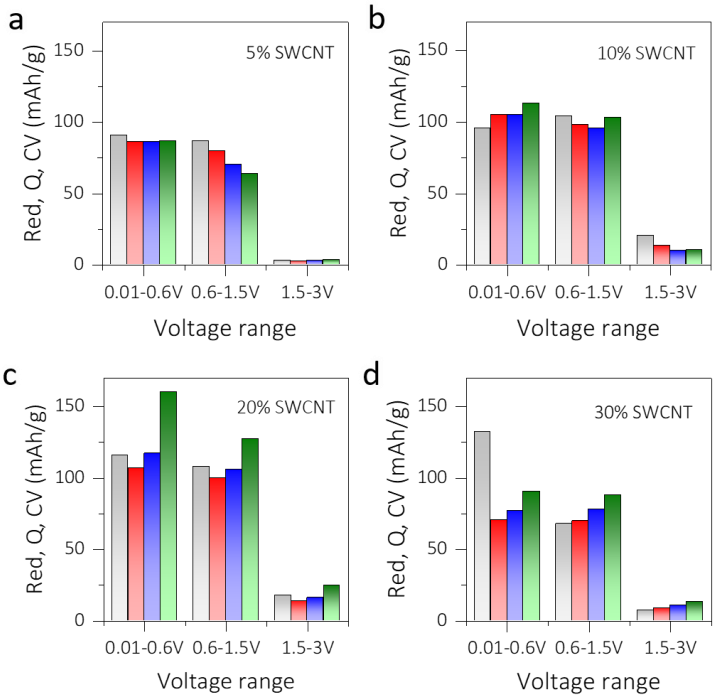

Figure 3.15 Capacity calculation from CV reduction peaks at 0.01 ~ 0.6 V, 0.6 ~ 1.5 V, 1.5 ~ 3.0 V voltage ranges: (a) InSe-5%SWCNTs, (b) InSe-10%SWCNTs, (c) InSe-20%SWCNTs, and (d) InSe-30%SWCNTs electrodes.

Table 3.2 Capacity calculation from CV reduction peaks of the (a) InSe-5%SWCNTs, (b) InSe-10%SWCNTs, (c) InSe-20%SWCNTs, and (d) InSe-30%SWCNTselectrodes.

Sample	0.1 - 0.6 V		0.6 - 1.5 V		1.5 - 3 V	
	Cycle No.	**Q (mAh/g)**	**Cycle No.**	**Q (mAh/g)**	**Cycle No.**	**Q (mAh/g)**
InSe-5% SWCNTs	1^{st}	90.74853	1^{st}	86.69175	1^{st}	2.85406
	10^{th}	85.94981	10^{th}	79.55029	10^{th}	2.46214
	50^{th}	85.84746	50^{th}	70.00916	50^{th}	2.78925
	100^{th}	86.61698	100^{th}	63.62684	100^{th}	3.33385
InSe-10% SWCNTs	**Cycle No.**	**Q (mAh/g)**	**Cycle No.**	**Q (mAh/g)**	**Cycle No.**	**Q (mAh/g)**
	1^{st}	95.72253	1^{st}	104.114	1^{st}	20.37
	10^{th}	105.1058	10^{th}	98.01653	10^{th}	13.27545
	50^{th}	104.931	50^{th}	95.43531	50^{th}	9.67099
	100^{th}	113.1698	100^{th}	102.9147	100^{th}	10.44169
InSe-20% SWCNTs	**Cycle No.**	**Q (mAh/g)**	**Cycle No.**	**Q (mAh/g)**	**Cycle No.**	**Q (mAh/g)**
	1^{st}	115.9493	1^{st}	107.7328	1^{st}	17.705
	10^{th}	106.8248	10^{th}	100.0488	10^{th}	13.78051
	50^{th}	117.0549	50^{th}	105.7677	50^{th}	15.83715
	100^{th}	160.272	100^{th}	127.1025	100^{th}	24.27425
InSe-30% SWCNTs	**Cycle No.**	**Q (mAh/g)**	**Cycle No.**	**Q (mAh/g)**	**Cycle No.**	**Q (mAh/g)**
	1^{st}	132.156	1^{st}	67.896	1^{st}	7.308
	10^{th}	70.236	10^{th}	69.768	10^{th}	8.604
	50^{th}	76.968	50^{th}	78.012	50^{th}	10.404
	100^{th}	90.612	100^{th}	88.092	100^{th}	12.96

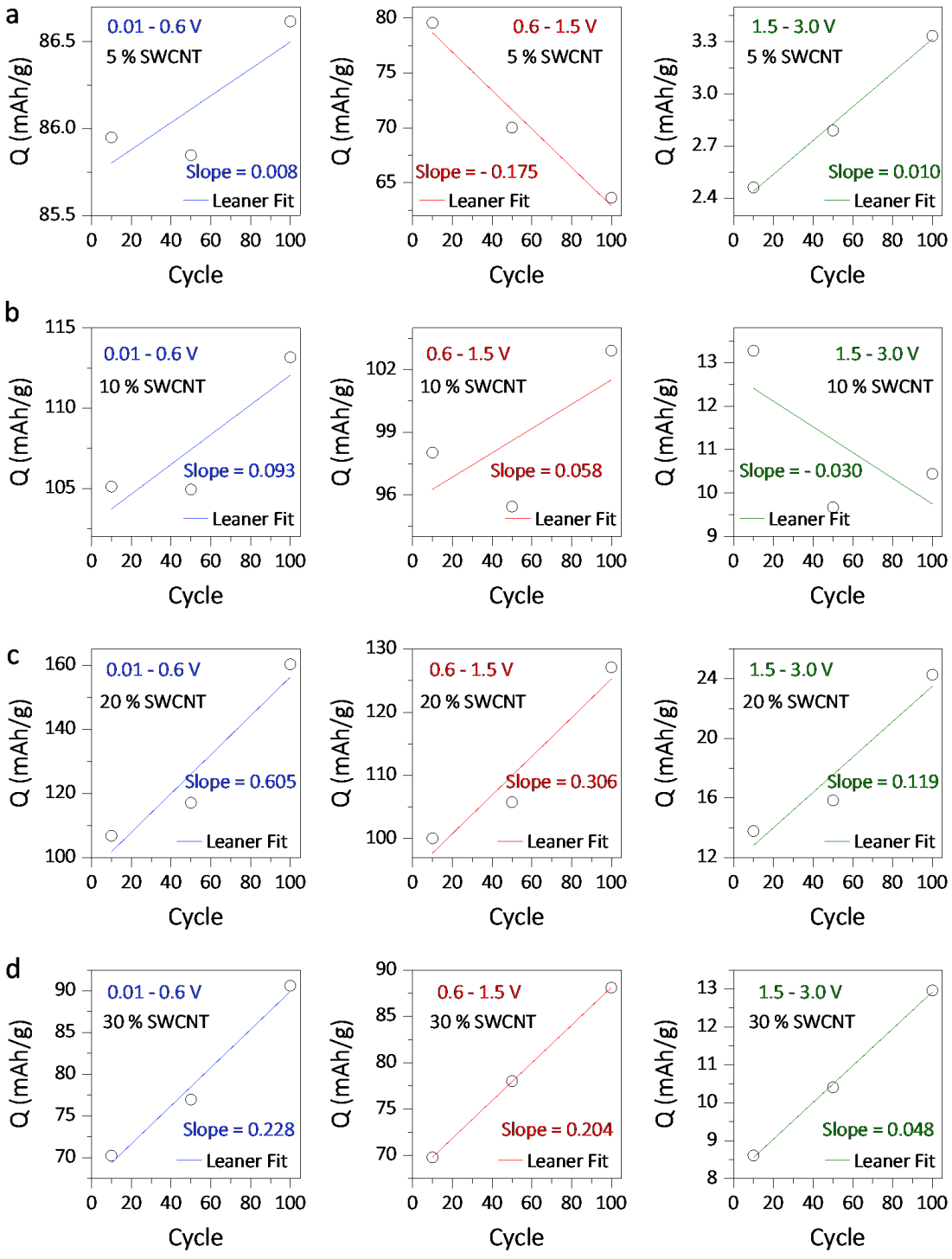

Figure 3.16 Linear fit lines of Q changings and corresponding slope values of these lines of (a) InSe-5%SWCNTs, (b) InSe-10%SWCNTs, (c) InSe-20%SWCNTs, and (d) InSe-30%SWCNTselectrodes.

3.2.4 Mechanism study of 2D InSe nanosheets and SWCNTs composite anodes

In the previous section, we could observe that 2D InSe nanosheets could improve the capacity over cycling. CV curves of a 2D InSe - SWCNTs composite electrode after different cycling times (1st, 10th, 50th and 100th) is one of apparent evidences. Because their CV peaks increased with the increase of the cycling times. What's more, in order to study the detail of the capacity enhancement, reduction peaks of CV curves after different cycling times were separated into three different voltage ranges (0.1 ~ 0.6 V, 0.6 ~ 1.5 V, and 1.5 ~3.0 V) and we calculated their specific capacities according to their integrated area. According to the results, it is apparent that the capacity significantly improved with the increasing of the cycling number in all three voltage ranges. However, the growth rates at the voltage range of 0.1 ~ 0.6 V and 0.6 ~ 1.5 V are much higher than the one at the range of 1.5 ~3.0 V. It means electrochemical reactions occurred at the 0.1 ~ 0.6 V and 0.6 ~ 1.5 V contributed more than the reaction happened at 1.5 ~3.0 V. The improvement of capacity was mainly from the electrochemical reactions occurred at the lower voltage range. Figure 3.17a and b show CV curves of a 2D InSe-20% SWCNTs composite electrode at a scan rate of 0.2 mV/s. The sharp anodic peak starts at 0.6 V in the first cycle, then gradually weakens in the following cycles, while another anodic peak at 1.0 V appeared after 2nd cycle and gradually weakens and shifts to higher voltages in the following cycles. It suggests that the composite electrode possibly undergoes some structural changes.

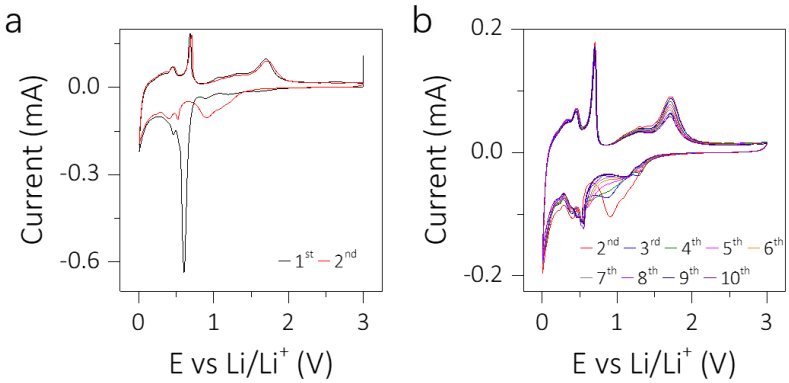

Figure 3.17 CV curves of a 2D InSe-20% SWCNTs composite electrode: (a) 1st and 2nd cycles, (b) from 2nd to 10th cycles.

To further understand the charge storage mechanisms, operando XRD measurements were carried out. As shown in Figure 3.18a, when the cell discharges from 3 V to 1 V versus Li/Li^+, the intensity of the (004) peak of InSe decreases together with increase of (111) peak of Li_2Se phase, and no other phases evolutions can be observed (Figure 3.19a presents XRD patterns of InSe, Li_2Se, InLi and In). It's believed at this first stage that evolution of pristine InSe phase follows the reaction (1) with a Li_2Se phase appearing during lithiation. Further lithiation from 1V to 0.5 V versus Li/Li^+ witness an appearance of (101) peak of indium phase and totally disappearance of the (004) peak of InSe. This can be due to the loss of selenium atoms in the pristine InSe crystal structure that results in an unstable $InSe_{(1-x)}$ phase, which decompose following the reaction (2) and is transformed into In and Li_2Se phase. At the last stage with further discharge to 0.05 V versus Li/Li^+, (101) peak disappears and (111) peak of InLi appears which indicates the reaction of Indium following the reaction (3). Therefore, for the first discharge, pristine InSe was transformed totally into InLi and Li_2Se phases follows the reaction (4).

Step 1:

$$InSe + 2xLi+ + 2xe^- \rightarrow InSe_{(1-x)} + xLi_2Se \quad (1)$$

Step 2:

$$InSe_{(1-x)} + 2(1-x)Li^+ + 2(1-x)e^- \rightarrow In + (1-x)Li_2Se \quad (2)$$

Step 3:

$$In + Li^+ + e^- \rightarrow InLi \quad (3)$$

First discharge:

$$InSe+3Li^++e^- \rightarrow InLi+Li_2Se \quad (4)$$

After first discharge, the operando XRD patterns present a reversible transition between (111) (220) peaks of InLi and (101) peak of Indium during charge-discharge cycles as well as reversible change of (111) peak of Li_2Se phase (Figure 3.18b). Figure 3.18b demonstrates clearly the XRD patterns evolution from 8th to 9th charge-discharge cycle. It can be seen that (111) and (220) peaks of InLi disappear and (101) peak of In appears at a voltage of about 1 V versus Li/Li^+, further charge to 3 V versus Li/Li^+ produces the right shift and intensity decrease of (111) peak of Li_2Se, and these evolutions are totally reversible upon discharging, corresponding to reaction (5) and (6), respectively. Therefore, it's believed that at the fully lithiated state, InLi and Li_2Se phases coexist. Upon de-lithiation (charging), InLi transformed into In and Li_2Se became Se.

$$InLi \leftrightarrow Li^+ + e^- + In \quad \text{(reversible)} \tag{5}$$

$$Li_2Se \leftrightarrow 2Li^+ + 2e^- + Se \quad \text{(reversible)} \tag{6}$$

Combining with the CV reduction curves analysis, a major contribution to the capacity in this system is due to the generation of InLi and Li_2Se and their subsequent reversible reaction with Li. Atomic scale In in the Li_2Se matrix accommodated a large amount of Li^+. Figure 3.19c presents the discharging spectrum and corresponding reactions during lithiation (discharging). When the battery is discharging, first, InSe reacts with Li^+ and $e^-$to produce Li_2Se and In. Then, In reacts with Li^+ in a reversible way to produce the electric currents.

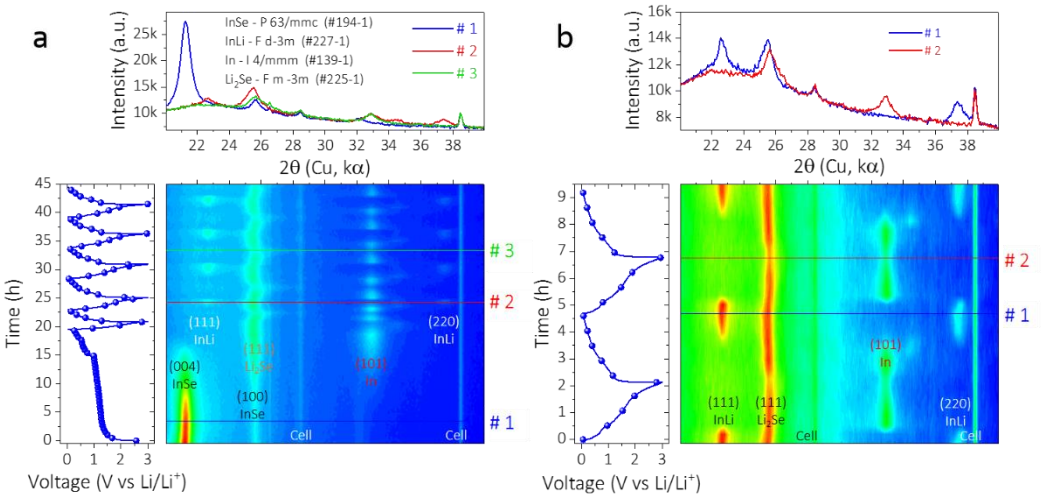

Figure 3.18 Contour profiles of *Operando* XRD patterns (a) from 0 to 5th charge/discharge cycles and (b) from 8th to 9th charge/discharge cycle. #1, #2, #3 in the bottom panel of (a) and (b) represent different charging/discharging states, whose operando XRD patterns can be found in the top panel of (a) and (b), respectively.

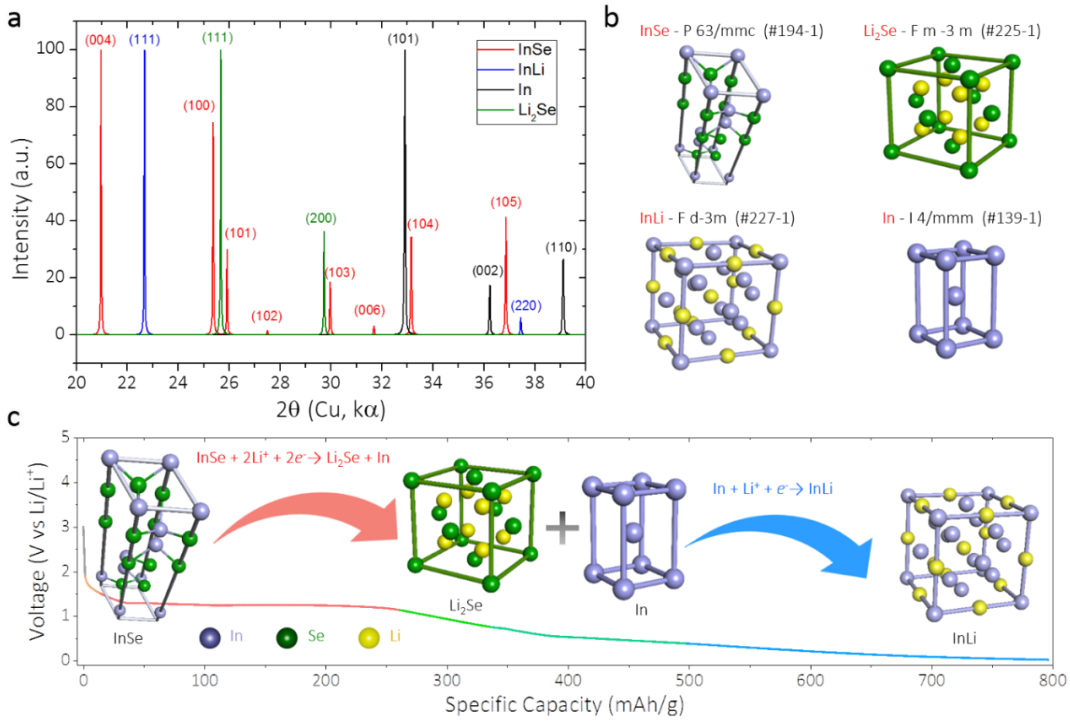

Figure 3.19 (a) XRD patterns and (b) crystal structure of InSe, Li_2Se, InLi, and In, (c) discharging spectrum and corresponding electrochemical reactions of the 2D InSe - 20 % SWCNTs electrodes.

To gain an in-depth understanding of how In atoms accommodate Li^+, DFT calculations were performed to calculate the adsorption of Li ion on In clusters. This work was carried out by the computational group of our collaborator Prof. Wang. The specific details of the calculations are presented in the computational methods included in the experimental section. The calculated binding energy for several configurations of cluster including different Li/In and In/Li_2Se ratio are plotted in Figure 3.20, indicating that indium is indeed capable of forming stable clusters without significantly increasing the binding energy (Figure 3.20a). We further performed the calculation of absorbed Li amount on an In_5-based cluster, which is assumed as the preferred and representative structure, as seen in the Figure 3.20b. The total binding energy is maintained at about -1.75 eV when one In_5 cluster has twenty Li absorbed. A higher absorbed Li^+ on the cluster (i.e. In_5Li_{30}) results in reduced binding energy, suggesting that the adsorption of 6 Li^+ per In_5 cluster is more challenging. The relaxed adsorption configurations and corresponding binding energies of In_3, In_4, In_5, and In_7 cluster with one Li_2Se absorbed were also calculated (Figure 3.20c) and indicated that In clusters have a high affinity for Se-containing molecules. Therefore, we deduce that, after repeated charging/discharging cycles, In particles gradually reduce their domain size and form nanoclusters. These nanoclusters are capable to accommodate four Li^+ per atomic In (In_5Li_{20}) instead of one Li^+ (InLi, reaction #3 and #5) through alloying reaction, as schematically demonstrated in Figure 3.21.We also note that these nanoclusters are highly reactive with electrolyte, contributing a partial of capacity associated with possible electrolyte decomposition like observed in other conversion type anodes.[20] As such, the capacity achieved is somewhat higher than the theoretical capacity.

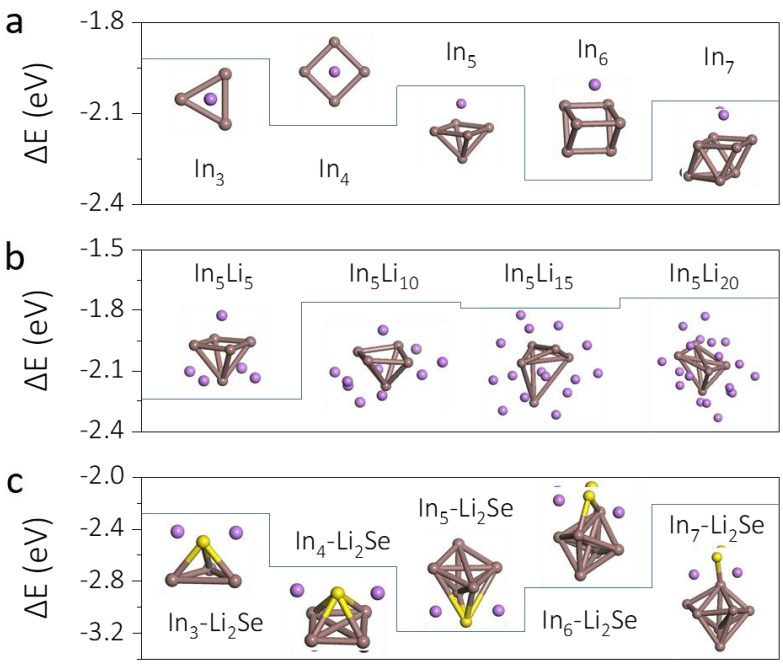

Figure 3.20 (a) DFT-calculated binding energies on different In model clusters configurations. (b,c) binding energy of different amount of Li^+ and Li_2Se on a In_5 cluster, respectively. Insets are possible configurations under each state, indicating the as-formed In particles are able to form stable clusters.

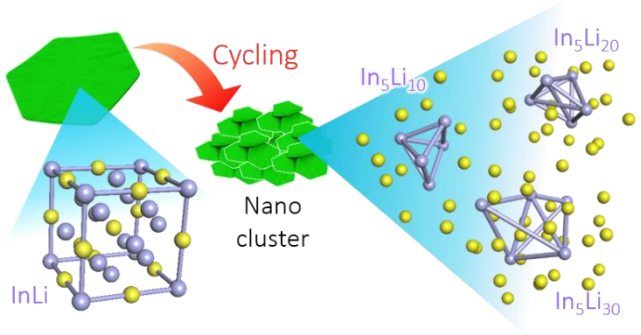

Figure 3.21 Schematically illustrated the In nanoclusters are able to accommodate 4 Li^+ per In unit, resulting in a much higher Li storage capacity beyond the theoretical value.

To check this point, we cycled four different cells for 50, 100, 200 and 900 times, respectively. Figure 3.22a indicates that the ever-increasing capacity behavior are observed in all cells in the initial 200 cycles, whose values are quite similar at each cycling stage. The capacity per InSe increases from 520 mAh/g to 1224 mAh/g after 245 cycles (cell 1). After relaxation for 2 weeks, the capacity of cell 1 still climbs up and reaches 1106 mAh/g, coupled with a high Coulombic efficiency of 97% (Figure 3.22a). The capacity of the 2D InSe-SWCNTs increases upon cycling phenomenon can also be observed in Figure 3.10 a and Figure 3.11e, and can be documented by the alloying of the continuously-formed nanoclusters, so-called "nanocluster-alloying" mechanism. To check this point, post-mortem SEM images of different cells suggest the InSe nanosheets decrease in size upon repeated cycling; hexagonal nanosheets with well-defined shapes are observed after 1 cycle, then become blurred after 50 cycles and disappeared completely after 500 cycles (Figure 3.22b-e). Nanoclusters are found after cycling for 500 times (Figure 3.22e), confirming the validation of DFT calculation and indicating the extra capacity originates from the reversible nanocluster-alloying mechanism. That is to say, the in-situ converted In gradually reduces its particle size, forms nanoclusters and stores much more Li through alloy process, contributing extra capacity to InSe as a result.

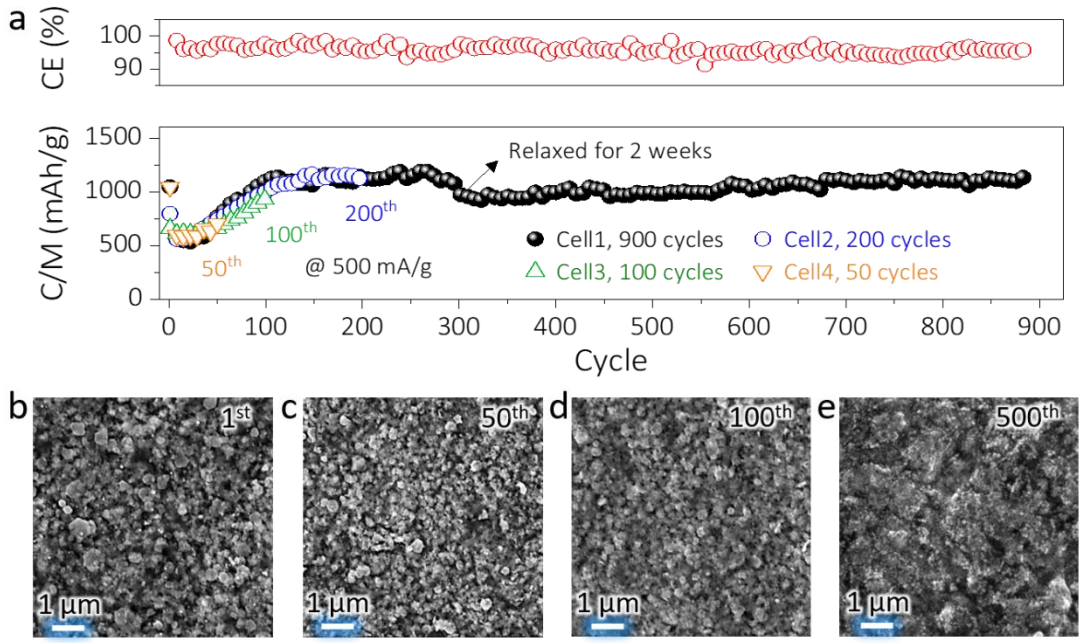

Figure 3.22 (a) Long-term cycling of different cells at 500 mA/g. Cell 1 was cycled for 280 times, then relaxed for two weeks and continued to cycle till 900 times; SEM images

of InSe-20% SWCNTs anodes after different cycling: (b) after 1 cycle, (c) after 50 cycles, (d) after 100 cycles, and (e) after 500 cycles.

According to this mechanism, a major contribution to the extra capacity in this system is due to the generation of In atoms and its subsequent reversible reaction with Li to form In/Li_x. Atomic scale In in the Li_2Se matrix accommodated a large amount of Li^+. However, in order to prove our mechanism, we should also check indium as an anode of LiBs. Therefore, we decided to test indium particle as an anode of a LiB. Here, we tried both nano size (Figure 3.23a) and micro size (Figure 3.26a) indium particles. To ensure that other conditions were consistent with an InSe-SWCNTs anode, we also added 20 wt% of SWCNTs to the indium particles.

As shown in Figure 3.23a, the size of In nanoparticle is ~ 70 nm. Here, we also used a colloidal solution processing method to fabricate the nano In-SWCNTs composite electrodes. From top (Figure 3.23b) and cross-section (Figure 3.23c) SEM images of a nano In-SWCNTs electrode, we could see In nanoparticles were well and uniformly spread within the SWCNTs networks and a thickness of the electrode is ~ 3 μm, consistent with the thickness obtained with a digital micrometer. Besides, elemental mapping of In and C by EDX in the SEM shows the homogeneous distribution of both nanoparticles and nanotubes in the composite (Figure 3.23d-f).

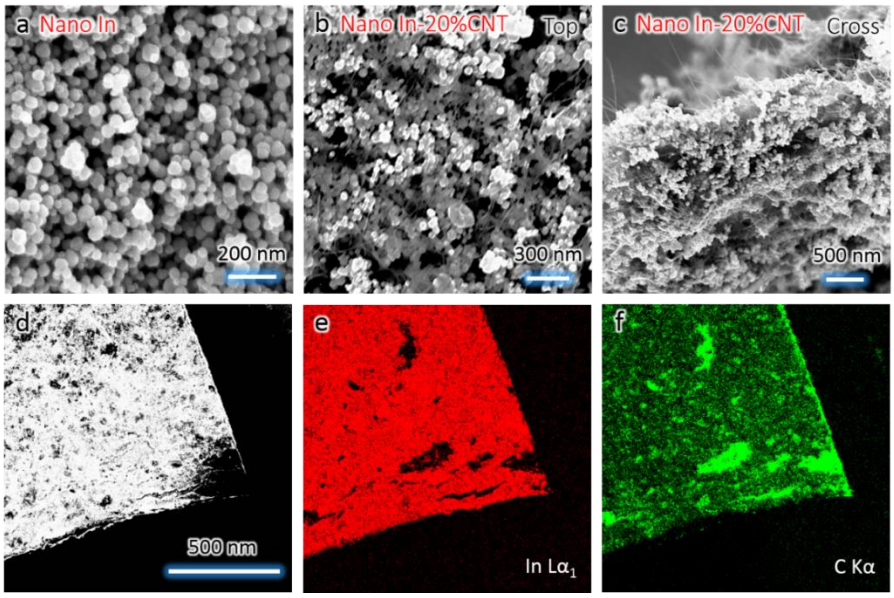

Figure 3.23 (a) SEM image of nano In, (b) top SEM view of the nano In-20% SWCNTs electrode, (c) cross-section SEM view of the nano In-20% SWCNTs electrode, EXD

mapping of the nano In-20% SWCNTs electrode: (d) SEM image of the nano In-20% SWCNTs electrode, element mapping of (e) indium and (f) carbon.

Then, nano In-SWCNTs electrodes were characterized electrochemically as LiBs' anodes. Figure 8a shows the rate performance of a nano In-SWCNTs electrode. At a 50 mA/g current density, specific capacity of the electrode was 936.2mAh/g, which is similar an InSe-SWCNTs electrode (952.5 mAh/g). However, increasing the current density, specific capacity of the nano In-SWCNTs electrode dropped a lot. For instance, at current density of 2000 mA/g, the specific capacity decreased to 384.8 mAh/g and this is almost half of the specific capacity of InSe sample (743.4 mA/g) at the same current density. It is apparent that the rate capability of InSe sample was better than nano In sample (Figure 3.24a). Besides, if we see the CV curves of nano In sample, they were very similar as InSe one (Figure 3.24b). The reduction peaks of the nano In-SWCNTs composite electrode could match with the InSe-SWCNTs composite electrode's reduction peaks (Figure 3.24b). What's more, the cycling behavior was also similar as an InSe sample (Figure 3.24c). The nano In-SWCNTs electrode also presented the rise of the specific capacity during cycling. This could confirm that our mechanism is right. However, compared to a 2D InSe-SWCNTs electrode, the degree of the capacity's improvement was smaller (Figure 3.24c). Various factors should be considered for this. Particle size is one of the important factors which needs to be studied here. In nanoparticles are classified as zero-dimensional (0D) nanomaterials; all dimensions at the nanoscale. So there is much greater interface area within the material; this can cause lager amount of SEI formed compared to 2D nanosheets. According to the cycling test (Figure 3.24c), we could see that capacity of a nano In-SWCNTs electrode decreased more dramatically than a 2D InSe-SWCNTs electrode for the first few cycles of charging and discharging processes. This is because more SEI existed in a nano In-SWCNTs electrode. The anode SEI, formed in the batteries' first few cycles and grown during aging, would act as the protective layer that inhibited the further decomposition of electrolyte on anode. However, SEI formation and growth sacrifice active Li^+ and electrolyte materials, leading to capacity losing, increasing battery resistance, and poor power density.[229] Therefore, we could see the capacity of a nano In-SWCNTs electrode is lower than that of a 2D InSe-SWCNTs electrode.

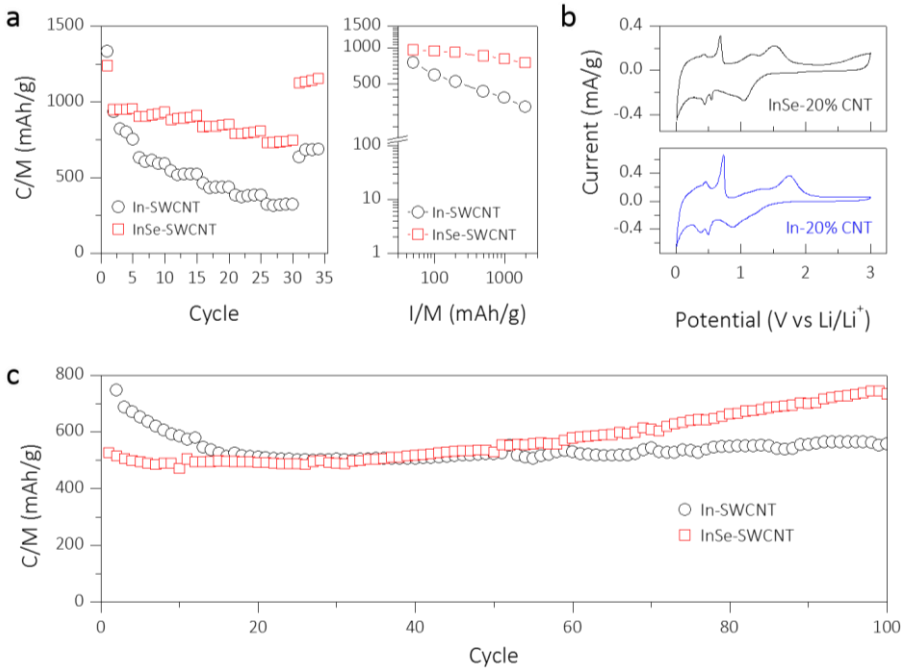

Figure 3.24 Comparison of (a) Specific capacities of nano In - 20% SWCNTs and InSe - 20% SWCNTs electrodes at different current densities (50 mA/g, 100 mA/g, 200 mA/g, 500 mA/g, 1000 mA/g, 2000 mA/g and backed to 50 mA/g in the end), (b) CV peaks and (c) cycling behavior between a InSe - 20% SWCNTs electrode and a nano In - 20% SWCNTs electrode.

To understand the effects of the size, we also studied the micro size indium metal. In order to mix them with SWCNTs, In powder (100 mesh, 99.99% trace metals basis) was dispersed in IPA solvent using bath sonication. Figure 3.25a shows the SEM image of the dispersed indium particles and size of them were dozens of microns. Then, micro In-SWCNTs composite electrodes were prepared by following the same procedure of nano In-WCNTs composite electrodes. According to top and cross-section SEM images (Figure 3.25b and c), we could see that SWCNTs were well mixed with micro In. But because of the large size of indium, most SWCNTs were spread onto the surface of the micro In. If we see the elemental mapping of In and C by EDX (Figure 3.25d-f), we could confirm that In and SWCNTs distributed in the composite homogeneously.

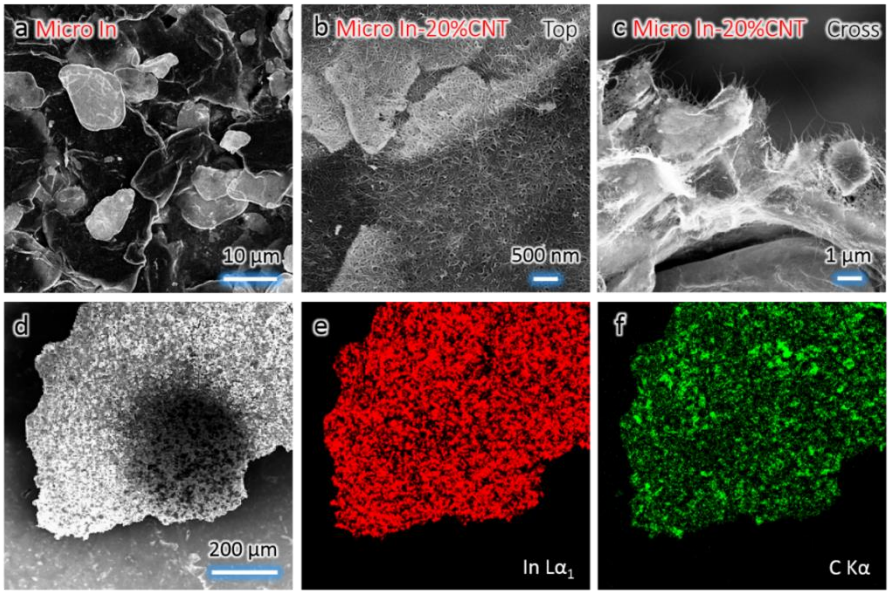

Figure 3.25 (a) SEM image of micro In, (b) top SEM view of the micro In-20% SWCNTs electrode, (c) cross-section SEM view of the micro In-20% SWCNTs electrode, (d) SEM image of the micro In-20% SWCNTs electrode, and EDX mapping of (e) indium and (f) carbon.

Then, the electrochemical performance of a micro In-SWCNTs electrode was investigated by CV and GCD measurements. As shown in Figure 3.26a, specific capacity of a micro In-SWCNTs electrode was much lower than a nano In-SWCNTs electrode. Specific capacity of the micro In sample was only around 300 mAh/g at 50 mA/g. Besides, compared to the nano size In, micro size In exhibited poor rate capability (Figure 3.26a). Capacity decreased dramatically with increasing of current density. At a high current density (2,000 mA/g), specific capacity of the electrode could drop to ~ 50 mAh/g. CV peaks of a micro In-SWCNTs electrode were also much smaller than a nano In-SWCNTs electrode (Figure 3.26b). However, we could also observe the increase of capacity during cycling (Figure 3.26c). Nevertheless, when we compared it with a nano In-SWCNTs electrode, the increase of capacity is not obvious (Figure 3.26c).Overall, according to comparison of electrochemical property of nano and micro size indium, we could clearly see the size influence the electrochemical performance of the In-SWCNTs composite electrodes. Specifically, nano-sized indium particles have higher capacity than micro-sized indium particles. This is consistent with the simulation results in ref. 169 which concluded that larger average size of the material contributed to lower electrode specific capacity.[230] This is because the decrease in particle size could shorten diffusion paths and

provide larger specific surface area. In addition, SWCNTs could more easily and uniformly mix with nano sized In than micro sized one (Figure 3.27). This was also confirmed by the SEM images of nano In-SWCNTs and micro In-SWCNTs electrodes (Figure 3.23b and Figure 3.25b). As shown in Figure 3.23b, In nanoparticles were embedded well into the SWCNTs networks, but for micro In, SWCNTs were mostly spread onto the surface (Figure 3.25b). So the electrochemical performance of the nano In-SWCNTs anodes were better than micro In-SWCNTs anodes.

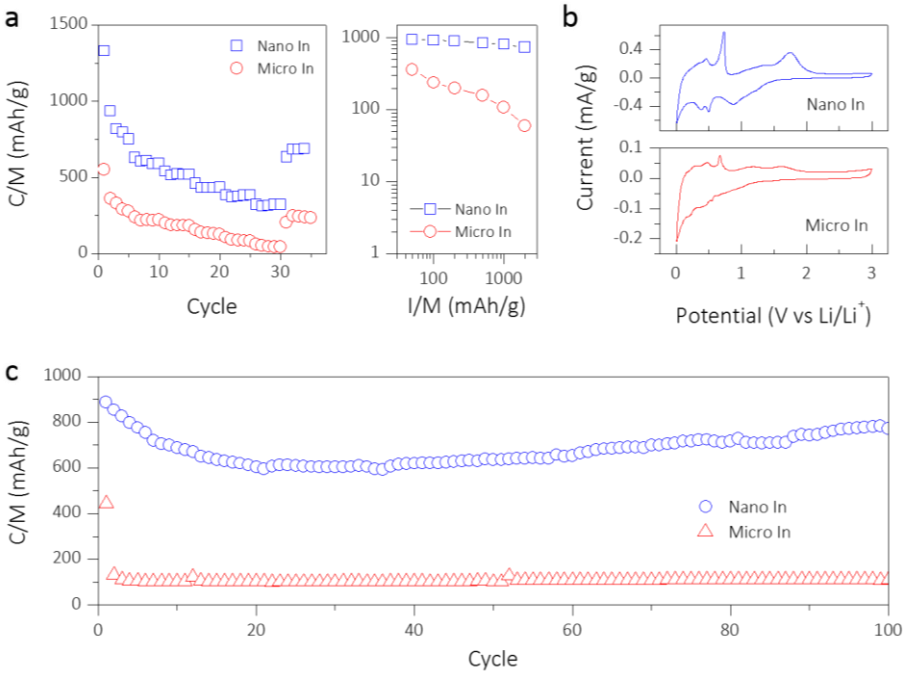

Figure 3.26 Comparison of (a) specific capacities of nano In-20% SWCNT and micro In-20% SWCNTs electrodes at different current densities (50 mA/g, 100 mA/g, 200 mA/g, 500 mA/g, 1000 mA/g, 2000 mA/g and backed to 50 mA/g in the end), (b) CV peaks and (c) cycling behavior of nano In-20% SWCNTs and micro In-20% SWCNTs electrodes.

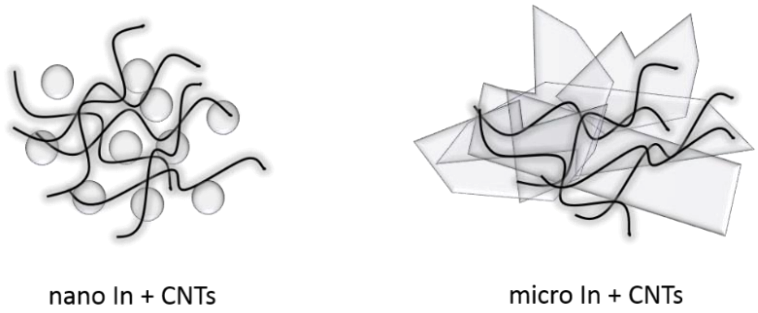

Figure 3.27 Comparison of nano and micro sized In with SWCNTs matrix.

3.3 Conclusion

In this work, hexagonal shape bulk InSe was synthesized *via* wet-chemistry synthesis which is a colloidal method. Then, LPE approach was applied to prepare the 2D InSe nanosheets. In order to improve the conductivity and flexibility of anode materials, 1D SWCNTs were added to obtain a 1D and 2D hybrid heterostructured InSe-SWCNTs composite. Compared to commercial bulk InSe, as-synthesized hexagonal shape bulk InSe exhibits much better electrochemical performance. The mass capacity of as-synthesized bulk InSe-SWCNTs electrode is almost 25 times that of the commercial bulk InSe-SWCNTs electrode. Furthermore, exfoliated 2D InSe-SWCNTs composite electrode further improved the electrochemical performance. It shows an excellent rate capability and high specific capacity (926 mAh/g and 595 mAh/g at 50 mA/g and 2 A/g, respectively). Importantly, the capacity per InSe of the 2D InSe-SWCNTs composite electrode increases over prolonged cycling up to 1224 mAh/g from 520 mAh/g. The enhanced capacity with the increase of cycle index (the capacity of the battery dramatically increased in the first 100 cycles and it continuously increased until 900 cycles), which to the best of our knowledge has not been reported for other electrode materials in LiBs.

In order to understand the mechanism, especially the improvement of capacity over cycling, CV, *in-situ* XRD, DFT, and *ex-situ* SEM analysis were carried out. According to CV and *in-situ* XRD measurements, we could know that when the battery is discharging, first, InSe reacts with Li^+ and e^- to produce Li_2Se and In atoms and this is an irreversible process. Then, In atoms subsequently react with Li^+ in a reversible way to produce the electric currents. Therefore, a major contribution to the extra capacity in this

system is due to the generation of In phase and its subsequent reversible reaction with Li^+. To gain an in-depth understanding of In atoms accommodate with Li^+, DFT calculations were carried out. According to these calculations, In accommodates Li^+ to form relatively stable In/Li_x clusters. In addition, *ex-situ* SEM measurements of the 2D InSe-SWCNTs composite electrodes after different cycling times told us that the size of 2D InSe nanosheets gradually decreased over cycling. The size of particle gradually become smaller during the cycling, and those smaller nano clusters accommodate more Li^+. According to all these results, we deduced a new "nanocluster-alloying" Li storage mechanism.

According to the mechanism study, we could know that the generation of In phase and their reversible reaction with Li^+ is the responsible of the capacity for this system. Based on this, we further explored this mechanism in indium anodes LiBs. The electrochemical performances of In-SWCNTs anodes were very similar as InSe-SWCNTs electrodes. CV peaks of an In-SWCNTs anode almost matched with an InSe-SWCNTs anode. What's more, the specific capacity of an In-SWCNTs electrode improved during charging and discharging cycles, same as an InSe-SWCNTs anode. It can further support our mechanism study and also show the possibility of indium used as an anode material.

3.4 Experimental methods

3.4.1 Materials

Indium acetate (InAcO), selenium (Se, 99.5 %), isopropyl alcohol (IPA), hexadecylamine, dodecylamine used throughout these experiments were purchased from Sigma Aldrich. Single wall carbon nanotube (SWCNT, P3-CNT) was purchased by Carbon Solutions, Inc. And polypropylene membrane (K2045 coated PP) was from Celgard LLC, Charlotte, NC.

3.4.2 Synthesis of bulk layered hexagonal shape InSe

InSe was prepared *via* self-confined synthesis by using the indium acetate ($In(CH_3COO)_3$) as indium (In) source and selenium (Se) powder as Se source (Figure 3.28).In typical synthesis, 494.76 mg (1.69 mmol) of $In(CH_3COO)_3$ and the corresponding 135.42 mg (1.71 mmol) of Se powder were added to a mixture of 30 mL of hexadecylamine and 5 mL of dodecylamine at 60 ℃ and the reaction temperature was increase rapidly to 150 ℃. At this temperature, the reaction mixture was stirred for 30 min in a flask under a nitrogen atmosphere. Then, the reaction temperature was further increased to 300 ℃ and reacted for 4 h. After cooling to 60 ℃, 10 mL of toluene was added to remove the residual amines, and the brown precipitates were isolated by centrifugation. The products were washed with isopropanol (IPA) for three times.

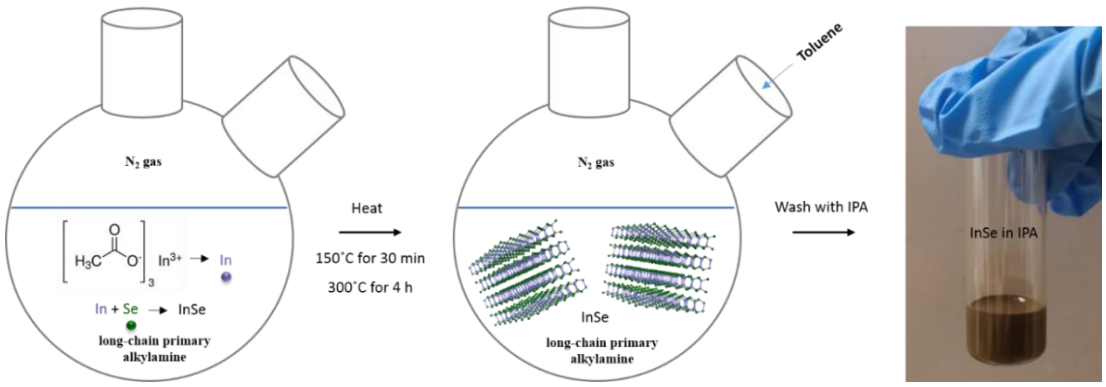

Figure 3.28 Synthesis process of layered hexagonal bulk InSe.

3.4.3 Preparation of 2D InSe nanosheets

Sonication assisted LPE method was applied to prepare 2D InSe. The total process is same as the **"2.4.2 Preparation of 2D metal chalcogenide nanosheets"** part.

In order to compare the as-synthesized hexagonal shape InSe with commercially available indium selenide (In_2Se_3), commercial bulk In_2Se_3powder were also exfoliated using the same process.

3.4.4 Assembly of the lithium-ion battery using 2D InSe and SWCNTs composites as anodes

Same as preparation of 2D MC-SWCNTs composites anodes, 2D InSe-SWCNTs composites electrodes were obtained using a facile vacuum filtration method of blended mixture of SWCNTs and 2D InSe nanosheets dispersionswith a polyethylene membrane (Celgard K2045, 0.06 µm pore size).

Several 2D InSe-SWCNTs composite films were prepared with SWCNTs contents of 5%, 10%, 20% and 40%, respectively, while keeping the filtrated volume constant.

The as-synthesized bulk hexagonal shape InSe-SWCNTs, commercial bulk InSe-SWCNTs, and exfoliated 2D commercial InSe-SWCNTs composites electrodes were prepared using the same approach, and the SWCNT loading fraction was controlled at 20%.

Then, CR-2032 coin cells were assembled using those 2D InSe-SWCNTs composite as anodes and Li foil as cathodes. Electrolyte was comprised of lithium hexafluorophosphate ($LiPF_6$) salt (as the concentration of 1.2 mol/L) in an organic solvent which is made up of ethylene carbonate, ethyl methyl carbonate (EMC) and fluoroethylene carbonate (FEC) (9:1 wt% of [EC+EMC]:FEC).

Electrochemical tests were performed *via* cyclic voltammetry (CV) and galvanostatic charge/discharge (GCD) with a voltage range of 0.01–3 V on a potentiostat (VMP3, Biologic). Testing conditions were same as MC-SWCNTs composites anodes.

3.4.5 Mechanism study of 2D InSe and SWCNTs composites anodes

In-situ X-ray diffraction measurement: *Operando* X-ray diffraction experiments are conducted using a Swagelock-type cell equipped with a beryllium window (X-ray transparent) as current collector at the working electrode. A lithium foil is used as both counter and reference electrodes and Whatman glass fiber (GFA) as separators. 1 M lithium hexafluorophosphate ($LiPF_6$) dissolved in ethylene carbonate (EC) and dimethyl carbonate (DMC) in a 1:1 volume ratio is used as the electrolyte. The electrochemical tests are made using a VMP (biologic France) during galvanostatic charge-discharge

measurements. At the same time X-rays diffraction (XRD) patterns were recorded using a Bruker D8 diffractometer ($\lambda_{CuK\alpha}$=1.5418 Å) equipped with a LynxEye detector. It should be noted that for the 1st discharge, the discharge currents were modified several times for selecting a proper rate current to ensure enough XRD patterns were collected for each cycle but not consuming too much time.

Density function theory calculations: This work was performed by our collaborator Prof. Wang's group. All electronic structure calculations were performed within the framework of DFT as implemented in the Vienna Ab initio Simulation Package (VASP). The DFT calculations of the In_x (x=3,4,5,7) nanocluster models were carried out using the optB88-vdw exchange-correlation functional.[231, 232] The geometries for the different models used were optimized until the forces on each relaxed atom were lower than 0.025 eV/Å and the electronic structure at each geometry optimization step was self-consistently converged with energy, density, and eigenvalue thresholds of 5E−4, 1E−4, and 5E−8 eV, respectively. A vacuum region of 15 Å was added to avoid the interactions between adjacent images. The Brillouin zone was sampled by Monkhorst-Pack method with a 5 × 5 × 1 k-point grid.[231, 232]

3.4.6 Preparation of In and SWCNTs composites anodes

To ensure that other conditions were consistent with an InSe-SWCNTs anode, 20 wt% of SWCNTs were added to indium particles to fabricate In - SWCNTs composite electrodes. First, different sized (nano and micro) In particles were dispersed in IPA solvent by ultrasonication. Then, the In particles dispersion mixed with SWCNTs dispersion (in IPA solvent) to obtain the mixture of In and SWCNTs. Afterwards, the mixture was sonicated using sonic bath for 30 min. Finally, In and SWCNTs hybrid electrodes were prepared *via* a facile vacuum filtration method.

4 2D transition metal dichalcogenides for solar cells

4.1 Introduction

Traditional solar energy conversion devices based on crystalline silicon face the challenge of the environment and their energy intensive production process.[106] Therefore, there is an urgent need to develop new, inexpensive, efficient semiconducting materials.[107, 233] In addition, high-performance, economically viable, large-scale producing and rich resources are the key to developing novel solar cell materials.

PSCs are one of the most promising candidate as the next generation solar cell technology.[119-121] Perovskites have intense light absorption coefficient (1.5×10^4 cm^{-1} at 550 nm), long electron and hole diffusion length (from 100 nm to 1 mm), high carrier mobility ($1 – 10$ cm^2 V^{-1} s^{-1}), and the possibility of solution-processing.[122-125] Emerging perovskite materials have opened the way to producing efficient, low-cost solar cells. In this sense, this new generation solar cell meets our research requirements.

However, the stability has become a major barrier for further development compared to silicon-based solar cells on the market.[234] Perovskites are very sensitive to environment such as air, UV light, water, thermal stress and other factors.[235-237] These stressors-induced degradation can be effectively reduced by inserting a buffer layer into the device structure.[234]

Normally, adding hole and electron transporting layers (HTL and ETL, respectively) in PSCs between the photoactive layer (i.e. the perovskite layer) and the electrodes to separate and collect the generated charges (holes at the photoanode and electrons at the back electrode) efficiently.[126] To date, TiO_2 is the most widely used ETL material for PSCs to prevent electrons and holes recombination at the photoanode. This kind of ETL typically consists of compact TiO_2 layer (c-TiO_2, 50 – 80 nm) and mesoporous TiO_2 layer (mp-TiO_2, 200 – 300 nm). For what regards the HTL, 2,2′,7,7′-tetrakis-(N,N-di-4-methoxyphenylamino)-9,9′-spirobifluorene (spiro-MeOTAD) represents the reference HTL material used for PSCs due to its facile implementation and high performance.[119, 121, 125, 130] It could effectively transfer holes from the perovskite to the electrode. However, spiro-OMeTAD is expensive (Sigma-Aldrich, 324 €/g), and it also has degradation issues induced by temperature, additives, and environmental conditions. Apparently, spiro-OMeTAD HTL is one of the main issues resulting in the

poor stability of PSCs.[105] One strategy to improve the stability of the PSCs could be replacing the spiro-OMeTAD with other hole transport materials such as copper (I) thiocyanate (CuSCN), nickel (II) oxide (NiO), and poly(3,4-ethylenedioxythiophene)polystyrene sulfonate (PEDOT:PSS).[135-137, 238] However, they are not easy to replace the role of the spiro-OMeTAD which allows us to achieve the high level PCE.

Another strategy is adding a buffer layer between the perovskite and the spiro-OMeTAD layer to prevent intermigration of iodine and metals between the perovskite layer and the spiro-OMeTAD layer. What's more, a buffer layer also can prevent a direct contact between the perovskite and the metal electrode can occur in solution-processed PSCs due to the incomplete coverage of the perovskite by the HTL, which results in a decrease of V_{oc} and FF because of high recombination losses.[138-140, 142]

Based on the large number of studies, there is no doubt that2D TMDs and MCs semiconductors represent one of the most promising materials for absorber, HTL, ETL, or buffer layer of solar cell devices.[118, 132, 143, 239, 240] These types of materials can realise large-scale commercial production of high-performance devices with low cost and a simple process. Here, 2D TMDs (MoS_2, $MoSe_2$, WS_2, etc.) nanosheets prepared by the LPE method were demonstrated as an absorber, HTL, or buffer layer of photovoltaic devices. We prepared solar cell devices by investigating various deposition conditions of 2D TMD layer properties in terms of the size on the nanoflakes and spin coating conditions followed with a characterization of the devices' efficiency and stability.

4.2 Results and discussion

4.2.1 Preparation of 2D transition metal dichalcogenides nanosheets

As mentioned above, LPE associated with ultrasonication was employed to prepare the 2D TMD exfoliations in NMP with different conditions. The LPE principle is simple. Because of the unique structure of layered materials (i.e. strong chemical bonds in-plane but weak interaction out-of-plane), ultrasonic energy can easily break up weak van der Waals interactions between each layer to obtain exfoliated 2D nanosheets with one or few layers. NMP proved to be the most promising solvent for the exfoliation of

layered TMD materials, as the surface energy of NMP matched most of the TMDs. However, it's a toxic solvent with a high boiling point. Therefore, exfoliated 2D TMDs nanosheets were centrifuged and then re-dispersed in IPA, which is a nontoxic solvent with a low environmental impact and a low boiling point. Finally, exfoliated 2D TMDs nanosheets dispersion in IPA was obtained as shown in Figure 4.1a-d. The change of solvent from NMP to IPA allows the dispersion be easily handled, environmentally-friendly, and available to fabricate high-performance devices. For instance, as shown in Figure 4.1, bulk MoS_2 (Figure 4.1a) was exfoliated to thinner 2D MoS_2nanosheets (Figure 4.1c and d) *via* LPE approach. 2D MoS_2 nanosheets could be stabilized in IPA solvent as shown in Figure 4.1b. What's more, as shown in Figure 4.2, different centrifugation rates gave distinct sizes of MoS_2nanosheet dispersions. The size of nanosheets ranged between 343.02 nm (at 500 rpm) and 42.61 nm (at 5,000 rpm). Other kinds of TMDs, such as 2D $MoSe_2$ nanosheets were prepared by the same LPE process.

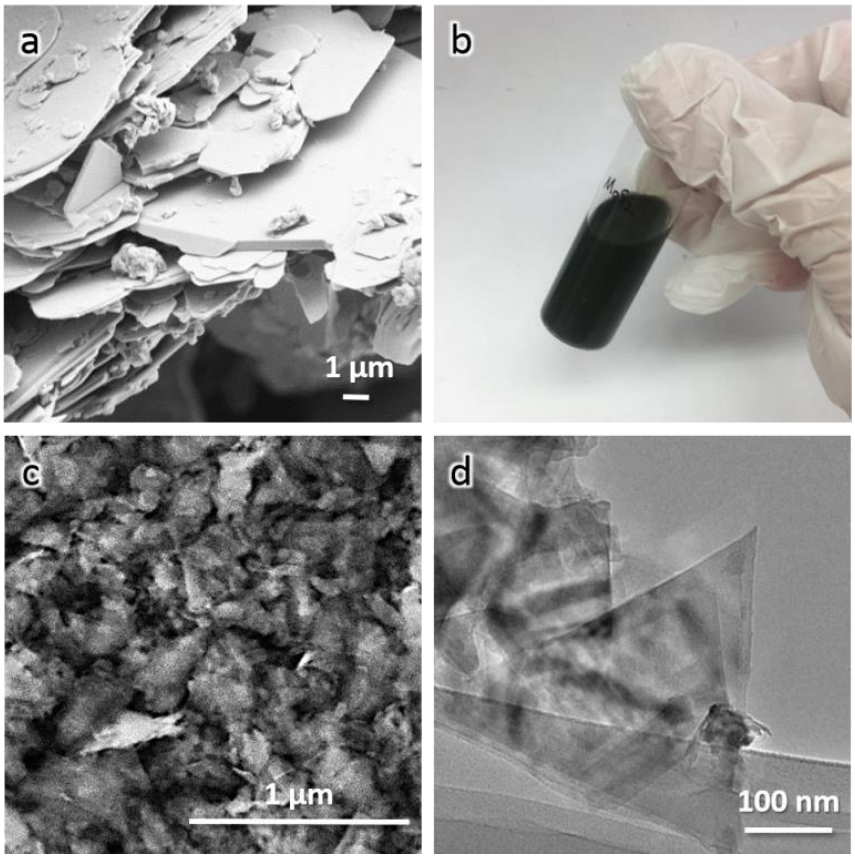

Figure 4.1 (a) SEM image of bulk MoS_2, (b) exfoliated MoS_2 dispersion in IPA solvent, (c) SEM image of exfoliated MoS_2, (d) TEM image of exfoliated MoS_2.

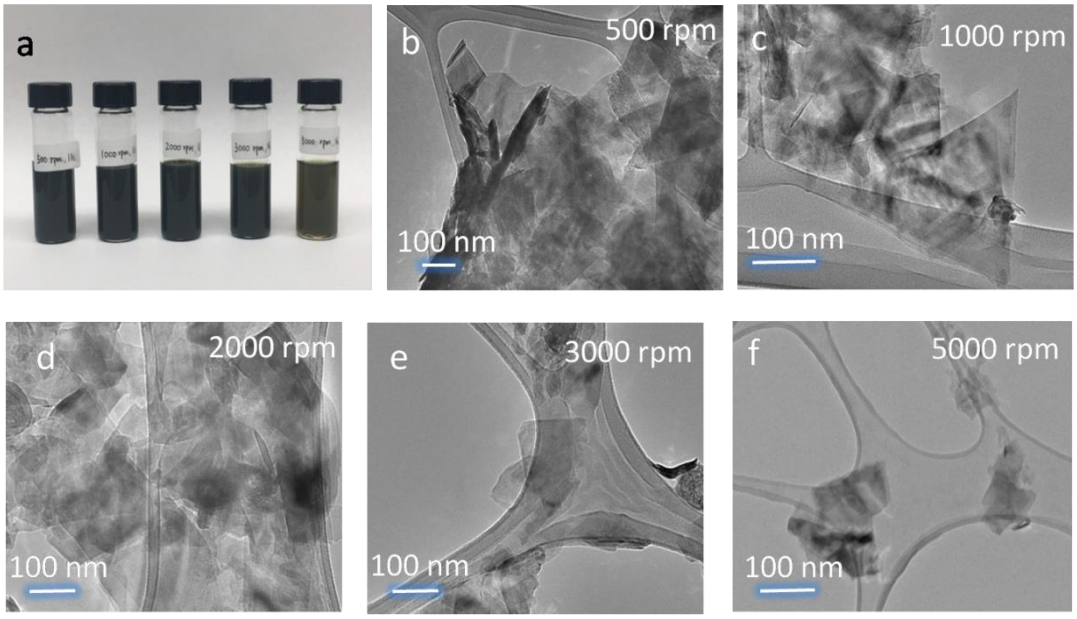

Figure 4.2 (a) Photo of exfoliated2DTMDs dispersions obtained by different centrifugation rates; TEM images of different samples of MoS_2 exfoliation: 5 h of sonication time and centrifugation rates of (b) 500 rpm, (c) 1,000 rpm, (d) 2,000 rpm, (e) 3,000 rpm and (f) 5,000 rpm; respectively.

4.2.2 Application of 2D transition metal dichalcogenides for solar cell devices

As mentioned before, 2D TMD semiconductors are promising candidates for the new generation solar cells. These types of materials can realise large-scale commercial production of high-performance devices with low cost and a simple process. Here, we prepare the 2D TMDs *via* LPE approach and applied them as an absorber, HTL, and buffer layer of solar cell devices.

4.2.2.1 2D transition metal dichalcogenides as an absorber of solar cells

Fabrication of solar cells using TMD materials has been studied by a lot of groups. Table 1.2 (**"1.3.2.1 2D MCs and TMDs as an absorber of solar cells "**) summarizes the results of the use of TMDs as photoactive layers.

LPE is an easy, low-cost, scalable and effective method to obtain 2D TMDs materials. Here, we prepared the 2D TMDs *via* LPE approach and studied its application as an active layer (absorber) of the solar cell.

To prepare the 2D TMDs absorbing layer, first we tried the spin coating method. However, obtained layer was very thin and transparent. In order to get a thicker 2D TMDs layer, we tried spray coating approach. Compared to spin coating, spray coating could obtain thicker layer of 2D TMDs. In order to absorb sunlight, spray coating method was used in this work. To investigate the PV performance of the 2D TMDs materials, IV measurements were conducted. As shown in the Figure 4.3, the I-V curves of the 2D TMDs (MoS_2, $MoSe_2$, and WS_2) solar cells suggest that the the 2D TMD materials obtained using the LPE method possess a diode characteristic. However, the photo current were near zero for all 2D MoS_2, $MoSe_2$, and WS_2 nanosheets, when light was put on these devices. To optimise the PV performance of the solar cell device, we selected the size and thickness of MoS_2 nanosheets by changing the centrifuging and sonicating conditions. I-V test was carried out under the same conditions for these samples. All details of the experiment have been described in the experiment section. According to size selection, we prepared five different size and thickness 2D MoS_2 nanosheets. From thin to thick, we labelled them as T1, T2, T3, T4 and T5 (Figure 4.4). However, no significant improvement of the photocurrent was observed for them (Figure 4.4). There is a limit to preparing very thin layer TMD nanosheets using the LPE approach. The main reason for 0 % of PCE is probably that only reducing the number of MoS_2 layers to a very low value (at least two or three layers) has the potential to achieve a dramatic change in the PV performance of solar cells.

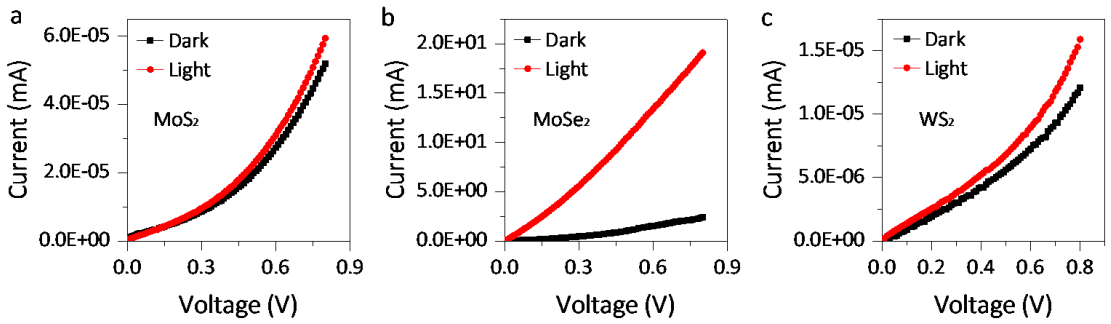

Figure 4.3 I-V curves of TMD solar cells assembled by (a) MoS_2, (b) $MoSe_2$, and (c) WS_2 under dark and under the light.

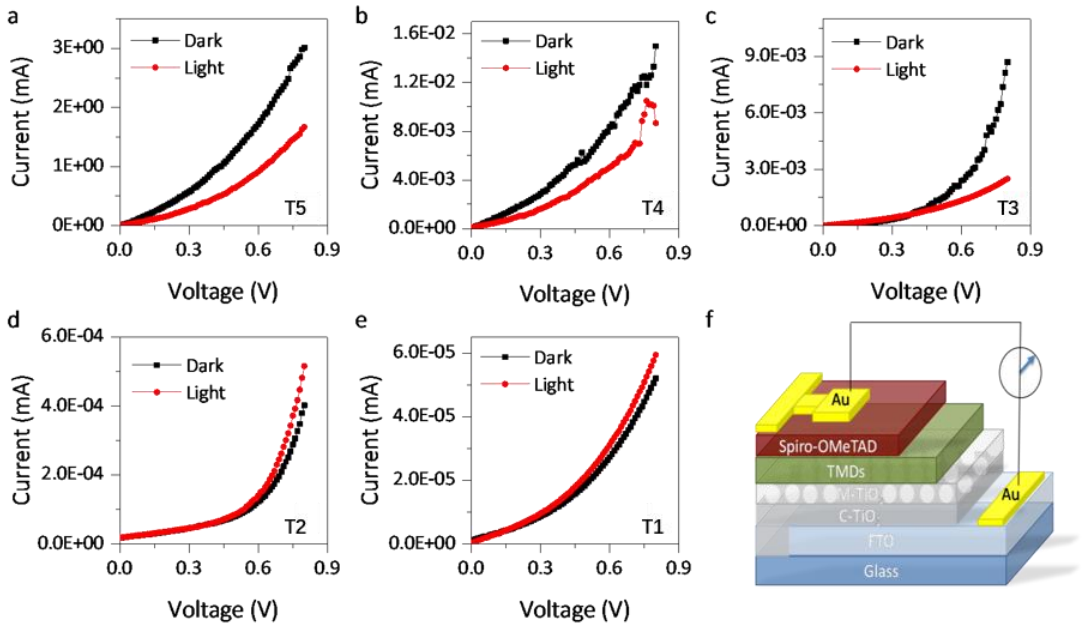

Figure 4.4 I-V curves of different size and thickness 2D MoS_2 nanosheets solar cells: (a) T5 (the thickest), (b) T4 (the second thick), (c) T3 (the middle thick), (d) T2 (the second thin), (e) T1 (the thinnest), and (f) TMD solar cell structure.

4.2.2.2 2D transition metal dichalcogenides as a hole transport layer of the perovskite solar cells

According to previous studies, we found that 2D TMDs nanosheets have a great potential to use as a HTL of the PSCs due to their high carrier mobility, low cost (e.g. MoS_2 Sigma-Aldrich, 0.85 €/g), and solution-processable properties.[118, 132, 143, 239-243] 2D MoS_2 nanoflakes have improved the efficient charge extraction across the HTL reducing recombination at the interfaces.[241, 242] Therefore, combination of 2D TMDs and perovskite gives us opportunity to obtain solar cells with good PCE and stability. In this work, 2D TMDs nanosheets were prepared *via* the LPE approach. Then, these 2D TMDs were utilized as a HTL of the Glass / FTO / compact-TiO_2 / mesoporous-TiO_2 / $FA_{85}MA_{15}PbI_{85}Br_{15}$ / 2D TMDs / Au structured PSC (Figure 4.5).

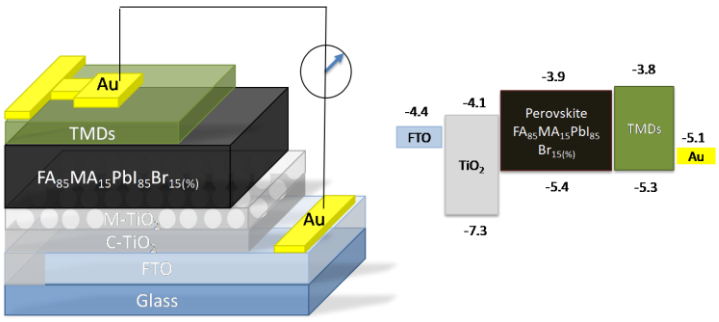

Figure 4.5 2D TMDs added as a HTL of the Glass / FTO / compact-TiO_2 / mesoporous-TiO_2 / $FA_{85}MA_{15}PbI_{85}Br_{15}$ / 2D TMDs / Au structured PSCs.

As shown in Figure 4.6, compared to the PSCs without HTL (PCE = 1.27 %), PSCs with TMDs (MoS_2 and $MoSe_2$) HTL could obtain 2.97 % and 2.62 % of PCE (Figure 4.6d). It confirms MoS_2 could assist the hole transport and collection at the electrode. However, these values are much smaller than PSC with spiro-OMeTAD HTL, which gives 11 % of PCE (Figure 4.6d). According to the analysis of V_{oc}, J_{sc}, and FF (three main factors of efficiency), it is obvious that low FF is the main issue of TMDs HTL in PSCs (Figure 4.6a-c).

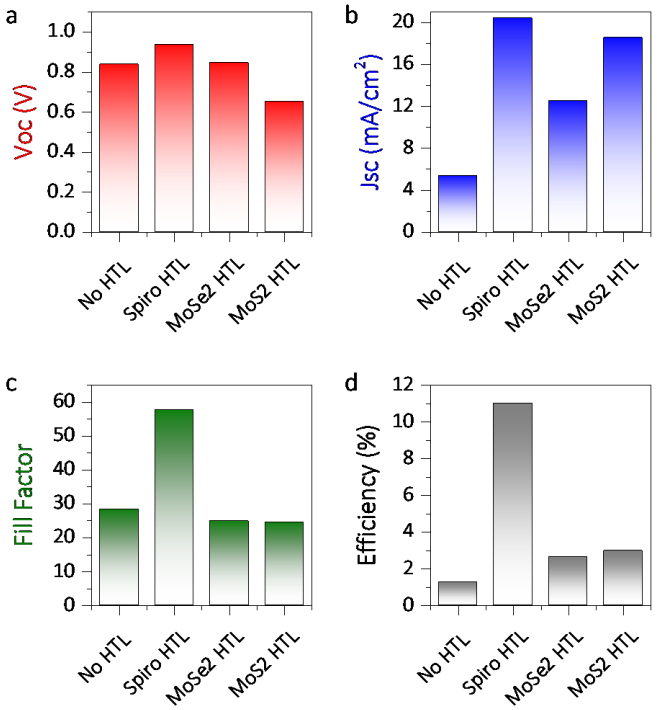

Figure 4.6 (a) V_{oc}, (b) J_{sc}, (c) FF, and (d) efficiency of PSCs without HTL, with spiro-OMeTAD HTL, with TMDs (MoS_2 and $MoSe_2$) HTL.

Figure 4.7 presents the IV curves of PSCs without HTL (Figure 4.7a), with spiro-OMeTAD (Figure 4.7b) HTL, or with TMDs HTL (Figure 4.7c and d). Solar cell I-V characteristic curves are graphs of output voltage versus current for different levels of insolation and temperature and can tell us a lot about a PV cell's ability to convert sunlight into electricity. As shown in Figure 4.7, PSCs with TMDs HTL have similar IV curves to PSCs without HTL while the PSC with spiro-OMeTAD has a rectangular-like curve.

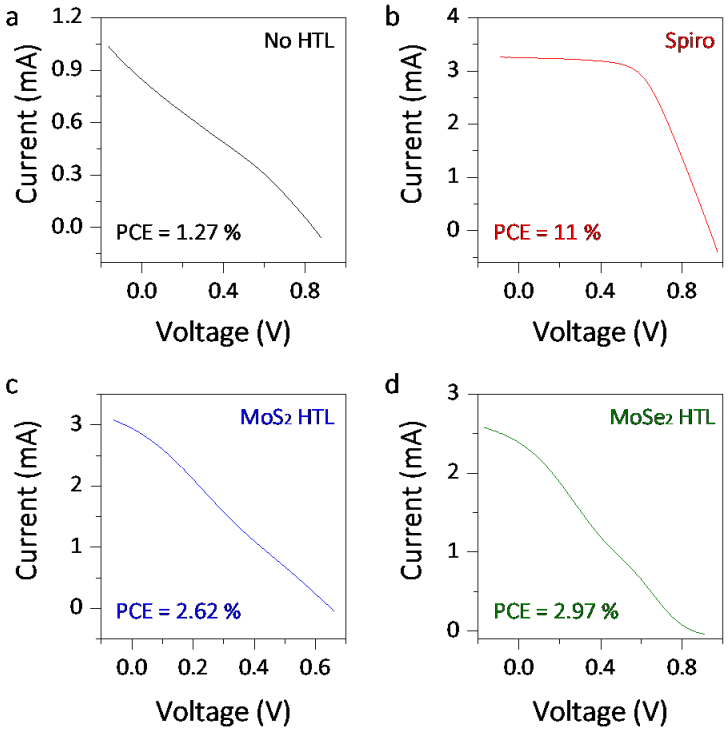

Figure 4.7 I-V curves of PSCs (a) without HTL, (b) with spiro-OMeTAD HTL, (c and d) with TMDs (MoS_2 and $MoSe_2$) HTL.

The most important values for calculating a particular solar cell power rating are the voltage (V_{mp}) and current (I_{mp}) at maximum power point (MPP). The MPP of a solar cell is positioned near the bend in the IV curve. The corresponding values of V_{mp} and I_{mp} can be estimated from the V_{oc} and the I_{sc}: $V_{mp} \cong (0.8 - 0.9)\ V_{oc}$ and $I_{mp} \cong (0.85 - 0.95)\ I_{sc}$. The maximum power delivered by the solar cell, MP, is the area of the largest rectangle under the IV curve. Therefore, according to the shape of IV curves, it is clear that the PSC with spiro-OMeTAD has the maximum output power among these PSCs. As shown in Figure 4.6, V_{oc}, I_{sc} and FF of PSCs with TMDs HTL are all smaller than standard PSCs (using spiro-OMeTAD as a HTL) but the FF is the main reason caused

lower PCE. However, the variation in maximum FF can be significant for solar cells made from different materials. It is defined as the ratio of MP to the area of the rectangle formed by V_{oc} and I_{sc} (Equation 1).

$$FF = \frac{MP}{(Voc)(Isc)}$$

It's a measure of the squareness of the IV characteristics of the solar cell. So according to IV curves (Figure 4.7), we could also know that the PSC with spiro-OMeTAD HTL has the best PV performance.

There are several factors that can significantly influence FF, and these factors interact with each other very intricately. Among them, the series resistance (R_s) which is composed of the resistance of the different semiconductor layers of the cell and the shunt resistance (R_{sh}) which arises because of the leakage across the junction are probably the problem of low FF in these devices. Therefore, in order to optimize the FF, surface and interaction between different layers of PSCs should be improved. So here we studied the deposition conditions of TMD layer first. Because good quality of TMD layer leads to the improvement of FF, further the PCE of the device.

In order to optimize the device, the amount of 2D TMD dispersion used for per sample increased from 40 μL to 100 μL and the spin-coating speed decreased from 4,000 rpm to 2,000 rpm. As shown in the Figure 4.8, FF improved apparently after changing the deposition condition which further leads to the enhancement of PCE of the PSC with the TMD HTL. According to AFM, we found that the thickness of MoS_2 layer is around 20 nm with the new deposition condition (Figure 4.9a and b). Figure 4.9c shows the cross-section image of the PSC using 2D MoS_2 as a HTL. According to it, we could see the interfaces between each layer and also get the information of the thickness of each layer. Interfaces between each layer of the solar cell were smooth and the thickness of the MoS_2 HTL is around 20 nm, which fits with the AFM result. IV curves after changing the deposition conditions of TMD layer (Figure 4.10) also confirm that FF increased after optimization. As shown in Figure 4.11, V_{oc}, I_{sc} and FF of PSCs with TMDs HTL increased especially FF after optimization of TMD layer deposition condition. PCE of the PSC with MoS_2 or $MoSe_2$ HTLs improved to 6.09 % and 4.31 %. IV curves of these optimized PSCs also support the conclusion (Figure 4.12). PSCs with TMDs HTL revealed a significant increase in PCE with respect to the cell with no HTL (1.27 %),

confirming that the 2D MoS_2 nanoflakes ease the hole transport and collection at the Au electrode.

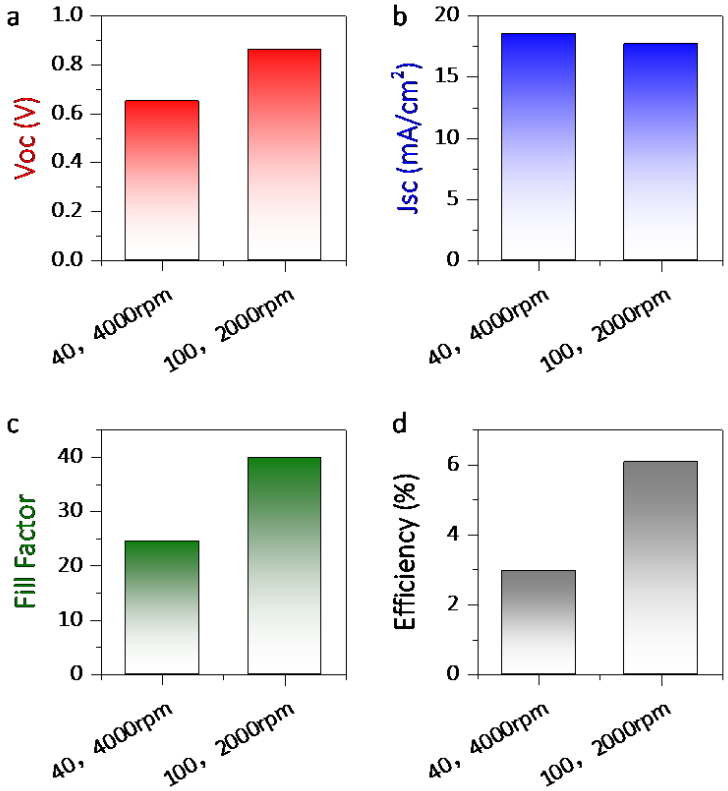

Figure 4.8 (a) V_{oc}, (b) J_{sc}, (c) FF, and (d) efficiency of optimized PSCs with MoS_2 HTL.

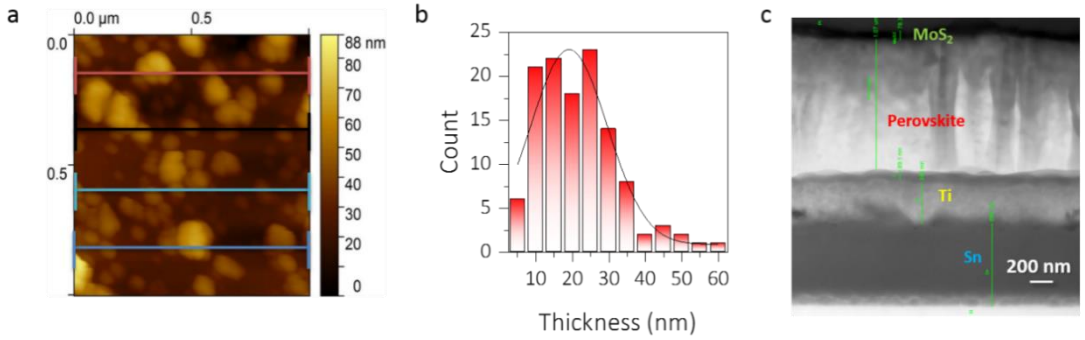

Figure 4.9 (a)AFM image of 2D MoS_2 (XS size: centrifuged at 5,000 rpm) layer (spin coated at 2,000 rpm for 20 sec), (b) thickness distribution of 2D MoS_2 layer, (c) cross-section TEM image of the PSC using MoS_2 as a HTL.

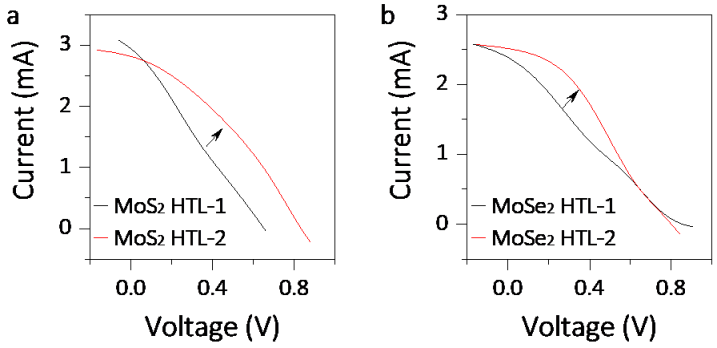

Figure 4.10 Change of I-V curves of PSCs with (a) MoS_2 or (b) $MoSe_2$ HTL before and after optimization of spin coating conditions.

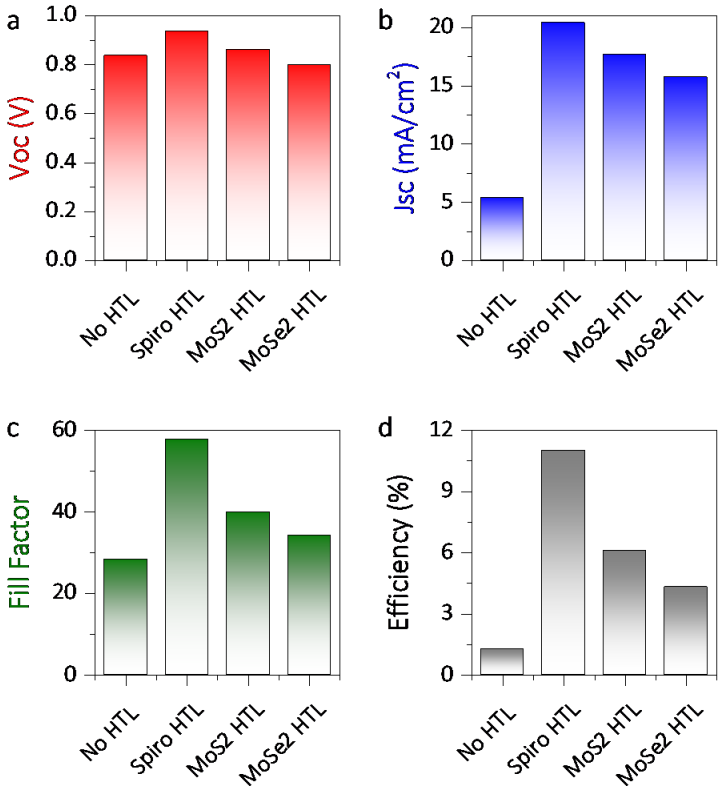

Figure 4.11 (a) V_{oc}, (b) J_{sc}, (c) FF and (d) efficiency of PSCs with TMDs HTL after optimization.

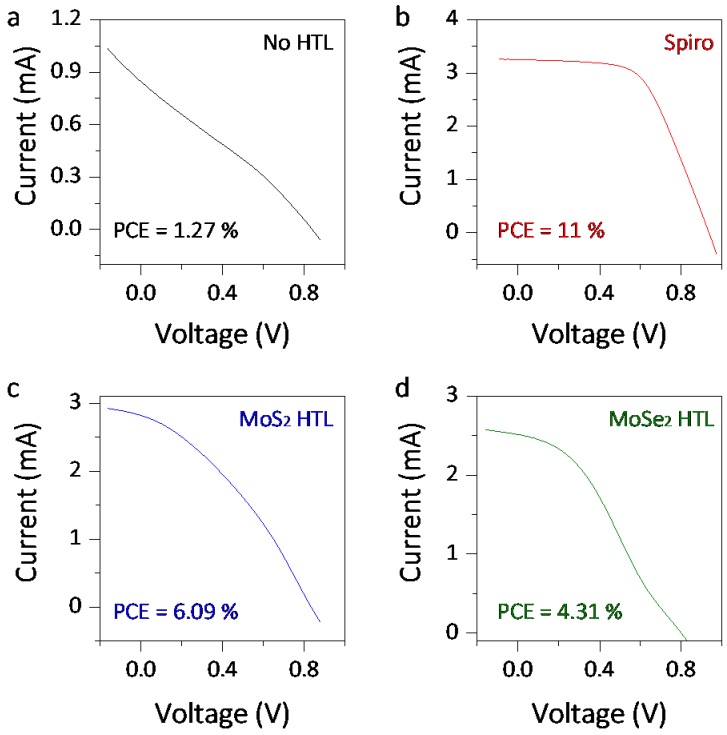

Figure 4.12 Comparison of I-V curves of PSCs (a) without HTL, (b) with Spiro-MeOTAD HTL, (c) with MoS_2 HTL and (d) with $MoSe_2$ HTL after optimization.

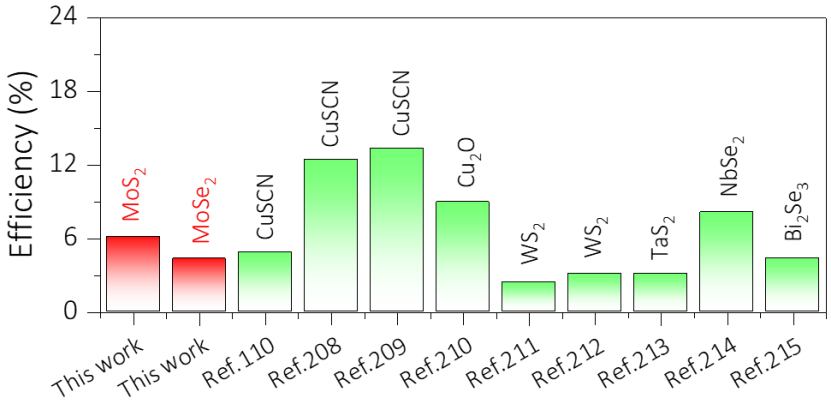

Figure 4.13 Compared to other inorganic hole transport materials for PSCs having similar structure as we studied here.

Compared to other inorganic hole transport materials such as copper(I) thiocyanate (CuSCN),[135, 244, 245] copper(I) oxide (Cu_2O),[246] tungsten disulfide (WS_2),[247, 248] tantalum(IV) sulfide (TaS_2),[249] niobium diselenide ($NbSe_2$),[250] and bismuth selenide (Bi_2Se_3)[251] for PSCs having similar structure as we studied here, liquid exfoliated 2D

MoS_2 and $MoSe_2$ nanoflakes studied in this work present the medium range of PCE which is optimistic (Figure 4.13). Many factors such as size of TMDs, thickness of TMD layer, and TMD layer deposition process all could be optimized.

4.2.2.3 2D transition metal dichalcogenides as a buffer layer of the perovskite solar cells

There is a long list of materials used as HTL instead of spiro-OMeTAD as mentioned before. However, despite these recent results, spiro-OMeTAD still represents the reference HTL material used for the fabrication of PSCs.

A significant limitation that poses severe concerns in view of the possible commercialization of PSCs is their lifetime stability, which is adversely affected by the presence of the spiro-OMeTAD. Another factor limiting the device stability regards the interface created by the spiro-OMeTAD and the perovskite layer.[138-142] Recent analysis using *in-situ* TEM characterization of PSCs operating under illumination reported evidence of iodine migration from the perovskite layer to the spiro-OMeTAD, with consequent degradation of the cell efficiency.[29] Furthermore, it is known that a direct contact between the perovskite and the metal electrode results in high recombination losses, which results in a decrease of V_{oc} and FF.[138-142] Such losses can occur in solution-processed PSCs due to the incomplete coverage of the perovskite by the HTL. Another source of loss is the metal electrode that can also get in contact with the perovskite by migrating through the HTL. One strategy to minimize such detrimental effect could be the increase of the HTL thickness, which is however associated with an increase of the PSCs series resistance, determining a reduction of the solar cell PCE. Therefore, adding buffer layer between perovskite and spiro-OMeTAD HTL could also be a promising strategy to deal with this issue.

Here, we used 2D TMD materials to create a buffer layer for PSCs. We did not know whether our 2D TMDs obtained *via* LPE method were n-type or p-type semiconductors. Therefore, we tried three different positions in PSCs. More specifically, 2D TMD materials were used as 1) a buffer layer between ETL and the perovskite layer (after, it is simply called “ETL buffer”), 2) a buffer layer between the perovskite layer and HTL (called “HTL buffer”), and 3) both between ETL and the perovskite layer and between the perovskite layer and HTL (called “sandwich buffer”).

As shown in Figure 4.14, MoS_2 was applied as an ETL buffer, a HTL buffer and sandwich buffers. It is apparent that MoS_2 layer is more suitable to use as a HTL buffer for the PSC. According to Figure 4.14a-c, we could know that all V_{oc}, J_{sc}, and FF of MoS_2 HTL buffer higher than ETL and sandwich buffers. This is because the band gap and work function of 2D MoS_2 more fit to be added between the perovskite and the sprio-OMeTAD HTL. Compared to standard PSC, PSC with 2D MoS_2 HTL buffer layer has lower FF (Figure 4.14c). However, the V_{oc} and I_{sc} increased so that the PCE of the device could main at 14.3 % (Figure 4.14d).

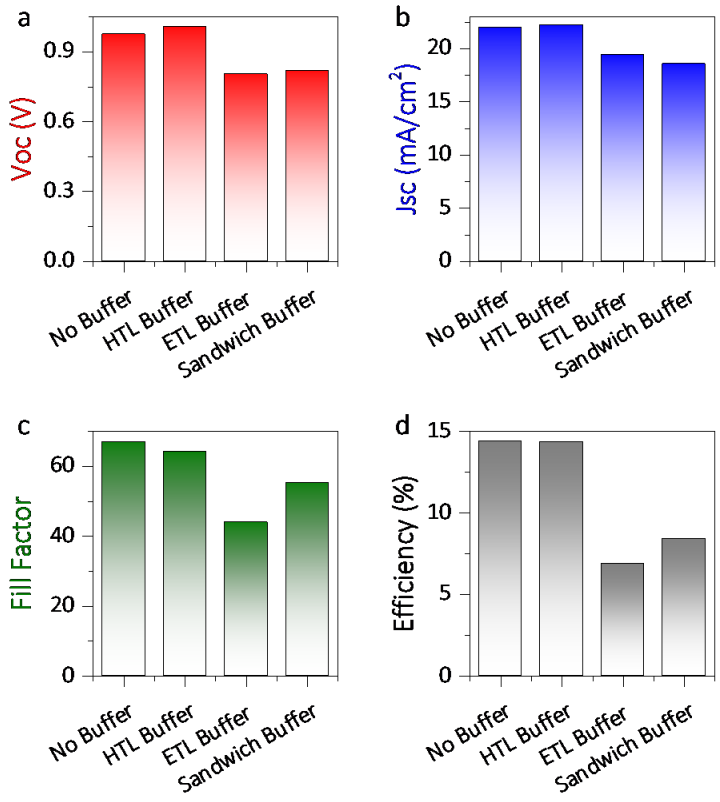

Figure 4.14 (a) V_{oc}, (b) J_{sc}, (c) FF, and (d) efficiency of four different PSCs: (1) Standard PSCs, (2) PSCs adding MoS_2 for buffer layer between perovskite layer and HTL (HTL buffer), (3) PSCs adding MoS_2 for buffer layer between mesoporous TiO_2 layer and perovskite layer (ETL buffer), and (4) PSCs adding MoS_2 for both HTL and ETL buffers (sandwich buffer).

IV characteristic curves of these three different buffers also support the conclusion that MoS_2 is suitable for HTL buffer (Figure 4.15a-d). What's more, as mentioned in previous study, when exfoliated MoS_2 was used as a HTL of PSC, we could

see an apparent enhancement of efficiency compared to the PSC without HTL (6.09 % vs. 1.27 %) which approves 2D MoS_2 nanosheets indeed contribute to the hole transport and collection at the electrode. Therefore, 2D MoS_2 is a potential candidate for a HTL buffer of PSCs and practical experiment proved it.

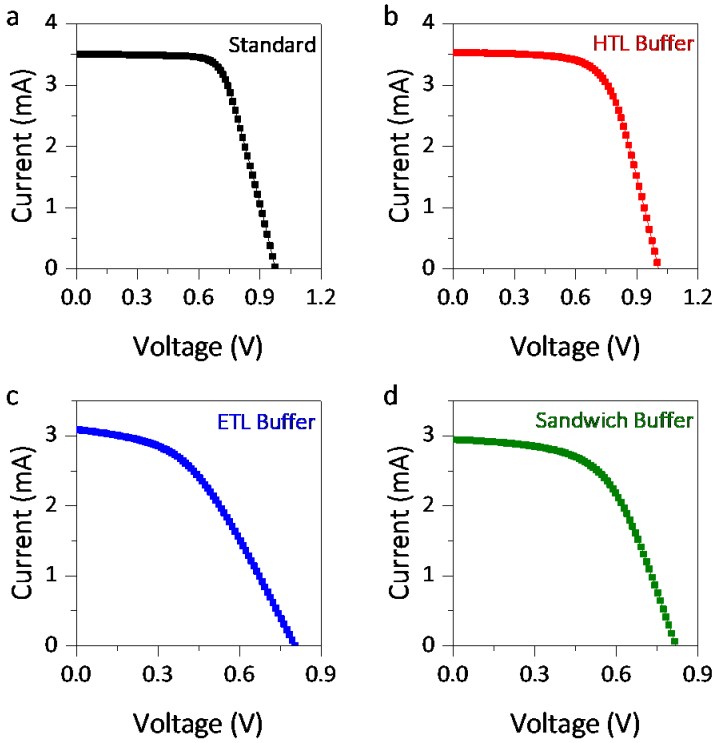

Figure 4.15 I-V curves of four different PSCs: (a) Standard PSCs (Glass / FTO / compact-TiO_2 / mesoporous-TiO_2 / $FA_{85}MA_{15}PbI_{85}Br_{15}$ / sprio-OMeTAD / Au), (b) PSCs adding MoS_2 for buffer layer between perovskite layer and HTL (HTL buffer), (c) PSCs adding MoS_2 for buffer layer between mesoporous TiO_2 layer and perovskite layer (ETL buffer), and (d) PSCs adding MoS_2 for both HTL and ETL buffers (sandwich buffer).

PCEs of these MoS_2 buffer layers kept being checked for a week (Figure 4.16a-d). PCEs of all these samples increased after one week but with different degrees. Increase of the FF is the main contribution to the improvement of efficiency of the cell. Apparently, MoS_2 HTL buffer layer exhibited the best performance among those different buffers.

As shown in IV curves, standard PSCs and PSCs with 2D MoS_2 HTL buffer have almost the same rectangular shape after 1 week which gives higher MP (Figure 4.17a and b). However, IV curves shapes of PSCs with ETL and sandwich buffer were still far from rectangles after 1 week (Figure 4.17c and d).

According to the previous study, we safely make the conclusion that 2D MoS_2 could be utilized as a HTL buffer of PSCs. Based on this, exfoliated 2D $MoSe_2$ nanosheets were also tried as a HTL buffer in PSCs. As shown in Figure 4.18, $MoSe_2$ is also one of the promising materials for a HTL buffer of the PSC. $MoSe_2$ showed similar V_{oc} and J_{sc} with 2D MoS_2 (Figure 4.18a and b), but higher fill factor (Figure 4.18c) than MoS_2 which results in the higher PCE of the device (Figure 4.18d). It is worth to mention that every batch of cells were fabricated in the same condition. However, we couldn't keep every batch of cells work same so there is a difference between the efficiency.

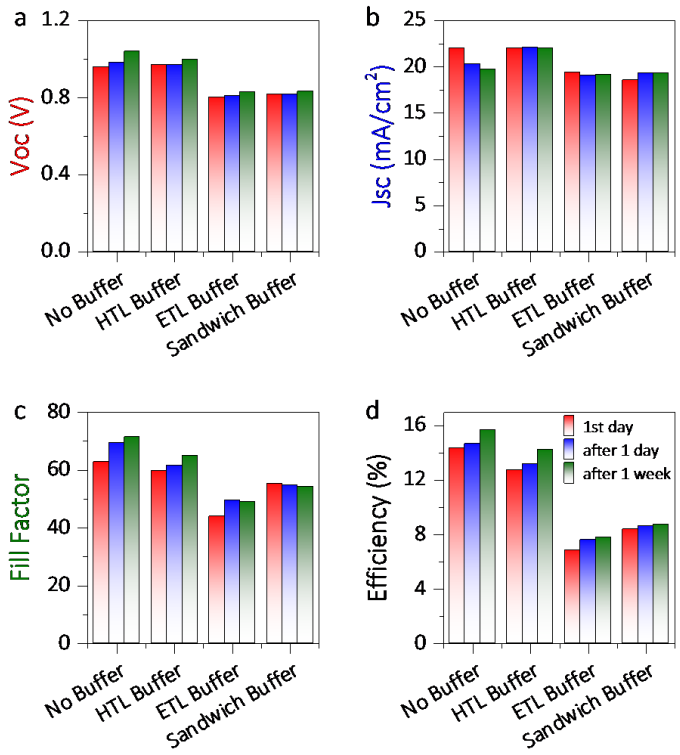

Figure 4.16 Changes of (a) V_{oc}, (b) J_{sc}, (c) FF, and (d) efficiency of four different PSCs: (1) Standard PSCs (Glass / FTO / compact-TiO_2 / mesoporous-TiO_2 / $FA_{85}MA_{15}PbI_{85}Br_{15}$ / sprio-OMeTAD / Au), (2) HTL buffer (Glass / FTO / compact-TiO_2 / mesoporous-TiO_2 / $FA_{85}MA_{15}PbI_{85}Br_{15}$ / 2D MoS_2 / sprio-OMeTAD / Au), (3) ETL buffer (Glass / FTO / compact-TiO_2 / mesoporous-TiO_2 / 2D MoS_2 / $FA_{85}MA_{15}PbI_{85}Br_{15}$ / sprio-OMeTAD / Au), and (4) sandwich buffer (Glass / FTO / compact-TiO_2 / mesoporous-TiO_2 / 2D MoS_2 / $FA_{85}MA_{15}PbI_{85}Br_{15}$ / 2D MoS_2 / sprio-OMeTAD / Au) after 1 day and 1 week.

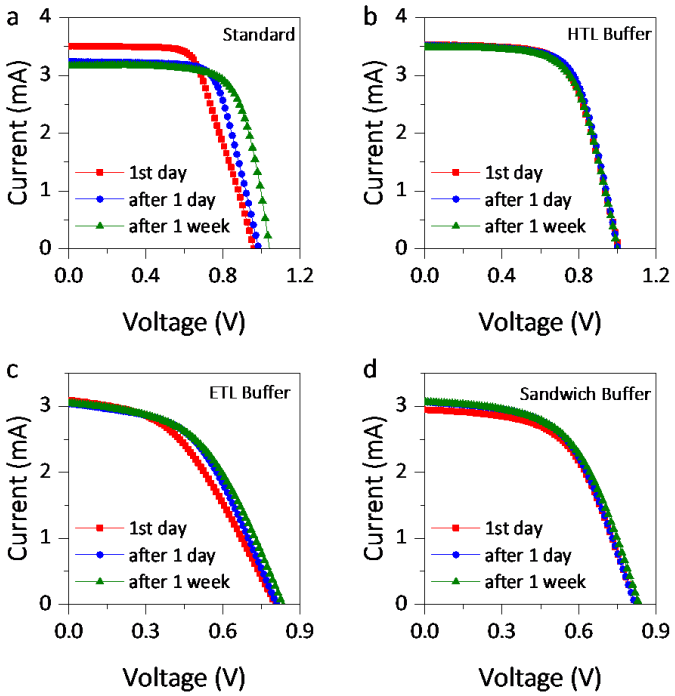

Figure 4.17 I-V curves of four different PSCs: (a) Standard PSCs (Glass / FTO / compact-TiO_2 / mesoporous-TiO_2 / $FA_{85}MA_{15}PbI_{85}Br_{15}$ / sprio-OMeTAD / Au), (b) HTL buffer (Glass / FTO / compact-TiO_2 / mesoporous-TiO_2 / $FA_{85}MA_{15}PbI_{85}Br_{15}$ / 2D MoS_2 / sprio-OMeTAD / Au), (c) ETL buffer (Glass / FTO / compact-TiO_2 / mesoporous-TiO_2 / 2D MoS_2 / $FA_{85}MA_{15}PbI_{85}Br_{15}$ / sprio-OMeTAD / Au), and (d) sandwich buffer (Glass / FTO / compact-TiO_2 / mesoporous-TiO_2 / 2D MoS_2 / $FA_{85}MA_{15}PbI_{85}Br_{15}$ / 2D MoS_2 / sprio-OMeTAD / Au) after 1 day and 1 week.

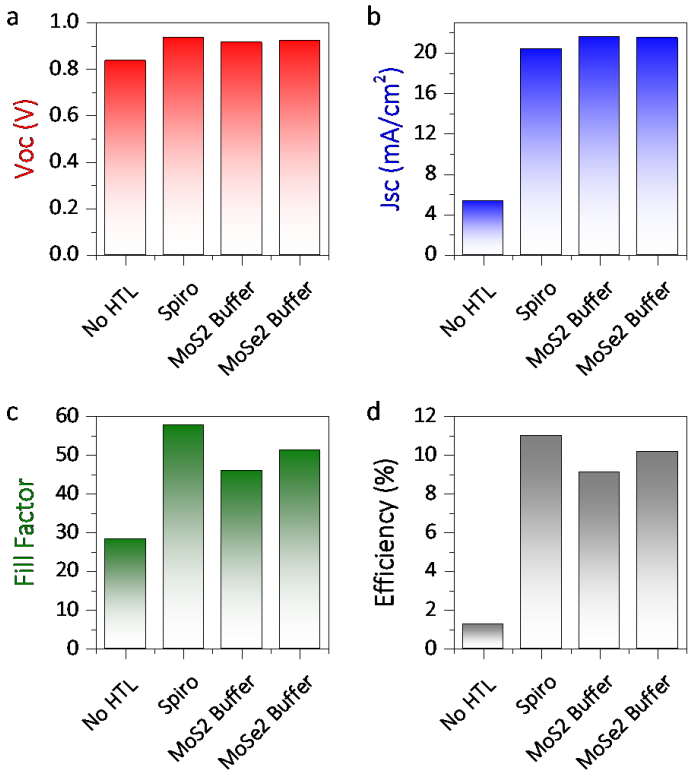

Figure 4.18 (a) V_{oc}, (b) J_{sc}, (c) fill factor, and (d) efficiency of PSCs without HTL, standard PSCs with spiro-OMeTAD HTL, PSCs adding TMD (MoS_2 and $MoSe_2$) layer between perovskite layer and HTL.

From IV curves of standard, MoS_2 HTL buffer, and $MoSe_2$ HTL buffer, we can get the same conclusion (Figure 4.19). Adding a 2D TMD buffer layer reduced the PCE of the PSC to some extent. It is mainly caused by the sacrifice of the FF. However, this factor could be improved by optimizing the deposition process. This will be discussed later in this summary.

Then, different sizes of TMDs (here we used $MoSe_2$) were tried as a HTL buffer of PSCs. Figure 4.20 illustrated the V_{oc}, J_{sc}, FF and efficiency of three different size 2D $MoSe_2$ (large [L], medium [M], and small [S]) and Figure 4.20 showed the IV characteristic curves of them. According to them, we could see that small size $MoSe_2$ gave the better PV performance which has higher J_{sc} and FF than the other two. Therefore, we focus on the small size TMDs for following experiments.

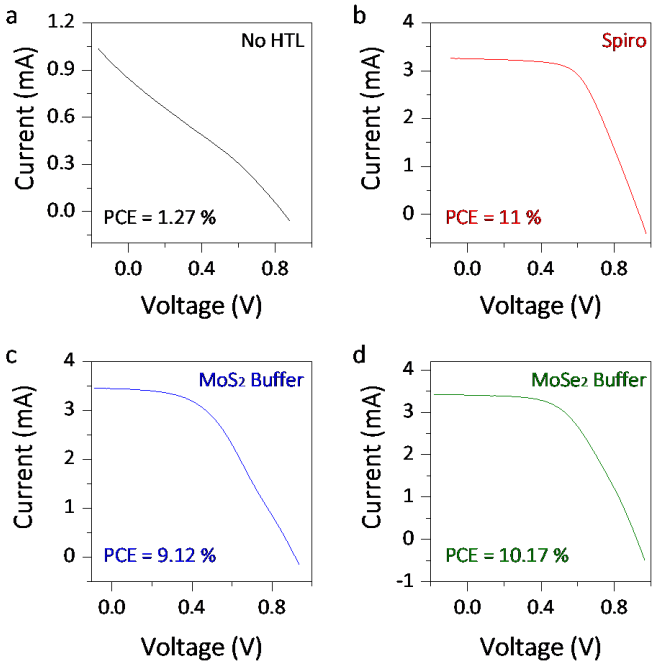

Figure 4.19 I-V curves of PSCs without HTL, standard PSCs with spiro-OMeTAD HTL, PSCs adding TMD (MoS_2 and $MoSe_2$) layer between perovskite layer and HTL.

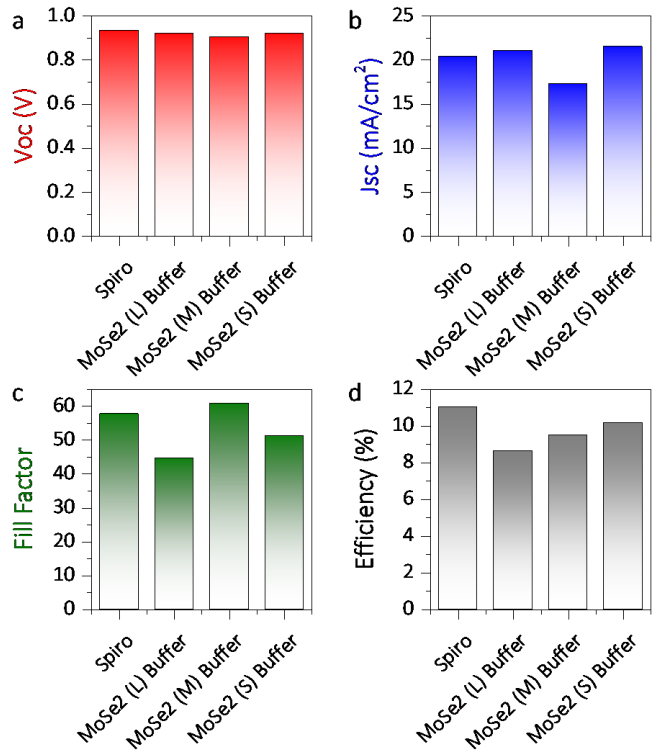

Figure 4.20 (a) V_{oc}, (b) J_{sc}, (c) FF, and (d) efficiency of standard PSCs with spiro-OMeTAD HTL and PSCs adding different size of $MoSe_2$ layer between perovskite layer and HTL.

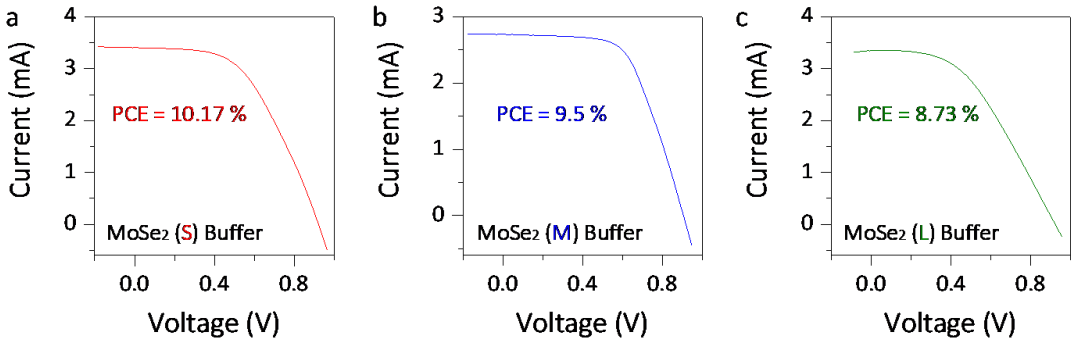

Figure 4.21 I-V curves of (a) small, (b) medium, and (c) large size $MoSe_2$ for buffer layer between perovskite layer and HTL of PSCs.

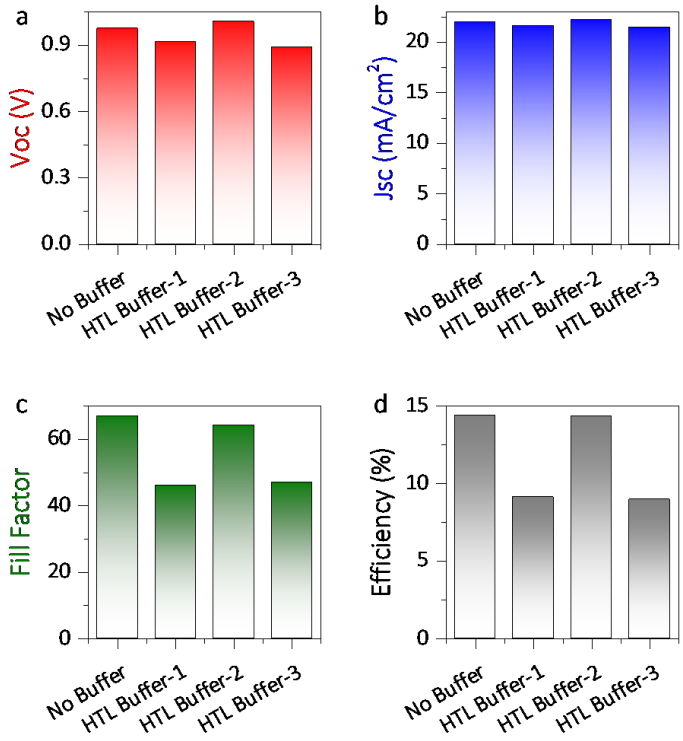

Figure 4.22 (a) V_{oc}, (b) J_{sc}, (c) FF, and (d) efficiency of four different PSCs: (1) Standard PSCs, (2) PSCs spin-coating MoS_2 layer for buffer layer between perovskite layer and HTL and (HTL buffer-1), (3) PSCs spin-coating and annealing MoS_2 layer for buffer layer between perovskite layer and HTL and (HTL buffer-2), and (4)PSCs spin-coating and annealing with perovskite layer and MoS_2 layer together for MoS_2 buffer layer between perovskite layer and HTL and (HTL buffer-3).

In order to optimize the devices, an annealing process was added after the deposition of TMDs layers. As shown in Figure 4.22, the solar cell device worked better when the MoS_2 layer was annealed after deposition *via* spin coating. Its fill factor increased apparently (from 45.97 to 64.14) and V_{oc} (from 0.92 V to 1.01 V) and J_{sc} (from 21.64 mA/cm^2 to 22.22 mA/cm^2) also increased slightly which lead to the enhancement of efficiency (From 9.12 % to 14.34 %). Here, two different annealing process were tried. One is annealing perovskite and MoS_2 layer separately (annealed perovskite at 100 ℃ for 1 h first and annealed MoS_2 layer at 100 ℃ for 30 min later). The other one is after deposition of MoS_2 layer, both perovskite and MoS_2 layers were annealed together (at 100 ℃ for 1 h). When the perovskite layer and MoS_2 layer were annealed together, V_{oc}, J_{sc} and FF all dropped compared to annealing separately. However, compared to the samples without annealing process, we could see that FF increased a little bit (from 45.97 to 46.94). Therefore, we could make a conclusion that annealing process indeed improved the fill factor which is main issue of limit the solar cells' efficiency before. It is helpful to increase the FF and further improve the efficiency of solar cell devices. However, compared to annealing together with perovskite layer, annealing MoS_2 layer separately from perovskite resulted on a better performance of the solar cells.

Efficiency of these solar cells was measured again after 1 day. According to the Figure 4.23, efficiency of solar cells with (MoS_2 layer) annealing process increased while the cell without (MoS_2 layer) annealing process decreased after 1 day. This is mainly because FF and J_{sc} decreased if they are not annealed after deposition. Efficiency changes of PSCs with 2D MoS_2 buffer layer adding annealing process were checked continuously for three weeks. As shown in Figure 4.23, the efficiency of them all increased even after 3 weeks. However, the PSC with MoS_2 HTL buffer layer annealed separately from perovskite layer showed better performance than the one annealed together (Figure 4.23 and 4.24). To get a deeper understanding of what is causing these two different annealing methods to perform different, the interfaces of the PSCs with a MoS_2 HTL buffer layer were studied *via* FIB-TEM and elemental mapping. As shown in Figure 4.25, the interface between ETL and the perovskite layer of the PSC with a MoS_2 HTL buffer layer annealed separately from the perovskite layer is much smoother than the one with a MoS_2 HTL buffer layer annealed together with the perovskite layer. Interfaces between different layers are very important in PSCs because they effect directly to PCE of the cells. Besides the band gap matching of layers, the smooth and intimate connections

between each layer are also essential to achieve a high PCE for solar cell devices. Figure 4.26 and Figure 4.27 show elemental mappings of these two PSCs using different annealing methods. According to them, we could clearly distinguish each layer, such as FTO, compact and mesoporous TiO_2 layers, the perovskite layers, sprio-OMeTAD HTL, and the Au electrode, etc. It is apparent that both these two cells with a MoS_2 HTL buffer layer efficiently prevent migration of lead, iodine, and bromide from the perovskite layer to the spiro-OMeTAD hole transport layer. In the meanwhile, a MoS_2 HTL buffer layer also prevents the migration of metals (i.e. Au) from electrode to the spiro-OMeTAD layer to the perovskite layer. Furthermore, it also prevented a direct contact between the perovskite and the Au electrode which could occur in solution-processed PSCs due to the incomplete coverage of the perovskite by the HTL. However, a MoS_2 HTL buffer layer is not clear in the elemental mapping because the signal of the Mo and S elements over mapping with other elements seriously.

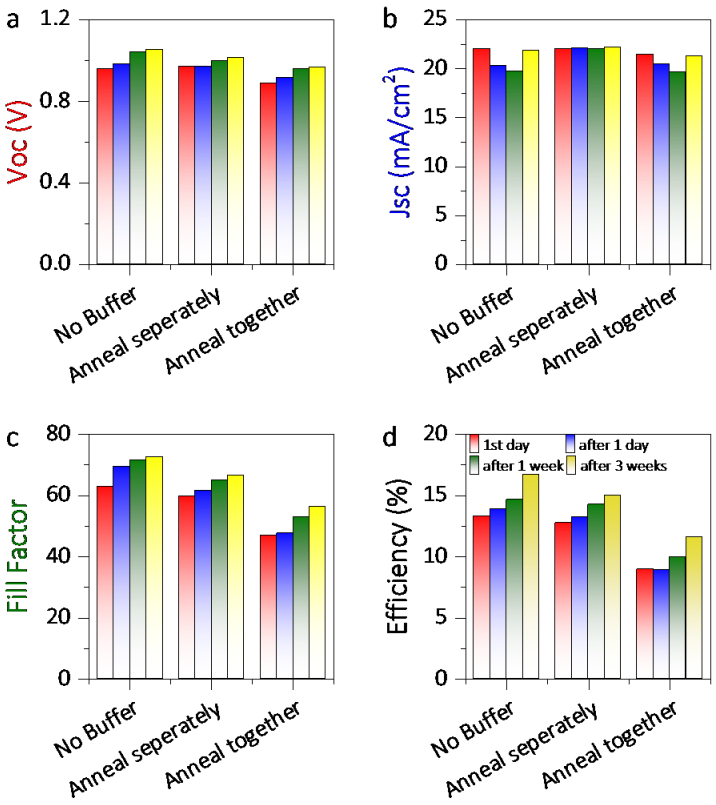

Figure 4.23 (a) V_{oc}, (b) J_{sc}, (c) FF, and (d) efficiency of PSCs with different MoS_2 annealing methods after 1 day, 1 week, and 3 weeks.

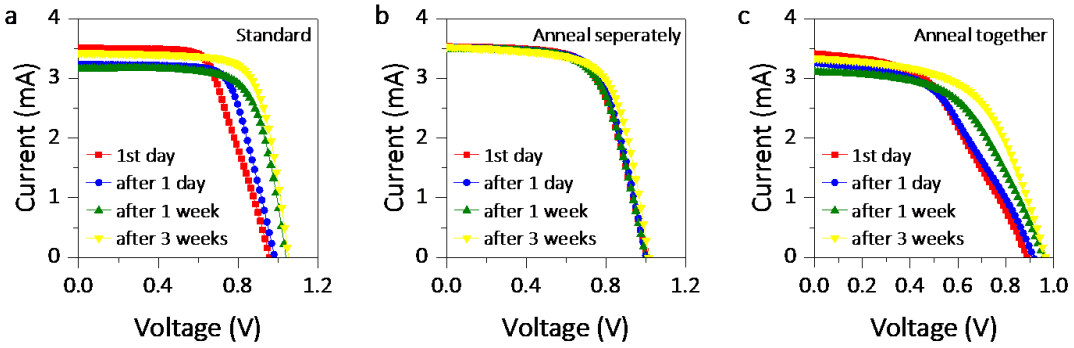

Figure 4.24 Change of I-V curves of PSCs with different MoS_2 annealing approaches after 1 day, 1 week, and 3 weeks.

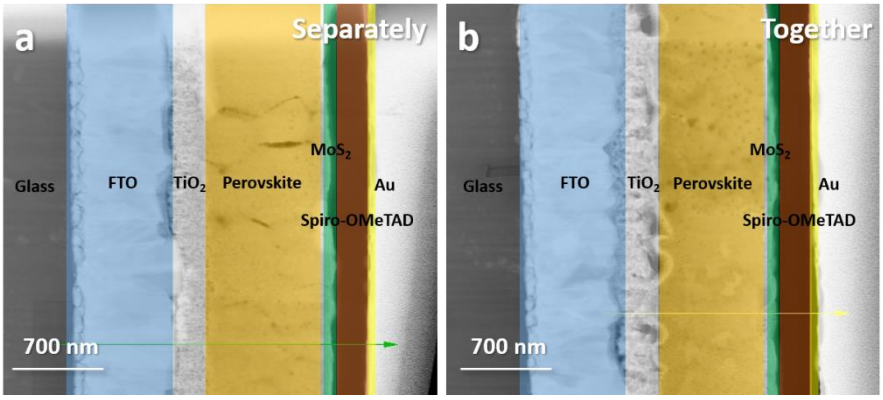

Figure 4.25 Cross-section TEM images of the PSCs with a MoS_2 HTL buffer (a) annealing separately from the perovskite layer and (b) annealing together with the perovskite layer.

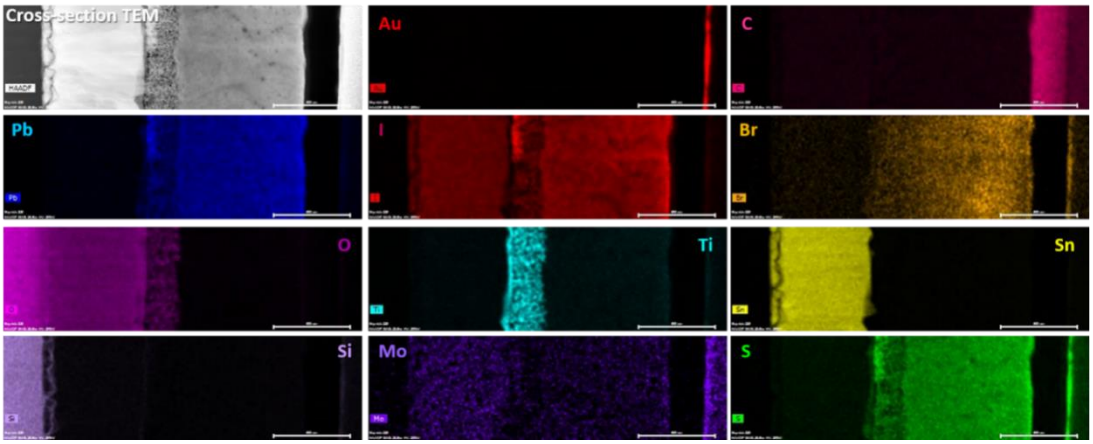

Figure 4.26 Elemental mapping of the PSC with a MoS_2 HTL buffer annealed separately from the perovskite layer.

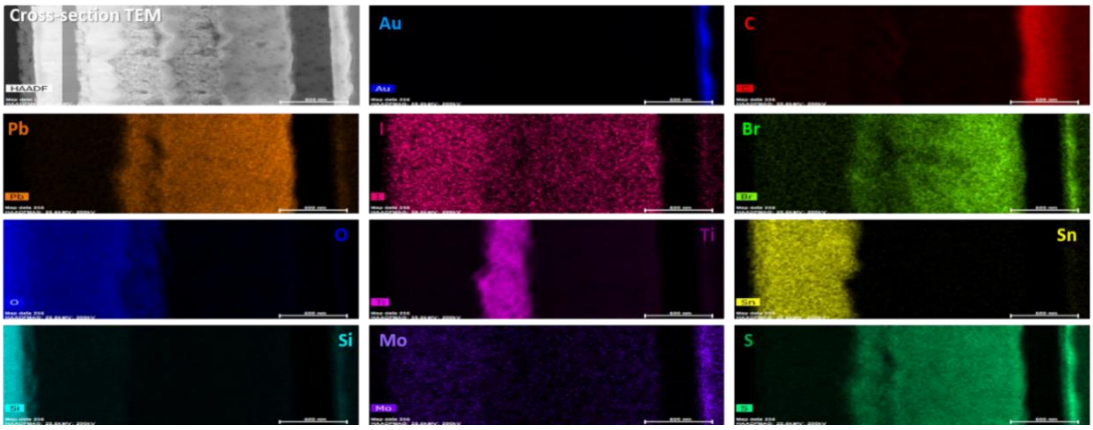

Figure 4.27 Elemental mapping of the PSC with a MoS_2 HTL buffer annealed together with the perovskite layer

To further optimize of the PSC with a MoS_2 HTL buffer layer, annealing time of 2D MoS_2 HTL buffer layer was also studied. According to this study, we found that 1 h is enough to get a good quality 2D MoS_2 buffer layer (Figure 4.28). PCEs of PSCs with different annealing time of 2D MoS_2 HTL buffer layers all increased after one day and one week (Figure 4.29).

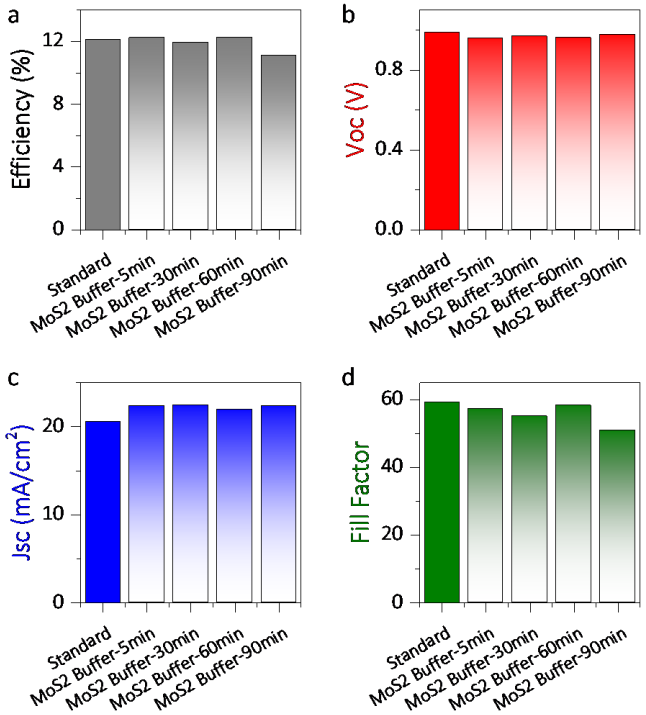

Figure 4.28 (a) Efficiency, (b) V_{oc}, (c) J_{sc}, and (d) FF of PSCs with different MoS_2 annealing time.

According to all these optimisms, we could say that MoS_2 HTL buffer annealed at 100 ℃ for a while after spin coating process could give a good quality PSCs. Compared to the standard PSC, the efficiency of this PSCs adding MoS_2 HTL buffer layer is a little bit lower. However, as mentioned before, the main reason for adding MoS_2 buffer layer is because of the poor stability of the standard PSCs. MoS_2 buffer layer could be a barrier toward the metal electrode migration, and additional energy-matching layer to further ease the hole collection of the spiro-OMeTAD.

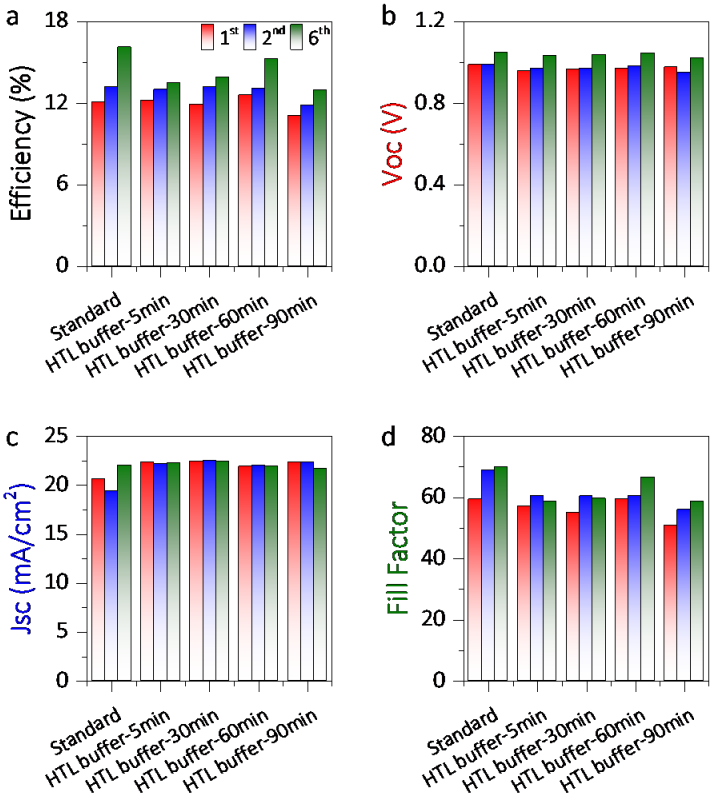

Figure 4.29 (a) Efficiency, (b) V_{oc}, (c) J_{sc}, and (d) FF of PSCs with different MoS_2 annealing time after 1day and 1 week.

Stability test of PSCs with and without MoS_2 HTL buffer layer was conducted. As shown in Figure 4.30, after 55 min standard cell's efficiency dropped 21.8% of initial value while the cell adding MoS_2buffer layer could remain 93.1 % of initial efficiency. The main contribution of it is fill factor. Adding MoS_2 buffer layer could stabilize or even increase fill factor of device so that the stability of the cell could be improved (Figure 4.31).

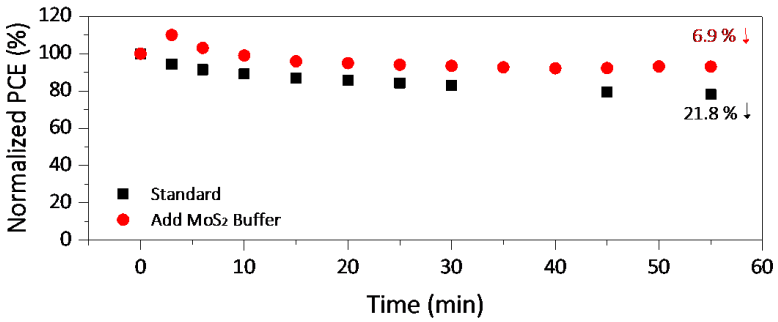

Figure 4.30 Comparison of the stability of PSCs with and without MoS_2 buffer layer.

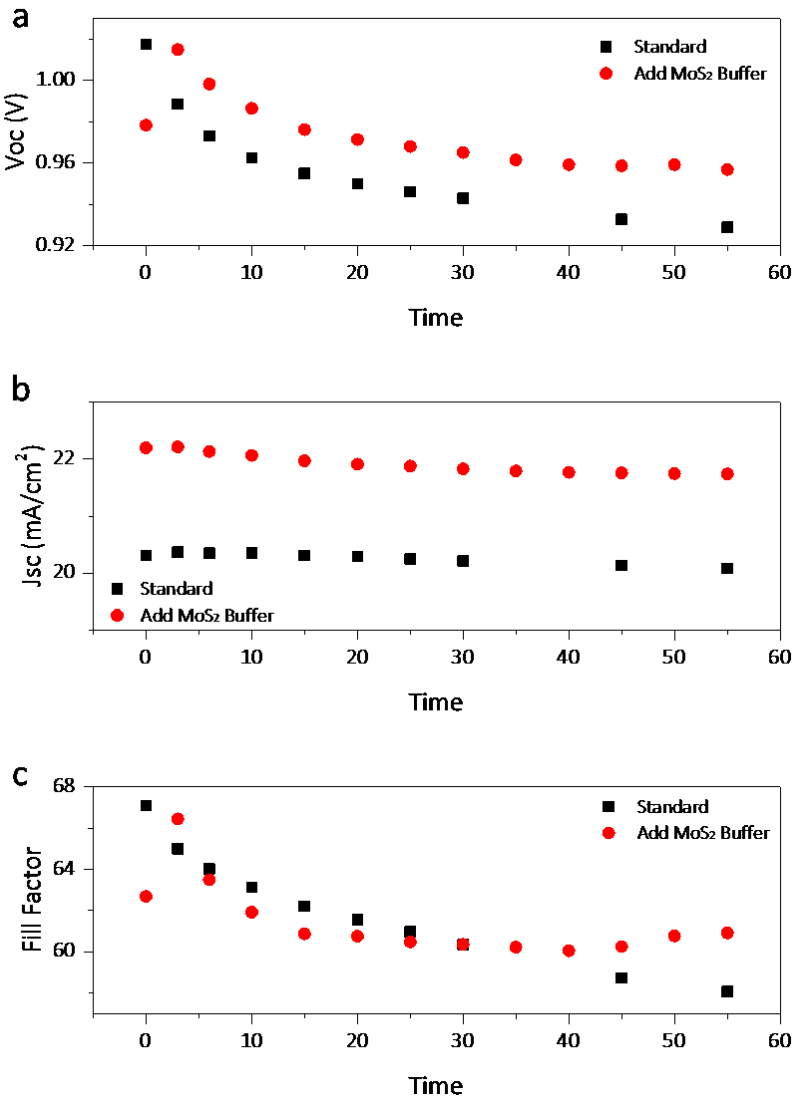

Figure 4.31 Comparison of (a) V_{oc}, (b) J_{sc}, and (c) fill factor of PSCs with and without MoS_2 buffer layer.

Based on previous study, we also tried to see if the increase of the deposition times allows us to get a PSC with better PCE and stability. Same amount of deposition solution (100 μL) and the spin-coating condition (2,000 rpm for 20 s) were applied. But this time we increased the deposition times from one time to three times. Figure 4.32 exhibits the efficiency, V_{oc}, J_{sc}, and FF of the PSCs with different times of deposition of a MoS_2 HTL buffer layer. Here, the MoS_2 HTL buffer layer deposed once, twice and third were labelled as MoS2-1, MoS2-2, MoS2-3, respectively. Increasing the times for deposition led to the increase of the PCE of PSCs. According to Figure 4.32, we can state that this is mainly caused by enhancements of V_{oc} and fill factor of the solar cells. Then, we continued to check the PCE and other factors of these PSCs, and as shown in Figure 4.33, after 3days the PCE of these PSCs with different deposition times became similar (all around 12 ~ 13 %). Therefore, increasing the deposition times for MoS_2 layer doesn't significantly optimize the PCE of the PSCs. In addition, we also tested the stability of these sample cells, according to Figure 4.34, we could confirm that adding a MoS_2 HTL buffer layer enhanced the stability of the PSCs indeed. However, difference between different times of deposition was not apparent. Similar as previous study, a MoS_2 HTL buffer layer helps to maintain the J_{sc} and fill factor which results in better stability of the PSCs (Figure 4.35).

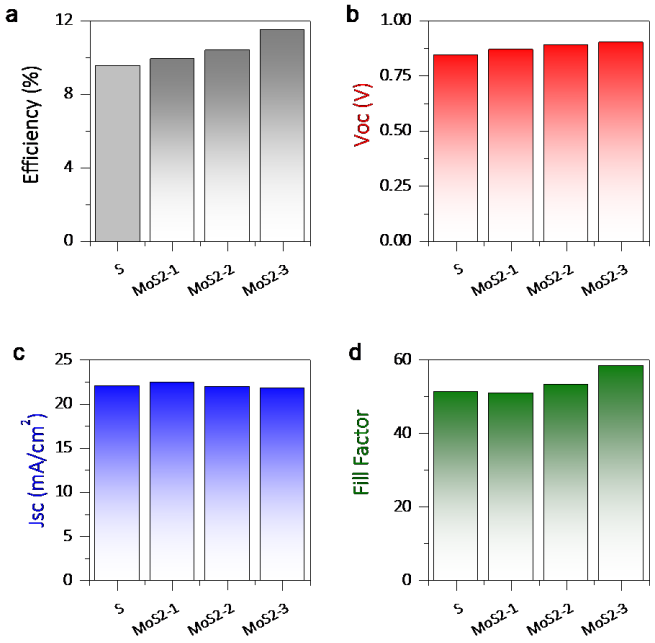

Figure 4.32 (a) Efficiency, (b) V_{oc}, (c) J_{sc}, and (d) FF of PSCs with different times of deposition of a MoS_2 HTL buffer layer.

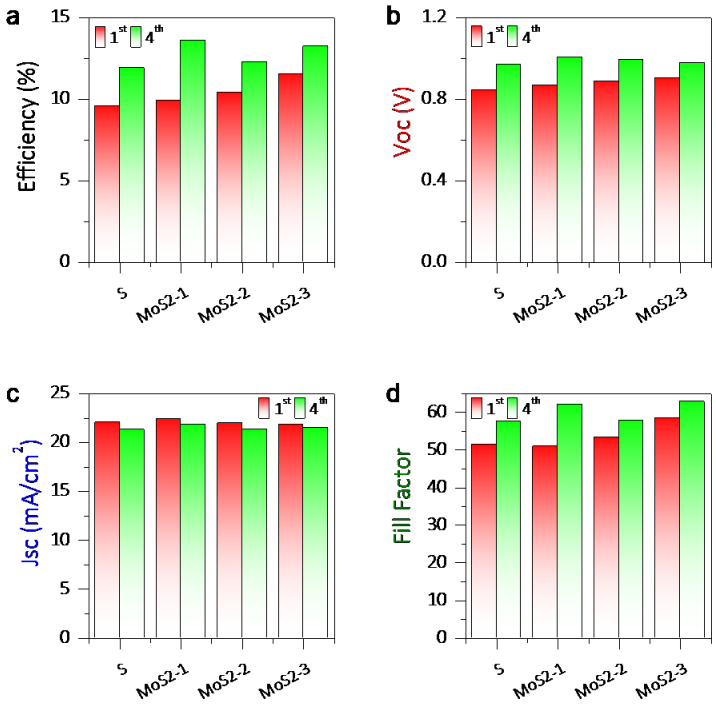

Figure 4.33 (a) Efficiency, (b) V_{oc}, (c) J_{sc}, and (d) FF of PSCs with different times of deposition of a MoS_2 HTL buffer layer. S is the standard PSCs and MoS2-1, MoS2-2, MoS2-3 are PSCs with once, twice, third deposed MoS_2 buffer layer.

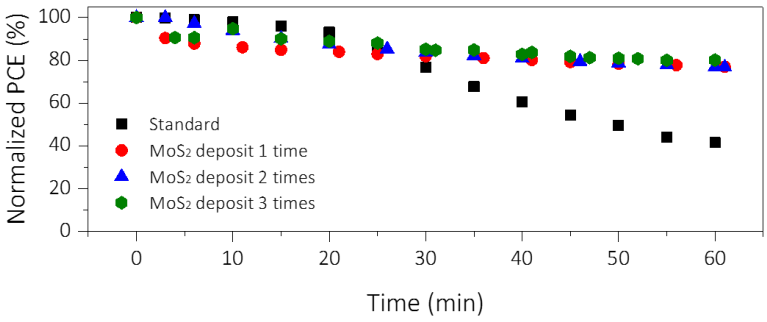

Figure 4.34 Comparison of the normalized efficiency of PSCs with different times of deposition of a MoS_2 HTL buffer layer.

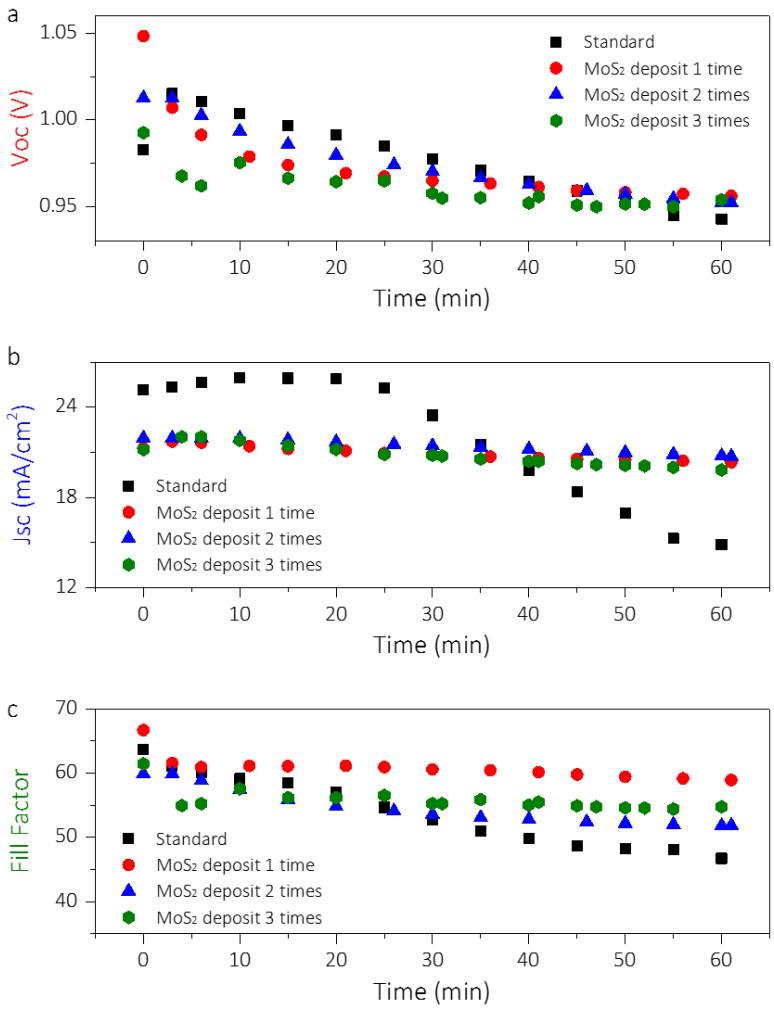

Figure 4.35 Comparison of (a) V_{oc}, (b) J_{sc}, and (c) FF of PSCs with different times of deposition of a MoS_2 HTL buffer layer.

In addition, IV curves of forward and backward scans for the standard PSC and the PSC adding MoS_2 buffer layer are shown in Figure 4.36. No appreciable difference was observed between backward and forward scans for the standard PSC (Figure 4.36a), while J_{sc} increased apparently leading to the increase of PCE for the PSC adding MoS_2 buffer layer (Figure 4.36b). As we know, MoS_2 could accelerate the hole transport, and this probably leads to the increase of the J_{sc}. It is worth to study further and understand the mechanism of it.

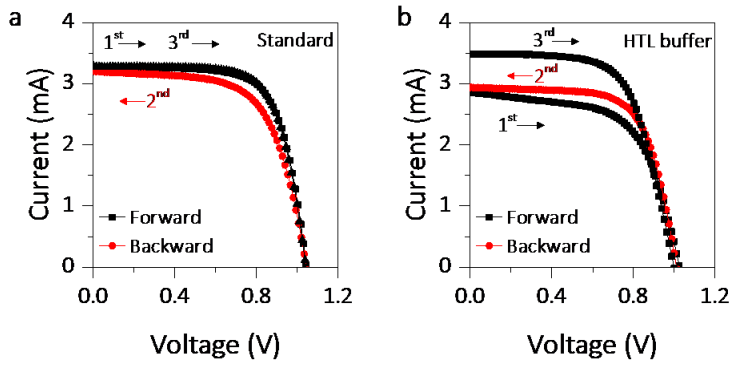

Figure 4.36 Forward and backward scans of (a) standard PSC and (b) the PSC adding MoS_2 HTL buffer.

4.3 Conclusions

This work mainly studied the preparation of 2D TMD nanosheets through the sonication-assisted LPE method and energy application of these 2D materials in solar cell devices. First, a liquid exfoliation process was successfully applied to layered TMD materials. This method is non-destructive, insensitive to air and water and gives defect-free 2D TMDs and further could be scale-up. What's more, through controlling the LPE processing parameters (e.g. centrifuging rate and sonication time) of the exfoliation, nanosheets of different sizes and thicknesses were obtained. As mentioned above, if the number of layer changes, the electronic band structure of TMD will also change. The TMD nanosheets were used to fabricate solar cell devices for energy applications. Three different applications were tried: 1) 2D TMDs as an absorber; 2) 2D TMDs as a HTL of PSCs; 3) 2D TMDs as a buffer layer between perovskite and HTL (spiro-OMeTAD layer) of PSCs.

According to the results, we could know that 2D TMDs obtained *via* LPE method are not suitable to be an active layer of solar cells because of the limitation of reducing of thickness of TMDs. Then, 2D TMDs were tried as a HTL of the PSC. PSCs with TMDs HTL revealed a significant increase in PCE with respect to the cell with no HTL, confirming that the 2D TMDs ease the hole transport and collection at the Au electrode. Based on this knowledge, 2D TMDs were also tried as a buffer layer between perovskite and HTL of the PSC.Adding MoS_2 buffer layer improved the stability of the PSC. Because MoS_2 buffer layer could be a barrier toward the metal electrode migration, and

additional energy-matching layer to further ease the hole collection of the spiro-OMeTAD.

Through this practical, the preparation, size selection and TMD solar cell design and fabrication were mastered, thereby building the foundation for further research. However, there is still a large space to improve the PV performance of these types of solar cells. First, standard PSC should be optimized. For instance, according to the cross-section TEM image of standard PSC in this work, the thickness of perovskite layer is around 900 nm which is much thicker than the other PSCs (300 ~ 400 nm). All PSCs prepared in this work have a ~ 900 nm thickness perovskite layer. Therefore, the thickness of perovskite layer should be optimized to around 350 nm first. There are many approaches that can reduce the thickness of perovskite layer such as reducing the concentration of perovskite solution, increasing the spin-coating speed, and so on. As shown in Figure 4.37, decreasing the concentration of the perovskite solution seems to improve the PCE of the PSCs to some extent. If the concentration of the perovskite precursor is decreased, the thickness of the perovskite layer could become thinner. Therefore, charges generated in thinner perovskite layer could be separated and move to each side faster compared to thick perovskite layer, so PCE of the PSC get improved. Besides, increasing the spin coating speed could also help to decrease the thickness of the perovskite layer of PSCs. According to the simple try, as shown in Figure 4.38, we could see that the increase of the spin coating speed led to the increase of the PCE.

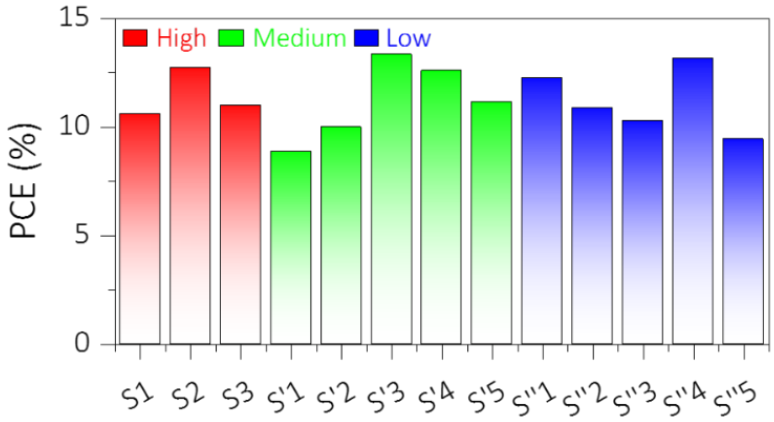

Figure 4.37 PCE of the standard PSCs using different concentrations (high [red], medium [green], and low [blue]) of perovskite precursors.

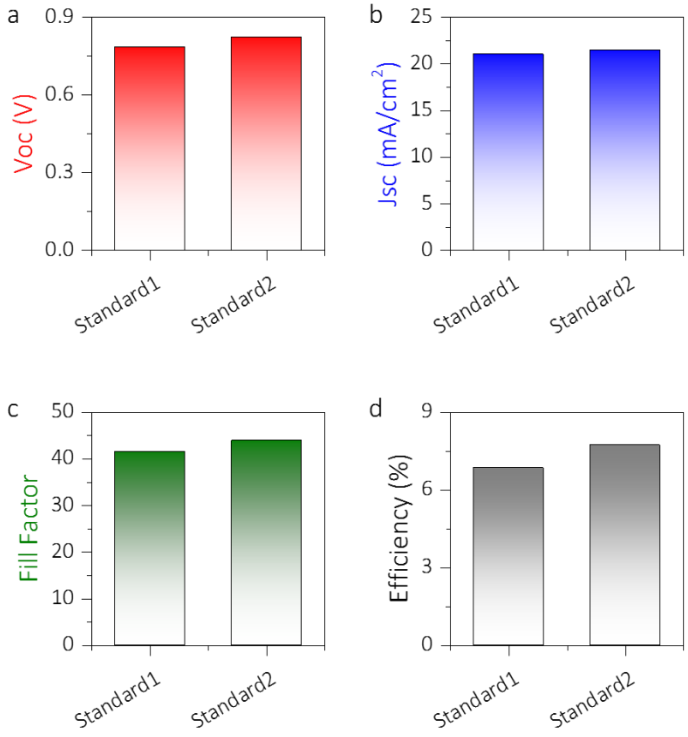

Figure 4.38 PCE of the standard PSCs using different spin coating speeds (standard 1: a two-step programme at 1000 and 4000 rpm for 10 and 30 s, standard 2: a three-step programme at 1000, 4000, and 6000 rpm for 10, 10, 20 s, respectively) to prepare the perovskite layer.

4.4 Experimental methods

4.4.1 Materials

Molybdenum disulfide (MoS_2), molybdenum diselenide ($MoSe_2$), tungsten sulfide (WS_2), gallium (II) sulfide (GaS), gallium (II) selenide (GaSe), and gallium (II) telluride(GaTe) powders and N-Methyl-2-pyrrolidone (NMP), isopropyl alcohol (IPA), hexadecylamine, dodecylamine, used throughout the 2D TMDs preparation experiments were purchased from Sigma Aldrich. The zinc power, hydrochloric acid, titanium diisopropoxide bis(acetylacetonate), lead (II) iodide (PbI_2), lead (II) bromide ($PbBr_2$), formamidinium iodide (FAI), methylammonium bromide (MABr),dimethylformamide (DMF), dimethyl sulfoxide (DMSO), 2,2′,7,7′-tetrakis-(N,N-di-4-

methoxyphenylamino)-9,9′-spirobifluorene (spiro-MeOTAD), chlorobenzene (anhydrous, 99.8 %), 4-tert-butylpyridine (TBP), bis(trifluoromethane) sulfonimide lithium salt and acetonitrile used for solar cell device fabrication were also purchased from Sigma Aldrich.Moreover,tris(2-(1H-pyrazol-1-yl)-4-tert-butylpyridine)cobalt(III)tri[bis(trifluoromethane)sulfonimide] (FK 209 Co(III)TFSI) salt and titanium dioxide pastes and fluorine doped tine oxide(FTO) glass substrates with a sheet resistance of ~8 Ω/sq were provided by Dyesol.

4.4.2 Preparation of 2D transition metal dichalcogenides nanosheets

Here, a typical methodology for the preparation of an exfoliated 2D TMD dispersion is described (as shown in Figure 4.39). In the initial MoS_2 experiments, 4 g of MoS_2 powder were added to 80 mL of NMP, and a probe sonic tip was utilised to sonicate the solution for a certain number of hours (power: 60% amplitude). The sonic tip was pulsed for 6 s on and 2 s off to avoid damage to the processor and reduce solvent heating, and thus, degradation. The beaker was connected to a cooling system that allowed for cold water (5°C) to flow around the dispersion during sonication. It was then centrifuged at different centrifugation rates (500 rpm, 1,000 rpm, 2,000 rpm, 3,000 rpm, 5,000 rpm) for 1 h, and the supernatant was retained (size selection of MoS_2). The same methodology was used to obtain the exfoliated $MoSe_2$ and WS_2 dispersions.

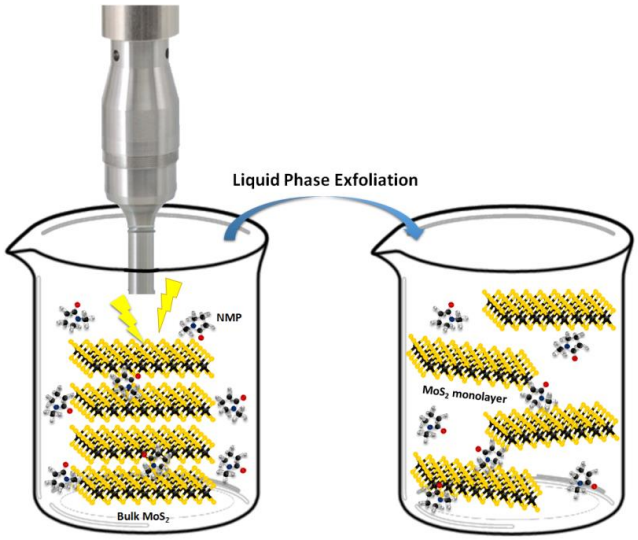

Figure 4.39 Preparation of 2D TMDs nanosheets *via* sonication assisted LPE method.

Then, the exfoliated TMDs nanosheets were transferred from NMP to IPA. Specifically, exfoliated TMDs nanosheets in NMP solvent were centrifuged at high spin rate (10,000 rpm) to obtain the TMDs nanosheets. Then, these TMDs nanosheets were re-dispersed in IPA through bath sonication and exfoliated 2D TMDs nanosheets dispersion in IPA were obtained.

4.4.3 Fabrication of solar cell devices with 2D transition metal dichalcogenides materials

4.4.3.1 2D transition metal dichalcogenides as absorber of solar cells

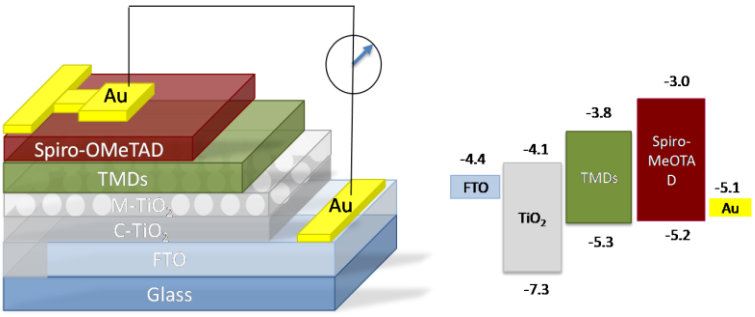

Figure 4.40 Sketch and band energy diagram of the solar cell using 2D TMDs as an active layer.

Firstly, liquid exfoliated 2D TMDs were applied as an absorber of solar cell devices. Figure 4.40 shows the structure and energy band gap of the solar cell with 2D TMDs tried in this work.

Substrate and ETL preparation

Solar cells were fabricated on FTO glass substrates with a sheet resistance of ~8 Ω/sq. The impurities were removed from the FTO-coated substrate *via* a three-step cleaning process (soapy water, deionized (DI) water and isopropanol (IPA) for 15 min each). The back side of the FTO glasses were covered with tapes. One side of the FTO glasses were etched using zinc power and 4 M HCl solution. Then, compact TiO_2 layer was deposited on FTO *via* dip-coating (Figure 4.45a is the photo of dip coater used in

this work) twice and annealing at 200 ˚C for 10 min and 450 ˚C for 30 min, respectively.[252] A precursor dip-coating solution was prepared by mixing 6 mL of titanium diisopropoxidebis(acetylacetonate) (TiAcac) solution with 54 mL of IPA. Then, mesoporous TiO_2 layer was deposited by spin coating for 20 s at 4,000 rpm with a ramp of 2,000 rpm/s, using 30 nm particle Ti paste (mixed titaniumoxide paste [Dyesol 30 NR-D] and ethanol with the ratio of 150 mg : 1 mL). After the spin coating, the substrates were immediately annealed in a hot plate (Figure 4.41b) following the program presented below:

Temp (˚C)	200	325	375	450	500
Time (min)	10	5	5	15	15

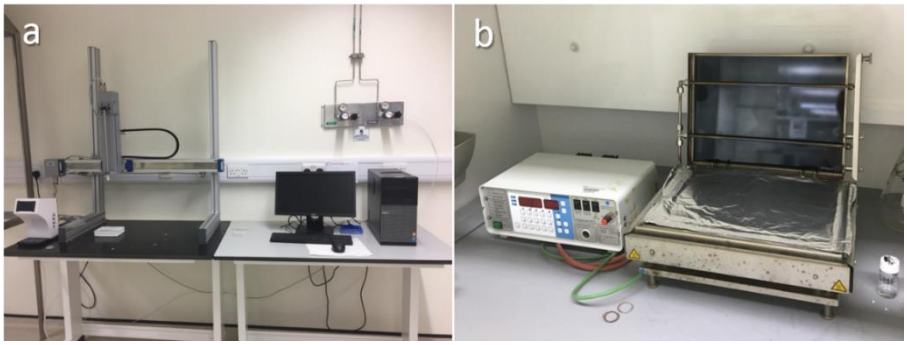

Figure 4.41 Photos of (a) a dip coater and (b) a hot plate.

Deposition of 2D TMDs photoactive layer

For the 2D TMDs absorbing layer, two different methods were tried: spin coating and spray coating approaches (Figure 4.42). Figure 4.43 presents the spin coater and spray printing machine used in this work.

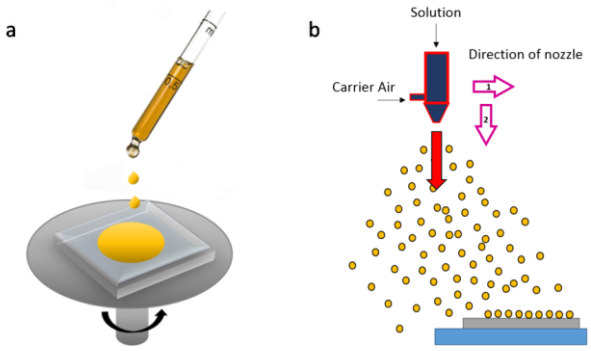

Figure 4.42 (a) Spin coating a TMD layer and (b) spray coating a TMD layer using 2D TMD dispersion.

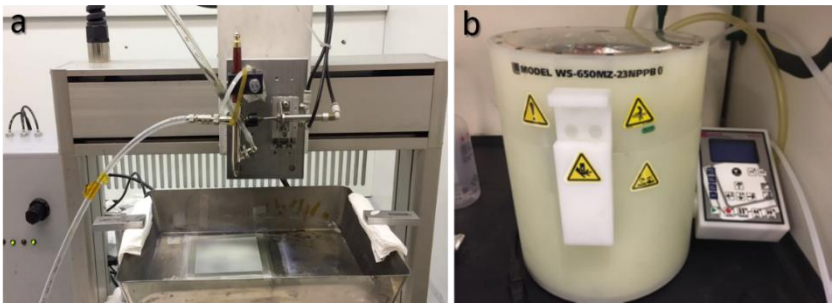

Figure 4.43 Photos of (a) a spray printer and (b) a spin coater.

HTL and top electrode preparation

After the deposition of the 2D TMD layer, a spirofluorene-linked methoxy triphenylamines (spiro-OMeTAD, from Sigma-Aldrich) solution (70 mM in chlorobenzene) was spun at 4,000 rpm. for 20 s. The spiro-OMeTAD was doped with bis(trifluoromethylsulfonyl)imide lithium salt (Li-TFSI, from Sigma-Aldrich), tris(2-(1H-pyrazol-1-yl)-4-tert-butylpyridine)-cobalt(III) tris(bis(trifluoromethylsulfonyl)imide) (FK209, from Sigma-Aldrich) and 4-tert-Butylpyridine (TBP, from Sigma-Aldrich).[253-255] The molar ratio of additives for spiro-OMeTAD was: 0.5, 0.03 and 3.3 for Li-TFSI, FK209 and TBP, respectively. Finally, around 20 nm of gold top electrode, which was used as a current collector, was thermally evaporated under high vacuum (Figure 4.45 is the thermal evaporator used in this study). Figure 4.44 presents the fabrication process of the solar cell based on 2D TMD materials.

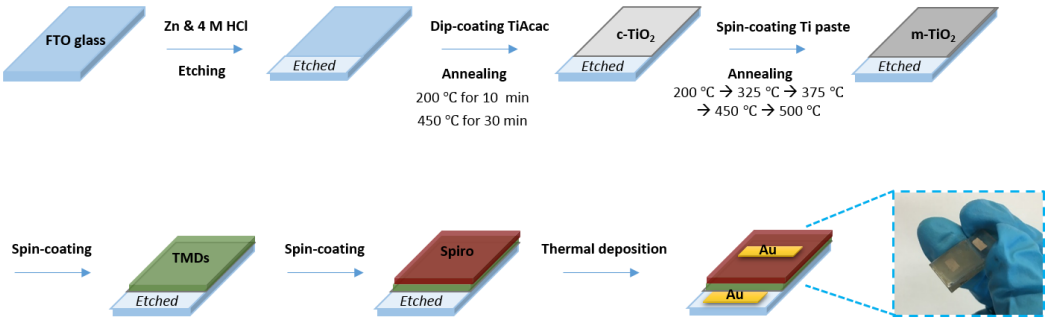

Figure 4.44 2D TMDs based (active layer) solar cell assemble process.

Figure 4.45 Thermal evaporator for Au deposition.

4.4.3.2 2D transition metal chalcogenides as a hole transport layer of the perovskite solar cells

Secondly, liquid exfoliated 2D TMDs were used as a HTL of PSCs (Figure 4.5). Assembly process shows in Figure 4.46. The FTO-coated glass substrate was cleaned and etched (details of them described in previous section "**4.4.3.12D transition metal chalcogenides as absorber of solar cells**"). Then, compact TiO_2 layer and mesoporous TiO_2 layer were deposited as shown in Figure 4.46.

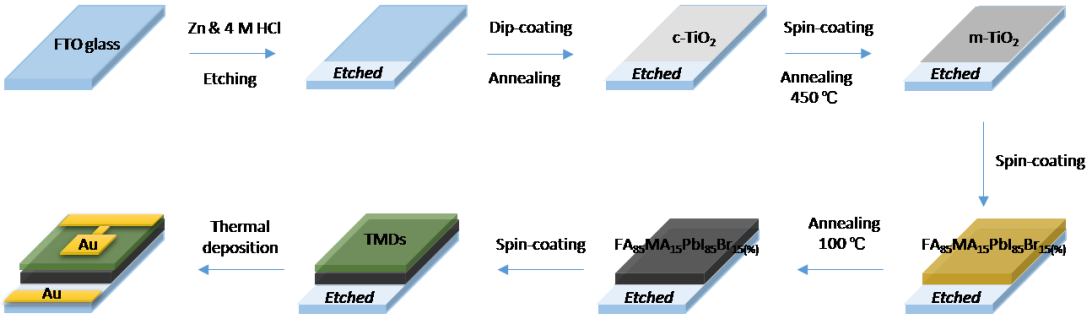

Figure 4.46 Glass / FTO / compact-TiO_2 / mesoporous-TiO_2 / $FA_{85}MA_{15}PbI_{85}Br_{15}$ / 2D TMDs / Au structured PSCs assemble process.

Perovskite precursor solution and film preparation

The perovskite solution was prepared first. Typically, 1.1 mM (508 mg/mL) of PbI_2, 0.183 mM (67.1 mg) of $PbBr_2$, 1.05 mM (180.5 mg) of FAI, and 0.183 mM (20.4 mg) of MABr were dissolved into a mixture of DMF : DMSO (800 µL : 200 µL) solvent. Then, the perovskite solution was spin coated in a two-step programme at 1,000 and 4,000 rpm for 10 and 30 s, respectively. During the second step, 300 µL of chlorobenzene was poured onto the spinning substrate 20 s prior the end of the programme to smooth the film. Finally, the substrate was annealed at 100 ˚C for 1 h in nitrogen-filled glove box (Figure 4.47).

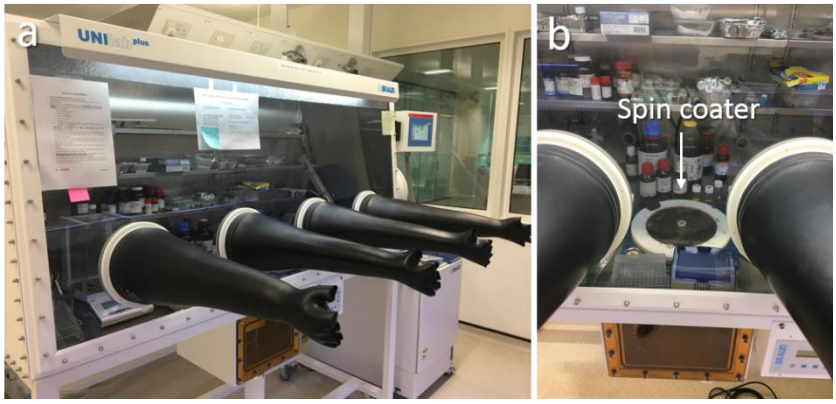

Figure 4.47 (a) Glove box for the preparation of the perovskite layer and (b) spin coater inside the glove box.

4.4.3.3 2D transition metal chalcogenides as a buffer layer of perovskite solar cells

Here, we also tried 2D TMDs as a buffer layer of PSCs to improve the PV performance, especially the stability of the PSCs. Structure and band gaps of the PSCs with a 2D TMD buffer layer shows in Figure 4.48. A 2D TMD layer was added between the perovskite layer (photoactive layer) and the spiro-OMeTAD layer (HTL). Figure 4.49 shows the fabrication process.

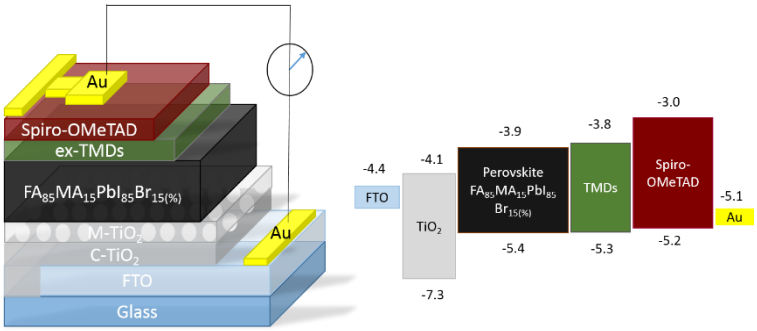

Figure 4.48 Applied 2D TMDs as a buffer layer between the perovskite and spiro-OMeTAD of PSCs.

Treatment of the FTO-coated glass substrate, deposition of ETL, the perovskite layer, HTL and Au contact layer were already described in the previous sections.

Preparation of the 2D TMD buffer layer

As shown in Figure 4.49, three different approaches were tried to prepare the 2D TMD buffer layer. First method is spin coating the 2D TMD layer at 2000 rpm for 20 s without any other treatment. Second and third methods added the heat treatment (100 ˚C for 1 h) after spin coating the 2D TMD dispersion onto the substrate. In the second method, the TMD layer was spin coated and annealed after annealing the perovskite layer at 100 ˚C for 1 h. But in the third method, the TMD layer was annealed together with the perovskite layer at 100 ˚C for 1 h.

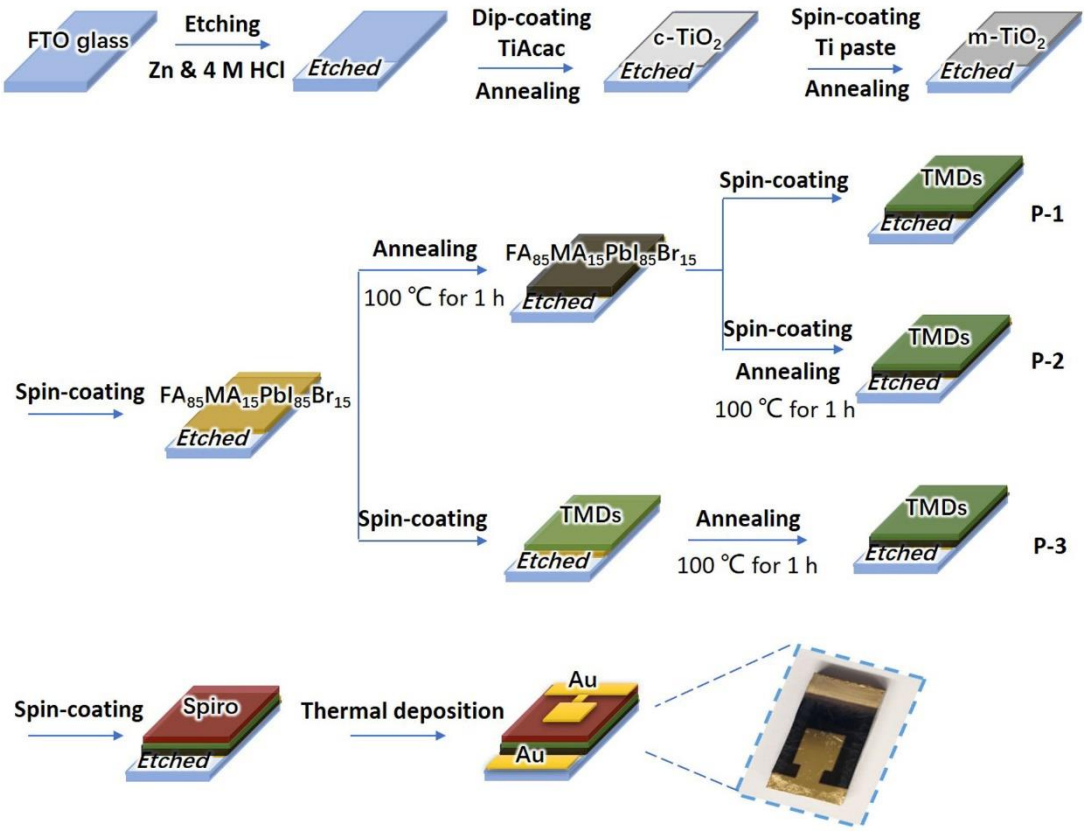

Figure 4.49 Three different method to fabricate the PSCs adding a 2D TMDs buffer layer.

4.4.3.4 Characterization of 2D transition metal chalcogenides and solar cell devices

Several characterization techniques were conducted for the full analysis of the dispersions and solar cell devices. They include the UV-Vis-IR spectroscopy, scanning electron microscopy (SEM), focused ion beam transmission electron microscopy (FIB-TEM), etc.

To investigate the PV performance of the solar cells, current-voltage (I-V) tests were conducted using IV tester (Figure 4.50).

Figure 4.50 IV tester (Newport Corporation)

5 Conclusions and future work

We have demonstrated the liquid phase exfoliation of bulk layered MC and TMD cystals to give few-layered 2D MC and TMD nanosheets, which are further utilized as anode materials of LiBs or new generation solar cells.

First, 2D MC (e.g. GaS, GaSe, GaTe and InSe) nanosheets obtained by LPE method were percolated in SWCNTs networks *via* a colloidal solution processing approachfor flexible anode to store Li. Due to shortened Li^+ diffusion paths and enhanced electron transport kinetics, the binder-free flexible MC-SWCNT composite anodes exhibit a relatively good electrochemical performance, confirming their potential to be used as anode materials for batteries.

Furthermore, according to general comparison of these different 2D MC nanosheets, we found the 2D InSe which synthesized in the lab by wet-chemical synthesis method exhibits a superior electrochemical performance (including high capacity and excellent rate capability) to that of the other 2D MCs. Importantly, the capacity 2D InSe-SWCNT composite increases over prolonged cycling up to 1224 mAh/g from 520 mAh/g, which is believed to largely relate with the reversible alloy reaction, as confirmed by the *in-situ* XRD results. Then, combining with the DFT calculations and post-cycling SEM images, we indicate that the in-situ formed In particles gradually reduce their domain size, forming nanoclusters upon cycling which are capable to accommodate four Li^+ instead of one per atomic In, and leading to extra capacity as increasing the cycling numbers.

Based on this, we also demonstrated the In-SWCNT composite for anodes of LiBs. The electrochemical performances of In-SWCNTs anodes are similar as InSe-SWCNTs electrodes. CV peaks of an In-SWCNTs anode almost matched with an InSe-SWCNTs anode. What's more, the capacity of an In-SWCNTs electrode also gradually improved during charging and discharging cycles. It can further confirm our mechanism and simultaneously show the possibility of In used as an anode material. Such a new "nanoscluster-alloying" Li storage mechanism may shed light on the exploration of other electrochemical materials to build new architectures with excellent performance in LiBs, wearable electronics and smart energy storage devices, to name just a few.

Last, we studied the 2D TMD nanosheets for solar cell devices. Sonication-assisted LPE method produces the high quality few-layered 2D TMD nanosheets. Through controlling the LPE processing parameters, we obtained 2D TMD nanosheets

with different sizes and thicknesses. The resulted 2D TMDs are not suitable to be an active material for solar cell devices due to the limitation of reducing of thickness of TMDs. Therefore, 2D TMDs were tried as a HTL and a HTL buffer layer of solar cells. We demonstrated the use of 2D TMDs as a HTL buffer layer of PSCs (Glass / FTO / compact-TiO_2 / mesoporous-TiO_2 / $FA_{85}MA_{15}PbI_{85}Br_{15}$ / 2D TMDs / Spiro-OMeTAD / Au). 2D TMD nanosheets are exfoliated in IPA *via* sonication-assisted LPE approach. Then, the 2D TMD dispersions are spin-coated onto the perovskite layer and annealed before the deposition of the Spiro-OMeTAD hole transport layer to remove IPA solvent. PCE of the standard PSC dropped to 78.2 % of original value after endurance test of 1 h under solar simulator (AM1.5G including UV) illumination in ambient air. However, when a 2D TMD buffer layer is added between the perovskite layer and HTL (the Spiro-OMeTAD layer), the stability of the PSC improved significantly. PCE of the PSC adding a 2D MoS_2 HTL buffer layer could maintain 93.1 % of initial PCE after 1 h of illumination. Adding a 2D MoS_2 nanoflakes HTL buffer layer into the PSCs structure could efficiently enhance the stability of the PSCs, boosting further development of PSCs in view of their commercialization.

Besides, 2D materials for a buffer layer between ETL and perovskite layer are also worth to be investigated. Then, this can be combined with TMD HTL buffer layer to sandwich the perovskite layer which probably produce a more stable PSC. Among the huge groups of 2D materials, 2D MCs has a great potential as ETL buffer layer of PSCs. Furthermore, 2D MCs also can be easily obtained by LPE approach. Here, we liquid exfoliated three different MCs (GaS, GaSe, and GaTe) (Figure 5.1) and tested them as an ETL buffer of PSCs. As shown in Figure 5.2 and Figure 5.3, these MC materials seem to be promising as an ETL buffer. But in order to confirm it, more experiments should be conducted.

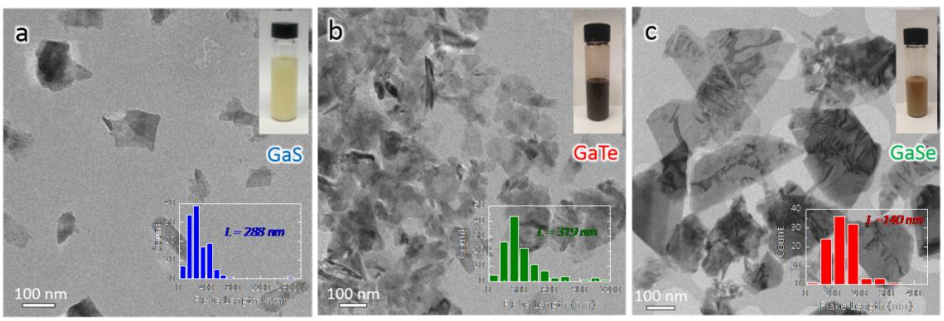

Figure 5.1 (a) 2D GaS, (b) 2D GaTe, and (c) 2D GaSe prepared by LPE method.

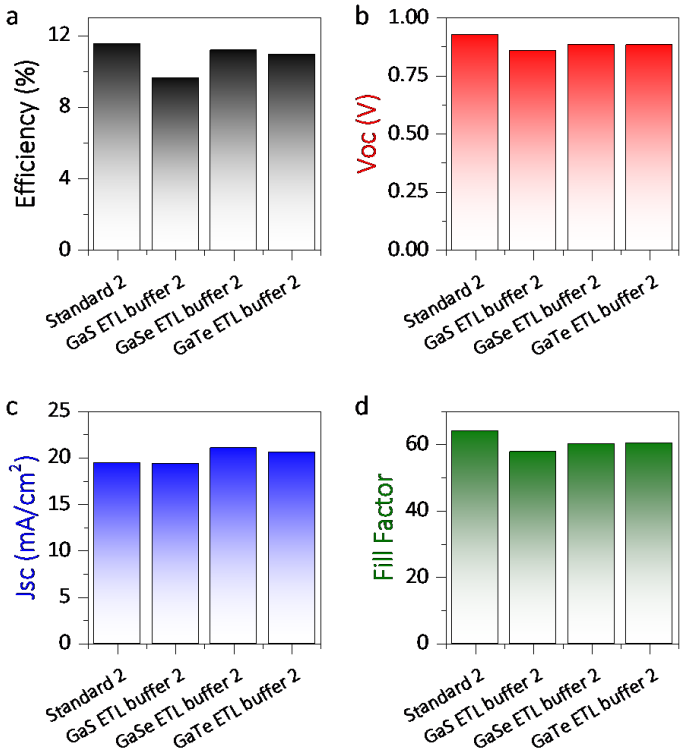

Figure 5.2 (a) efficiency, (b) V_{oc}, (c) J_{sc}, and (d) FF of PSCs adding MC (GaS, GaSe, and GaTe) ETL buffers.

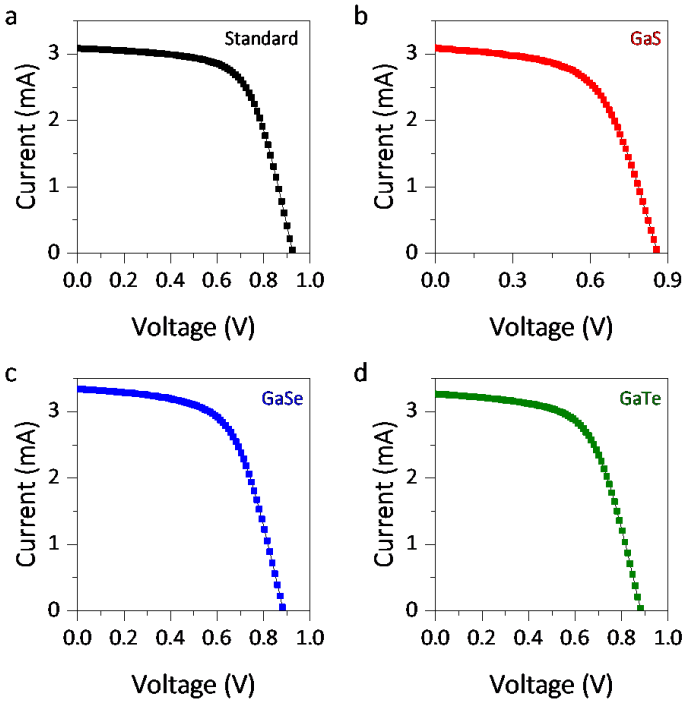

Figure 5.3 IV curves of (a) standard PSC, and PSCs adding (b) GaS, (c) GaSe, and (d) GaTe ETL buffers.

Based on the study of a 2D TMDs HTL buffer layer and a 2D MC ETL buffer, we could stabilize the PSC sandwiched by two buffers (Figure 5.4). If we could solve the poor stability of PSCs, it could give them possibility to be commercialized and compete with silicon-based solar cells in PV market.

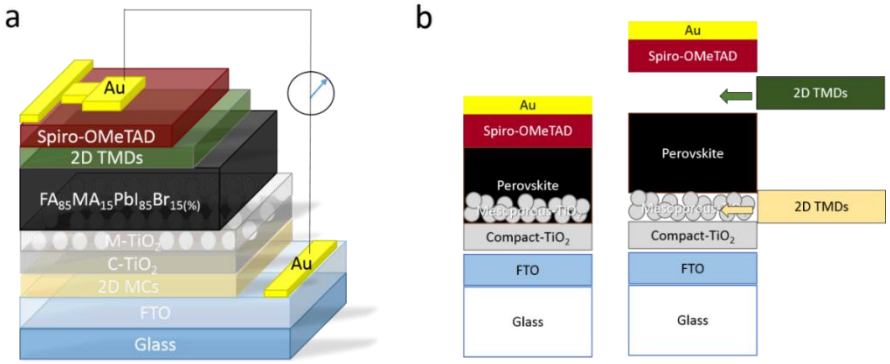

Figure 5.4 Structure design of the PSC sandwiched by two different buffer layers.

6 References

1. Novoselov, K. S.; Geim, A. K.; Morozov, S. V.; Jiang, D.; Zhang, Y.; Dubonos, S. V.; Grigorieva, I. V.; Firsov, A. A., Electric Field Effect in Atomically Thin Carbon Films. *Science* **2004,** *306* (5696), 666-669.

2. Novoselov, K. S.; Falʹko, V. I.; Colombo, L.; Gellert, P. R.; Schwab, M. G.; Kim, K., A roadmap for graphene. *Nature* **2012,** *490* (7419), 192-200.

3. Weiss, N. O.; Zhou, H.; Liao, L.; Liu, Y.; Jiang, S.; Huang, Y.; Duan, X., Graphene: An Emerging Electronic Material (Adv. Mater. 43/2012). *Adv. Mater.* **2012,** *24* (43), 5776-5776.

4. Wang, Q. H.; Kalantar-Zadeh, K.; Kis, A.; Coleman, J. N.; Strano, M. S., Electronics and optoelectronics of two-dimensional transition metal dichalcogenides. *Nat. Nanotechnol.* **2012,** *7* (11), 699-712.

5. Geim, A. K.; Grigorieva, I. V., Van der Waals heterostructures. *Nature* **2013,** *499* (7459), 419-425.

6. Lin, Y.; Williams, T. V.; Connell, J. W., Soluble, Exfoliated Hexagonal Boron Nitride Nanosheets. *J. Phys. Chem. Lett.* **2010,** *1* (1), 277-283.

7. Chhowalla, M.; Shin, H. S.; Eda, G.; Li, L.-J.; Loh, K. P.; Zhang, H., The chemistry of two-dimensional layered transition metal dichalcogenide nanosheets. *Nat. Chem.* **2013,** *5* (4), 263-275.

8. Huang, X.; Zeng, Z.; Zhang, H., Metal dichalcogenide nanosheets: preparation, properties and applications. *Chem. Soc. Rev.* **2013,** *42* (5), 1934-1946.

9. Xu, M.; Liang, T.; Shi, M.; Chen, H., Graphene-Like Two-Dimensional Materials. *Chem. Rev.* **2013,** *113* (5), 3766-3798.

10. Osada, M.; Sasaki, T., Exfoliated oxide nanosheets: new solution to nanoelectronics. *J. Mater. Chem.* **2009,** *19* (17), 2503-2511.

11. Wang, Q.; O'Hare, D., Recent Advances in the Synthesis and Application of Layered Double Hydroxide (LDH) Nanosheets. *Chem. Rev.* **2012,** *112* (7), 4124-4155.

12. Zhang, H., Ultrathin Two-Dimensional Nanomaterials. *ACS Nano* **2015,** *9* (10), 9451-9469.

13. Zeng, Z.; Yin, Z.; Huang, X.; Li, H.; He, Q.; Lu, G.; Boey, F.; Zhang, H., Single-Layer Semiconducting Nanosheets: High-Yield Preparation and Device Fabrication. *Angew. Chem. Int.* **2011,** *50* (47), 11093-11097.

14. Coleman, J. N.; Lotya, M.; O'Neill, A.; Bergin, S. D.; King, P. J.; Khan, U.; Young, K.; Gaucher, A.; De, S.; Smith, R. J.; Shvets, I. V.; Arora, S. K.; Stanton, G.; Kim, H.-Y.; Lee, K.; Kim, G. T.; Duesberg, G. S.; Hallam, T.; Boland, J. J.; Wang, J. J.; Donegan, J. F.; Grunlan, J. C.; Moriarty, G.; Shmeliov, A.; Nicholls, R. J.; Perkins, J. M.; Grieveson, E. M.; Theuwissen, K.; McComb, D. W.; Nellist, P. D.; Nicolosi, V., Two-Dimensional Nanosheets Produced by Liquid Exfoliation of Layered Materials. *Science* **2011,** *331* (6017), 568-571.

15. Zeng, Z.; Sun, T.; Zhu, J.; Huang, X.; Yin, Z.; Lu, G.; Fan, Z.; Yan, Q.; Hng, H. H.; Zhang, H., An Effective Method for the Fabrication of Few-Layer-Thick Inorganic Nanosheets. *Angew. Chem. Int.* **2012,** *51* (36), 9052-9056.

16. Yin, Z.; Li, H.; Li, H.; Jiang, L.; Shi, Y.; Sun, Y.; Lu, G.; Zhang, Q.; Chen, X.; Zhang, H., Single-Layer MoS2 Phototransistors. *ACS Nano* **2012,** *6* (1), 74-80.

17. Splendiani, A.; Sun, L.; Zhang, Y.; Li, T.; Kim, J.; Chim, C.-Y.; Galli, G.; Wang, F., Emerging Photoluminescence in Monolayer MoS2. *Nano Lett.* **2010,** *10* (4), 1271-1275.

18. Zhang, Y.; Ye, J.; Matsuhashi, Y.; Iwasa, Y., Ambipolar MoS2 Thin Flake Transistors. *Nano Lett.* **2012,** *12* (3), 1136-1140.

19. He, Q.; Zeng, Z.; Yin, Z.; Li, H.; Wu, S.; Huang, X.; Zhang, H., Fabrication of Flexible MoS2 Thin-Film Transistor Arrays for Practical Gas-Sensing Applications. *Small* **2012,** *8* (19), 2994-2999.

20. Zhang, C.; Park, S.-H.; Ronan, O.; Harvey, A.; Seral-Ascaso, A.; Lin, Z.; McEvoy, N.; Boland, C. S.; Berner, N. C.; Duesberg, G. S.; Rozier, P.; Coleman, J. N.; Nicolosi, V., Enabling Flexible Heterostructures for Li-Ion Battery Anodes Based on Nanotube and Liquid-Phase Exfoliated 2D Gallium Chalcogenide Nanosheet Colloidal Solutions. *Small* **2017,** *13* (34), 1701677.

21. Duan, X.; Wang, C.; Pan, A.; Yu, R.; Duan, X., Two-dimensional transition metal dichalcogenides as atomically thin semiconductors: opportunities and challenges. *Chem. Soc. Rev.* **2015,** *44* (24), 8859-8876.

22. Radisavljevic, B.; Radenovic, A.; Brivio, J.; Giacometti, V.; Kis, A., Single-layer MoS2 transistors. *Nat. Nanotechnol.* **2011,** *6* (3), 147-150.

23. Nourbakhsh, A.; Zubair, A.; Sajjad, R. N.; Tavakkoli K. G, A.; Chen, W.; Fang, S.; Ling, X.; Kong, J.; Dresselhaus, M. S.; Kaxiras, E.; Berggren, K. K.; Antoniadis, D.; Palacios, T., MoS2 Field-Effect Transistor with Sub-10 nm Channel Length. *Nano Lett.* **2016,** *16* (12), 7798-7806.

24. Zhang, W.; Huang, Z.; Zhang, W.; Li, Y., Two-dimensional semiconductors with possible high room temperature mobility. *Nano Res.* **2014,** *7* (12), 1731-1737.

25. Jariwala, D.; Sangwan, V. K.; Lauhon, L. J.; Marks, T. J.; Hersam, M. C., Emerging Device Applications for Semiconducting Two-Dimensional Transition Metal Dichalcogenides. *ACS Nano* **2014,** *8* (2), 1102-1120.

26. Xia, F.; Wang, H.; Xiao, D.; Dubey, M.; Ramasubramaniam, A., Two-dimensional material nanophotonics. *Nat. Photonics* **2014,** *8* (12), 899-907.

27. Mak, K. F.; Shan, J., Photonics and optoelectronics of 2D semiconductor transition metal dichalcogenides. *Nat. Photonics* **2016,** *10* (4), 216-226.

28. Rahman, M.; Davey, K.; Qiao, S.-Z., Advent of 2D Rhenium Disulfide (ReS2): Fundamentals to Applications. *Adv. Funct. Mater.* **2017,** *27* (10), 1606129.

29. Lin, Z.; McCreary, A.; Briggs, N.; Subramanian, S.; Zhang, K.; Sun, Y.; Li, X.; Borys, N. J.; Yuan, H.; Fullerton-Shirey, S. K.; Chernikov, A.; Zhao, H.; McDonnell, S.; Lindenberg, A. M.; Xiao, K.; LeRoy, B. J.; Drndić, M.; Hwang, J. C. M.; Park, J.; Chhowalla, M.; Schaak, R. E.; Javey, A.; Hersam, M. C.; Robinson, J.; Terrones, M., 2D materials advances: from large scale synthesis and controlled heterostructures to improved characterization techniques, defects and applications. *2D Mater.* **2016,** *3* (4), 042001.

30. Wang, J.; Wei, Y.; Li, H.; Huang, X.; Zhang, H., Crystal phase control in two-dimensional materials. *Sci. China Chem.* **2018,** *61* (10), 1227-1242.

31. Clarke, R.; Marseglia, E.; Hughes, H. P., A low-temperature structural phase transition in β-MoTe2. *Philos. Mag. B* **1978,** *38* (2), 121-126.

32. Duerloo, K.-A. N.; Li, Y.; Reed, E. J., Structural phase transitions in two-dimensional Mo- and W-dichalcogenide monolayers. *Nat. Commun.* **2014,** *5* (1), 4214.

33. Li, Y.; Duerloo, K.-A. N.; Wauson, K.; Reed, E. J., Structural semiconductor-to-semimetal phase transition in two-dimensional materials induced by electrostatic gating. *Nat. Commun.* **2016,** *7* (1), 10671.

34. Xia, J.; Li, D.-F.; Zhou, J.-D.; Yu, P.; Lin, J.-H.; Kuo, J.-L.; Li, H.-B.; Liu, Z.; Yan, J.-X.; Shen, Z.-X., Pressure-Induced Phase Transition in Weyl Semimetallic WTe2. *Small* **2017,** *13* (40), 1701887.

35. Yoo, E.; Kim, J.; Hosono, E.; Zhou, H.-s.; Kudo, T.; Honma, I., Large Reversible Li Storage of Graphene Nanosheet Families for Use in Rechargeable Lithium Ion Batteries. *Nano Lett.* **2008,** *8* (8), 2277-2282.

36. Zhu, J.; Yang, D.; Yin, Z.; Yan, Q.; Zhang, H., Graphene and Graphene-Based Materials for Energy Storage Applications. *Small* **2014,** *10* (17), 3480-3498.

37. Xu, Y.; Chen, C.-Y.; Zhao, Z.; Lin, Z.; Lee, C.; Xu, X.; Wang, C.; Huang, Y.; Shakir, M. I.; Duan, X., Solution Processable Holey Graphene Oxide and Its Derived Macrostructures for High-Performance Supercapacitors. *Nano Lett.* **2015,** *15* (7), 4605-4610.

38. El-Kady, M. F.; Strong, V.; Dubin, S.; Kaner, R. B., Laser Scribing of High-Performance and Flexible Graphene-Based Electrochemical Capacitors. *Science* **2012,** *335* (6074), 1326-1330.

39. Yang, X.; Cheng, C.; Wang, Y.; Qiu, L.; Li, D., Liquid-Mediated Dense Integration of Graphene Materials for Compact Capacitive Energy Storage. *Science* **2013,** *341* (6145), 534-537.

40. Gao, S.; Sun, Y.; Lei, F.; Liang, L.; Liu, J.; Bi, W.; Pan, B.; Xie, Y., Ultrahigh Energy Density Realized by a Single-Layer β-Co(OH)2 All-Solid-State Asymmetric Supercapacitor. *Angew. Chem. Int.* **2014,** *53* (47), 12789-12793.

41. Cao, X.; Shi, Y.; Shi, W.; Rui, X.; Yan, Q.; Kong, J.; Zhang, H., Preparation of MoS2-Coated Three-Dimensional Graphene Networks for High-Performance Anode Material in Lithium-Ion Batteries. *Small* **2013,** *9* (20), 3433-3438.

42. Sun, Y.; Gao, S.; Xie, Y., Atomically-thick two-dimensional crystals: electronic structure regulation and energy device construction. *Chemical Society Reviews* **2014,** *43* (2), 530-546.

43. Peng, X.; Peng, L.; Wu, C.; Xie, Y., Two dimensional nanomaterials for flexible supercapacitors. *Chem. Soc. Rev.* **2014,** *43* (10), 3303-3323.

44. Acerce, M.; Voiry, D.; Chhowalla, M., Metallic 1T phase MoS2 nanosheets as supercapacitor electrode materials. *Nat. Nanotechnol.* **2015,** *10* (4), 313-318.

45. Gu, X.; Cui, W.; Li, H.; Wu, Z.; Zeng, Z.; Lee, S.-T.; Zhang, H.; Sun, B., A Solution-Processed Hole Extraction Layer Made from Ultrathin MoS2 Nanosheets for Efficient Organic Solar Cells. *Adv. Energy Mater.* **2013,** *3* (10), 1262-1268.

46. Lukatskaya, M. R.; Mashtalir, O.; Ren, C. E.; Dall'Agnese, Y.; Rozier, P.; Taberna, P. L.; Naguib, M.; Simon, P.; Barsoum, M. W.; Gogotsi, Y., Cation Intercalation and High Volumetric Capacitance of Two-Dimensional Titanium Carbide. *Science* **2013,** *341* (6153), 1502-1505.

47. Wu, C.; Lu, X.; Peng, L.; Xu, K.; Peng, X.; Huang, J.; Yu, G.; Xie, Y., Two-dimensional vanadyl phosphate ultrathin nanosheets for high energy density and flexible pseudocapacitors. *Nat. Commun.* **2013,** *4* (1), 2431.

48. Kang, J.; Tongay, S.; Zhou, J.; Li, J.; Wu, J., Band offsets and heterostructures of two-dimensional semiconductors. *Appl. Phys. Lett.* **2013,** *102* (1), 012111.

49. Hu, P.; Wang, L.; Yoon, M.; Zhang, J.; Feng, W.; Wang, X.; Wen, Z.; Idrobo, J. C.; Miyamoto, Y.; Geohegan, D. B.; Xiao, K., Highly Responsive Ultrathin GaS Nanosheet Photodetectors on Rigid and Flexible Substrates. *Nano Lett.* **2013,** *13* (4), 1649-1654.

50. Late, D. J.; Liu, B.; Matte, H. S. S. R.; Rao, C. N. R.; Dravid, V. P., Rapid Characterization of Ultrathin Layers of Chalcogenides on SiO2/Si Substrates. *Adv. Funct. Mater.* **2012,** *22* (9), 1894-1905.

51. Jie, W.; Chen, X.; Li, D.; Xie, L.; Hui, Y. Y.; Lau, S. P.; Cui, X.; Hao, J., Layer-Dependent Nonlinear Optical Properties and Stability of Non-Centrosymmetric Modification in Few-Layer GaSe Sheets. *Angew. Chem. Int.* **2015,** *54* (4), 1185-1189.

52. Yuan, X.; Tang, L.; Liu, S.; Wang, P.; Chen, Z.; Zhang, C.; Liu, Y.; Wang, W.; Zou, Y.; Liu, C.; Guo, N.; Zou, J.; Zhou, P.; Hu, W.; Xiu, F., Arrayed van der Waals Vertical Heterostructures Based on 2D GaSe Grown by Molecular Beam Epitaxy. *Nano Lett.* **2015,** *15* (5), 3571-3577.

53. Hu, P.; Wen, Z.; Wang, L.; Tan, P.; Xiao, K., Synthesis of Few-Layer GaSe Nanosheets for High Performance Photodetectors. *ACS Nano* **2012,** *6* (7), 5988-5994.

54. Liu, F.; Shimotani, H.; Shang, H.; Kanagasekaran, T.; Zólyomi, V.; Drummond, N.; Fal'ko, V. I.; Tanigaki, K., High-Sensitivity Photodetectors Based on Multilayer GaTe Flakes. *ACS Nano* **2014,** *8* (1), 752-760.

55. Yuan, X.; Tang, L.; Wang, P.; Chen, Z.; Zou, Y.; Su, X.; Zhang, C.; Liu, Y.; Wang, W.; Liu, C.; Chen, F.; Zou, J.; Zhou, P.; Hu, W.; Xiu, F., Wafer-scale arrayed p-n junctions based on few-layer epitaxial GaTe. *Nano Res.* **2015,** *8* (10), 3332-3341.

56. Wang, Z.; Safdar, M.; Mirza, M.; Xu, K.; Wang, Q.; Huang, Y.; Wang, F.; Zhan, X.; He, J., High-performance flexible photodetectors based on GaTe nanosheets. *Nanoscale* **2015,** *7* (16), 7252-7258.

57. Feng, W.; Zhou, X.; Tian, W. Q.; Zheng, W.; Hu, P., Performance improvement of multilayer InSe transistors with optimized metal contacts. *Phys. Chem. Chem. Phys.* **2015,** *17* (5), 3653-3658.

58. Chen, Z.; Biscaras, J.; Shukla, A., A high performance graphene/few-layer InSe photo-detector. *Nanoscale* **2015,** *7* (14), 5981-5986.

59. Mudd, G. W.; Molas, M. R.; Chen, X.; Zólyomi, V.; Nogajewski, K.; Kudrynskyi, Z. R.; Kovalyuk, Z. D.; Yusa, G.; Makarovsky, O.; Eaves, L.; Potemski, M.; Fal'ko, V. I.; Patanè, A., The direct-to-indirect band gap crossover in two-dimensional van der Waals Indium Selenide crystals. *Sci. Rep.* **2016,** *6* (1), 39619.

60. Cho, S.; Kim, S.; Kim, J. H.; Zhao, J.; Seok, J.; Keum, D. H.; Baik, J.; Choe, D.-H.; Chang, K. J.; Suenaga, K.; Kim, S. W.; Lee, Y. H.; Yang, H., Phase patterning for ohmic homojunction contact in MoTe₂. *Science* **2015,** *349* (6248), 625-628.

61. Zhou, W.; Guo, Y.; Liu, J.; Wang, F. Q.; Li, X.; Wang, Q., 2D SnSe-based vdW heterojunctions: tuning the Schottky barrier by reducing Fermi level pinning. *Nanoscale* **2018,** *10* (28), 13767-13772.

62. Kouser, S.; Thannikoth, A.; Gupta, U.; Waghmare, U. V.; Rao, C. N. R., 2D-GaS as a Photocatalyst for Water Splitting to Produce H2. *Small* **2015,** *11* (36), 4723-4730.

63. Zhang, Y.; Chang, T.-R.; Zhou, B.; Cui, Y.-T.; Yan, H.; Liu, Z.; Schmitt, F.; Lee, J.; Moore, R.; Chen, Y.; Lin, H.; Jeng, H.-T.; Mo, S.-K.; Hussain, Z.; Bansil, A.;

Shen, Z.-X., Direct observation of the transition from indirect to direct bandgap in atomically thin epitaxial MoSe2. *Nat. Nanotechnol.* **2014,** *9* (2), 111-115.

64. Ambrosi, A.; Sofer, Z.; Pumera, M., 2H → 1T phase transition and hydrogen evolution activity of MoS2, MoSe2, WS2 and WSe2 strongly depends on the MX2 composition. *Chem. Commun.* **2015,** *51* (40), 8450-8453.

65. Novoselov, K. S.; Castro Neto, A. H., Two-dimensional crystals-based heterostructures: materials with tailored properties. *Phys. Scr.* **2012,** *T146*, 014006.

66. Zhan, Y.; Liu, Z.; Najmaei, S.; Ajayan, P. M.; Lou, J., Large-Area Vapor-Phase Growth and Characterization of MoS2 Atomic Layers on a SiO2 Substrate. *Small* **2012,** *8* (7), 966-971.

67. Lin, Y.-C.; Zhang, W.; Huang, J.-K.; Liu, K.-K.; Lee, Y.-H.; Liang, C.-T.; Chu, C.-W.; Li, L.-J., Wafer-scale MoS2 thin layers prepared by MoO3 sulfurization. *Nanoscale* **2012,** *4* (20), 6637-6641.

68. Walker, G. F., Macroscopic Swelling of Vermiculite Crystals in Water. *Nature* **1960,** *187* (4734), 312-313.

69. Backes, C.; Higgins, T. M.; Kelly, A.; Boland, C.; Harvey, A.; Hanlon, D.; Coleman, J. N., Guidelines for Exfoliation, Characterization and Processing of Layered Materials Produced by Liquid Exfoliation. *Chem. Mater.* **2017,** *29* (1), 243-255.

70. Shen, J.; He, Y.; Wu, J.; Gao, C.; Keyshar, K.; Zhang, X.; Yang, Y.; Ye, M.; Vajtai, R.; Lou, J.; Ajayan, P. M., Liquid Phase Exfoliation of Two-Dimensional Materials by Directly Probing and Matching Surface Tension Components. *Nano Lett.* **2015,** *15* (8), 5449-5454.

71. Backes, C.; Szydłowska, B. M.; Harvey, A.; Yuan, S.; Vega-Mayoral, V.; Davies, B. R.; Zhao, P.-l.; Hanlon, D.; Santos, E. J. G.; Katsnelson, M. I.; Blau, W. J.; Gadermaier, C.; Coleman, J. N., Production of Highly Monolayer Enriched Dispersions of Liquid-Exfoliated Nanosheets by Liquid Cascade Centrifugation. *ACS Nano* **2016,** *10* (1), 1589-1601.

72. Li, H.; Shi, Y.; Chiu, M.-H.; Li, L.-J., Emerging energy applications of two-dimensional layered transition metal dichalcogenides. *Nano Energy* **2015,** *18*, 293-305.

73. Wu, J.; Schmidt, H.; Amara, K. K.; Xu, X.; Eda, G.; Özyilmaz, B., Large Thermoelectricity via Variable Range Hopping in Chemical Vapor Deposition Grown Single-Layer MoS2. *Nano Lett.* **2014,** *14* (5), 2730-2734.

74. Xiao, J.; Choi, D.; Cosimbescu, L.; Koech, P.; Liu, J.; Lemmon, J. P., Exfoliated MoS2 Nanocomposite as an Anode Material for Lithium Ion Batteries. *Chem. Mater.* **2010,** *22* (16), 4522-4524.

75. Chia, X.; Pumera, M., Layered transition metal dichalcogenide electrochemistry: journey across the periodic table. *Chem. Soc. Rev.* **2018,** *47* (15), 5602-5613.

76. Voiry, D.; Yang, J.; Chhowalla, M., Recent Strategies for Improving the Catalytic Activity of 2D TMD Nanosheets Toward the Hydrogen Evolution Reaction. *Adv. Mater.* **2016,** *28* (29), 6197-6206.

77. Duong, D. L.; Yun, S. J.; Lee, Y. H., van der Waals Layered Materials: Opportunities and Challenges. *ACS Nano* **2017,** *11* (12), 11803-11830.

78. Choi, W.; Choudhary, N.; Han, G. H.; Park, J.; Akinwande, D.; Lee, Y. H., Recent development of two-dimensional transition metal dichalcogenides and their applications. *Mater. Today* **2017,** *20* (3), 116-130.

79. Bao, W.; Cai, X.; Kim, D.; Sridhara, K.; Fuhrer, M. S., High mobility ambipolar MoS2 field-effect transistors: Substrate and dielectric effects. *Appl. Phys. Lett.* **2013,** *102* (4), 042104.

80. Frey, G. L.; Elani, S.; Homyonfer, M.; Feldman, Y.; Tenne, R., Optical-absorption spectra of inorganic fullerenelike. *Phys. Rev. B* **1998,** *57* (11), 6666-6671.

81. Islam, M. R.; Kang, N.; Bhanu, U.; Paudel, H. P.; Erementchouk, M.; Tetard, L.; Leuenberger, M. N.; Khondaker, S. I., Tuning the electrical property via defect engineering of single layer MoS2 by oxygen plasma. *Nanoscale* **2014,** *6* (17), 10033-10039.

82. Mak, K. F.; Lee, C.; Hone, J.; Shan, J.; Heinz, T. F., Atomically Thin: A New Direct-Gap Semiconductor. *Phys. Rev. Lett.* **2010,** *105* (13), 136805.

83. Choudhary, N.; Islam, M. R.; Kang, N.; Tetard, L.; Jung, Y.; Khondaker, S. I., Two-dimensional lateral heterojunction through bandgap engineering of MoS2 via oxygen plasma. *Journal of Physics: Condens. Matter* **2016,** *28* (36), 364002.

84. Fuhrer, M. S.; Hone, J., Measurement of mobility in dual-gated MoS2 transistors. *Nat. Nanotechnol.* **2013,** *8* (3), 146-147.

85. Choudhary, N.; Patel, M. D.; Park, J.; Sirota, B.; Choi, W., Synthesis of large scale MoS2 for electronics and energy applications. *J. Mater. Res.* **2016,** *31* (7), 824-831.

86. Varghese, S. S. V., S.H.; Swaminathan, S.; Singh, K.K.; Mittal, V., Two-Dimensional Materials for Sensing: Graphene and Beyond. *Electronics* **2015,** *4*, 651-687.

87. Lee, J.; Dak, P.; Lee, Y.; Park, H.; Choi, W.; Alam, M. A.; Kim, S., Two-dimensional Layered MoS2 Biosensors Enable Highly Sensitive Detection of Biomolecules. *Sci. Rep.* **2014,** *4* (1), 7352.

88. Perea-López, N.; Lin, Z.; Pradhan, N. R.; Iñiguez-Rábago, A.; Laura Elías, A.; McCreary, A.; Lou, J.; Ajayan, P. M.; Terrones, H.; Balicas, L.; Terrones, M., CVD-grown monolayered MoS 2 as an effective photosensor operating at low-voltage. *2D Mater.* **2014,** *1* (1), 011004.

89. Da Silveira Firmiano, E. G.; Rabelo, A. C.; Dalmaschio, C. J.; Pinheiro, A. N.; Pereira, E. C.; Schreiner, W. H.; Leite, E. R., Supercapacitor Electrodes Obtained by Directly Bonding 2D MoS2 on Reduced Graphene Oxide. *Adv. Energy Mater.* **2014,** *4* (6), 1301380.

90. Stephenson, T.; Li, Z.; Olsen, B.; Mitlin, D., Lithium ion battery applications of molybdenum disulfide (MoS2) nanocomposites. *Energy Environ.l Sci.* **2014,** *7* (1), 209-231.

91. Yang, Y.; Fei, H.; Ruan, G.; Xiang, C.; Tour, J. M., Edge-Oriented MoS2 Nanoporous Films as Flexible Electrodes for Hydrogen Evolution Reactions and Supercapacitor Devices. *Adv. Mater.* **2014,** *26* (48), 8163-8168.

92. Cao, L.; Yang, S.; Gao, W.; Liu, Z.; Gong, Y.; Ma, L.; Shi, G.; Lei, S.; Zhang, Y.; Zhang, S.; Vajtai, R.; Ajayan, P. M., Direct Laser-Patterned Micro-Supercapacitors from Paintable MoS2 Films. *Small* **2013,** *9* (17), 2905-2910.

93. Choudhary, N.; Patel, M.; Ho, Y.-H.; Dahotre, N. B.; Lee, W.; Hwang, J. Y.; Choi, W., Directly deposited MoS2 thin film electrodes for high performance supercapacitors. *J. Mater. Chem. A* **2015,** *3* (47), 24049-24054.

94. Chen, X.; Zhu, Y.; Peng, W.; Li, Y.; Zhang, G.; Zhang, F.; Fan, X., Direct exfoliation of the anode graphite of used Li-ion batteries into few-layer graphene sheets:

a green and high yield route to high-quality graphene preparation. *J. Mater. Chem. A* **2017,** *5* (12), 5880-5885.

95. Maruyama, S.; Fukutsuka, T.; Miyazaki, K.; Abe, Y.; Yoshizawa, N.; Abe, T., Lithium-ion intercalation and deintercalation behaviors of graphitized carbon nanospheres. *J. Mater. Chem. A* **2018,** *6* (3), 1128-1137.

96. Novák, P.; Joho, F.; Lanz, M.; Rykart, B.; Panitz, J.-C.; Alliata, D.; Kötz, R.; Haas, O., The complex electrochemistry of graphite electrodes in lithium-ion batteries. *J.Power Sources* **2001,** *97-98*, 39-46.

97. Lian, P.; Zhu, X.; Liang, S.; Li, Z.; Yang, W.; Wang, H., Large reversible capacity of high quality graphene sheets as an anode material for lithium-ion batteries. *Electrochim. Acta* **2010,** *55* (12), 3909-3914.

98. Gao, M.; Liu, N.; Chen, Y.; Guan, Y.; Wang, W.; Zhang, H.; Wang, F.; Huang, Y., An in situ self-developed graphite as high capacity anode of lithium-ion batteries. *Chem. Commun.* **2015,** *51* (60), 12118-12121.

99. Pan, D.; Wang, S.; Zhao, B.; Wu, M.; Zhang, H.; Wang, Y.; Jiao, Z., Li Storage Properties of Disordered Graphene Nanosheets. *Chemi. Mater.* **2009,** *21* (14), 3136-3142.

100. Wang, A.; Kadam, S.; Li, H.; Shi, S.; Qi, Y., Review on modeling of the anode solid electrolyte interphase (SEI) for lithium-ion batteries. *npj Comput. Mater.* **2018,** *4* (1), 15.

101. Liu, Y.; He, X.; Hanlon, D.; Harvey, A.; Khan, U.; Li, Y.; Coleman, J. N., Electrical, Mechanical, and Capacity Percolation Leads to High-Performance MoS2/Nanotube Composite Lithium Ion Battery Electrodes. *ACS Nano* **2016,** *10* (6), 5980-5990.

102. Zhou, J.; Qin, J.; Zhang, X.; Shi, C.; Liu, E.; Li, J.; Zhao, N.; He, C., 2D Space-Confined Synthesis of Few-Layer MoS2 Anchored on Carbon Nanosheet for Lithium-Ion Battery Anode. *ACS Nano* **2015,** *9* (4), 3837-3848.

103. Shi, Y.; Huang, J.-K.; Jin, L.; Hsu, Y.-T.; Yu, S. F.; Li, L.-J.; Yang, H. Y., Selective Decoration of Au Nanoparticles on Monolayer MoS2 Single Crystals. *Sci. Rep.* **2013,** *3* (1), 1839.

104. Wang, P.-p.; Sun, H.; Ji, Y.; Li, W.; Wang, X., Three-Dimensional Assembly of Single-Layered MoS2. *Adv. Mater.* **2014,** *26* (6), 964-969.

105. Chapin, D. M.; Fuller, C. S.; Pearson, G. L., A New Silicon p-n Junction Photocell for Converting Solar Radiation into Electrical Power. *J. Appl. Phys.* **1954,** *25* (5), 676-677.

106. Jean, J.; Brown, P. R.; Jaffe, R. L.; Buonassisi, T.; Bulović, V., Pathways for solar photovoltaics. *Energy Environ. Sci.* **2015,** *8* (4), 1200-1219.

107. Polman, A.; Knight, M.; Garnett, E. C.; Ehrler, B.; Sinke, W. C., Photovoltaic materials: Present efficiencies and future challenges. *Science* **2016,** *352* (6283), aad4424.

108. Sivula, K.; van de Krol, R., Semiconducting materials for photoelectrochemical energy conversion. *Nat. Rev. Mater.* **2016,** *1*, 15010.

109. Arul, N. S.; Nithya, V. D., *Two Dimensional Transition Metal Dichalcogenides: Synthesis, Properties, and Applications*. Springer Singapore: 2019.

110. Jariwala, D.; Davoyan, A. R.; Wong, J.; Atwater, H. A., Van der Waals Materials for Atomically-Thin Photovoltaics: Promise and Outlook. *ACS Photo.* **2017,** *4* (12), 2962-2970.

111. Bernardi, M.; Palummo, M.; Grossman, J. C., Extraordinary Sunlight Absorption and One Nanometer Thick Photovoltaics Using Two-Dimensional Monolayer Materials. *Nano Lett.* **2013,** *13* (8), 3664-3670.

112. Tributsch, H.; Bennett, J. C., Electrochemistry and photochemistry of MoS2 layer crystals. I. *J. Electroanal. Chem. Interf. Electrochem.* **1977,** *81* (1), 97-111.

113. Groenendijk, D. J.; Buscema, M.; Steele, G. A.; Michaelis de Vasconcellos, S.; Bratschitsch, R.; van der Zant, H. S. J.; Castellanos-Gomez, A., Photovoltaic and Photothermoelectric Effect in a Double-Gated WSe2 Device. *Nano Lett.* **2014,** *14* (10), 5846-5852.

114. Lu, Y.; Yao, X.; Yin, J.; Peng, G.; Cui, P.; Xu, X., MoS2 nanoflowers consisting of nanosheets with a controllable interlayer distance as high-performance lithium ion battery anodes. *RSC Adv.* **2015,** *5* (11), 7938-7943.

115. Memaran, S.; Pradhan, N. R.; Lu, Z.; Rhodes, D.; Ludwig, J.; Zhou, Q.; Ogunsolu, O.; Ajayan, P. M.; Smirnov, D.; Fernández-Domínguez, A. I.; García-Vidal, F. J.; Balicas, L., Pronounced Photovoltaic Response from Multilayered Transition-Metal Dichalcogenides PN-Junctions. *Nano Lett.* **2015,** *15* (11), 7532-7538.

116. Wang, Z.; He, X.; Zhang, X.-X.; Alshareef, H. N., Hybrid van der Waals p–n Heterojunctions based on SnO and 2D MoS2. *Adv. Mater.* **2016,** *28* (41), 9133-9141.

117. Fontana, M.; Deppe, T.; Boyd, A. K.; Rinzan, M.; Liu, A. Y.; Paranjape, M.; Barbara, P., Electron-hole transport and photovoltaic effect in gated MoS2 Schottky junctions. *Sci. Rep.* **2013,** *3* (1), 1634.

118. Akama, T.; Okita, W.; Nagai, R.; Li, C.; Kaneko, T.; Kato, T., Schottky solar cell using few-layered transition metal dichalcogenides toward large-scale fabrication of semitransparent and flexible power generator. *Sci. Rep.* **2017,** *7* (1), 11967.

119. Burschka, J.; Pellet, N.; Moon, S.-J.; Humphry-Baker, R.; Gao, P.; Nazeeruddin, M. K.; Grätzel, M., Sequential deposition as a route to high-performance perovskite-sensitized solar cells. *Nature* **2013,** *499* (7458), 316-319.

120. Jeon, N. J.; Noh, J. H.; Yang, W. S.; Kim, Y. C.; Ryu, S.; Seo, J.; Seok, S. I., Compositional engineering of perovskite materials for high-performance solar cells. *Nature* **2015,** *517* (7535), 476-480.

121. Liu, M.; Johnston, M. B.; Snaith, H. J., Efficient planar heterojunction perovskite solar cells by vapour deposition. *Nature* **2013,** *501* (7467), 395-398.

122. Kojima, A.; Teshima, K.; Shirai, Y.; Miyasaka, T., Organometal Halide Perovskites as Visible-Light Sensitizers for Photovoltaic Cells. *J. Am. Chem. Soc.* **2009,** *131* (17), 6050-6051.

123. Green, M. A.; Ho-Baillie, A.; Snaith, H. J., The emergence of perovskite solar cells. *Nat. Photonics* **2014,** *8* (7), 506-514.

124. Motta, C.; El-Mellouhi, F.; Sanvito, S., Charge carrier mobility in hybrid halide perovskites. *Sci. Rep.* **2015,** *5* (1), 12746.

125. Wojciechowski, K.; Saliba, M.; Leijtens, T.; Abate, A.; Snaith, H. J., Sub-150 °C processed meso-superstructured perovskite solar cells with enhanced efficiency. *Energy Environ. Sci.* **2014,** *7* (3), 1142-1147.

126. Chatterjee, S.; Bera, A.; Pal, A. J., p–i–n Heterojunctions with BiFeO3 Perovskite Nanoparticles and p- and n-Type Oxides: Photovoltaic Properties. *ACS Appl. Mater. Interfaces* **2014,** *6* (22), 20479-20486.

127. Zhao, X.; Wang, M., Organic hole-transporting materials for efficient perovskite solar cells. *Mater. Today Energy* **2018,** *7*, 208-220.

128. Tong, X.; Lin, F.; Wu, J.; Wang, Z. M., High Performance Perovskite Solar Cells. *Adv. Sci.* **2016,** *3* (5), 1500201.

129. Ameen, S.; Rub, M. A.; Kosa, S. A.; Alamry, K. A.; Akhtar, M. S.; Shin, H.-S.; Seo, H.-K.; Asiri, A. M.; Nazeeruddin, M. K., Perovskite Solar Cells: Influence of Hole Transporting Materials on Power Conversion Efficiency. *ChemSusChem* **2016,** *9* (1), 10-27.

130. Jena, A. K.; Numata, Y.; Ikegami, M.; Miyasaka, T., Role of spiro-OMeTAD in performance deterioration of perovskite solar cells at high temperature and reuse of the perovskite films to avoid Pb-waste. *J. Mater. Chem. A* **2018,** *6* (5), 2219-2230.

131. Fang, Q.; Shang, Q.; Zhao, L.; Wang, R.; Zhang, Z.; Yang, P.; Sui, X.; Qiu, X.; Liu, X.; Zhang, Q.; Zhang, Y., Ultrafast Charge Transfer in Perovskite Nanowire/2D Transition Metal Dichalcogenide Heterostructures. *J. Phys. Chem. Lett.* **2018,** *9* (7), 1655-1662.

132. Kohnehpoushi, S.; Nazari, P.; Nejand, B. A.; Eskandari, M., MoS2: a two-dimensional hole-transporting material for high-efficiency, low-cost perovskite solar cells. *Nanotechnology* **2018,** *29* (20), 205201.

133. Huang, P.; Wang, Z.; Liu, Y.; Zhang, K.; Yuan, L.; Zhou, Y.; Song, B.; Li, Y., Water-Soluble 2D Transition Metal Dichalcogenides as the Hole-Transport Layer for Highly Efficient and Stable p–i–n Perovskite Solar Cells. *ACS Appl. Mater. Interfaces* **2017,** *9* (30), 25323-25331.

134. Yun, J.-M.; Noh, Y.-J.; Yeo, J.-S.; Go, Y.-J.; Na, S.-I.; Jeong, H.-G.; Kim, J.; Lee, S.; Kim, S.-S.; Koo, H. Y.; Kim, T.-W.; Kim, D.-Y., Efficient work-function engineering of solution-processed MoS2 thin-films for novel hole and electron transport layers leading to high-performance polymer solar cells. *J. Mater. Chem. C* **2013,** *1* (24), 3777-3783.

135. Qin, P.; Tanaka, S.; Ito, S.; Tetreault, N.; Manabe, K.; Nishino, H.; Nazeeruddin, M. K.; Grätzel, M., Inorganic hole conductor-based lead halide perovskite solar cells with 12.4% conversion efficiency. *Nat. Commun.* **2014,** *5* (1), 3834.

136. Malinkiewicz, O.; Roldán-Carmona, C.; Soriano, A.; Bandiello, E.; Camacho, L.; Nazeeruddin, M. K.; Bolink, H. J., Metal-Oxide-Free Methylammonium Lead Iodide Perovskite-Based Solar Cells: the Influence of Organic Charge Transport Layers. *Adv. Energy Mater.* **2014,** *4* (15), 1400345.

137. Seo, J.; Park, S.; Chan Kim, Y.; Jeon, N. J.; Noh, J. H.; Yoon, S. C.; Seok, S. I., Benefits of very thin PCBM and LiF layers for solution-processed p–i–n perovskite solar cells. *Energy Environ. Sci.* **2014,** *7* (8), 2642-2646.

138. Juarez-Perez, E. J.; Wuβler, M.; Fabregat-Santiago, F.; Lakus-Wollny, K.; Mankel, E.; Mayer, T.; Jaegermann, W.; Mora-Sero, I., Role of the Selective Contacts in the Performance of Lead Halide Perovskite Solar Cells. *J. Phys. Chem. Lett.* **2014,** *5* (4), 680-685.

139. Etgar, L.; Gao, P.; Xue, Z.; Peng, Q.; Chandiran, A. K.; Liu, B.; Nazeeruddin, M. K.; Grätzel, M., Mesoscopic CH3NH3PbI3/TiO2 Heterojunction Solar Cells. *J. Am. Chem. Soc.* **2012,** *134* (42), 17396-17399.

140. Laban, W. A.; Etgar, L., Depleted hole conductor-free lead halide iodide heterojunction solar cells. *Energy Environ. Sci.* **2013,** *6* (11), 3249-3253.

141. Shi, J.; Dong, J.; Lv, S.; Xu, Y.; Zhu, L.; Xiao, J.; Xu, X.; Wu, H.; Li, D.; Luo, Y.; Meng, Q., Hole-conductor-free perovskite organic lead iodide heterojunction thin-film solar cells: High efficiency and junction property. *Appl. Phys. Lett.* **2014,** *104* (6), 063901.

142. Eperon, G. E.; Burlakov, V. M.; Goriely, A.; Snaith, H. J., Neutral Color Semitransparent Microstructured Perovskite Solar Cells. *ACS Nano* **2014,** *8* (1), 591-598.

143. Najafi, L.; Taheri, B.; Martín-García, B.; Bellani, S.; Di Girolamo, D.; Agresti, A.; Oropesa-Nuñez, R.; Pescetelli, S.; Vesce, L.; Calabrò, E.; Prato, M.; Del Rio Castillo, A. E.; Di Carlo, A.; Bonaccorso, F., MoS2 Quantum Dot/Graphene Hybrids for Advanced Interface Engineering of a CH3NH3PbI3 Perovskite Solar Cell with an Efficiency of over 20%. *ACS Nano* **2018,** *12* (11), 10736-10754.

144. Chia, X.; Eng, A. Y. S.; Ambrosi, A.; Tan, S. M.; Pumera, M., Electrochemistry of Nanostructured Layered Transition-Metal Dichalcogenides. *Chem.Rev.* **2015,** *115* (21), 11941-11966.

145. Kheirabadi, N.; Shafiekhani, A., Graphene/Li-ion battery. *J. Appl. Phys.* **2012,** *112* (12), 124323.

146. Nitta, N.; Wu, F.; Lee, J. T.; Yushin, G., Li-ion battery materials: present and future. *Mater. Today* **2015,** *18* (5), 252-264.

147. Chan, C. K.; Peng, H.; Liu, G.; McIlwrath, K.; Zhang, X. F.; Huggins, R. A.; Cui, Y., High-performance lithium battery anodes using silicon nanowires. *Nat. Nanotechnol.* **2008,** *3* (1), 31-35.

148. Su, X.; Wu, Q.; Li, J.; Xiao, X.; Lott, A.; Lu, W.; Sheldon, B. W.; Wu, J., Silicon-Based Nanomaterials for Lithium-Ion Batteries: A Review. *Adv. Energy Mater.* **2014,** *4* (1), 1300882.

149. Ma, D.; Cao, Z.; Hu, A., Si-Based Anode Materials for Li-Ion Batteries: A Mini Review. *Nanomicro Lett.* **2014,** *6* (4), 347-358.

150. Meng, X.; He, K.; Su, D.; Zhang, X.; Sun, C.; Ren, Y.; Wang, H.-H.; Weng, W.; Trahey, L.; Canlas, C. P.; Elam, J. W., Gallium Sulfide–Single-Walled Carbon Nanotube Composites: High-Performance Anodes for Lithium-Ion Batteries. *Adv. Funct. Mater.* **2014,** *24* (34), 5435-5442.

151. Wu, C.; Maier, J.; Yu, Y., Generalizable Synthesis of Metal-Sulfides/Carbon Hybrids with Multiscale, Hierarchically Ordered Structures as Advanced Electrodes for Lithium Storage. *Adv. Mater.* **2016,** *28* (1), 174-180.

152. Chhowalla, M.; Liu, Z.; Zhang, H., Two-dimensional transition metal dichalcogenide (TMD) nanosheets. *Chem. Soc. Rev.* **2015,** *44* (9), 2584-2586.

153. Zhang, C. J.; Pinilla, S.; McEvoy, N.; Cullen, C. P.; Anasori, B.; Long, E.; Park, S.-H.; Seral-Ascaso, A.; Shmeliov, A.; Krishnan, D.; Morant, C.; Liu, X.; Duesberg, G. S.; Gogotsi, Y.; Nicolosi, V., Oxidation Stability of Colloidal Two-Dimensional Titanium Carbides (MXenes). *Chem. Mater.* **2017,** *29* (11), 4848-4856.

154. Zhang, C.; Kim, S. J.; Ghidiu, M.; Zhao, M.-Q.; Barsoum, M. W.; Nicolosi, V.; Gogotsi, Y., Layered Orthorhombic Nb2O5@Nb4C3Tx and TiO2@Ti3C2Tx Hierarchical Composites for High Performance Li-ion Batteries. *Adv Funct. Mater.* **2016,** *26* (23), 4143-4151.

155. Deng, Z.; Jiang, H.; Li, C., 2D Metal Chalcogenides Incorporated into Carbon and their Assembly for Energy Storage Applications. *Small* **2018,** *14* (22), 1800148.

156. Kim, H.; Kim, H.; Ding, Z.; Lee, M. H.; Lim, K.; Yoon, G.; Kang, K., Recent Progress in Electrode Materials for Sodium-Ion Batteries. *Adv. Energy Mater.* **2016,** *6* (19), 1600943.

157. Hu, X.; Zhang, W.; Liu, X.; Mei, Y.; Huang, Y., Nanostructured Mo-based electrode materials for electrochemical energy storage. *Chem. Soc. Rev.* **2015,** *44* (8), 2376-2404.

158. Tang, Y.; Zhang, Y.; Li, W.; Ma, B.; Chen, X., Rational material design for ultrafast rechargeable lithium-ion batteries. *Chem. Soc. Rev.* **2015,** *44* (17), 5926-5940.

159. Nguyen, E. P.; Carey, B. J.; Daeneke, T.; Ou, J. Z.; Latham, K.; Zhuiykov, S.; Kalantar-zadeh, K., Investigation of Two-Solvent Grinding-Assisted Liquid Phase Exfoliation of Layered MoS2. *Chem. Mater.* **2015,** *27* (1), 53-59.

160. *NFPA 704: Standard System for the Identification of the Hazards of Materials for Emergency Response*, https://www.nfpa.org/codes-and-standards/all-codes-and-standards/list-of-codes-andstandards/detail?code=704.

161. Jang, J.-t.; Jeong, S.; Seo, J.-w.; Kim, M.-C.; Sim, E.; Oh, Y.; Nam, S.; Park, B.; Cheon, J., Ultrathin Zirconium Disulfide Nanodiscs. *J. Am. Chem. Soc.* **2011,** *133* (20), 7636-7639.

162. Seo, J.-w.; Jun, Y.-w.; Park, S.-w.; Nah, H.; Moon, T.; Park, B.; Kim, J.-G.; Kim, Y. J.; Cheon, J., Two-Dimensional Nanosheet Crystals. *Angew. Chem. Inte.* **2007,** *46* (46), 8828-8831.

163. Feng, C.; Huang, L.; Guo, Z.; Liu, H., Synthesis of tungsten disulfide (WS2) nanoflakes for lithium ion battery application. *Electrochem. Commun.* **2007,** *9* (1), 119-122.

164. Fang, X.; Hua, C.; Wu, C.; Wang, X.; Shen, L.; Kong, Q.; Wang, J.; Hu, Y.; Wang, Z.; Chen, L., Synthesis and Electrochemical Performance of Graphene-like WS2. *Chem –Eur J.* **2013,** *19* (18), 5694-5700.

165. Shiva, K.; Ramakrishna Matte, H. S. S.; Rajendra, H. B.; Bhattacharyya, A. J.; Rao, C. N. R., Employing synergistic interactions between few-layer WS2 and reduced graphene oxide to improve lithium storage, cyclability and rate capability of Li-ion batteries. *Nano Energy* **2013,** *2* (5), 787-793.

166. Seo, J.-w.; Jang, J.-t.; Park, S.-w.; Kim, C.; Park, B.; Cheon, J., Two-Dimensional SnS2 Nanoplates with Extraordinary High Discharge Capacity for Lithium Ion Batteries. *Adv. Mater.* **2008,** *20* (22), 4269-4273.

167. Kim, T.-J.; Kim, C.; Son, D.; Choi, M.; Park, B., Novel SnS2-nanosheet anodes for lithium-ion batteries. *J. Power Sources* **2007,** *167* (2), 529-535.

168. Du, Y.; Yin, Z.; Rui, X.; Zeng, Z.; Wu, X.-J.; Liu, J.; Zhu, Y.; Zhu, J.; Huang, X.; Yan, Q.; Zhang, H., A facile, relative green, and inexpensive synthetic approach toward large-scale production of SnS2 nanoplates for high-performance lithium-ion batteries. *Nanoscale* **2013,** *5* (4), 1456-1459.

169. Sennu, P.; Christy, M.; Aravindan, V.; Lee, Y.-G.; Nahm, K. S.; Lee, Y.-S., Two-Dimensional Mesoporous Cobalt Sulfide Nanosheets as a Superior Anode for a Li-Ion Battery and a Bifunctional Electrocatalyst for the Li–O2 System. *Chem. Mater.* **2015,** *27* (16), 5726-5735.

170. Rout, C. S.; Kim, B.-H.; Xu, X.; Yang, J.; Jeong, H. Y.; Odkhuu, D.; Park, N.; Cho, J.; Shin, H. S., Synthesis and Characterization of Patronite Form of Vanadium Sulfide on Graphitic Layer. *J. Am. Chem. Soc.* **2013,** *135* (23), 8720-8725.

171. Chen, D.; Ji, G.; Ding, B.; Ma, Y.; Qu, B.; Chen, W.; Lee, J. Y., In situ nitrogenated graphene–few-layer WS2 composites for fast and reversible Li+ storage. *Nanoscale* **2013,** *5* (17), 7890-7896.

172. Zhang, Q.; Tan, S.; Mendes, R. G.; Sun, Z.; Chen, Y.; Kong, X.; Xue, Y.; Rümmeli, M. H.; Wu, X.; Chen, S.; Fu, L., Extremely Weak van der Waals Coupling in Vertical ReS2 Nanowalls for High-Current-Density Lithium-Ion Batteries. *Adv. Mater.* **2016,** *28* (13), 2616-2623.

173. Bhandavat, R.; David, L.; Singh, G., Synthesis of Surface-Functionalized WS2 Nanosheets and Performance as Li-Ion Battery Anodes. *J. Phys. Chem. Lett.* **2012,** *3* (11), 1523-1530.

174. Luo, B.; Fang, Y.; Wang, B.; Zhou, J.; Song, H.; Zhi, L., Two dimensional graphene–SnS2 hybrids with superior rate capability for lithium ion storage. *Energy Environ. Sci.* **2012,** *5* (1), 5226-5230.

175. Liu, S.; Lu, X.; Xie, J.; Cao, G.; Zhu, T.; Zhao, X., Preferential c-Axis Orientation of Ultrathin SnS2 Nanoplates on Graphene as High-Performance Anode for Li-Ion Batteries. *ACS Appl. Mater. Interfaces* **2013,** *5* (5), 1588-1595.

176. de las Casas, C.; Li, W., A review of application of carbon nanotubes for lithium ion battery anode material. *J. Power Sources* **2012,** *208*, 74-85.

177. Goriparti, S.; Miele, E.; De Angelis, F.; Di Fabrizio, E.; Proietti Zaccaria, R.; Capiglia, C., Review on recent progress of nanostructured anode materials for Li-ion batteries. *J. Power Sources* **2014,** *257*, 421-443.

178. Saint, J.; Morcrette, M.; Larcher, D.; Tarascon, J. M., Exploring the Li–Ga room temperature phase diagram and the electrochemical performances of the LixGay alloys vs. Li. *Solid State Ion.* **2005,** *176* (1), 189-197.

179. Senoh, H.; Kageyama, H.; Takeuchi, T.; Nakanishi, K.; Ohta, T.; Sakaebe, H.; Yao, M.; Sakai, T.; Yasuda, K., Gallium (III) sulfide as an active material in lithium secondary batteries. *J. Power Sources* **2011,** *196* (13), 5631-5636.

180. Sugiawati, V. A.; Vacandio, F.; Ein-Eli, Y.; Djenizian, T., Electrodeposition of polymer electrolyte into carbon nanotube tissues for high performance flexible Li-ion microbatteries. *APL Mater.* **2019,** *7* (3), 031506.

181. Mostafa, S.; Behafarid, F.; Croy, J. R.; Ono, L. K.; Li, L.; Yang, J. C.; Frenkel, A. I.; Cuenya, B. R., Shape-Dependent Catalytic Properties of Pt Nanoparticles. *J. Am. Chem. Soc.* **2010,** *132* (44), 15714-15719.

182. Hourahine, B.; Papoff, F., The geometrical nature of optical resonances: from a sphere to fused dimer nanoparticles. *Meas. Sci. Technol.* **2012,** *23* (8), 084002.

183. Hourahine, B.; Papoff, F., Optical control of scattering, absorption and lineshape in nanoparticles. *Opt. Express* **2013,** *21* (17), 20322-20333.

184. Okamoto, H., In-Se Phase Diagram ASM Alloy Phase Diagrams Center. *ASM International* **1998**, http://www1.asminternational.org/ AsmEnterprise/APD.

185. Popović, S.; Tonejc, A.; Čelustka, B.; Gržeta-Plenković, B.; Trojko, R., Revised and new crystal data for indium selenides. *J. Appl. Crystallogr.* **1979,** *12* (4), 416-420.

186. Hogg, J. H. C.; Sutherland, H. H.; Williams, D. J., The crystal structure of tetraindium triselenide. *Acta Crystallogr. Section B* **1973,** *29* (8), 1590-1593.

187. Inoue, S.; Yoshida, T.; Morita, T., Crystal Structure of InSe Grown from Melt and Its Structure Transition. *Jpn. J. Appl. Phys.* **1982,** *21* (Part 1, No. 2), 242-248.

188. Hogg, J. H. C., The crystal structure of In6Se7. *Acta Crystallogr. Section B* **1971,** *27* (8), 1630-1634.

189. Han, G.; Chen, Z.-G.; Sun, C.; Yang, L.; Cheng, L.; Li, Z.; Lu, W.; Gibbs, Z. M.; Snyder, G. J.; Jack, K.; Drennan, J.; Zou, J., A new crystal: layer-structured rhombohedral In3Se4. *CrystEngComm* **2014,** *16* (3), 393-398.

190. Han, G.; Chen, Z.-G.; Yang, L.; Cheng, L.; Jack, K.; Drennan, J.; Zou, J., Thermal stability and oxidation of layer-structured rhombohedral In3Se4 nanostructures. *Appl. Phys. Lett.* **2013,** *103* (26), 263105.

191. Han, G.; Chen, Z.-G.; Ye, D.; Yang, L.; Wang, L.; Drennan, J.; Zou, J., In-doped Bi2Se3 hierarchical nanostructures as anode materials for Li-ion batteries. *J. Mater. Chem. A* **2014,** *2* (19), 7109-7116.

192. Manolikas, C., New results on the phase transformations of In2Se3. *J. Solid State Chem.* **1988,** *74* (2), 319-328.

193. Ye, J.; Soeda, S.; Nakamura, Y.; Nittono, O., Crystal Structures and Phase Transformation in In2Se3Compound Semiconductor. *Jpn. J. Appl. Phys.* **1998,** *37* (Part 1, No. 8), 4264-4271.

194. Popović, S.; Čelustka, B.; Bidjin, D., X-Ray Diffraction Measurement of Lattice Parameters of In2Se3. *Physica Status Solidi (a)* **1971,** *6* (1), 301-304.

195. Rhyee, J.-S.; Cho, E.; Lee, K. H.; Lee, S. M.; Kim, S. I.; Kim, H.-S.; Kwon, Y. S.; Kim, S. J., Thermoelectric properties and anisotropic electronic band structure on the In4Se3−x compounds. *Appl. Phys. Lett.* **2009,** *95* (21), 212106.

196. Rhyee, J.-S.; Cho, E.; Ahn, K.; Lee, K. H.; Lee, S. M., Thermoelectric properties of bipolar diffusion effect on In4Se3−xTex compounds. *Appl. Phys. Lett.* **2010,** *97* (15), 152104.

197. Shi, X.; Cho, J. Y.; Salvador, J. R.; Yang, J.; Wang, H., Thermoelectric properties of polycrystalline In4Se3 and In4Te3. *Appl. Phys. Lett.* **2010,** *96* (16), 162108.

198. Zhu, G. H.; Lan, Y. C.; Wang, H.; Joshi, G.; Hao, Q.; Chen, G.; Ren, Z. F., Effect of selenium deficiency on the thermoelectric properties of compounds. *Phys. Rev. B* **2011,** *83* (11), 115201.

199. Ahn, K.; Cho, E.; Rhyee, J.-S.; Kim, S. I.; Lee, S. M.; Lee, K. H., Effect of cationic substitution on the thermoelectric properties of In4−xMxSe2.95 compounds (M = Na, Ca, Zn, Ga, Sn, Pb; x = 0.1). *Appl. Phys. Lett.* **2011,** *99* (10), 102110.

200. Luo, Y.; Yang, J.; Li, G.; Liu, M.; Xiao, Y.; Fu, L.; Li, W.; Zhu, P.; Peng, J.; Gao, S.; Zhang, J., Enhancement of the Thermoelectric Performance of Polycrystalline In4Se2.5 by Copper Intercalation and Bromine Substitution. *Adv. Energy Mater.* **2014,** *4* (2), 1300599.

201. Tedenac, P. J.-C.; Vassilev, D. G. P.; Daouchi, B.; Rachidi, J.; Brun, G., Low-temperature Region of the In–Se System. *Cryst. Res. Technol.***1997,** *32* (4), 605-616.

202. Wang, J.-J.; Cao, F.-F.; Jiang, L.; Guo, Y.-G.; Hu, W.-P.; Wan, L.-J., High Performance Photodetectors of Individual InSe Single Crystalline Nanowire. *J. Am. Chem. Soc.* **2009,** *131* (43), 15602-15603.

203. Tan, X.; Zhou, J.; Yang, Q., Ascorbic acid-assisted solvothermal growth of γ-In2Se3 hierarchical flowerlike architectures. *CrystEngComm* **2011,** *13* (7), 2792-2798.

204. Revaprasadu, N.; Azad Malik, M.; Carstens, J.; O'Brien, P., Novel single-molecule precursor routes for the direct synthesis of InS and InSe quantum dots. *J. Mater. Chem.* **1999,** *9* (11), 2885-2888.

205. Hollingsworth, J. A.; Poojary, D. M.; Clearfield, A.; Buhro, W. E., Catalyzed Growth of a Metastable InS Crystal Structure as Colloidal Crystals. *J. Am. Chem. Soc.* **2000,** *122* (14), 3562-3563.

206. Yang, S.; Kelley, D. F., The Spectroscopy of InSe Nanoparticles. *J. Phys. Chem. B* **2005,** *109* (26), 12701-12709.

207. Park, K. H.; Jang, K.; Kim, S.; Kim, H. J.; Son, S. U., Phase-Controlled One-Dimensional Shape Evolution of InSe Nanocrystals. *J. Am. Chem. Soc.* **2006,** *128* (46), 14780-14781.

208. Zhou, W.; Yin, Z.; Sim, D. H.; Zhang, H.; Ma, J.; Hng, H. H.; Yan, Q., Growth of dandelion-shaped CuInSe2nanostructures by a two-step solvothermal process. *Nanotechnology* **2011,** *22* (19), 195607.

209. Hsiang, H.-I.; Lu, L.-H.; Chang, Y.-L.; Ray, D.; Yen, F.-S., Solvo-Thermal Synthesis and Characterization of Indium Selenide Nanocrystals. *J. Am. Ceram. Soc.* **2011,** *94* (11), 3757-3760.

210. Siciliano, T.; Tepore, A.; Micocci, G.; Genga, A.; Siciliano, M.; Filippo, E., Synthesis and characterization of indium monoselenide (InSe) nanowires. *J. Mater. Sci. Mater. Electron.* **2011,** *22* (6), 649-653.

211. Ning, J.; Xiao, G.; Xiao, N.; Wang, L.; Liu, B.; Zou, B., Shape and crystal phase controlled synthesis of InSe nanocrystals via a simple and facile way. *J. Cryst. Growth* **2011,** *336* (1), 1-5.

212. Sucharitakul, S.; Goble, N. J.; Kumar, U. R.; Sankar, R.; Bogorad, Z. A.; Chou, F.-C.; Chen, Y.-T.; Gao, X. P. A., Intrinsic Electron Mobility Exceeding 103 cm2/(V s) in Multilayer InSe FETs. *Nano Lett.* **2015,** *15* (6), 3815-3819.

213. Xu, K.; Yin, L.; Huang, Y.; Shifa, T. A.; Chu, J.; Wang, F.; Cheng, R.; Wang, Z.; He, J., Synthesis, properties and applications of 2D layered MIIIXVI (M = Ga, In; X = S, Se, Te) materials. *Nanoscale* **2016,** *8* (38), 16802-16818.

214. Bandurin, D. A.; Tyurnina, A. V.; Yu, G. L.; Mishchenko, A.; Zólyomi, V.; Morozov, S. V.; Kumar, R. K.; Gorbachev, R. V.; Kudrynskyi, Z. R.; Pezzini, S.; Kovalyuk, Z. D.; Zeitler, U.; Novoselov, K. S.; Patanè, A.; Eaves, L.; Grigorieva, I. V.; Fal'ko, V. I.; Geim, A. K.; Cao, Y., High electron mobility, quantum Hall effect and anomalous optical response in atomically thin InSe. *Nat. Nanotechnol.* **2017,** *12* (3), 223-227.

215. Lei, S.; Ge, L.; Najmaei, S.; George, A.; Kappera, R.; Lou, J.; Chhowalla, M.; Yamaguchi, H.; Gupta, G.; Vajtai, R.; Mohite, A. D.; Ajayan, P. M., Evolution of the Electronic Band Structure and Efficient Photo-Detection in Atomic Layers of InSe. *ACS Nano* **2014,** *8* (2), 1263-1272.

216. Wang, J.-J.; Wang, Y.-Q.; Cao, F.-F.; Guo, Y.-G.; Wan, L.-J., Synthesis of Monodispersed Wurtzite Structure CuInSe2 Nanocrystals and Their Application in High-Performance Organic−Inorganic Hybrid Photodetectors. *J. Am. Chem. Soc.* **2010,** *132* (35), 12218-12221.

217. Hayashi, T.; Ueno, K.; Saiki, K.; Koma, A., Investigation of the growth mechanism of an InSe epitaxial layer on a MoS2 substrate. *J. Cryst. Growth* **2000,** *219* (1), 115-122.

218. Wang, D.; Li, Y., Effective Octadecylamine System for Nanocrystal Synthesis. *Inorg. Chem.* **2011,** *50* (11), 5196-5202.

219. Mourdikoudis, S.; Liz-Marzán, L. M., Oleylamine in Nanoparticle Synthesis. *Chem.Mater.* **2013,** *25* (9), 1465-1476.

220. Park, K. H.; Jang, K.; Son, S. U., Synthesis, Optical Properties, and Self-Assembly of Ultrathin Hexagonal In2S3 Nanoplates. *Angew. Chem. Int.* **2006,** *45* (28), 4608-4612.

221. Huo, C.; Yan, Z.; Song, X.; Zeng, H., 2D materials via liquid exfoliation: a review on fabrication and applications. *Sci. Bull.* **2015,** *60* (23), 1994-2008.

222. Fargues, D.; Tyuliev, G.; Brojerdi, G.; Eddrief, M.; Balkanski, M., Ultra-high vacuum deposition of sodium on indium monoselenide: intercalation or chemical reaction. *Surf. Sci.* **1997,** *370* (2), 201-208.

223. Wagner, C. D.; Muilenberg, G. E., *Handbook of X-ray Photoelectron Spectroscopy: A Reference Book of Standard Data for Use in X-ray Photoelectron Spectroscopy*. Perkin-Elmer: 1979.

224. O. Del Pozo-Zamudio, S. S., J. Klein, R. C. Schofield, E. A. Chekhovich, O. Ceylan, E. Margapoti, A. I. Dmitriev, G. V. Lashkarev, D. N. Borisenko, N. N. Kolesnikov, J. J. Finley, A. I. Tartakovskii, Photoluminescence and Raman investigation of stability of InSe and GaSe thin films. *Mesoscale and Nanoscale Phys.* **2015**.

225. Du, F.; Tang, H.; Pan, L.; Zhang, T.; Lu, H.; Xiong, J.; Yang, J.; Zhang, C., Environmental Friendly Scalable Production of Colloidal 2D Titanium Carbonitride MXene with Minimized Nanosheets Restacking for Excellent Cycle Life Lithium-Ion Batteries. *Electrochim. Acta* **2017,** *235*, 690-699.

226. Li, W.-J.; Zhou, Y.-N.; Fu, Z.-W., Fabrication and lithium electrochemistry of InSe thin film. *Appl. Surf. Sci.* **2011,** *257* (7), 2881-2885.

227. Wang, D.; Romer, F.; Connell, L.; Walter, C.; Saiz, E.; Yue, S.; Lee, P. D.; McPhail, D. S.; Hanna, J. V.; Jones, J. R., Highly flexible silica/chitosan hybrid scaffolds with oriented pores for tissue regeneration. *J. Mater. Chem. B* **2015,** *3* (38), 7560-7576.

228. D. Stauffer, A. A., Introduction To Percolation Theory. *Computer (Long. Beach. Calif).* **1994,** *1*, 192.

229. Liu, Y.; Xie, K.; Pan, Y.; Wang, H.; Chen, Y.; Li, Y.; Zheng, C., Impacts of the Properties of Anode Solid Electrolyte Interface on the Storage Life of Li-Ion Batteries. *J. Phys. Chem. C* **2018,** *122* (17), 9411-9416.

230. Röder, F.; Sonntag, S.; Schröder, D.; Krewer, U., Simulating the Impact of Particle Size Distribution on the Performance of Graphite Electrodes in Lithium-Ion Batteries. *Energy Technol.* **2016,** *4* (12), 1588-1597.

231. Kresse, G.; Hafner, J., Ab initio molecular dynamics for liquid metals. *Phys. Rev. B* **1993,** *47* (1), 558-561.

232. Kresse, G.; Furthmüller, J., Efficient iterative schemes for ab initio total-energy calculations using a plane-wave basis set. *Phys. Rev. B* **1996,** *54* (16), 11169-11186.

233. Sivula, K.; van de Krol, R., Semiconducting materials for photoelectrochemical energy conversion. *Nat. Rev. Mater.* **2016,** *1* (2), 15010.

234. Ava, T. T.; Al Mamun, A.; Marsillac, S.; Namkoong, G., A Review: Thermal Stability of Methylammonium Lead Halide Based Perovskite Solar Cells. *Appl. Sci.* **2019,** *9* (1).

235. Niu, G.; Guo, X.; Wang, L., Review of recent progress in chemical stability of perovskite solar cells. *J. Mater. Chem. A* **2015,** *3* (17), 8970-8980.

236. Grätzel, M., The light and shade of perovskite solar cells. *Nat. Mater.* **2014,** *13* (9), 838-842.

237. Li, X.; Tschumi, M.; Han, H.; Babkair, S. S.; Alzubaydi, R. A.; Ansari, A. A.; Habib, S. S.; Nazeeruddin, M. K.; Zakeeruddin, S. M.; Grätzel, M., Outdoor Performance and Stability under Elevated Temperatures and Long-Term Light Soaking of Triple-Layer Mesoporous Perovskite Photovoltaics. *Energy Technol.* **2015,** *3* (6), 551-555.

238. Wang, K.-C.; Shen, P.-S.; Li, M.-H.; Chen, S.; Lin, M.-W.; Chen, P.; Guo, T.-F., Low-Temperature Sputtered Nickel Oxide Compact Thin Film as Effective Electron Blocking Layer for Mesoscopic NiO/CH3NH3PbI3 Perovskite Heterojunction Solar Cells. *ACS Appl. Mater. Interfaces* **2014,** *6* (15), 11851-11858.

239. Singh, E.; Kim, K. S.; Yeom, G. Y.; Nalwa, H. S., Atomically Thin-Layered Molybdenum Disulfide (MoS2) for Bulk-Heterojunction Solar Cells. *ACS Appl. Mater. Interfaces* **2017,** *9* (4), 3223-3245.

240. Capasso, A.; Matteocci, F.; Najafi, L.; Prato, M.; Buha, J.; Cinà, L.; Pellegrini, V.; Carlo, A. D.; Bonaccorso, F., Few-Layer MoS2 Flakes as Active Buffer Layer for Stable Perovskite Solar Cells. *Adv. Energy Mater.* **2016,** *6* (16), 1600920.

241. Wang, D.; Elumalai, N. K.; Mahmud, M. A.; Yi, H.; Upama, M. B.; Lee Chin, R. A.; Conibeer, G.; Xu, C.; Haque, F.; Duan, L.; Uddin, A., MoS2 incorporated hybrid hole transport layer for high performance and stable perovskite solar cells. *Synth. Met.* **2018,** *246*, 195-203.

242. Ray, R.; Sarkar, A. S.; Pal, S. K., Improving performance and moisture stability of perovskite solar cells through interface engineering with polymer-2D MoS2 nanohybrid. *Sol. Energy* **2019,** *193*, 95-101.

243. Kakavelakis, G.; Paradisanos, I.; Paci, B.; Generosi, A.; Papachatzakis, M.; Maksudov, T.; Najafi, L.; Del Rio Castillo, A. E.; Kioseoglou, G.; Stratakis, E.; Bonaccorso, F.; Kymakis, E., Extending the Continuous Operating Lifetime of Perovskite Solar Cells with a Molybdenum Disulfide Hole Extraction Interlayer. *Adv. Energy Mater.* **2018,** *8* (12), 1702287.

244. Ito, S.; Tanaka, S.; Vahlman, H.; Nishino, H.; Manabe, K.; Lund, P., Carbon-Double-Bond-Free Printed Solar Cells from TiO2/CH3NH3PbI3/CuSCN/Au: Structural Control and Photoaging Effects. *ChemPhysChem* **2014,** *15* (6), 1194-1200.

245. Ito, S.; Tanaka, S.; Nishino, H., Lead-Halide Perovskite Solar Cells by CH3NH3I Dripping on PbI2–CH3NH3I–DMSO Precursor Layer for Planar and Porous Structures Using CuSCN Hole-Transporting Material. *J. Phys. Chem. Lett.* **2015,** *6* (5), 881-886.

246. Yu, W.; Li, F.; Wang, H.; Alarousu, E.; Chen, Y.; Lin, B.; Wang, L.; Hedhili, M. N.; Li, Y.; Wu, K.; Wang, X.; Mohammed, O. F.; Wu, T., Ultrathin Cu2O as an efficient inorganic hole transporting material for perovskite solar cells. *Nanoscale* **2016,** *8* (11), 6173-6179.

247. Liu, M.-H.; Zhou, Z.-J.; Zhang, P.-P.; Tian, Q.-W.; Zhou, W.-H.; Kou, D.-X.; Wu, S.-X., p-type Li, Cu-codoped NiOx hole-transporting layer for efficient planar perovskite solar cells. *Opt. Express* **2016,** *24* (22), A1349-A1359.

248. Chen, W.; Liu, F.-Z.; Feng, X.-Y.; Djurišić, A. B.; Chan, W. K.; He, Z.-B., Cesium Doped NiOx as an Efficient Hole Extraction Layer for Inverted Planar Perovskite Solar Cells. *Adv. Energy Mater.* **2017,** *7* (19), 1700722.

249. Wu, Y.; Xie, F.; Chen, H.; Yang, X.; Su, H.; Cai, M.; Zhou, Z.; Noda, T.; Han, L., Thermally Stable MAPbI3 Perovskite Solar Cells with Efficiency of 19.19% and Area over 1 cm2 achieved by Additive Engineering. *Adv. Mater.* **2017,** *29* (28), 1701073.

250. Xie, F.; Chen, C.-C.; Wu, Y.; Li, X.; Cai, M.; Liu, X.; Yang, X.; Han, L., Vertical recrystallization for highly efficient and stable formamidinium-based inverted-structure perovskite solar cells. *Energy Environ. Sci.* **2017,** *10* (9), 1942-1949.

251. Liu, Z.; Zhang, M.; Xu, X.; Bu, L.; Zhang, W.; Li, W.; Zhao, Z.; Wang, M.; Cheng, Y.-B.; He, H., p-Type mesoscopic NiO as an active interfacial layer for carbon counter electrode based perovskite solar cells. *Dalton Trans.* **2015,** *44* (9), 3967-3973.

252. Giordano, F.; Abate, A.; Correa Baena, J. P.; Saliba, M.; Matsui, T.; Im, S. H.; Zakeeruddin, S. M.; Nazeeruddin, M. K.; Hagfeldt, A.; Graetzel, M., Enhanced electronic properties in mesoporous TiO2 via lithium doping for high-efficiency perovskite solar cells. *Nat. Commun.* **2016,** *7* (1), 10379.

253. Abate, A.; Hollman, D. J.; Teuscher, J.; Pathak, S.; Avolio, R.; D'Errico, G.; Vitiello, G.; Fantacci, S.; Snaith, H. J., Protic Ionic Liquids as p-Dopant for Organic Hole Transporting Materials and Their Application in High Efficiency Hybrid Solar Cells. *J. Am. Chem. Soc.* **2013,** *135* (36), 13538-13548.

254. Abate, A.; Leijtens, T.; Pathak, S.; Teuscher, J.; Avolio, R.; Errico, M. E.; Kirkpatrik, J.; Ball, J. M.; Docampo, P.; McPherson, I.; Snaith, H. J., Lithium salts as "redox active" p-type dopants for organic semiconductors and their impact in solid-state dye-sensitized solar cells. *Phys. Chem. Chem. Phys.* **2013,** *15* (7), 2572-2579.

255. Abate, A.; Staff, D. R.; Hollman, D. J.; Snaith, H. J.; Walker, A. B., Influence of ionizing dopants on charge transport in organic semiconductors. *Phys. Chem. Chem. Phys.* **2014,** *16* (3), 1132-1138.